Spring 2020

Tow-Path Characterization for Automated Fiber Placement

Roudy Wehbe

TOW-PATH CHARACTERIZATION FOR AUTOMATED FIBER PLACEMENT

by

Roudy Wehbe

Bachelor of Engineering
The Lebanese American University, 2015

Master of Science
University of South Carolina, 2017

Submitted in Partial Fulfillment of the Requirements

For the Degree of Doctor of Philosophy in

Mechanical Engineering

College of Engineering and Computing

University of South Carolina

2020

Accepted by:

Zafer Gürdal, Major Professor

Ramy Harik, Major Professor

Michael Sutton, Committee Member

Sayata Ghose, Committee Member

Cheryl L. Addy, Vice Provost and Dean of the Graduate School

ACKNOWLEDGEMENTS

I would like to thank the Boeing Company for their support of the presented work. This research was mostly performed under contract SSOW-BRT-W0915-0006 through the University of South Carolina. Also, I would like to express my gratitude to my advisor Dr. Ramy Harik for the opportunity to be a part of the McNair Center, for his advice, and the unconditional support throughout my studies. Also, I would like to thank my research advisor Prof. Zafer Gürdal for the opportunity to be on this project, and my committee members Professor Michael Sutton and Dr. Sayata Ghose for the invaluable input, comments, and suggestions for the accomplished work. Many people have contributed to the achievement of the presented work. Grateful acknowledgements to Dr. Brian Tatting for the shared knowledge and research skills especially in the geometric modeling, physics-based modeling, and the numerical techniques: I have gained a lot of knowledge and I am very thankful for this experience. Also, many thanks to Sreehari Rajan with the supervision of Prof. Michael Sutton for their expertise in conducting the experimental investigations using DIC. The team of graduate students including Anis Baz Radwan, Christopher Sacco, Mazen Al Bazzan and the AFP operator Andrew Anderson under the supervision of Dr. Ramy Harik are gratefully acknowledged for pushing the limits to complete the steering on the cylinder experiments, one of the best and most memorable experiments I have worked on. Finally, I would like to thank all the members of the McNair Center for their friendship and support. And last but not least, my deepest appreciation for my family for their unconditional love and support throughout my studies.

ABSTRACT

Automated Fiber Placement (AFP) is a manufacturing process used to fabricate large composite structures for aerospace applications. During the process, the machine head deposits multiple bands of composite material named tows over a prescribed path. Temperature, speed, and compaction pressure can be varied to obtain a good layup quality. For conventional laminated plate structures manufactured using the AFP process, fibers are laid at constant angles (0°, 90°, ±45°) in straight paths. However, to manufacture complex shell structures or variable stiffness plates, curved paths are necessary in the design leading to a length mismatch between the parallel edges of the towpath. Since finite width fiber tows are originally straight, a form of tow deformation is necessary to absorb the difference in length thus ensuring good adherence to the surface substrate. In this work, several possible tow deformation mechanisms are proposed and classified as follows: (1) elastic strain deformations (tensile, compressive, shear), (2) large in-plane deformations (fiber waviness and bunching), and (3) large out-of-plane deformations (tow wrinkling and folding). Usually, large tow deformations are unfavorable and considered as defects, thus process interruption may be necessary to perform manual repairs. The aim of this proposal is to develop models able to capture tow deformations when placed on a curved path and to validate their occurrence during the AFP process. The proposed work is tackled from three different perspectives: (1) geometrical modeling, (2) physics-based modeling, and (3) experimental investigations.

Understanding the geometry of a given layup is necessary to determine critical locations for defect occurrence. A worst-case scenario is considered where all other deformation mechanisms are suppressed in favor of out-of-plane wrinkling. Governing equations for a tow placed on a general surface are derived, and a simple deformation function is applied to the shorter edge of tow showing different wrinkle patterns along the length. A simplified form of the governing equations is provided for the special case of tows steered on a flat surface. Finally, examples are presented visualizing the wrinkles patterns and showing critical locations of wrinkling for a given layup for flat and general surfaces. Relationships between the wrinkles wavelength and the steering radius can be obtained from existing mechanics models and experimental data. This information is used to improve the geometrical model, thus obtaining more accurate results for wrinkles modeling.

In the physics-based model, the influence of the material properties and tow geometry on the deformations is studied. The tow is modeled as multiple fiber bundles laying on a stiff foundation. In a first step, only in-plane deformations are allowed, thus capturing the elastic deformation mode (tensile/compressive strains) and the large in-plane deformations (fiber waviness and bunching). In a second step, out-of-plane deformations are allowed, enabling the modeling of additional tow deformations mentioned earlier such as tow wrinkling. In a last step, the interaction between the neighboring fiber bundles is investigated by considering the transverse and shear stiffness properties of the uncured tow.

Finally, experimental investigations measuring tow deformations over steered paths are carried using the Digital Image Correlation (DIC) technique. Thermoset pre-impregnated carbon fiber tows are speckled first, then placed using an AFP machine over

multiple paths with different radii of curvature. Shape and strain measurements of the deformed tows are acquired using a Stereo DIC setup. Quantified measurements of wavelength, width, and amplitude for tow wrinkles are obtained as a function of the steering radius. The effect of the substrate, time, and temperature on the formation of wrinkles is also studied. Other experiments using DIC are carried out to determine the deformation of neighboring tows within a course when steered along a constant curvature path. To understand the effect of AFP process parameters on tow deformations, a benchmark reference path on a flat surface with a linear increase in the curvature is proposed. Based on the location of the first visible defect along the length of the path, a critical steering radius is determined for each set of process parameters used. Finally, steering experiments are performed on a cylindrical tool with varying process parameters. The quality of the manufactured steered paths is assessed through image processing of acquired profilometry scans during manufacturing. Recommendations regarding optimal set of process parameters for future manufacturing activities are provided based on the measured defects along the path.

TABLE OF CONTENTS

ACKNOWLEDGEMENTS iii

ABSTRACT iv

LIST OF TABLES ix

LIST OF FIGURES x

LIST OF SYMBOLS xviii

LIST OF ABBREVIATIONS xxiii

CHAPTER 1 INTRODUCTION 1

1.1 PREAMBLE 1

1.2 AFP PROCESS DESCRIPTION 4

1.3 DEFECTS DURING THE AFP PROCESS 5

1.4 DOCUMENT OUTLINE 8

CHAPTER 2 LITERATURE REVIEW 11

2.1 DIFFERENT ASPECTS OF WRINKLING PHENOMENON 11

2.2 WRINKLING IN COMPOSITE LAMINATES 15

2.3 WRINKLING AND OTHER STEERING DEFECTS IN AFP 19

2.4 LAYUP STRATEGIES FOR AFP 26

2.5 SUMMARY 36

CHAPTER 3 GEOMETRICAL MODEL FOR TOW WRINKLING IN AFP 39

3.1 MODEL DEFINITION AND GOVERNING EQUATIONS 40

3.2 APPLICATION FOR PATHS ON FLAT AND GENERAL SURFACES 55

3.3 Model Improvements and Application to Thermoset Materials 62

3.4 Conclusions 72

Chapter 4 Physics-Based Model of Tow Deformations in AFP 75

4.1 In-Plane Deformations for a Single Fiber bundle 76

4.2 Out-of-plane deformations for a single fiber bundle 92

4.3 Interaction of fiber bundles in the transverse direction 103

Chapter 5 Experimental Investigations of AFP Steered Tows 117

5.1 Experimental Investigation of Prepreg Tow Wrinkling using Stereo DIC 117

5.2 Effect of Processing Parameters on Tow deformations 138

5.3 Steering Experiments on Cylindrical Shell 165

Chapter 6 Conlusions and Future Work 183

References 191

Appendix A Numerical Solution For Nonlinear Systems of Differential Equations 197

A.1 Newton's Method for Nonlinear Problems 197

A.2 Finite Difference Technique For Linear ODE 198

A.3 Initial & Boundary Conditions 201

Appendix B Critical Radius of Curvature as Function of Process Parameters For the Spiral Tests 205

LIST OF TABLES

Table 2.1 Examples of wrinkling of skins on softer elastic foundations [4] 12

Table 3.1 Material properties and geometry of uncured tow obtained from [17,23,27]... 65

Table 4.1 Material property and geometry of the tow 84

Table 4.2 Material property and geometry of the tow 89

Table 4.3 Material property and geometry of the tow deforming out-of-plane..... 100

Table 4.4 Material property and geometry of the tow 103

Table 4.5 Material property and geometry of the tow deforming out-of-plane..... 108

Table 4.6 Material property and geometry of the tow deforming out-of-plane..... 116

Table 5.1 Camera and lens parameters for stereovision system [59] 118

Table 5.2 Stereo DIC parameters [59] 119

Table 5.3 Summary of the wavelength, width, and amplitude measurements of the wrinkles [59] 125

Table 5.4 Process parameters and their corresponding levels for the steering tests 145

Table 5.5 Recommended process parameters 147

Table 5.6 Process parameters used in the linear tests 161

Table 5.7 Course description and corresponding process parameters 170

Table 5.8 The parameters and levels considered in the steering experiments on the cylinder 171

Table 5.9 Areal percentage of defects for the steered portion of the constant curvature arcs and the spiral curves 179

LIST OF FIGURES

Figure 1.1 Gantry type Automated Fiber Placement Machine at the McNair Center for aerospace innovation and research 3

Figure 1.2 Schematic of typical defects during AFP process 6

Figure 1.3 Length mismatch between a tow and a curved tow-path 7

Figure 1.4 Deformation mechanisms for differential length absorption..... 8

Figure 2.1 Wavy pattern in an originally flat eggplant leaf after 12 days of injection of growth hormone [3] 12

Figure 2.2 Basic wrinkling/buckling model of a thin film laying on soft foundation [4]..... 12

Figure 2.3 Wrinkle patterns in a film subjected to non-uniform strain field [8] 13

Figure 2.4 Wrinkles in a polyethylene sheet under uniaxial tensile strain [5]..... 13

Figure 2.5 Schematic of the diaphragm forming process [9]..... 15

Figure 2.6 Consolidation over external radius process [10] 16

Figure 2.7 CT image of a corner wrinkle on a spar [10]..... 16

Figure 2.8 Wrinkles in layup over internal radius (Left), wrinkles converting to in-plane fiber waviness after cure (Right) [11]..... 17

Figure 2.9 Wrinkle formation due to shear slip between the composite and the mold [13] 17

Figure 2.10 Level of misalignment generated by draping narrow and wide UD prepreg strips across a 100mm diameter hemisphere [14]..... 18

Figure 2.11 Overview of the most common steering defect [1] 19

Figure 2.12 In-plane waviness and sheared tows due to steering [18] 19

Figure 2.13 Quality assessment of a steered layup by comparing defect persistence after adding and removing a 90° course [22] 21

Figure 2.14 Wrinkle modeled as an anisotropic plate on one-parameter elastic foundation [23] 23

Figure 2.15 Wrinkle modeled as an anisotropic plate resting on viscoelastic Pasternak foundation [27] 23

Figure 2.16 Projection of a major axis on the surface [42] 29

Figure 2.17 Reference curve using an iterative algorithm [47] 29

Figure 2.18 Geodesic reference curve on a Y shape tube [47] 30

Figure 2.19 Linear angle variation reference curve [48] 31

Figure 2.20 Cross section of placement surface showing calculation of offset points [41] 33

Figure 2.21 Error associated with placing a point on a surface with circular arc cross section [41] 33

Figure 2.22 (a) Initial path generation, (b) Curve offset by taking perpendicular arcs, (c) Path extension [42] 34

Figure 2.23 Different steps of the Fast Marching Method to offset a reference curve [55] 35

Figure 3.1 Surface and Path definition 43

Figure 3.2 Parallel curves on the surface 47

Figure 3.3 Schematic of a wrinkle of a general surface 50

Figure 3.4 Schematic of a wrinkle for the simplification 54

Figure 3.5 Deformed tow placed on a circular path: 4 different mode shapes 56

Figure 3.6. Effect of tow width on the wrinkles' amplitude 57

Figure 3.7 Example NURBS surface 58

Figure 3.8 Geodesic curvature of the reference path on the NURBS surface 59

Figure 3.9 First 4 mode shapes of a tow placed on a NURBS surface 60

Figure 3.10 Wrinkling map for the 45° layup on the NURBS surface 61

Figure 3.11 Geodesic curvature color map for different layup on the NURBS surface ... 62

Figure 3.12 Wrinkle wavelength as a function of steering radius based on mechanics model (3.55) 65

Figure 3.13 Shape of the wrinkle used in geometrical model and the improved model based on mechanics 68

Figure 3.14 Shape of the wrinkle used in the improved model based on experimental data 68

Figure 3.15 Measured wrinkle amplitude as a function of steering radius 69

Figure 3.16 Measured wrinkle width as a function of steering radius 69

Figure 3.17 Measured wrinkle wavelength as a function of steering radius 69

Figure 3.18 Comparison between the geometrical model and the improved model from experimental data for a steering radius of 305 mm 70

Figure 3.19 Model prediction vs experimental measurements of the out-of-plane displacements for a path steered at 305 mm radius at a line 1 mm above the bottom edge 71

Figure 3.20 Wrinkle prediction for a layup sinusoidal paths with variable amplitudes (units in mm) 72

Figure 4.1: Schematic of a tow during AFP 76

Figure 4.2 Strain-rotation relationship and displacement components 79

Figure 4.3 Iterative approach to obtain the unknown forces fx and fy 82

Figure 4.4. Deformed fiber bundles under compression at different tow length 85

Figure 4.5. Solution of equation (4.20) for 4 bundles under compression at L = 20 mm 86

Figure 4.6. Deformed fiber bundles under tension at different tow length 87

Figure 4.7. Solution of equation (4.20) for 4 bundles under tension at L = 40 mm 88

Figure 4.8: Deformed fiber bundles for $k = 106\ N/m2$ 89

Figure 4.9: Effect of the foundation stiffness on the displacement in the transverse direction 91

Figure 4.10: Effect of the steering radius on the displacement in the transverse direction for $k = 0$ 92

Figure 4.11: Effect of the steering radius on the displacement in the transverse direction for $k = 107\ N/m2$ 92

Figure 4.12: Strain-rotation relationship in 3D 93

Figure 4.13 Iterative approach to obtain the unknown forces 98

Figure 4.14: Deformed fiber bundles in 3D under combined loading 99

Figure 4.15: Maximum z-displacement of the fiber bundles at L/2 99

Figure 4.16: Solution of equation (4.51) for 5 bundles under combined loading 100

Figure 4.17: Effect of the length on the out-of-plane deformation of bundles under compression 102

Figure 4.18: Effect of the foundation stiffness in the z-direction on the wrinkle formation 103

Figure 4.19. Transverse strain between neighboring fiber bundles 104

Figure 4.20 Shear strain between neighboring fiber bundles 104

Figure 4.21: Deformed fiber bundles under compression with variable E2 109

Figure 4.22: Effect of E2 on the maximum transverse displacement for fibers under compression 109

Figure 4.23: Deformed fiber bundles under compression with variable $G12$ 110

Figure 4.24: Effect of G12 on the maximum transverse displacement for fibers under compression 111

Figure 4.25: Effect of $E2$ and k on the maximum transverse displacement for fibers under combined loading 113

Figure 4.26: Effect of E2 on the out-of-plane displacement of the fiber bundles 116

Figure 5.1 Image acquisition process [59] 119

Figure 5.2 Speckled and stitched images of the 4 different paths [59] 121

Figure 5.3 Photograph of the tool, initial layers of the substrate, AFP head and initial length of patterned, unspooled tow that is imaged before re-spooling [59] 122

Figure 5.4 Out-of-plane displacement for the straight path showing the locations and magnitudes of the overlaps in the substrate [59] 123

Figure 5.5 Out-of-plane displacement for the 4 different path at a line 1 mm above the bottom edge of the tow in the reference configuration [59] 123

Figure 5.6 Effect of substrate gap and overlap on the out-of-plane displacement for the 305 mm radius path [59] 124

Figure 5.7 Out-of-plane displacement for a line at 1 mm above the bottom edge of the reference configuration for the path steered at 305 mm [59] 126

Figure 5.8 Transverse strain map for the tow steered at 305 mm radius [59] 127

Figure 5.9 Observed defects other than wrinkling during steering [59] 127

Figure 5.10 Second steering design during the first manufacturing trial 129

Figure 5.11 Second steering design during the second manufacturing trial 129

Figure 5.12 Obtained defects in the second design during the first trial for 635 mm radius 130

Figure 5.13 Completed second design (photograph taken after completing the experiment) 130

Figure 5.14 Average of the measured wrinkles amplitude for the placed tows during test2 133

Figure 5.15 Average of the measured wrinkles width for the placed tows during test2 133

Figure 5.16 Average of the measured wrinkles wavelength for the placed tows during test 2 134

Figure 5.17 Third steering design 135

Figure 5.18 Steering defects during the 3rd design for 318 mm radius of curvature 136

Figure 5.19 Average of the measured wrinkles amplitude for the placed tows during test 3 137

Figure 5.20 Average of the measured wrinkles width for the placed tows during test 3 137

Figure 5.21 Average of the measured wrinkles wavelength for the placed tows during test 3 137

Figure 5.22 Single tow steered at different radii of curvature [17] 139

Figure 5.23 Eight tows course steered at different radii of curvature [19] 139

Figure 5.24 Example of a clothoid with different values of a and $0 < s < 4$ 141

Figure 5.25 Benchmark path with $Rmin = 300\ mm$ and $Lmax = 750\ mm$ 142

Figure 5.26 Programmed curved paths in CATIA 143

Figure 5.27 Power of Humm3 (Watts) as function of voltage and pulse duration for 60 Hz frequency 144

Figure 5.28 AFP monitor displaying the actual feed rate during manufacturing 146

Figure 5.29 Pressure sensors and thermocouples placed along the curved path 146

Figure 5.30 Tow folding 148

Figure 5.31 Tow wrinkling 148

Figure 5.32 In-plane fiber waviness 148

Figure 5.33 Through thickness tow splitting 148

Figure 5.34 Obtained layup for the speed test 149

Figure 5.35 Speed profiles for the placed courses 151

Figure 5.36 Critical radius of curvature for the laid tows during the speed test 151

Figure 5.37 Obtained layup for the temperature test 153

Figure 5.38 Temperature and pressure measurements for course 103 during the temperature test 154

Figure 5.39 Measured peak temperature as function of heater voltage 155

Figure 5.40 Critical radius of curvature for the laid tows during the temperature test ... 155

Figure 5.41 Obtained layup for the compaction test 156

Figure 5.42 Tow folding at low compaction force (course 101, 178 N compaction) 157

Figure 5.43 In-plane waviness at high compaction force (course 104, 750 N compaction) 157

Figure 5.44 Critical radius of curvature for the laid tows during the compaction test ... 157

Figure 5.45 Obtained layup for the tow tension test 158

Figure 5.46 Critical radius of curvature for the laid tows during the tow tension test ... 158

Figure 5.47 Obtained layup for the high speed, pressure, and temperature test 159

Figure 5.48 Critical radius of curvature for the laid tows during the tow tension test ... 160

Figure 5.49 Sensors placed along the length of a course oriented at 0° 161

Figure 5.50 Average of measured peak temperatures as function of layup speed and heater voltage for both linear and steered tests 163

Figure 5.51 Average of measured pressure as function of roller compaction and layup speed for both linear and steered tests 164

Figure 5.52 Average of measured pressure as function of speed and heater voltage for the linear tests at constant compaction force of 445N 165

Figure 5.53 Steered paths on flattened cylinder..... 167

Figure 5.54 Steered paths on cylinder..... 167

Figure 5.55 Programmed constant curvature arcs on cylindrical mandrel 168

Figure 5.56 Programmed spiral curves on cylindrical mandrel 168

Figure 5.57 Recorded feedrate at 10% and 100% for courses 150 and 154 respectively 172

Figure 5.58 Temperature readings from the thermocouples for course 137..... 173

Figure 5.59 Measured temperature as function of the feedrate 174

Figure 5.60 Profilometry scanning of steered layup using ACSIS system..... 175

Figure 5.61 Sheared tows..... 175

Figure 5.62 Fiber waviness 175

Figure 5.63 Stitched scans for R50 176

Figure 5.64 Stitched scans for R25 176

Figure 5.65 Stitched scans for the spiral courses 177

Figure 5.67 Defect detection for the processed scan of the R50 courses 180

Figure 5.68 Defect detection for the processed scan of the R25 courses 180

Figure 5.69 Stitched scans for R25 181

Figure 5.70 Defect detection for the processed scan of the R12.5 courses 181

Figure 5.71 Defect detection for the spiral courses 182

Figure A.1 Finite difference region of interest 199

Figure A.2 The governing algebraic equations in matrix form 200

Figure A.3 Boundary conditions applied to the system of algebraic equations..... 204

LIST OF SYMBOLS

A. Geometric Modelling

- ***Latin Symbols***

a_w Amplitude of the wrinkle

$\boldsymbol{B}$ Binormal vector

$\boldsymbol{C}$ Curve in parametric form

$\boldsymbol{C_p}$ Curve in parametric form parallel to $\boldsymbol{C}$

d Distance

e, f, g Coefficients of the second fundamental form

E, F, G Coefficients of the first fundamental form

$\boldsymbol{G}$ Geodesic curve

k Amplitude of the wrinkling rotation angle

k_g Geodesic curvature

K Gaussian curvature

$\boldsymbol{KV}$ Knot vector for a 2D curve

l_w Wrinkle/tow length separated from the substrate

L Length of a tow

s Parameter along the arc-length

$\boldsymbol{S}$ Parametric surface

$\boldsymbol{S_{tow}}$ Parametric surface of a tow on the surface $\boldsymbol{S}$

$\boldsymbol{S_w}$ Wrinkled surface of a tow

n Parameter in the normal direction

N Number of wrinkles

$\boldsymbol{N}$ Normal vector

$N_{i,p}$ B-spline basis function of degree p

p Degree of a spline curve or degree of a spline surface in the u-direction

$\boldsymbol{P}$ Point in three dimensional coordinates

q Degree of a spline surface in the v-direction

R Radius of curvature

$\mathcal{R}$ Rodrigues' rotation matrix

t Parameter in the tangential direction

$\boldsymbol{T}$ Tangent vector

u Surface parameter in the first direction

u_c Coordinates of a path in the *u*-direction

$\boldsymbol{U}$ Knot vector of a spline surface in the u-direction

v Surface parameter in the second direction

v_c Coordinates of a path in the *v*-direction

$\boldsymbol{V}$ Knot vector of a spline surface in the v-direction

w Width of a tow

w_i Weight of a control point i

- ***Greek Symbols***

β Wrinkle rotation angle

Γ_{jk}^{i} Christoffel symbols

ε_l Strain in the longitudinal direction

λ_w Wavelength of the wrinkles

ρ Radius of curvature

- ***Mathematical Operators***

B Bold style representing a vector quantity

$\times$ Cross product

$\cdot$ Dot product

$\| \ \|$ Euclidean norm of a vector

$\widehat{\ }$ Unit Vector

$_s$ Subscript representing differentiation with respect to the selected variable

$'$ Differentiation with respect to the parameter t

B. Physics-Based Modelling

- ***Latin Symbols***

A Cross-sectional area

A_{ij} Components of the extensional stiffness matrix

$\boldsymbol{C}, \boldsymbol{C_p}$ Curve representing the centerline of the tow path, curve parallel to the centerline

d Distance from the neutral axis/ centerline of the tow path

D_{ij} Components of the bending stiffness matrix

E_1, E_2 Modulus of elasticity along, orthogonal to the fiber's direction

f_x, f_y, f_z Forces in the *x*, *y*, and *z*-direction

$\mathbf{f}$ System of the nonlinear governing equations

$\boldsymbol{F}$ Force vector

$\mathcal{F}$ Integrand part of the Euler-Lagrange functional

$\boldsymbol{G}$	Error vector function
G_{12}	Shear modulus
H	Tow thickness
i	Index referring to a fiber bundle
I	Moment of inertia
j	Index referring to a discretized point within the finite difference technique
J	Jacobian matrix
k_x, k_y, k_z	Elastic modulus of the foundation in the *x*, *y*, and *z*-direction
K	Energy stored in elastic foundation
l'	Strain along the length
L	Length of the tow
$\boldsymbol{\mathcal{O}}$	Error term in Taylor series expansion
n	Number of fiber bundles within the tow
N	Number of finite difference steps within a region of interest
r	Direction perpendicular to the fiber path (radial direction)
s	Direction along the fiber path (arc-length)
u	Displacement in the *x*-direction
u_r, u_s	Displacement in the radial direction, along the fiber direction
U	Elastic strain energy
U_r, U_s	Elastic strain energy due to transverse, shear strains between fiber bundles
v	Displacement in the *y*-direction
w	Displacement in the *z*-direction
w_b	Width of a fiber bundle within the tow

w_t Tow width

W Work done by the forces

$\boldsymbol{X}$ Vector containing the unknown functions of the governing equations

- ***Greek Symbols***

β Out-of-plane rotation angle

γ In-plane rotation angle

γ_{sr} Shear strain between fiber bundles

δ Newton's step

Δ Finite difference step

$\boldsymbol{\Delta}$ Total displacement vector

ϵ^o Mid-plain strain

ε_r Transverse strain between fiber bundles

ζ, ξ, ψ Intermediate integration variables

κ^0 Mid-plane curvature

ν_{12} Poisson's ratio

Π Total energy

ρ Radius of curvature

LIST OF ABBREVIATIONS

AFP ..... Automated Fiber Placement

ATL ..... Automated Tape Laying

BC ..... Boundary Condition

BVP ..... Boundary Value Problem

CAD ..... Computer Aided Design

CFRP ..... Carbon Fiber Reinforced Plastics

CTS ..... Continuous Tow Shearing

DIC ..... Digital Image Correlation

FEA ..... Finite Element Analysis

FMM ..... Fast Marching Method

FRP ..... Fiber Reinforced Plastics

FW ..... Filament Winding

GFRP ..... Glass Fiber Reinforced Plastics

IVP ..... Initial Value Problem

LU ..... Lower-Upper

NURBS ..... Non-Uniform Rational B-Spline

ODE ..... Ordinary Differential Equation

RDCB ..... Rigid Double Cantilever Beam

RTM ..... Resin Transfer Molding

STL ..... Stereolithography

UD ..... Unidirectional

VARTM ..... Vacuum Assisted Resin Transfer Molding

CHAPTER 1

INTRODUCTION

1.1 PREAMBLE

Composite materials are known to man since thousands of years; the usage of wood and natural glue, straw reinforced clay bricks to build structures are few of these examples. Recent development in the constituent materials, mainly continuous fibers and polymer matrices, made the newly engineered composite materials more competitive and desirable. This advancement attracted several industries such as the aerospace, automotive, and renewable energy, due to the possibility of simultaneously increasing the performance and reducing the weight of structures.

Specifically, for the aerospace industries, fiber reinforced plastics (FRP) are attractive compared to their metallic counterparts due their improved mechanical properties, possibility of weight reduction, better corrosion resistance, and enhanced maintenance. However, these advantages can be undermined due to defects that occur during the manufacturing process, resulting in weaker parts than designed.

Manufacturing high performance composites part for aerospace applications is historically done using glass-fiber reinforced plastics (GFRP), or carbon-fiber reinforced plastics (CFRP) in a manual layup process. Hand layup consists of cutting and laying the fibers in a mat form on an open mold successively to achieve the required part thickness in a prescribed set of orientations referred to as the stacking sequence. Hand layup can use

either dry or wet fibers, and the fibers can be unidirectional (UD) or woven. For the dry process, dry fibers are placed on the surface of the mold, and resin is either poured or infused to the part under vacuum, in resin transfer processes such as resin transfer molding (RTM) or vacuum assisted RTM (VARTM). Consequent oven curing might be necessary to achieve the desired properties. To avoid the risk of partially wetting the fibers, getting high void contents, and/or low fiber volume fraction, high performance composites usually use pre-impregnated fibers or also called prepreg. The process of hand laying prepreg is similar to the dry fibers, with additional option to use debulking process between the consecutive layers to reduce the amount of air entrapped between layers. The curing process is usually done at high pressure and temperature in an autoclave to further reduce the number of voids. For some complex parts, hand layup can be done on a flat tool and later forming process is used to obtain the final shape. Quality control during the manufacturing process of the hand layup is usually done by visual inspection, with recent notable efforts to have automated inspection systems.

To meet the increasing demand of the aerospace industry, the productivity of the composite manufacturing must be augmented. Several programs such as the Boeing 787 and the Airbus A350 have approximately 50% by weight of their structural components made from composites. Automation is a solution to achieve this high volume of production. First, Filament Winding (FW) and Automated Tape Laying (ATL) introduced in the 1960s and 1970s, then Automated Fiber Placement (AFP) was commercially available in the 1980s [1] to answer both productivity and consistency of the manufacturing process. ATL consists of delivering a wide tape of prepreg, generally on flat or slightly curved surfaces, while removing automatically the backing material from the prepreg. Temperature, speed

and tape tension can be varied during the process to achieve a good layup. The problem with using wide prepreg tapes is the possibility of having significant defects such as wrinkling while laying on complex structures, as well as the increase in material waste. As for FW, wrapping the fiber bundles around the structure requires continuous tension to ensure compaction from layer to layer. This limits the fibers from changing direction easily and restricts the fibers from being cut until the structure is finished. AFP was introduced in the 1980s as a combination of the best of the two processes. AFP is similar to the ATL process; however, the wide tape is replaced by several narrow prepreg slices called tows or slit tape which can be individually controlled. The advantage of using narrower tapes is two folds: (1) to reduce waste, (2) to increase process flexibility enabling advanced capabilities such as manufacturing complex surfaces.

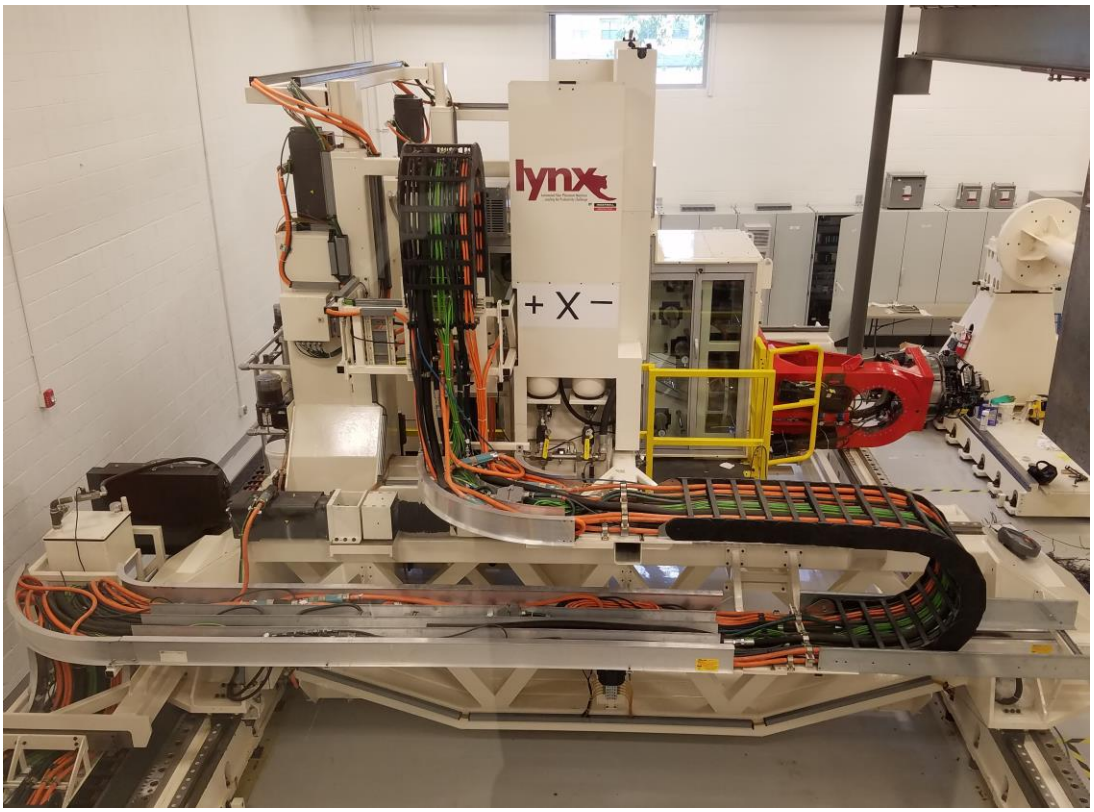

Figure 1.1 Gantry type Automated Fiber Placement Machine at the McNair Center for aerospace innovation and research

1.2 AFP PROCESS DESCRIPTION

Automated fiber placement consists of using numerically controlled robot or gantry type machine (Figure 1.1) to deliver the material with required position and orientation. Typical material that is laid down using AFP machines have a width of ⅛ in, ¼ in, or ½ in. A single strip of material is named tow. Normally AFP delivers multiple tows in a single sequence to form a course, while a sequence of courses is termed ply. Industry tends to optimize production rates and thus higher number of tows and larger tow width are preferred. The choice of tow width heavily depends on the complexity of the manufactured part to avoid defects such as wrinkling or folding which will be demonstrated in this work. The occurrence of such defects is usually undesirable; this current topic is heavily researched to understand the effect of defects on the manufactured part. Smaller width tows are capable of manufacturing more complex shapes, while wider ones are used for flatter parts. Hence, reducing the quantity of defects by using narrower tows comes to the cost of lowering productivity.

The main material used for AFP is impregnated tows or slit tape. Other material such as dry fiber or thermoplastic are used to a lesser extent with a tendency to increase in the future. Individual tows are wound on a bobbin and stored in the creel for the gantry type machine or directly mounted on the machine head for the robotic type. Additional backing material is supplied between the tows to reduce the shredding defect while unspooling. The tows are fed through the machine head to the tow tensioner then through the compaction roller where additional heat and pressure is applied for the material to adhere to the surface. The roller material is usually flexible to increase the contact area and to reduce the void between the layers. Typical external heating sources used in AFP are

torches, laser, infrared radiation, and recently pulsed light sources. Another advantage of the AFP process is the ability to control the tows individually and to cut and restart the tows as necessary. The cut-restart capability allows for further reduction in waste material compared to the ATL and hand layup, while controlling the speed of the tows individually makes it possible to lay material over complex surfaces and some in-plane steering. The limitation of the cutting and restarting mechanism is dictated by the minimal course length which corresponds to the distance between the nip point and the cutting mechanism and dictates the smallest features that the AFP can manufacture.

1.3 DEFECTS DURING THE AFP PROCESS

Due to the complexity of the AFP mechanism, the material being used, or the part to be manufactured, several defects may arise during the manufacturing process and can be detrimental to the produced part. Some of these defects can be related to the material variability, some to the machine or process parameters and some to the design or geometrical model by itself.

For instance, defects such as gaps and overlaps (see schematic in Figure 1.2) occurring between adjacent tows or courses can be related to some machine tolerances, calibration error or material variability, and sometimes cannot be detected during the design phase. However, these features are necessary and present in the design especially for the case of complex surfaces and variable stiffness panels to avoid excessive steering that might lead to other defects such as wrinkling. Other similar position errors can occur at the edge of the part or at the start or end of a tow, whereas a twist and a fold can sometimes be related to the machine rotational movements or material tack. A spliced tow is also present in the material provided by the manufacturer and corresponds to a small

overlapping region necessary to join two tows in the spool. A schematic of these defect is presented in Figure 1.2. The presence of these defects during the manufacturing is usually undesirable, and in most cases, the process is interrupted for manual repairs, which leads to a decrease in the productivity. An experimental study [2] was conducted on the coupon level isolating 4 types of these defects (gap, overlap, half gap/overlap, and twist) and trying to understand their effect on the ultimate strength. However, the influence on the overall structure is not well understood yet, and further research is needed to decide whether or not a repair is necessary during manufacturing.

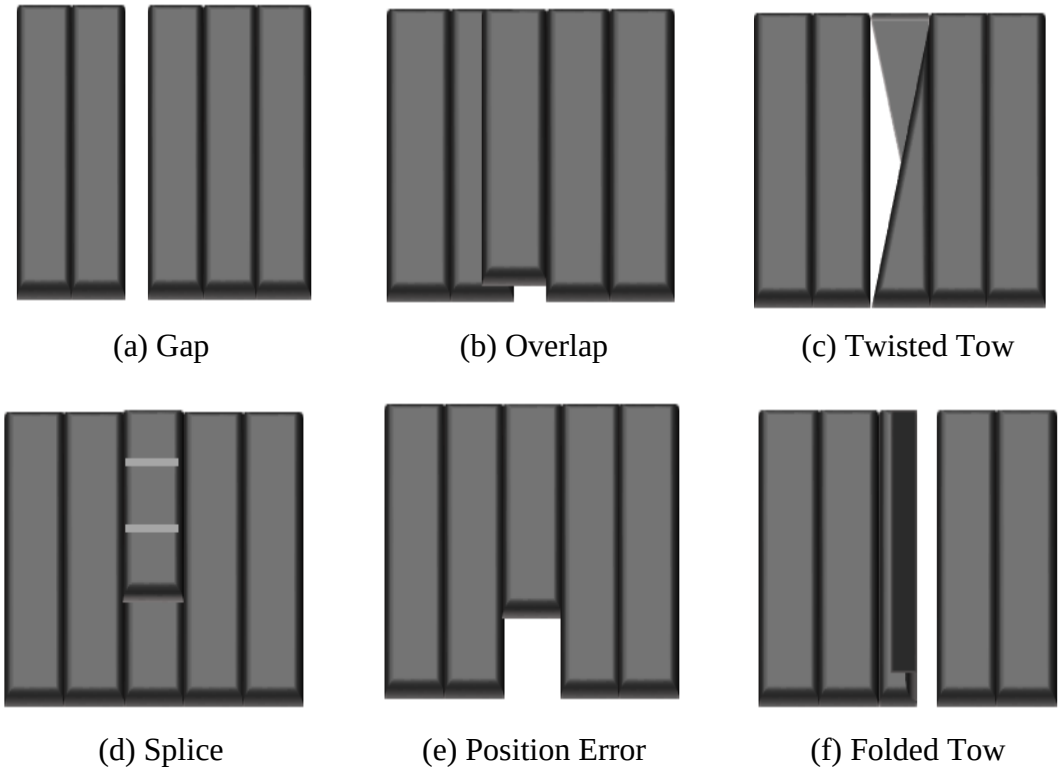

(a) Gap (b) Overlap (c) Twisted Tow

(d) Splice (e) Position Error (f) Folded Tow

Figure 1.2 Schematic of typical defects during AFP process

One major defect that occurs during steering is tow wrinkling. Wrinkling or sometimes referred to as puckering, or tow buckling is the out-of-plane deformation of the tow edges that resembles buckling patterns. Tow wrinkling during AFP process is mainly

observed on flat surfaces while steering the fiber-tow to follow non straight (curved/non-geodesic) paths. It also occurs on complex curved surfaces even if the center of the tow follows a geodesic path due to the finite width of the tow and the surface curvature. The primary reason for wrinkling occurrence is the mismatch in length between the prescribed path on the surface and the actual length of the tow delivered from the machine head (Figure 1.3). If the length of the tow fed from the machine head has a length L, and it has to be placed on a curved path whose centerline has a length L, then the portion of the tow laying inside the vicinity of the curve has to absorb an additional length of ΔL, and the portion laying on the outer side of the vicinity has to extend an additional length of ΔL.

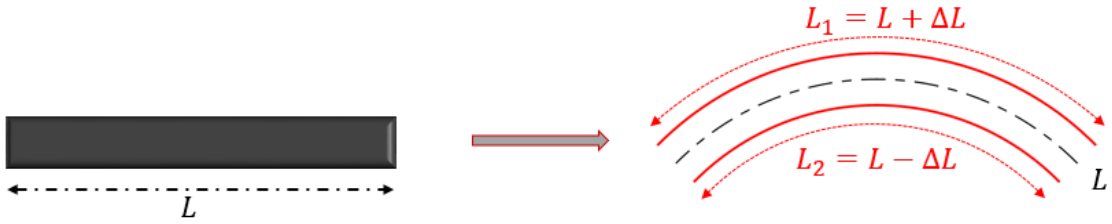

Figure 1.3 Length mismatch between a tow and a curved tow-path

To absorb these differential lengths caused by the mismatch between the tow and the prescribed path, six deformation mechanisms are suggested and presented in Figure 1.4. These mechanisms can be classified under three categories: (I) elastic deformations, (II) in-plane deformations, and (III) out-of-plane deformations. For the case (I) of elastic deformations, the excess of length on the shorter/inner side of the tow-path is absorbed by compressive strains in the tow, and the shortage in length on the longer/outer side of the tow-path is absorbed by tensile strains in the tow, in a way similar to the beam bending theory. Also, shear deformations between individual fibers within the tow especially near the start and the end of the tow-path can absorb some of the differential length. As for the case (II) of in-plane deformations, tow bunching occurs on the tensile side of the tow and

is characterized by a local increase in the thickness of the tow and fiber misalignment. In this case, the fibers laying on the outer side of the tow-path are actually shorter than the path itself and tend to move towards the centerline where the length is somehow similar. The presence of good tackiness or adhesion between the tow and the surface beneath (other tows, or the tool surface) is essential for this mechanism, otherwise the tow will tend to lift from the surface and fold over itself as presented in the out-of-plane mechanism (III). As for the compressive side, the in-plane waviness can occur in the presence of a good surface adhesion, otherwise, out-of-plane wrinkling can occur.

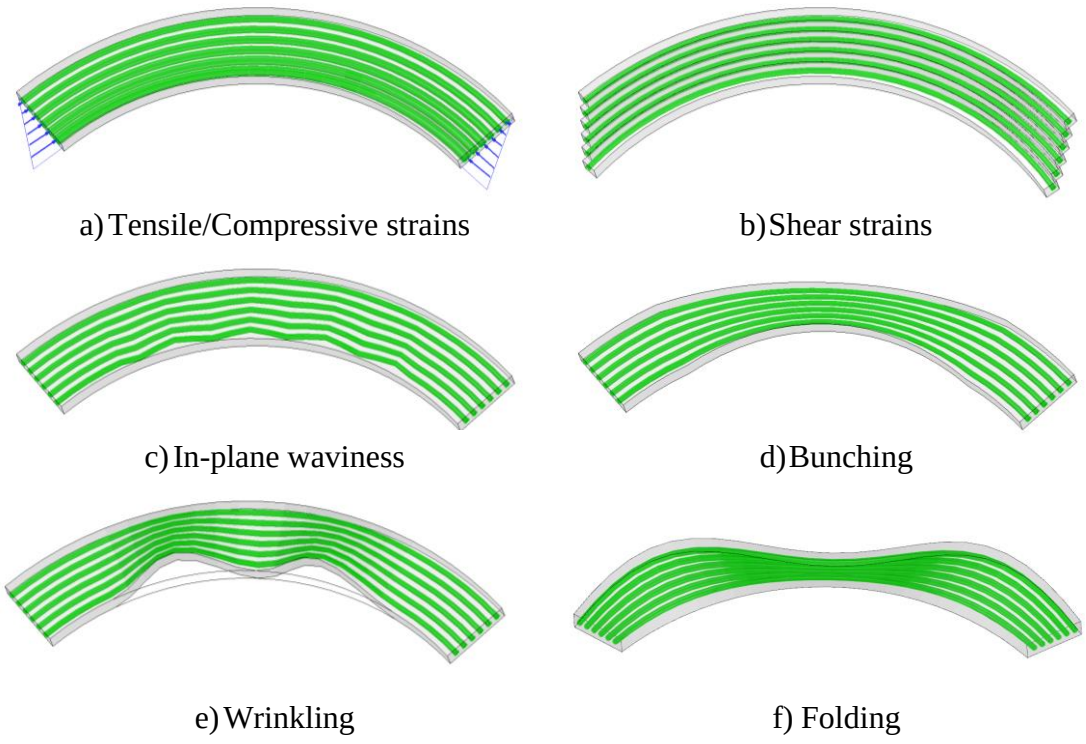

Figure 1.4 Deformation mechanisms for differential length absorption

1.4 DOCUMENT OUTLINE

In this document, modeling and understanding tow deformations are accomplished through three different aspects: (1) Geometrical modeling, (2) physics-based modeling, and

(3) experimental investigations. Hence, the remaining chapters in this document will include the following:

Chapter 2 presents a literature survey of the wrinkling phenomenon occurring in several aspects and fields, and the effort made to model it. Then, the wrinkling and other forms of large fiber deformations are investigated in several manufacturing processes of composites laminates, especially automated fiber placement. Finally, several layup strategies are demonstrated as potential candidates for wrinkling analysis from a geometrical perspective.

Chapter 3 investigates the geometrical aspect of tow wrinkling. A worst-case scenario is considered where all other deformation mechanisms are suppressed in favor of out-of-plane wrinkling. Therefore, the difference in length between the edges of the tow-path is absorbed by an out-of-plane wrinkle. Governing equations for a tow placed on a general surface are derived, and a cosine shape function is applied to the shorter edge of tow showing different wrinkle patterns along the length. A simplified form of the governing equations is provided for the special case of tows steered on a flat surface. Several modeling examples are presented visualizing the wrinkles pattern and showing critical locations of wrinkling for a given layup for flat and general surfaces. Finally, information regarding the wrinkles wavelength and width are determined either from mechanics models or experimental investigations and implemented in the geometrical model to get a better approximation of the wrinkles pattern.

Chapter 4 presents the physics-based model for the tow deformations. The tow is modeled as multiple fiber bundles laying on a stiff foundation. In a first step, only in-

plane deformations are allowed, thus capturing the elastic deformation mode (tensile/compressive strains) and the large in-plane deformations (fiber waviness and bunching). In a second step, out-of-plane deformations are allowed, thus tow wrinkling and folding can occur in addition to the other deformation mechanisms. Finally, the interaction between the neighboring fiber bundles is investigated by considering the transverse and shear stiffness properties of the uncured tow.

Chapter 5 presents the experimental investigations of tow deformations on flat and cylindrical surfaces. Stereo DIC is used to acquire shape and strain measurements for thermoset pre-impregnated carbon fiber tows placed using an AFP machine over multiple paths with different radii of curvature. Measurements of wrinkles wavelength, width, and amplitude are obtained as a function of the steering radius. The effect of the substrate, time, and temperature on the formation of wrinkles is discussed. Investigations regarding the effect of process parameters on tow deformations are carried through several experimental tests using a novel proposed curved path. Finally, steering experiments are performed on a cylindrical tool while varying the process parameters and capturing the quality of the layups through image processing of acquired profilometry scans during manufacturing.

Chapter 6 ends with concluding remarks and possible work to be investigated in the future.

CHAPTER 2

LITERATURE REVIEW

This literature review chapter starts by generally discussing the wrinkling phenomenon in nature, and the effort made to model it as a thin film on a compliant substrate. Then, an overview of wrinkling during composite manufacturing is presented such as wrinkling during forming process, and during consolidation over an internal or an external radius. Afterwards, wrinkling and other tow deformations during the AFP process are described, the reasons behind their formation are explained, and the current literature on their investigation is also discussed. Finally, the geometric aspect behind the layup strategies for the AFP process is presented from the creation of the reference curves to obtaining total surface coverage and their relationship to tow wrinkling.

2.1 DIFFERENT ASPECTS OF WRINKLING PHENOMENON

Wrinkling, or the word referring to the creation of lines, ridges, or creases on a surface due to a contraction, folding, crushing or the like, is a common phenomenon in life, and is mainly observed in elderly people skin and fabric or clothing items. However, this phenomenon stretches to several other aspects and can be observed in the nature in flowers and leaves [3] due to the natural excessive growth of cells making a wavy patterns (Figure 2.1). In addition, the scale of this phenomenon extends from elastomers at the nanoscale to mountains over several kilometers as presented in [4] and reproduced here in Table 2.1. Other case studies on wrinkling were discussed in [4], which were based on the buckling

model of a thin film laying on soft foundation (Figure 2.2), such as wrinkling in human skin, wrinkling in rigid sheets on elastic and viscoelastic foundations. It was concluded that wrinkling is not always a bad phenomenon as depicted in the wrinkling of human skin, it can also be used as a guide in materials assembly, fabrication of several functional devices and assist in measuring material properties.

Figure 2.1 Wavy pattern in an originally flat eggplant leaf after 12 days of injection of growth hormone [3]

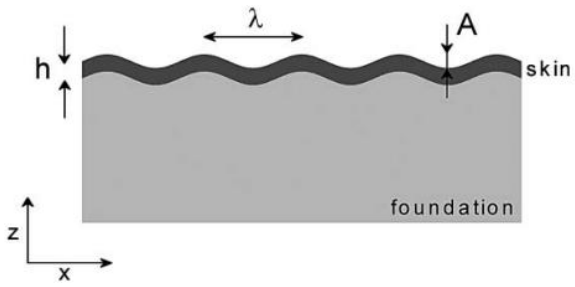

Figure 2.2 Basic wrinkling/buckling model of a thin film laying on soft foundation [4]

Table 2.1 Examples of wrinkling of skins on softer elastic foundations [4]

Context	*Wavelength (m)*	*Skin*	*Foundation*	*Compressive force*
Mountains	10^{3}	Earth crust	Earth mantle	Tectonics
‘‘Mosquito’’ wing failure	10^{-1}	Plywood	Balsa	Bending
Modern sandwich failure	10^{-2}	Glass fiber-reinforced epoxy	Polyurethane foam	Bending
Skin wrinkling	10^{-3}	Epidermis	Dermis	Skin stretching/compression
Fruits	10^{-3}	Skin	Flesh	Drying
Physically treated elastomers	10^{-8}-10^{-3}	Metal or oxide film	Elastomer	Pre-stretching, stretching or thermal expansion

A general theory for wrinkling is presented in [5] based on the balance between the bending energy and the stretching energy of the thin film on a substrate, and constraining the problem by imposing the geometry with a Lagrange multiplier, and minimizing the

total energy of the system. This theory can be extended to cover a large amount of physical problems using a scaling law, in which the wavelength of the wrinkles λ is proportional to $K^{-1/4}$ with K being the stiffness of the elastic substrate, and the amplitude of the wrinkles is proportional to the wavelength λ. In addition, this work identifies two main wrinkling behavior: the compression wrinkles which arise in one dimensional stress field and the tensile wrinkles which arise in two-dimensional stress field (Figure 2.3). The general theory presented in [5] was inspired from wrinkling problem that appears in thin stretched elastic sheets as shown in Figure 2.4. These wrinkles appear due to compressive stresses induced by Poisson's effect in the central region of the sheet [6]. However, it has been recently shown that Poisson's effect is not only the main reason, but also shear warping deformations triggering the wrinkles in stretched sheet [7].

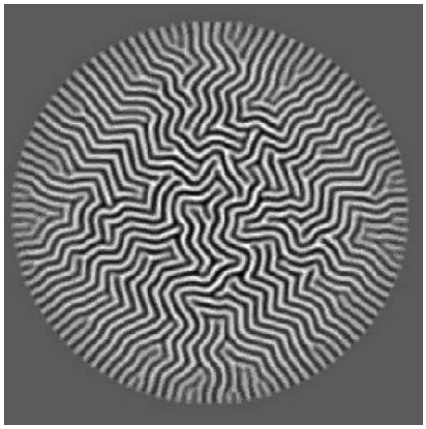

Figure 2.3 Wrinkle patterns in a film subjected to non-uniform strain field [8]

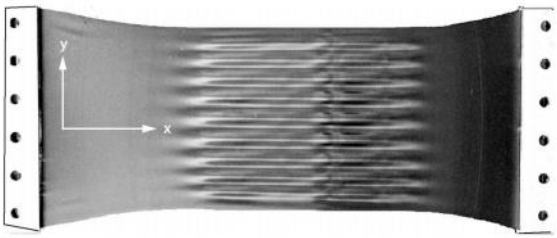

Figure 2.4 Wrinkles in a polyethylene sheet under uniaxial tensile strain [5]

Although the wrinkling phenomenon has been heavily studied for the past decades, three main issues concerning the wrinkling/buckling theories presented above were highlighted in [4], and are necessary to fully understand the wrinkling problem:

1. The morphology of buckles and wrinkles depends on the direction of the force acting on the foundation, and for the case of multidirectional stresses, wrinkling can be hard to predict.
2. Simple theories which were presented in [4], assumes the skin to be much stiffer than the foundation, however in other instances the skin is not much stiffer than the foundation.
3. The system is assumed to be bilayer neglecting the effect of the interface and laying on completely flat surface.

Relating tow wrinkling during AFP to the wrinkling phenomenon presented in the literature above, these main issues hold true. First, the stresses applied on the tow are not uniform even for the simple case of 2D steering since the tow undergoes in-plane bending to follow its path which results in a combination of both tension and compression depending on the side of the tow. These stresses are even more complex especially for the case of doubly curved surfaces where out-of-plane bending, and twisting are involved and necessary to adhere to the surface. Second, it is true that the tow in the fiber direction is much stiffer than the viscoelastic foundation, however in the transverse direction, the stiffness of the tow and the stiffness of the foundation are close. Third, the tow is not always laying on a completely flat surface even for the case of the 2D steering, where the surface can be flat if directly placed on the mold, or it can be non-uniform depending on the existence of previous layers, their direction, and the presence of possible features/defects as discussed earlier and presented in Figure 1.2. For these highlighted issues, tow wrinkling during AFP process can be hard to predict and a complex task to model.

2.2 WRINKLING IN COMPOSITE LAMINATES

Wrinkling during manufacturing of composites parts appears in several processes. For instance, during the process of diaphragm forming shown in Figure 2.5, laminate wrinkling can appear while trying to shape a flat stack of preform on a curved mold. A laminate wrinkling scaling law is derived in [9] based on ideal kinematics assumptions. The shear strain between the fibers is assumed to absorb the differential length, and a general formula for the complex shapes is derived based on ideal kinematics law. Differential geometry examples are discussed with two examples: hemisphere and curved C-channel. The difference between the proposed ideal prediction and actual results is explained by the deviation of the actual material; from the ideal kinematics laws, and an empirical scaling law is proposed.

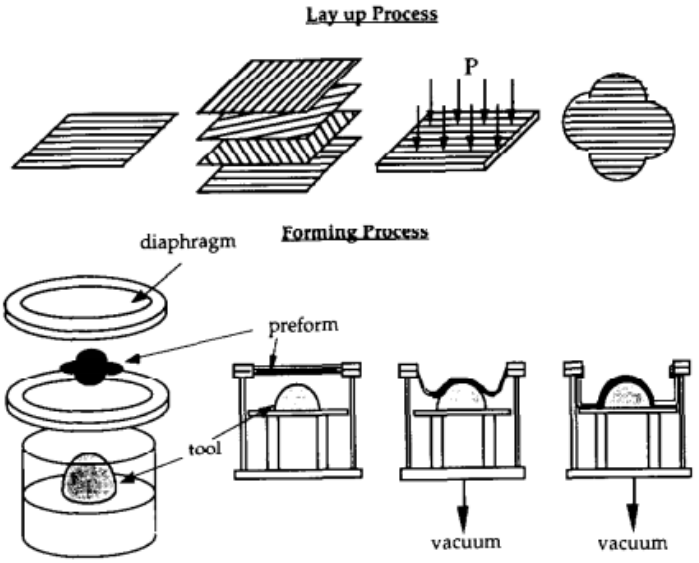

Figure 2.5 Schematic of the diaphragm forming process [9]

Another example of wrinkling in composites manufacturing occurs during consolidation of plies over an external radius (Figure 2.6). As the outer layer is forced to a tighter geometry and if the layers cannot shear between each other, these layers can form

wrinkles (Figure 2.7). A 1D model is presented in [10] and consists of solving the buckling problem by minimizing the total potential energy of the one dimensional system assuming that the laminate is laying on an elastic foundation and constrained at both ends with point forces. As a result, the critical conditions of wrinkling appearance can be established. Results from this model showed a good agreement with wrinkles observed on a spar demonstrator.

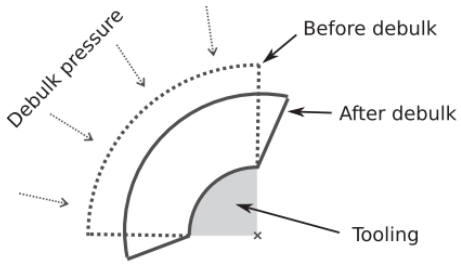

Figure 2.6 Consolidation over external radius process [10]

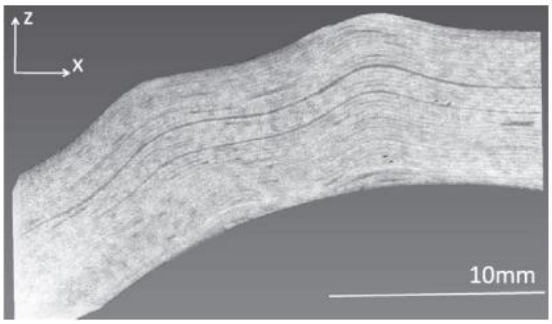

Figure 2.7 CT image of a corner wrinkle on a spar [10]

A similar wrinkling behavior can appear while laying prepreg material over internal radius (Figure 2.8).Two layup procedures were investigated in [11] for this case: the conventional layup consisting of laying the prepreg mats consecutively directly on the mold, and an alternate method consisting of laying the material on a flat surface and then bending the whole stack to conform to the inner radius. It was shown that in the later method the amount of wrinkling on the inner radius is increased, however, the spring-in values were decreased. These values were confirmed using Finite Element Analysis (FEA) simulation. A recent study on internal wrinkling instabilities in layered media is presented in [12] and uses large deformation Cosserat continuum model to capture these instabilities at a fraction of computational cost compared to conventional modeling techniques. The

same wrinkling problem occurring during consolidation over external radius discussed in [10] is modeled in [12] showing good agreement in the results.

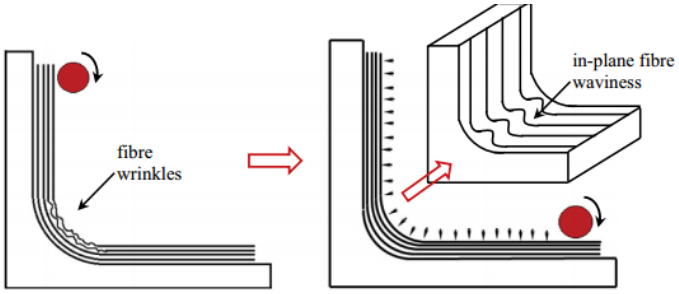

Figure 2.8 Wrinkles in layup over internal radius (Left), wrinkles converting to in-plane fiber waviness after cure (Right) [11]

Another mechanism for wrinkling formation is presented in [13] and it is due to shear between plies (Figure 2.9). For this case, the shear forces are generated as a mismatch between the thermal expansion of the tool and the composite, as well as ply slippage during consolidation into an inner radius. It was found that this type of wrinkling as well as fiber misalignment in the plies can be eliminated by increasing the frictional shear stress between the tool and the part by removing the release film slip layer.

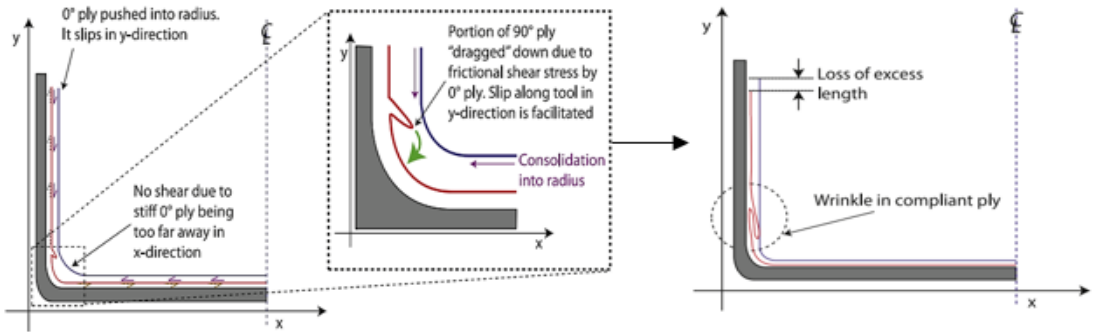

Figure 2.9 Wrinkle formation due to shear slip between the composite and the mold [13]

In addition to ply wrinkling, fiber wrinkling, waviness and misalignment can occur during manufacturing, and are considered as defects. A general overview of these defects, their origin and variability in composite manufacturing is presented in [14]. The main focus

of this work is on defects related to autoclave and resin transfer molding, however some of the listed defects are also common to the automated fiber placement process. Specifically, fiber waviness or wrinkling that occurs when draping unidirectional prepreg over a single curved (Figure 2.10) or doubly curved surface. This kind of defect is not optional and does not occur due to poor manufacturing, instead it is a function of the geometry [14]. This defect will lead to fiber misalignment and thus degradation in the overall properties of the produced part. This topic was further developed in [15], by discussing the effect of variability, misalignment and fiber waviness defects on the properties of the composite laminate or structure for unidirectional and woven fibers. It differentiates between design induced defects which can only be eliminated at the design stage, and process induced defects which can be eliminated by the correct choice of manufacturing process. Furthermore, examples of defects caused by the excess of length on one side of the unidirectional prepreg are shown in [15]. This excess of length can cause waviness for the unidirectional prepreg when wound on a drum for transportation or storing purposes, or it can cause wrinkling, or out-of-plane buckling for tows following curved trajectory during the AFP process, or it can lead to wrinkling and waviness of lay-up around sharp corners of mold sections

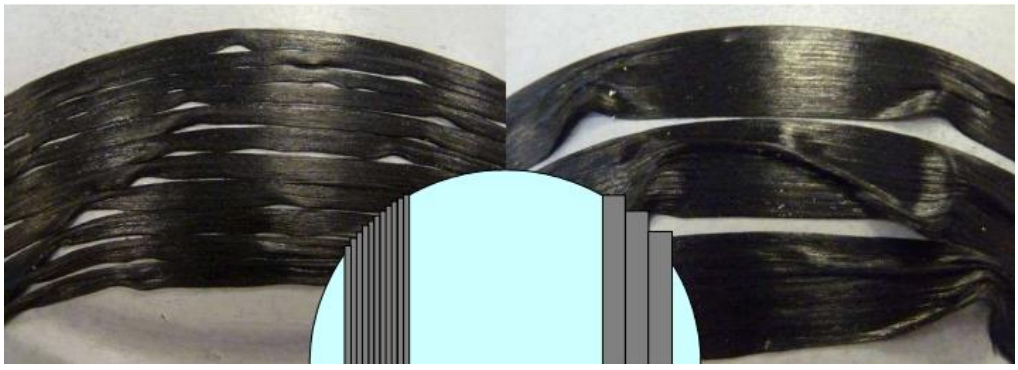

Figure 2.10 Level of misalignment generated by draping narrow and wide UD prepreg strips across a 100mm diameter hemisphere [14]

2.3 WRINKLING AND OTHER STEERING DEFECTS IN AFP

Concerning the AFP process, an extensive overview of the automated prepreg layup is presented in [1] by discussing the history and past issues of both ATL and AFP, and for both thermoset and thermoplastic materials. Future research opportunities for the AFP were also discussed, such as productivity, steering and control, and others. Specifically, [1] classifies the defects that arise from fiber steering in three categories as illustrated in Figure 2.11: tow buckling occurring on the inside radius of the tow due to compressive forces, tow pull-up occurring on the outside of a tow due to tensile forces, and tow misalignment occurring as a result of variability in the layup system, layup control, or prepreg material. Other tow deformation mechanisms are also mentioned and or studied in the literature such as in-plane waviness [16–18], and sheared tows [18] (see Figure 2.12).

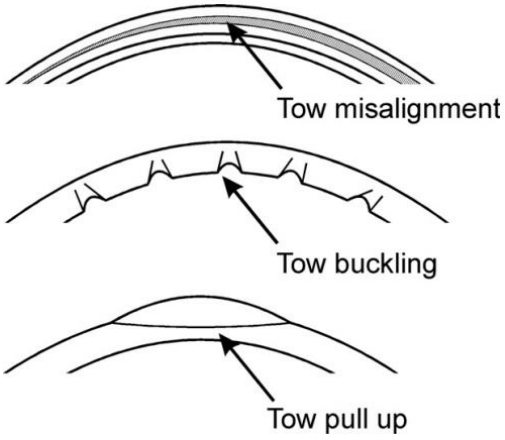

Figure 2.11 Overview of the most common steering defect [1]

Figure 2.12 In-plane waviness and sheared tows due to steering [18]

A discussion of the effect of the tape width on the out-of-plane buckling of the tows when placed on a curved surface is presented in [15]. This defect is increased by increasing the width of the tape, or if the path is non-geodesic on the surface. Experimental trials on the effect of tow width on the minimum steering radius to avoid wrinkling during AFP

were carried out in [19]. A minimum radius of 1250 mm was found for ¼ in tows for a defect free layup, whereas 500 mm was the minimum radius if using ⅛ in wide tows. This vast difference between the two widths makes the ⅛ in tow more favorable for steering and for the fabrication of geometrically complex parts. Additional parameters such as layup speed, heater temperature, and tool temperature where also tested in [19]. The quality of a steered path is also evaluated experimentally in [20] by comparing the ratio of the wrinkled area of the tow between different trials. Experimental results show that lower steering radii can be achieved with smaller tow thickness, higher layup temperatures, and lower layup rates. Regarding the roller compaction, it was shown in [20] that low compaction forces as well as extremely high compaction forces resulted in poorer layup quality, hence intermediate compaction forces are suggested. A possible explanation for this phenomenon is discussed in [21]: at higher level of pressure, higher tack is achieved between the roller and the tow surfaces, thus allowing the roller to pull the prepreg away from the substrate and form wrinkles. In addition, different roller stiffnesses and geometries are tested [21]. It is recommended that solid rollers (as opposed to the perforated ones) with more compliant material provide a smooth and even pressure distribution, as well as larger contact width thus providing higher tack levels and dwell time during the process. Two novel approaches to evaluate the quality of the steered paths is presented in [22] where two different materials (low and high tack) are tested at various process parameters. The first method consists of capturing the exact wrinkle size by image acquisition of the layup using profilometry scanning. This method will be used later in Chapter 5 as metric to quantify tow deformations. The second method consists of laying a 90° course over the steered path and observe the persistence of the defects before and after removal of the 90° course (Figure

2.13). In the case of large tow deformations such as a large wrinkle or fold, these defects are suppressed to a significant area of fiber misalignment after placing an additional layer. For the case of smaller wrinkles, these defects can either disappear or form a small area of fiber waviness after placing an additional layer. This method can experimentally give an insight on the effect of successive layers on the persistence of significant tow deformations.

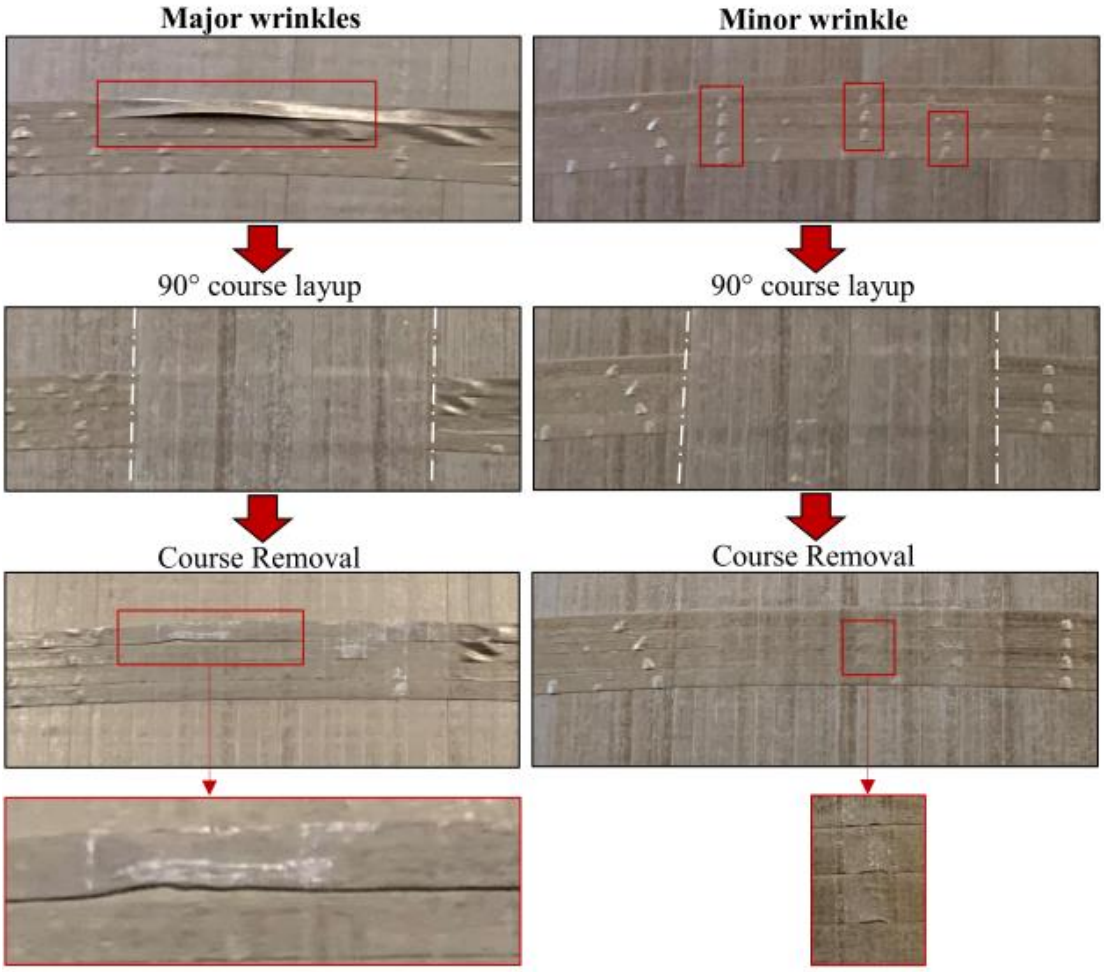

Figure 2.13 Quality assessment of a steered layup by comparing defect persistence after adding and removing a 90° course [22]

Moving from experimental investigations of tow deformations to the modeling techniques presented in the literature, an analytical approach to model wrinkling of tows during the AFP process is presented in [23]. This model isolates the formation of successive

wrinkles within the steered tow The model assumes the tow to be a thin plate laying on an elastic foundation (Figure 2.14), and it solves parametrically for the critical steering radius. Parametric results show that the steering radius can be decreased by decreasing the width of the tape similarly as discussed earlier in [15] and [19]. Also, increasing the tackiness or stiffness of the foundation reduces the limit of the steering radius. However, the theoretical solution was not backed up by experimental results, since other process parameters were not included in the model such as the speed of the layup, the applied temperature and pressure, and the viscoelastic behavior of the resin. A similar approach is used in [24] where a closed form solution is obtained by applying more realistic clamped boundary conditions. Results show that tack stiffness has the most influence on wrinkling formation. In addition, parametric studies on the foundation stiffness show that increasing the temperature of the layup within the admissible limits can increase the quality of the layup. However, this work is limited to the study of dry fiber and does not include any viscoelastic effect of the resin, if thermoset prepreg were to be used. In addition, very limited amount of experimental results with undefined parameters were conducted to back up the results. The stiffness parameter used in this work is also hard to measure and quantify even for the dry fibers, hence assumed values were used in this work. Improvements to the same analytical model are presented in [17] by considering a two-parameter Pasternak foundation. In addition to the normal stiffness of the spring elements in the substrate, a shear stiffness (which is determined experimentally using a bias extension test similar to the one presented in [25] and [26]) is added thus slightly improving the model accuracy. Another additional improvement of the model is presented in [27] by including the viscoelastic behavior to the foundation (but not the material stiffness). In essence, the

wrinkle is modeled as an anisotropic plate resting on a viscoelastic Pasternak foundation (Figure 2.15). By adding the viscoelastic properties of the foundation, the time-dependent behavior of the wrinkle formation could be captured. In [27], the unknown parameters used to model the viscoelastic foundation (long term modulus, instantaneous modulus, and relaxation time) are back-calculated by fitting the wrinkle wavelength to the experimental measurements rather than using a probe tack test (as accomplished in previous work [17,23]) while highlighting the rate-dependency issues of tackiness testing. The major issue in these models (other than obtaining accurate material properties of the uncured tow) is that several deformation mechanisms (in-plane waviness, tow folding and fiber bunching) are ignored once a specific shape function for the plate buckling problem is assumed. In addition, and under certain processing conditions, the tow may not behave as a plate but rather as a collection of fiber bundles with additional in-plane degrees of freedom thus resulting in other deformation mechanisms which may or may not be more critical than wrinkling.

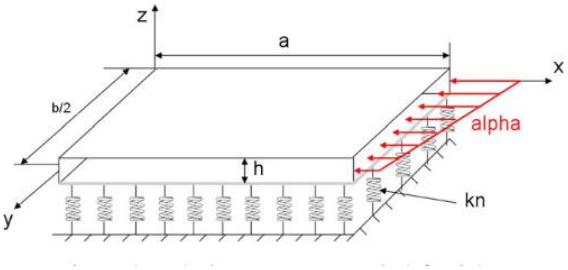

Figure 2.14 Wrinkle modeled as an anisotropic plate on one-parameter elastic foundation [23]

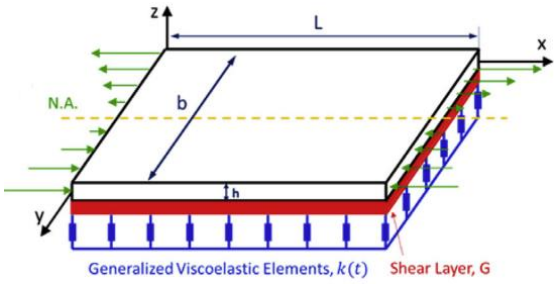

Figure 2.15 Wrinkle modeled as an anisotropic plate resting on viscoelastic Pasternak foundation [27]

In addition to analytical models for tow wrinkling, in-plane waviness is studied and modeled in [16]. The concept is based on the micro-buckling of fibers (without breaking) within a soft matrix under high curvatures which acts as a stress relief mechanism for

folding of deployable space structures [28]. In such micromechanics models, the fiber waviness's wavelength and amplitude are dependent on several parameters such as fiber volume fraction, modulus, and diameter, the shear stiffness of the soft matrix, the plate thickness, the applied curvature, and the distance from the compressive edge to the neutral axis. It is determined that the later one is difficult to measure especially during the AFP process, and therefore it is approximated from experimental measurements of the waviness amplitudes.

Finite element simulations of tow steering using AFP are also presented in the literature to validate experimental and analytical studies [18,29,30]. In [18], a cohesive zone model with a bilinear traction-separation law is used to capture the contact between the prepreg and the tool (tackiness) and to predict the damage initiation and evolution in the steered path (in the form of delamination leading to wrinkles or blisters). The bilinear law is fitted to experimental data from a probe tack test [31] where the main three parameters (stiffness, maximum traction, and fracture energy) can be extracted. Results show a possibility to capture some of the defects such as wrinkles and blisters, however, a validation with their experimental results is not presented. In addition, the traction-separation law for the in-plane shear is assumed; this is mainly due to the fact that the bias extension test is incapable of capturing the traction-separation law for the in-plane shear and can only provide a qualitative assessment of the shear modulus of a layup (rather than a single tow). In [30], the tackiness is modeled based on experimental data from peel tests [32–35]. Sensitivity studies are carried in [30] on material properties dominated by the uncured state of the matrix which are difficult to characterize experimentally such as transverse and shear stiffnesses ($E_2$and G_{12}) or the bending rigidity D_{11}. Results show that

higher values of E_2 and G_{12} restrict the tow from deforming in-plane and larger out-of-plane displacement for the fibers are observed. At higher values of D_{11} fewer wrinkles were observed but with larger amplitudes. A major issue in such models is the computational time required to finish the analysis.

Finding an accurate measurement for the uncured properties of a thermoset tow to be used in the FEA simulations or analytical models is deemed to be a difficult task due to the high anisotropy of the material, the viscoelastic response of the uncured resin, and the effect of environmental conditions such as humidity, shelf life and out time. For instance, micromechanics models (such as Puck's formulas) are used in [23] to obtain the Poisson's ratio, longitudinal, transverse and shear stiffnesses of the uncured tow based on the constituents properties. In [24], the bending rigidity is extracted from an overhang test and other matrix dominated stiffnesses are neglected since they are smaller by orders of magnitude. In [17], a simple tensile test is used to find the longitudinal stiffness of the tow, and a bias extension test is used to determine the shear stiffness. Many other properties are still based on the work presented in [23]. Regarding measuring the tackiness of the tow, several test are employed notably the probe tack test [17,23,31,36], the peel test [32–35], and most recently a rigid double cantilever beam (RDCB) [37]. The convenience of using the probe tack test and peel test is in the control of the processing condition of the experiment such as temperature of tow, the applied compaction force, the retraction rate, and other environmental conditions. The limitation of using a probe tack test or a peel test is that they can only provide a measurement for the traction (and possibly separation) in the normal direction and not in the shear. The RDCB specimen proposed in [37] can capture both traction-separation laws in normal (Mode I) and shear (Mode II), as well as in mixed-

mode loading conditions. The RDCB test has a more accurate measurement of these quantities due to the existence of a closed form solution for the J-integral in terms of measurable quantities (far field load, crack root rotation, and elastic properties of the adherent) [37]. Results show significant difference in the traction-separation relations for Mode I and Mode II which should be used for better modeling of tackiness in FEA simulations. Measurements of Mode III tractions-separation laws are still yet to be accomplished.

To sum up, wrinkling during manufacturing of composite structure is a common phenomenon and it was discussed and modeled in several cases such as diaphragm forming, consolidation of prepregs over an external or an internal radius, or it can happen due to shear between the layers, or due to a layup over complex surfaces. Concerning the AFP process, wrinkling and other tow deformations were mainly experimentally investigated during steering on a flat mold, where the process parameters and tow width are changed to achieve tighter radii of curvature. Several attempts are made to model wrinkling and other tow deformations during the AFP process. Validating analytical and simulative studies by comparing them to experimental results is a difficult task. This is mainly due to the oversimplification of the models that neglect other tow deformation in favor of wrinkling, as well as due to the complexity of measuring and determining the material properties of uncured thermoset tows.

2.4 LAYUP STRATEGIES FOR AFP

This section describes the geometric aspect behind the wrinkling phenomenon during the AFP process. Starting from a given tool shape, a coverage strategy is necessary to obtain the path that the machine head has to follow to lay down the fiber tows and

fabricate the part. Typical strategies start from a given reference curve depending on the load requirement or fiber direction needed to achieve this load. Then, this curve can be propagated in several ways, or other curve-path can be recreated to achieve full coverage. This summary of the literature contains two major section: the first one discusses several ways to create reference or initial curves on the tool surface such as fixed-angle curves, geodesic curves, and variable angles guide curves. The second section discusses strategies to propagate these curves to cover the mold surface such as the parallel method or shifted method. For more details on tool path planning for AFP, readers can refer to [38].

2.4.1 Reference Curves

Before covering the surface, an initial (or reference) curve is needed. In this section, the different strategies to find the reference curve will be detailed. Both, a parametrical approach, and the use of a mesh, can be found in the literature. Each method has its advantages and drawbacks which have been summed up by [39] for automated spray painting: a mesh provides useful information, such as the different areas of the facets and their normal, which are important to generate the toolpath along the course, however the mesh is an approximation of the geometry and more precision comes at the computational cost. Most references found in the literature use a parametrical approach, since the surface would be precisely known. In this review, reference curves are classified under three categories: fixed-angle reference curves, geodesic curves, and the remaining types of reference curves are grouped under variable-angle guide curves.

2.4.1.1 Fixed angle reference curves

Using a fix angle strategy, the fiber angle in the reference curve is constant all along the surface. This layup strategy is very used as it allows a complete control of the fiber

angles along the surface and resembles the conventional layup of quasi-isotropic laminates where the angles $90°, 0°$ and $\pm 45°$ are the main used ones. Starting from a meshed surface, the method presented in [40] uses the mesh information contained in an STL (Stereolithography) file to generate the topology of the surface including the vectors/edges, the nodes, the facets, and the normal vectors of the facets. From these features, a slicing algorithm is used to find the reference curve which is the intersection between a plane at a fixed direction and each triangular element on the meshed surface. An advantage of this method is that finding another fix angle path is relatively simple: the meshed plane can be rotated by the required angle from the previous path to obtain the new one.

A similar approach to find a fixed angle curve on a parametric surface is found in the literature [41–43] by intersecting the parametric surface $\boldsymbol{S}(u, v)$:

$$\boldsymbol{S}(u, v) = X(u, v)\hat{\imath} + Y(u, v)\hat{\jmath} + Z(u, v)\hat{k} \ , \tag{2.1}$$

with the plane $P(x, y, z)$ defined by the projection of the major axis into the surface (Figure 2.16):

$$P(x, y, z) = a\, x + b\, y + c\, z + d = 0 \ , \tag{2.2}$$

resulting the following equation:

$$f(u, v) = a\, X(u, v) + b\, Y(u, v) + c\, Z(u, v) + d = 0 \ . \tag{2.3}$$

A numerical solution for equation (2.3) is usually required to find the reference curve if the parametrization of the surface is complex, and geometrical algorithms such the ones presented in [44] have to be used. For the case of simple surface parametrization such as the case of conical shells presented in [45], a closed form solution for the reference curve at a fixed angle can be obtained, hence resulting in fast and efficient substitution.

Another approach to generate a fixed angle path is presented in [46] and [47]: starting from a given point $\boldsymbol{P_i}$, a vector $\boldsymbol{d}$ tangent to the surface is projected following the major direction (Figure 2.17). Another vector $\boldsymbol{t}$ is found by rotating $\boldsymbol{d}$ by an angle ψ around the normal to the surface $\boldsymbol{n}$. Another point $\boldsymbol{P_f}$ is defined on the vector $\boldsymbol{t}$ at a small distance from $\boldsymbol{P_i}$. Finally, $\boldsymbol{P_f}$ is projected on the surface to find the next point $\boldsymbol{P_{i+1}}$. This process iterates until the path reaches the boundary of the surface.

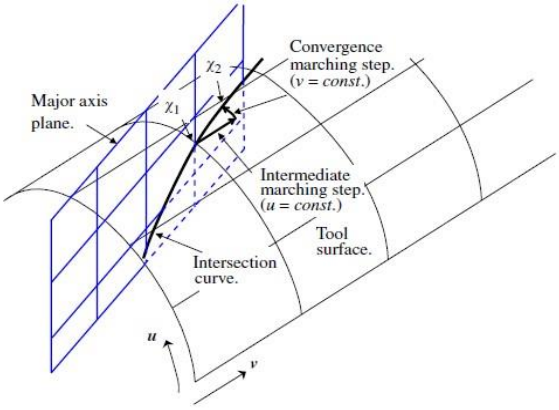

Figure 2.16 Projection of a major axis on the surface [42]

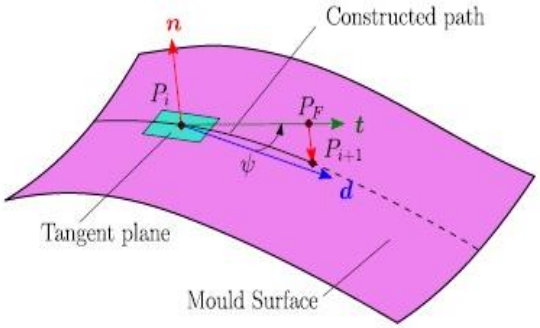

Figure 2.17 Reference curve using an iterative algorithm [47]

The main disadvantage of using this method as a reference curve is it might violate the amount of curvature or the minimal steering radius at which the fiber tows start to buckle, hence resulting in a difficult manufacturing process if not impossible in some severe cases.

2.4.1.2 Geodesic guide curves

A layup strategy to avoid steering is to compute a geodesic guide curve. The geodesic path can also be known as the natural path, it is the shortest path between two points along a three-dimensional surface in Cartesian space. For the case of a flat plate, a geodesic path is only a straight line connecting two points. Also, a geodesic path can be

obtained by specifying a starting point and a direction of travel. For a general parametric surface, a geodesic path has to satisfy a system of differential equations (discussed later in section 3.1.3 Geodesic Path Definition and Geodesic curvature, equation (3.18)) for which a numerical solution is needed. For the case of a cone, a closed form solution for a geodesic path can be obtained [45].

For more complex shapes, such as the Y shape investigated in [47], geodesic paths cannot be easily generated. Starting from one branch of the Y surface, and given an initial fiber angle, a geodesic path can be defined. However, once at the junction of the Y, the geodesic path might change or won't be able to propagate on the remaining part of the surface. Several solutions to continue the path were presented: proceed in the direction of the minimum curvature, try to reach a geodesic path on the other branch of the Y (Figure 2.18) or create a straight path on the other branch respecting the steering conditions for the courses.

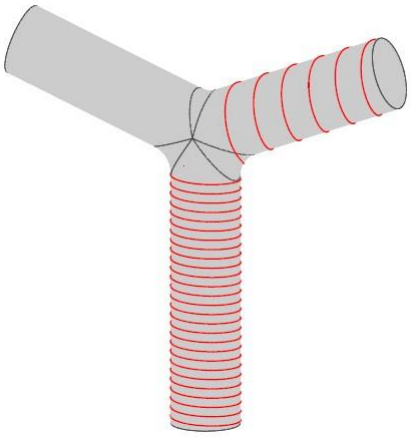

Figure 2.18 Geodesic reference curve
on a Y shape tube [47]

2.3.1.3 *Variable angle guide curves*

It has been shown in the literature that fiber-steered composite laminates have higher mechanical performance than conventional straight-fiber laminates, such as

improvements in the buckling load [48], and many others. The linear angle variation strategy is the most used method to generate variable stiffness plates.

This strategy consists of linearly variating the fiber angle between two points, each one having a different fiber angle T_0 and T_1 separated by a distance d (Figure 2.19). T_0 defines the angle at the starting point of this path which is usually placed at the center of the rectangular panel. The axis system of fiber orientation is defined by rotating the rosette by an angle ϕ. The fiber path is then defined by $\phi < T_0|T_1 >$ and varies linearly along the radial distance r from T_0 to T_1. Hence, the representation of such path in polar coordinates can be:

$$\theta(r) = \begin{cases} \phi + (T_0 - T_1) \cdot \dfrac{r}{d} + T_0, & -d \le r \le 0 \\ \phi + (T_1 - T_0) \cdot \dfrac{r}{d} + T_0, & 0 \le r \le d \end{cases} \tag{2.4}$$

The reference curve repeats indefinitely with a 2 d period until it reaches a boundary.

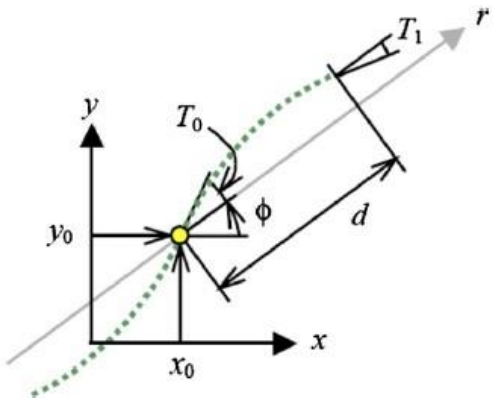

Figure 2.19 Linear angle variation reference curve [48]

Another approach to obtain variable angle guide curves is to use non-linear angle variation. Non-linear angle variations have been employed to obtain higher structural performance [49]. The method described in [49] uses a streamline analogy to predict the thickness build up as a function of the fiber orientation Piecewise quadratic Bezier curves

were used in [50], whereas spline functions were used in [51] to describe variable angle curves.

2.4.2 Coverage strategies

To assure that the surface is totally covered by the material, three different techniques are highlighted here. The first one consists of recreating other independent guide curves using one of the techniques presented earlier until full surface coverage is obtained. The second method consists of shifting the guide curve to cover the surface. This technique is usually used in variable stiffness plates [48]. And the third method consists of creating curves parallel to the reference guide curve. The last two methods were investigated in [52], where the parallel method had more restriction on the radius of curvature, thus resulting in a reduced design space compared to the shifted technique. However, gaps and overlaps are inevitable if the shifted method has to be used, resulting in possible degradation of the properties.

In this section, the different techniques used in the literature to only compute parallel curves are presented here, since shifted curves can be easily obtained by applying a simple translation. In addition, parallel curves are necessary to understand in the scope of this thesis, since the edges of the tow are computed from a given centerline using this technique, as well as other parallel paths during a course using the AFP process.

For the case of a planar curve derived in [53], a parallel curve to a regular plane curve $\boldsymbol{\alpha}$ at a small distance s is the plane curve given by:

$$\boldsymbol{parcurve}[\boldsymbol{\alpha}][s](t) = \boldsymbol{\alpha}(t) + \frac{s\,\boldsymbol{J}\,\boldsymbol{\alpha}'(t)}{\|\boldsymbol{\alpha}'(t)\|}, \tag{2.5}$$

where the operator $\boldsymbol{J}$ is given by $\boldsymbol{J}[\{p1, p2\}] = \{-p2, p1\}$, and s can be either positive or negative. If s is large, the parallel curve can self-intersect [53].

For the case of a general surface, a closed form solution for the parallel curves does not exist in most cases. Hence several algorithms have been developed to compute parallel curves or also referred to as offset curves numerically [41–43,54].

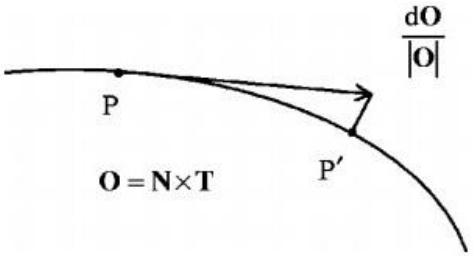

Figure 2.20 Cross section of placement surface showing calculation of offset points [41]

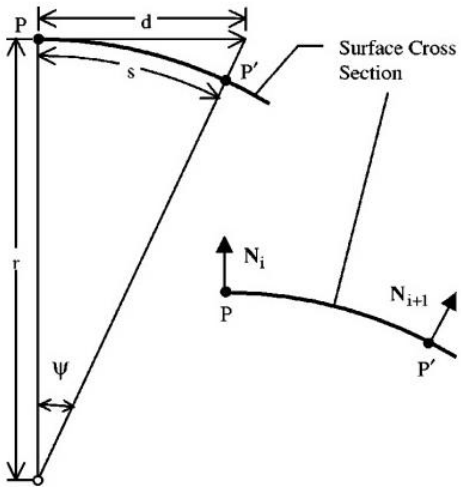

Figure 2.21 Error associated with placing a point on a surface with circular arc cross section [41]

For instance, a similar approach for the planar case is used in [41] to find parallel curves by following the vector normal to the reference curve. This vector named $\boldsymbol{O}$ (Figure 2.20) can be found by taking the cross product between the tangent vector to the curve and the normal vector to the surface. Then at a distance d along the vector $\boldsymbol{O}$, a point $\boldsymbol{P'}$ is projected to the surface following the normal vector using a Global Closest Technique. This process is repeated at every point-step along the curve to obtain the new parallel curve. The resulting error from using this technique (Figure 2.21) is reported to be [41]:

$$Error = d\left(1 - \frac{\psi}{\tan\psi}\right) \tag{2.6}$$

Therefore, the error increases by taking a further offset curve (in the case of wider roller), and in the case of highly curved surface.

A more accurate method is presented in[42] and [43] by taking the intersection between the plane perpendicular to the curve and the mold surface (Figure 2.22). To do so, a numerical approach presented in [44] is used to determine the resulting curve. Then, the offset point can be found by taking the required distance along the perpendicular arc. A last step is needed to obtain a complete offset path in the case where the reference path is shorter than the offset one that does not reach a boundary. In this case, the offset curve is completed by interpolating the last point from the calculated ones until it reaches the boundary.

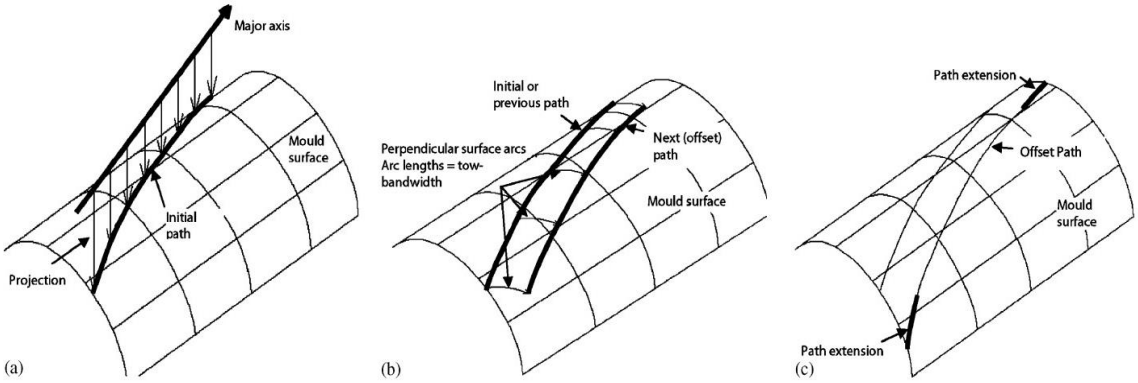

Figure 2.22 (a) Initial path generation, (b) Curve offset by taking perpendicular arcs, (c) Path extension [42]

Three other methods are presented in [54] to compute parallel curves on a parametric surface. The first method named section curves is similar to the ones presented in [42] and [43]. The other two consist of generating orthogonal curves to the reference by either taking vector-field curves or geodesic curves. Once the orthogonal curve is defined in either of these methods, the offset points can be calculated at the required distance from the reference curve, and finally the new parallel curve is obtained by interpolating these points.

For the case of a meshed surface, creating parallel curves on the surface has been introduced by [55] in a technique named Fast Marching Method (FMM) which is based on the Eikonal equation (Figure 2.23). This equation is mostly used in optic to calculate the propagation of a wave with a particular speed. Hence, from a wave, one can calculate the different position of this wave at every time once it starts propagating.

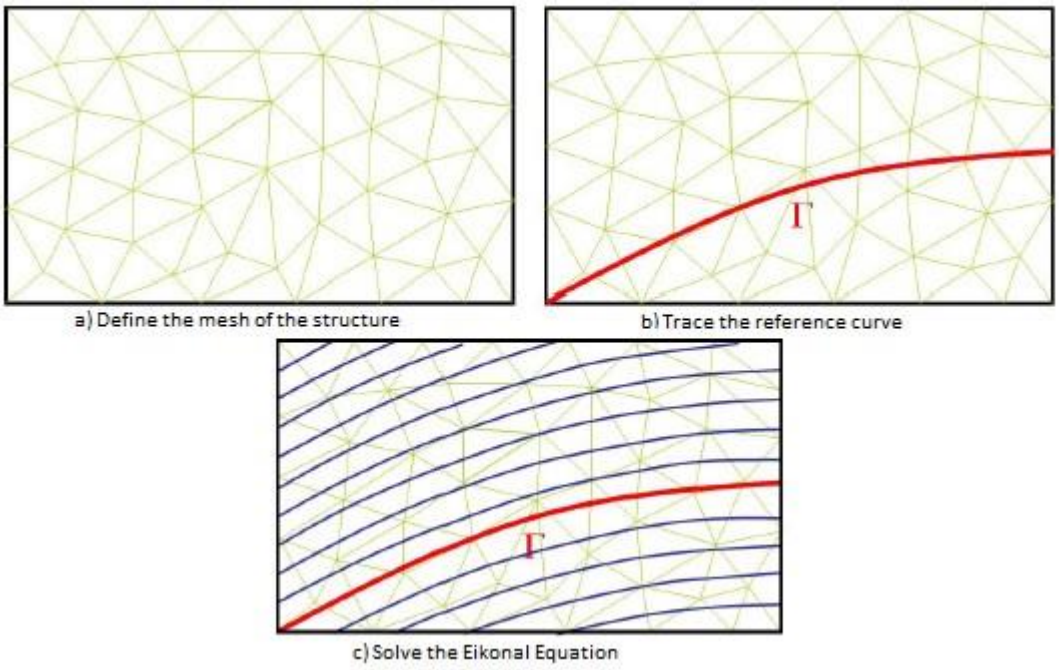

Figure 2.23 Different steps of the Fast Marching Method to offset a reference curve [55]

This method starts from a random discretized reference curve on the surface. For initialization, all the points have a time value of 0. Then, the reference curve is propagated at a defined speed so every node of the mesh will hit the propagated curve at a certain time. Knowing the time value of two nodes of one triangular mesh, one can calculate the time value of the last node based on the geometry of the triangle. Using the FMM method, this principle is propagated through all the mesh. Finally, the offset curve is obtained by

connecting the points having the same propagation time, indicating that they are equidistant from the reference curve.

To conclude, several mathematical algorithms exist to create reference curves on a surface and to propagate them based on the mechanical load requirements or geometrical and manufacturability constraints. Investigation of each of these methods concerning the wrinkling aspect is important during the design phase to detect possible defects and avoid them during the manufacturing phase. Some of these methods are more prone to wrinkling such as the parallel offset coverage strategy compared to the shifted one, or the fixed-angle reference curve compared to the geodesic one, hence a tradeoff analysis has to be done to determine the optimal strategy.

2.5 SUMMARY

After this extensive state-of-art literature review, the main points concerning wrinkling can be summarized as follow:

- Wrinkling is a very broad term and can occur in several physical aspect such as human skin, fabric or clothing items, flowers and leaves due to excessive growth [3], and it can occur from large scale as mountains folds to smaller sandwich structures failure and even to the nanoscale of physically treated elastomers (Table 2.1, [4]), and even in stretched sheets [6]. The model used in the literature to analyze this phenomenon is based on the wrinkling/buckling model of a thin stiff film laying on soft foundation [5]. However, this model does not fully translate to the AFP process due to three main concerns: multidirectional stress applied to the tow during the layup, the highly anisotropy of the tow making it much stiffer in the longitudinal direction compared to the transverse one, and

lastly the irregularities of the underlying surface leading to the necessity of multi-layer analysis.

- Wrinkling during manufacturing of composite structure has been discussed in the literature for several processes, such as diaphragm forming [9], draping (hand layup) [14], consolidation of prepreg over an external [10] and internal [11] radius, or due to shear between the prepreg and the mold [13]. The common reason behind such defect is the mismatch in dimension between the material and the mold surface.

- Wrinkling during the AFP process is also referred to as out-of-plane buckling or tow buckling [1,23], it happens on the compressive edge of the tow due to mismatch in length between the tow and the path. Other tow deformation mechanisms are also mentioned in the literature such as tow pull-up or folding [1], in-plane waviness [16,17], bunching or tow misalignment [1], and sheared tows [18].

- Tow deformations and steering limits are investigated experimentally by the mean of in-plane steering [18–20,22], where the process parameters are changed to obtain a defect free layup. The influence of a successive layer on the persistence of the steering defects is also explored in [22].

- Analytical models to describe wrinkling use the buckling model of a plate laying on an elastic [23,24], Pasternak [17], or viscoelastic Pasternak foundations [27]. By assuming the out-of-plane deformed shape in the buckling problem, other tow deformations cannot be captured in these models such as the in-plane deformations and tow folding, thus limiting their accuracies.

- Several attempts to simulate tow steering in FEA environment are presented in [18,29,30]. It should be noted that setting up these simulations correctly with accurate

measurements of the tow properties especially the tack in both normal and shear directions is very important to obtain meaningful results.

- Several algorithm to describe various types of layup strategies have been developed in the literature, including but not limited to: fixed-angle reference path [40–47], geodesic path [45,47,53], and other linear and non-linear angle variation reference curves [48,49], as well as the shifted coverage method [48,52] or the parallel offset one [41–43,53–55]. The choice of the reference curve, and the propagation technique to achieve full coverage of the surface heavily affect the wrinkling creation during manufacturing.

CHAPTER 3

GEOMETRICAL MODEL FOR TOW WRINKLING IN AFP

In this chapter, the geometrical aspect of wrinkling formation during AFP process is investigated. A worst-case scenario is assumed where all differential length between to the edges of the tow path is absorbed through an out-of-plane wrinkle on the compressive edge of the tow. All other material properties and process parameters are ignored in this model in favor of understanding the complex geometry of tow paths especially for layups on general surfaces. In the following sections, the relevant geometrical parameters for wrinkling analysis on a general surface are presented. Those parameters are the surface and its corresponding tangent and normal vectors, the relevant path on the surface, its tangent, normal and bi-normal vectors, its geodesic curvatures, computing parallel curves on the surface, the tow surface and the resulting strain, and finally the assumed shape function of the wrinkles and the concerning assumptions. The wrinkling model applied to the general surface is further reduced for the simple case of a flat surface where relevant simplified equations are shown. Lastly, several examples are presented for the cases of paths on flat and general surfaces. For further details regarding the geometrical model for wrinkling in AFP, reader can refer to the following references: [56] and [57].

3.1 MODEL DEFINITION AND GOVERNING EQUATIONS

3.1.1 Surface Definition

A general three-dimensional surface is represented through surface parameters (u, v) such that:

$$\boldsymbol{S}(u,v) = X(u,v)\hat{\imath} + Y(u,v)\hat{\jmath} + Z(u,v)\hat{k} \tag{3.1}$$

where the coefficient functions (X, Y, Z) are defined for each unit vector in three-dimensional Cartesian coordinates. Once the surface is defined, an orthonormal frame on that surface can be defined using the two tangent vectors and the normal vector in the u and v directions. The tangent vectors along the surface parameters u and v are denoted by $\boldsymbol{S_u}$ and $\boldsymbol{S_v}$, and are given by:

$$\boldsymbol{S_u}(u,v) = \frac{\partial \boldsymbol{S}(u,v)}{\partial u} \quad , \quad \boldsymbol{S_v}(u,v) = \frac{\partial \boldsymbol{S}(u,v)}{\partial v}, \tag{3.2}$$

where the subscripts represent differentiation with respect to those variables. These vectors are often normalized to produce unit vectors in the surface directions:

$$\widehat{\boldsymbol{S_u}}(u,v) = \frac{\partial \boldsymbol{S}(u,v)/\partial u}{\|\partial \boldsymbol{S}(u,v)/\partial u\|} \quad , \quad \widehat{\boldsymbol{S_v}}(u,v) = \frac{\partial \boldsymbol{S}(u,v)/\partial v}{\|\partial \boldsymbol{S}(u,v)/\partial v\|} \ , \tag{3.3}$$

where the operator $\|\cdot\|$ denotes the Euclidean norm and the hat symbol $\widehat{\ }$ signifies a unit vector.

The unit normal vector to the surface is defined as the cross product between the surface tangents and represents the third vector of the orthonormal frame for a surface:

$$\widehat{\boldsymbol{N}}(u,v) = \frac{\boldsymbol{S_u} \times \boldsymbol{S_v}}{\|\boldsymbol{S_u} \times \boldsymbol{S_v}\|} \quad \text{or} \quad \widehat{\boldsymbol{N}}(u,v) = \widehat{\boldsymbol{S_u}} \times \widehat{\boldsymbol{S_v}} \, . \tag{3.4}$$

For distance calculations on the surface, the infinitesimal distance between two points $\boldsymbol{P}(u, v)$ and $\boldsymbol{P}(u + \Delta u\,, v + \Delta v)$ on the surface is given by:

$$ds^2 = E\,du^2 + F\,du\,dv + G\,dv^2\ , \tag{3.5}$$

where the scalar quantities E, F and G are the coefficients of the first fundamental form relative to the surface $\boldsymbol{S}(u, v)$ and given by:

$$E(u, v) = \boldsymbol{S_u} \cdot \boldsymbol{S_u}\ , \tag{3.6}$$

$$F(u, v) = \boldsymbol{S_u} \cdot \boldsymbol{S_v}\ , \tag{3.7}$$

$$G(u, v) = \boldsymbol{S_v} \cdot \boldsymbol{S_v}\ , \tag{3.8}$$

and the symbol " $\cdot$ " denotes the dot product.

Many surface curvatures exist, however, one of the most important ones concerning the discussed problem is the Gaussian curvature K and is given by:

$$K = \frac{e\ g - f^2}{E\ G - F^2}\,, \tag{3.9}$$

where $e(u, v)$, $g(u, v)$, and $f(u, v)$ are the coefficients of the second fundamental form relative to the surface $\boldsymbol{S}(u, v)$ and given by:

$$e(u, v) = \boldsymbol{N}(u, v) \cdot \boldsymbol{S_{uu}}(u, v), \tag{3.10}$$

$$f(u, v) = \boldsymbol{N}(u, v) \cdot \boldsymbol{S_{uv}}(u, v), \tag{3.11}$$

$$g(u, v) = \boldsymbol{N}(u, v) \cdot \boldsymbol{S_{vv}}(u, v). \tag{3.12}$$

The Gaussian curvature can be positive on a hill, negative on a saddle point or zero as in developable surfaces. The importance of the Gaussian curvature from a manufacturing point of view is that for instance, in a milling operation where the tool has a spherical head, the radius of the tool should be less than the smallest radius of curvature of the surface.

From an AFP consideration, Gaussian curvature sets a limit on the manufacturability of a given surface especially for the case of a negative curvature where collision between the machine head and the surface might occur due to high curvature (in absolute value). In addition, a surface with zero Gaussian curvature called developable surface, can be laid down on a flat surface without stretching or distorting it, hence the possibility of obtaining wrinkle free layup for a given path direction.

3.1.2 Path Definition

The previous section defined an arbitrary surface on which the fiber tows have to be laid. An infinite number of possibilities exist for the definition of a fiber path over a general 3D surface, but the most common paths used in the literature are surface-plane intersection curves [41–44], geodesics [47,53,58], constant angle paths [45], and constant curvature paths [45,53] as discussed previously in Chapter 2, Reference Curves section. In the scope of this Chapter only the derivation of a geodesic path will be presented since it has direct relevance to the solution process, though the formulation allows for any arbitrary definition of a path. For the definitions of the surface and path Figure 3.1 is used as a reference. An arbitrary path on the surface is defined by:

$$\boldsymbol{C}(t) = \boldsymbol{S}\big(u_c(t), v_c(t)\big) \tag{3.13}$$

where $u_c(t), v_c(t) \in \Omega$, the domain of definition of the surface.

Another important feature in analyzing the path is the distance (arc length) along the path. The distance between two points on the surface along the curve $\boldsymbol{C}(t) = \boldsymbol{S}\big(u_c(t), v_c(t)\big)$ can be found through integration along the path of the distance between two points on a surface from equation (3.5):

$$d = \int_{t_a}^{t_b} \sqrt{E \left(\frac{du_c}{dt}\right)^2 + F \frac{du_c}{dt}\frac{dv_c}{dt} + G \left(\frac{dv_c}{dt}\right)^2}\, dt\,. \tag{3.14}$$

Using the length calculation along the curve, a re-parametrization of the path $\boldsymbol{C}(s)$ can be made as a function of the arclength s, where for a given length s_0 the location on the path $\boldsymbol{C}(s_0)$ can be determined, which is useful for the wrinkle shape function described in the later section.

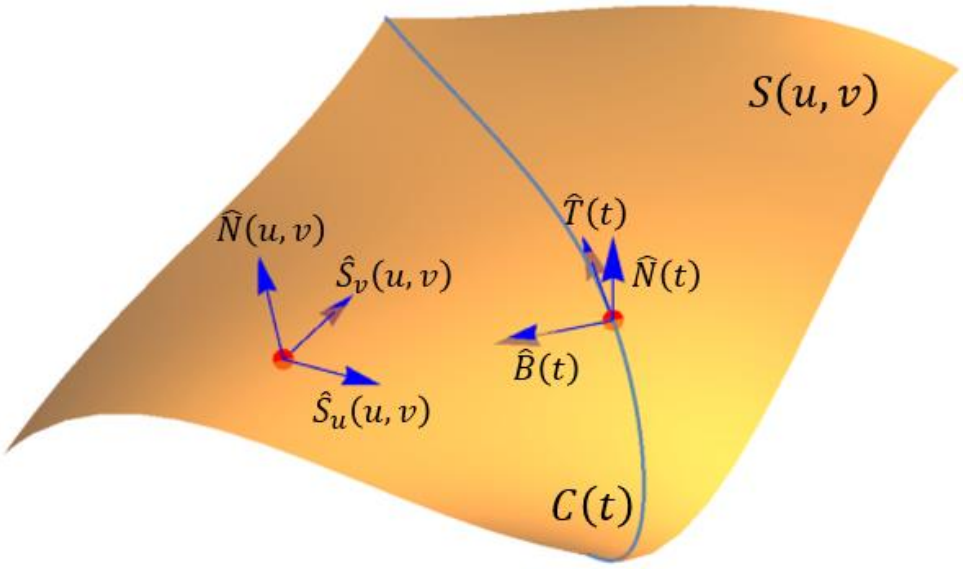

Figure 3.1 Surface and Path definition

In the analysis of a path along the surface, an additional useful orthonormal frame is defined using the following three vectors: $\widehat{\boldsymbol{T}}$ the unit tangent to the path, $\widehat{\boldsymbol{N}}$ the unit normal to the surface along the path, and $\widehat{\boldsymbol{B}}$ the unit in-plane normal. This last vector $\widehat{\boldsymbol{B}}$ (often referred to as the bi-normal or bi-tangent in the literature) is tangent to the surface at a given point but orthogonal to the tangent vector along the curve. It is represented through a cross-product of the normal and tangent vectors. These three vectors are expressed as:

$$\widehat{\boldsymbol{T}}(t) = \frac{d\boldsymbol{C}(t)/dt}{\|d\boldsymbol{C}(t)/dt\|} = \frac{\boldsymbol{S_u}\, du_c/dt + \boldsymbol{S_v}\, dv_c/dt}{\|\boldsymbol{S_u}\, du_c/dt + \boldsymbol{S_v}\, dv_c/dt\|} \tag{3.15}$$

$$\widehat{\boldsymbol{N}}(t) = \widehat{\boldsymbol{N}}(u_c(t), v_c(t)), \tag{3.16}$$

$$\widehat{\boldsymbol{B}}(t) = \widehat{\boldsymbol{N}}(t) \times \widehat{\boldsymbol{T}}(t). \tag{3.17}$$

3.1.3 Geodesic Path Definition and Geodesic curvature

A geodesic path on a surface is the shortest path connecting two points on that surface. A geodesic path can also be defined starting at a point with a given direction of travel. The equations governing the path of a geodesic arise from minimization of the integral in (3.14) with appropriate boundary conditions, and for a general surface is calculated numerically. A geodesic path has to satisfy the following system of differential equations [53]:

$$\begin{cases} u'' + \Gamma_{11}^1 u'^2 + 2\Gamma_{12}^1 u'v' + \Gamma_{22}^1 v'^2 = 0 \\ v'' + \Gamma_{11}^2 u'^2 + 2\Gamma_{12}^2 u'v' + \Gamma_{22}^2 v'^2 = 0 \end{cases} \tag{3.18}$$

where primes ($'$) represent differentiation with respect to the parameter t and Γ_{jk}^i are the Christoffel symbols of the surface $\boldsymbol{S}$ given by:

$$\Gamma_{11}^1 = \frac{G\, E_u - 2\, F\, F_u + F\, E_v}{2(E\, G - F^2)} \tag{3.19}$$

$$\Gamma_{11}^2 = \frac{2\, E\, F_u - E\, E_v - F\, E_u}{2(E\, G - F^2)} \tag{3.20}$$

$$\Gamma_{12}^1 = \frac{G\, E_v - F\, G_u}{2(E\, G - F^2)} \tag{3.21}$$

$$\Gamma_{12}^2 = \frac{E\, G_u - F\, E_v}{2(E\, G - F^2)} \tag{3.22}$$

$$\Gamma_{22}^1 = \frac{2\, G\, F_v - G\, G_u - F\, G_v}{2(E\, G - F^2)} \tag{3.23}$$

$$\Gamma_{22}^{2} = \frac{E\ G_v - 2\ F\ F_v + F\ G_u}{2(E\ G - F^2)}\ . \tag{3.24}$$

In order to solve this system of second order differential equations, four initial conditions have to be prescribed: $u(t_0) = u_0, v(t_0) = v_0,\ u(t_1) = u_1,\ v(t_1) = v_1$ for the geodesic path between two points $\boldsymbol{P_0} = \boldsymbol{S}(u_0, v_0)$ and $\boldsymbol{P_1} = \boldsymbol{S}(u_1, v_1)$; or $u(0) = u_0, v(0) = v_0,\ u'(0) = u_0',\ v'(0) = v_0'$ for the geodesic path starting at $\boldsymbol{P_0} = \boldsymbol{S}(u_0, v_0)$ with a direction $(u_0'\ , v_0')$.

Lastly, several specific measures of curvature can be defined for the geometric formulation that has been discussed. Gaussian curvature K applies to a surface and represents the intrinsic curvature of the surface at a given point as shown earlier in equation (3.9). For a space curve (one not laying on a specified surface), a curvature parameter can be derived from the path definition $\boldsymbol{C}(t)$ and its derivatives, where the curve tangent, normal, and binormal vector fields are related to the curvature and torsion by Frenet formulas. However, the most important estimate of curvature for the problem under consideration is referred to here as the geodesic curvature k_g, which measures the curvature within the tangent plane for a curve on a surface. This parameter depends on both the surface parameters and the path definition and provides a direct indication on where wrinkles might form for tow path. It is calculated as:

$$k_g = \left[\left(u_c'' + \Gamma_{11}^{1} {u_c'}^{2} + 2\Gamma_{12}^{1} u_c' v_c' + \Gamma_{22}^{1} {v_c'}^{2}\right) v_c' - \left(v_c'' + \Gamma_{11}^{2} {u_c'}^{2} + 2\Gamma_{12}^{2} u_c' v_c' + \Gamma_{22}^{2} {v_c'}^{2}\right) u_c'\right] \times \frac{\sqrt{E\ G - F^2}}{\left(E\ {u_c'}^{2} + 2\ F\ u_c' v_c' + G\ {v_c'}^{2}\right)^{\frac{3}{2}}}\ . \tag{3.25}$$

Note that for a geodesic curve that satisfies equation (3.25) the geodesic curvature is identically zero, which affirms that the geodesic is the "straightest" path on a surface.

3.1.4 Parallel Curves on the Surface and Tow Surface

For a given base curve (reference curve) on the surface, parallel paths (see Figure 3.2) on one or both sides of the base curve have to be defined in order to show the area covered by the carbon fiber tow. In addition, parallel curves can be used to generate the centerlines and the edges of adjacent tows, in the case if more than one tow is fed during a single course. Those parallel curves are computed by taking the same distance along the geodesics orthogonal to the base curve. Several algorithms to find parallel curves on general surfaces exist in the literature, such as projection techniques [41], orthogonal plane-surface intersection [42,43] , geodesic offset [54], and others as discussed previously in the literature review chapter. In this section, the algorithm used to compute parallel curves is similar to the one presented in [54], and is summarized as follows:

- Take n points $\boldsymbol{P_i}$ along the base curve: $\boldsymbol{P_i} = \{\boldsymbol{P_1}, \boldsymbol{P_2}, \dots, \boldsymbol{P_n}\}$, $i = 1 \dots n$
- Find each geodesic $\boldsymbol{G_i}$ starting at $\boldsymbol{P_i}$ in the direction orthogonal to the base curve
- Find the points $\boldsymbol{Q_i}$ on the geodesics at a distance d_i equal to the tow width or half-tow width, depending on the application
- Generate the parallel path $\boldsymbol{C_p}(t)$ by interpolating the points $\boldsymbol{Q_i}$

From these parallel path curve calculations, their lengths on the surface and geodesic curvatures can be computed from equations (3.14) and (3.25), respectively. Note that for the case where the base curve is parametrized by its arclength $\boldsymbol{C}(s)$, the obtained parallel curve $\boldsymbol{C_p}(s)$ has a different length due to the curvature (which drives the wrinkling problem), and the arclength parameter s does not reflect the length of the parallel curve anymore.

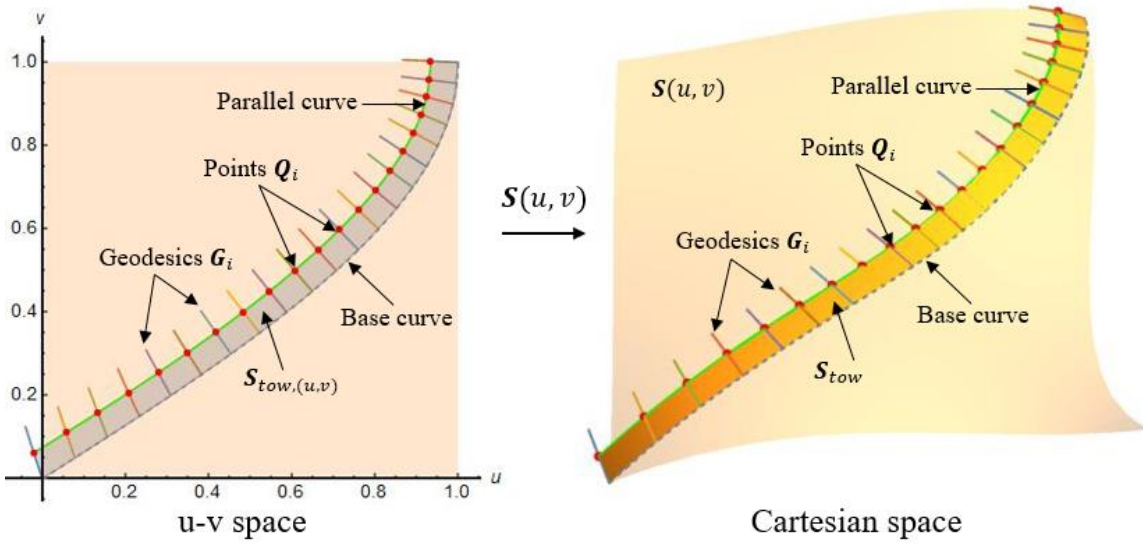

Figure 3.2 Parallel curves on the surface

Another important parameter to obtain from the geometry once the parallel path is computed, is the longitudinal strain ε_l or the strain along the length of the tow. ε_l is given by:

$$\varepsilon_l|_{t'_a \to t'_b} = \frac{d_{\boldsymbol{C_p}}\big|_{t'_a \to t'_b} - d_{\boldsymbol{C}}|_{t_a \to t_b}}{d_{\boldsymbol{C}}|_{t_a \to t_b}}, \tag{3.26}$$

where $d_{\boldsymbol{C}}|_{t_a \to t_b}$ is the distance between two points A and B along the reference curve $\boldsymbol{C}(t)$, $d_{\boldsymbol{C_p}}\big|_{t'_a \to t'_b}$ is the distance between A' and B' the corresponding points on the parallel curve $\boldsymbol{C_p}(t)$, hence $\varepsilon_l|_{t'_a \to t'_b}$ is the average strain between the two points A' and B' on the parallel curve. It is very important to first calculate the geodesic curvature k_g and to detect the location where there is a change of sign, its corresponding parameter t, and the boundaries associated with this change. If there is no change in the sign of the geodesic curvature, the boundaries A and B can be considered the start and the end of the tow. Then the strain calculation can be carried further to determine the severity of the anticipated defect. For

the case where the computed strain is negative, defects such as wrinkling, or in-plane waviness can be expected. For the case where the strain is positive, defects such as bunching, or folding can be expected. Lastly, for the case of zero strain, a defect free layup is anticipated such as the case of a straight path on a flat surface. Note that, this strain analysis is based on the length of the reference curve, or in other words, it is assumed that the machine head will deliver the exact amount of material as the length of the reference path.

The surface that should be covered by the tow is bounded by the initial path $\boldsymbol{C}(s)$ and the interpolated parallel curve $\boldsymbol{C_p}(s)$. The equation of the tow surface can be generated by first creating a ruled surface $\boldsymbol{S_{tow,(u,v)}}(s,n)$ in the (u,v) domain, where $n=0$ corresponds to the initial reference path $\{u_c(s), v_c(s)\}$ and $n=1$ corresponds to the parallel path $\{u_p(s), v_p(s)\}$:

$$\boldsymbol{S_{tow,(u,v)}}(s,n) = \begin{Bmatrix} u_{tow}(s,n) \\ v_{tow}(s,n) \end{Bmatrix} = (1-n)\begin{Bmatrix} u_c(s) \\ v_c(s) \end{Bmatrix} + n\begin{Bmatrix} u_p(s) \\ v_p(s) \end{Bmatrix}. \tag{3.27}$$

Then, the actual surface of the tow on the mold is generated by mapping $\boldsymbol{S_{tow,(u,v)}}(s,n)$ from (u,v) domain to the physical domain by:

$$\boldsymbol{S_{tow}}(s,n) = \boldsymbol{S}\big(u_{tow}(s,n), v_{tow}(s,n)\big). \tag{3.28}$$

3.1.5 Modeling Assumptions for Wrinkled Tow

The previous sections provided the necessary equations to calculate lengths and curvatures of prescribed paths and their parallel curves on a general surface, as well as the induced strain in the process. For paths with non-zero geodesic curvatures, the relative lengths of the inner and outer edges of a tow with a finite width will differ on the surface of a part. The AFP hardware on the other hand dispenses tows that have equal length on

both edges. The differential length on the part surface between the two edges of the tow has to be somehow absorbed through a deformation mechanism (Figure 1.4) within the tow to take the excess length on one edge of the tow that has to fit onto the part surface. Here it is assumed that the edge of the tow separates from the shorter edge on the surface while the tow's edge corresponding to the longer edge on the surface remains on its prescribed path. This will generate out-of-plane wrinkles along the length of the tow (see schematics in Figure 1.4 (e) and Figure 3.3). To summarize, the following assumptions are therefore considered in the modeling of the wrinkles:

1. The longest edge of the tow path will remain on the surface of the tool surface after placement.
2. The shortest edge of the tow path will totally lift from the surface to form the wrinkle.
3. The wrinkling formation is approximated by the rotation of the shortest edge around the longest.
4. The rotation angle is assumed to be a cosine function so that the shape of the obtained wrinkle is similar to the buckling of a plate with clamped-end conditions.
5. The shape of the buckled tow in the transverse direction will remain the same as the tow surface $\boldsymbol{S_{tow}}(s, n)$ before buckling (linear for the case of a flat plate, higher order for general surfaces).

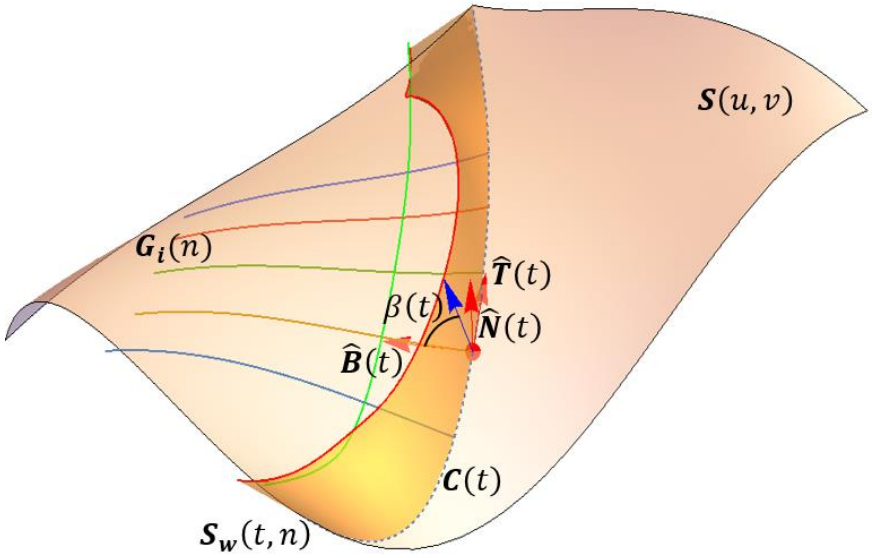

Figure 3.3 Schematic of a wrinkle of a general surface

Based on these assumptions, the wrinkled surface of the tow $\boldsymbol{S_w}(s,n)$ (Figure 3.3) is derived from the tow surface $\boldsymbol{S_{tow}}(s,n)$ in the following equation:

$$\boldsymbol{S_w}(s,n) = \boldsymbol{S_{tow}}(s,0) + \left(\boldsymbol{S_{tow}}(s,n) - \boldsymbol{S_{tow}}(s,0)\right) \cdot \mathcal{R}\left(\widehat{T}(s), \beta(s)\right), \tag{3.29}$$

where $\mathcal{R}\left(\widehat{\boldsymbol{T}}(s), \beta(s)\right)$ is Rodrigues' rotation matrix corresponding to the rotation by an angle $\beta(s)$ about the axis $\widehat{\boldsymbol{T}}(s)$, the unit tangent to the original path (assumption # 3). The first term in equation (3.29) $\boldsymbol{S_{tow}}(s,0)$ corresponds to the reference path (as discussed in the previous section), and represents the 1[nd] assumption concerning the reference edge remaining on the surface. For the case where the parallel path is the longest, the $\boldsymbol{S_{tow}}(s,0)$ terms in equation (3.29) should be replaced by $\boldsymbol{S_{tow}}(s,1)$. The second term in equation (3.29) represents the shape of the wrinkled tow in the transverse direction n at each location s. This shape remains unchanged as stated in assumption # 5. Rodrigues' rotation matrix $\mathcal{R}(\widehat{\boldsymbol{T}}, \beta)$ computes the rotation by an angle β about the unit axis $\widehat{\boldsymbol{T}} = \{T_x, T_y, T_z\}$ and is given in matrix form by:

$$\mathcal{R}(\widehat{\boldsymbol{T}}, \beta) =$$

$$\begin{pmatrix} \cos\beta + \hat{T}_x^2(1-\cos\beta) & -\hat{T}_z\sin\beta + \hat{T}_x\hat{T}_y(1-\cos\beta) & \hat{T}_y\sin\beta + \hat{T}_x\hat{T}_z(1-\cos\beta) \\ \hat{T}_z\sin\beta + \hat{T}_x\hat{T}_y(1-\cos\beta) & \cos\beta + \hat{T}_y^2(1-\cos\beta) & -\hat{T}_x\sin\beta + \hat{T}_y\hat{T}_z(1-\cos\beta) \\ -\hat{T}_y\sin\beta + \hat{T}_x\hat{T}_z(1-\cos\beta) & \hat{T}_x\sin\beta + \hat{T}_y\hat{T}_z(1-\cos\beta) & \cos\beta + \hat{T}_z^2(1-\cos\beta) \end{pmatrix}. \quad (3.30)$$

One of Rodrigues' rotation's conditions is that the rotation axis has to pass through the origin of the reference system. Hence the third term in equation (3.29) ensures that conditions by applying the necessary translation of "$-\boldsymbol{S_{tow}}(s, 0)$". Also, by choosing the rotation axis to be the unit tangent vector $\widehat{\boldsymbol{T}}(s)$, assumptions 1, 2, and 3 are respected. Lastly, the remaining term in equation (3.29) is the rotation angle $\beta(s)$. This angle is assumed to have a cosine shape function as stated in assumption # 4, and is given by:

$$\beta(s) = k\left(1 - \cos\left[\frac{2\pi(s - s_{i-1})}{s_i - s_{i-1}}\right]\right) \quad , \quad \text{for } i = 1, \dots, N \ . \quad (3.31)$$

Here s_i and s_{i-1} are the parameters corresponding to the starting and ending points of the tow section assuming rotation-free boundary conditions at the two ends along the length, and the amplitude k is computed so that the length of the shorter edge is set equal to the length of the longer one. The integer N in equation (3.31) represents the number of wrinkling waves along the tow or also referred here as the mode shape. Note that for $N = 1$ (1st mode shape, or only one wrinkle is assumed) the end points are equal to the start and end of the curve $\boldsymbol{C}(s)$. To calculate the amplitude k of the cosine shape function in equation (3.31), the equation for the parallel curve at a distance $n = 1$ in equation (3.31) $\boldsymbol{S_w}(s, 1)$ is computed and inserted into the length calculation using equation (3.14) (instead of the reference path) with the corresponding start and end points s_i and s_{i-1}, then an iterative method (such as Newton's method) is used to converge for a final value of k such that the total length of the shorter edge is equal to the length of the longer one.

Equation (3.31) represents the case where the wrinkles have equal wavelength along the analyzed tow section which is a good start for the wrinkling analysis. However, depending on the material properties of the tow, the properties of the tow-substrate interface, and the radius of curvature of the path, an approximate wavelength of the wrinkle can be determined based on mechanics models for tow wrinkling [17,24], or from experimental results [59]. In this case, equation (3.31) can be modified by taking the first mode shape only ($N = 1$), and then solving for the end-point s_i depending on the chosen wavelength for the wrinkle.

3.1.6 Simplification for Flat Surface

To provide a realistic example and verification with actual experiments for tow wrinkling, the previous equations are simplified for a flat surface. The equation for the surface (3.1) can be represented in three-dimensional space as:

$$\boldsymbol{S}(u,v) = u\hat{\imath} + v\hat{\jmath}\,. \tag{3.32}$$

Computations of the ensuing equations leads to the following relevant equations for the surface:

$$\begin{gathered} \widehat{\boldsymbol{S_u}}(u,v) = \hat{\imath} \quad , \quad \widehat{\boldsymbol{S_v}}(u,v) = \hat{\jmath}\,, \\ E = 1 \quad , \quad F = 0 \quad , \quad G = 1 \quad , \quad \text{All } \Gamma^i_{jk} = 0\,. \end{gathered} \tag{3.33}$$

The coefficients of the second fundamental form of the flat surface are all zero, leading to a zero Gaussian curvature as expected for the special case of a ruled surface:

$$e = f = g = 0, \text{and } K = 0. \tag{3.34}$$

The reference curve $\boldsymbol{C}(s)$ can be simplified and expressed as:

$$\boldsymbol{C}(s) = \boldsymbol{S}\big(u_c(s), v_c(s)\big) = u_c(s)\,\hat{\imath} + v_c(s)\,\hat{\jmath}, \tag{3.35}$$

with the corresponding normal, tangent, and in-plane normal vectors (Figure 3.4):

$$\widehat{\boldsymbol{N}}(u,v) = \hat{k} \tag{3.36}$$

$$\widehat{\boldsymbol{T}}(s) = \frac{u_c'(s)\,\hat{\imath} + v_c'(s)\,\hat{\jmath}}{\left(u_c'^{\,2}(s) + v_c'^{\,2}(s)\right)^{1/2}} = \hat{u}_c'(s)\hat{\imath} + \hat{v}_c'(s)\hat{\jmath} \tag{3.37}$$

$$\widehat{\boldsymbol{B}}(s) = \frac{-v_c'(s)\,\hat{\imath} + u_c'(s)\,\hat{\jmath}}{\left(u_c'^{\,2}(s) + v_c'^{\,2}(s)\right)^{1/2}} = -\hat{v}_c'(s)\hat{\imath} + \hat{u}_c'(s)\hat{\jmath} \tag{3.38}$$

with $\hat{u}_c'(s) = \frac{u_c'(s)}{\sqrt{u_c'^{\,2}(s)+v_c'^{\,2}(s)}}$, and $\hat{v}_c'(t) = \frac{v_c'(s)}{\sqrt{u_c'^{\,2}(s)+v_c'^{\,2}(s)}}$.

The equations for a geodesic path (3.18) reduce to a simple system of separable ODE's (Ordinary Differential Equation), reaffirming that the shortest path on a flat surface is a straight line:

$$\begin{cases} u'' = 0 \\ v'' = 0 \end{cases} \xrightarrow{yields} \begin{cases} u(t) = c_0 s + c_1 \\ v(t) = c_2 s + c_3 \end{cases}. \tag{3.39}$$

Therefore, the parallel edge curve at a distance d and the tow surface can be stated more simply as:

$$\boldsymbol{C_p}(s) = \begin{cases} x_p(s) = u_c(s) - d\;\hat{v}_c'(s) \\ y_p(s) = v_c(s) + d\;\hat{u}_c'(s) \end{cases}. \tag{3.40}$$

$$\boldsymbol{S_{tow}}(s,n) = \boldsymbol{C}(s) + n\,d\,\widehat{\boldsymbol{B}}(s), \qquad 0 \le s \le L, \qquad 0 \le n \le 1, \tag{3.41}$$

and d being equal to the tow width. The in-plane curvature (simplified version of the geodesic curvature) is calculated from:

$$k_g(s) = \frac{u_c' v_c'' - u_c'' v_c'}{\left(u_c'^{\,2} + v_c'^{\,2}\right)^{3/2}}. \tag{3.42}$$

The shape of the wrinkled tow surface $\boldsymbol{S_w}(s,n)$ shown in Figure 3.4 is represented as:

$$\boldsymbol{S_w}(s,n) = \boldsymbol{C}(s) + n\,d\left[\cos\left(\beta(s)\right)\widehat{\boldsymbol{B}}(s) + \sin\left(\beta(s)\right)\widehat{\boldsymbol{N}}(s)\right], \tag{3.43}$$

or explicitly in terms of the Cartesian three-dimensional space:

$$\boldsymbol{S_w}(s,n) = \begin{cases} x_w(s,n) = u_c(s) - n\,d\,\hat{v}_c'(s)\cos\left(\beta(s)\right) \\ y_w(s,n) = v_c(s) + n\,d\,\hat{u}_c'(s)\cos\left(\beta(s)\right) \\ z_w(s,n) = n\,d\,\sin\left(\beta(s)\right) \end{cases} \tag{3.44}$$

where $\beta(s)$ is the same cosine shape function for the wrinkle rotation angle as shown earlier in equation (3.31). The amplitude k of the rotation angle $\beta(s)$ is found using the length calculations for the parallel edge at n=1 and setting it equal to the original path length:

$$\int_{s_{i-1}}^{s_i} \sqrt{\left(\frac{dx_w}{ds}\right)^2 + \left(\frac{dy_w}{ds}\right)^2 + \left(\frac{dz_w}{ds}\right)^2}\; ds = \frac{L}{N} \qquad for\ \ i = 1, \dots, N \tag{3.45}$$

Lastly, the maximum height the wrinkle will reach occurs at $s_{max} = (s_i - s_{i-1})/2$, resulting in a maximum rotation angle $\beta = 2k$. From equation (3.45), the amplitude of the wrinkle can be obtained to be:

$$a_w = z_w(s_{max}, 1) = d\ \sin(2k). \tag{3.46}$$

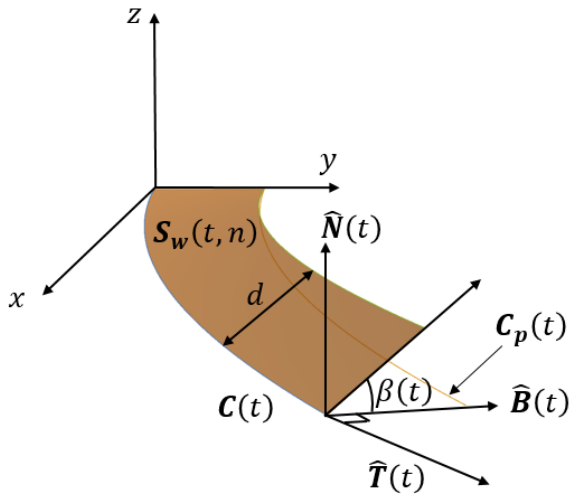

Figure 3.4 Schematic of a wrinkle for the simplification of flat surface

3.2 APPLICATION FOR PATHS ON FLAT AND GENERAL SURFACES

This section demonstrates the implementation of the developed wrinkling equations for paths placed on flat and general surfaces. The first example considers a simple circular path on a flat surface where the effect of the wrinkles number and tow width are investigated while keeping the curvature constant. The second example consists of analyzing the wrinkled shape of a tow placed on a general surface, and the effect of the geodesic curvature on the wrinkling amplitudes. Then, several different layups with fixed-angle reference curves are considered for wrinkling analysis.

3.2.1 Examples for Paths on a Flat Surface

To investigate the presented algorithm, a simple constant curvature path is first considered. This path is a circular arc, with a possible parametrization defined as:

$$\boldsymbol{C}(t) = \left\{\cos\left(\frac{\pi}{2}t\right), \sin\left(\frac{\pi}{2}t\right)\right\} \quad , \quad 0 \leq t \leq 1, \tag{3.47}$$

where the radius of curvature is constant with a value of 1. A tow width of $w = 0.2$ (non-dimensional units) is first considered, and the parallel path is computed from equation (3.40), then the wrinkled shaped of the tow in equation (3.44) is calculated for the first 4 mode shapes ($N = 1, \dots, 4$) and visualized in Figure 3.5.

In Figure 3.5, the reference curve $\boldsymbol{C}(t)$ shown in blue remains on the surface while the parallel edge shown in orange will totally lift from the surface and form the wrinkle. Also, it can be directly observed that the amplitude of the wrinkles is affected by the mode shape. With higher mode shape the amplitude of the wrinkles decreases significantly. In addition, within a mode shape the amplitude of the wrinkles for this case is the same; i.e. the three wrinkles in the 3rd mode shape have the same amplitude, similarly for the four

wrinkles in the 4th mode shape. This is due to the fact that this circular path has a constant curvature of $k_g = 1$ and constant width $w = 0.2$ leading to a constant differential length.

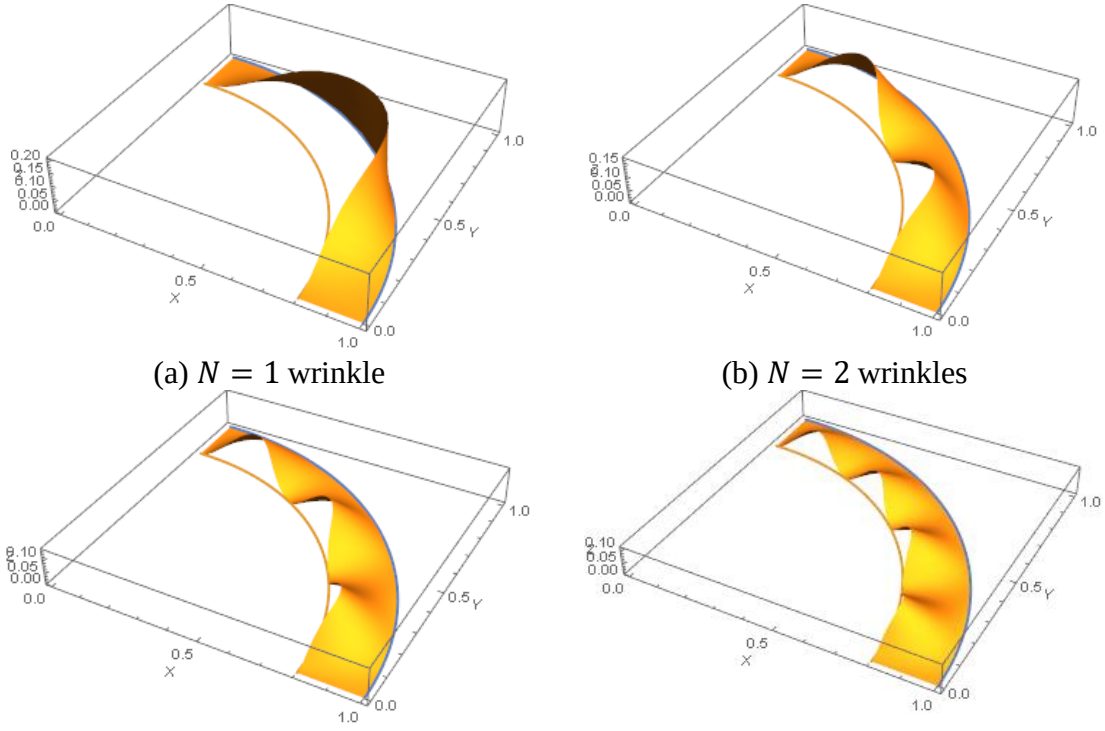

(a) $N = 1$ wrinkle (b) $N = 2$ wrinkles

(c) $N = 3$ wrinkles (d) $N = 4$ wrinkles

Figure 3.5 Deformed tow placed on a circular path: 4 different mode shapes

Another important geometrical feature to investigate is the effect of tow width on the severity of the wrinkles' formation. To accomplish that, the same reference path $\boldsymbol{C}(t)$ defined in equation (3.47) is considered for analysis, with different values of the tow width ranging from $w = 0.05$ to $w = 0.3$, resulting in different parallel paths $\boldsymbol{C_p}(t)$. Four of these different tows with different tow width are shown in Figure 3.6.

To obtain a fair comparison between different tow widths, the same mode shape is applied for all the paths. Visual interpretation of Figure 3.6 shows that increasing the tow width increases the amplitude of the wrinkle.

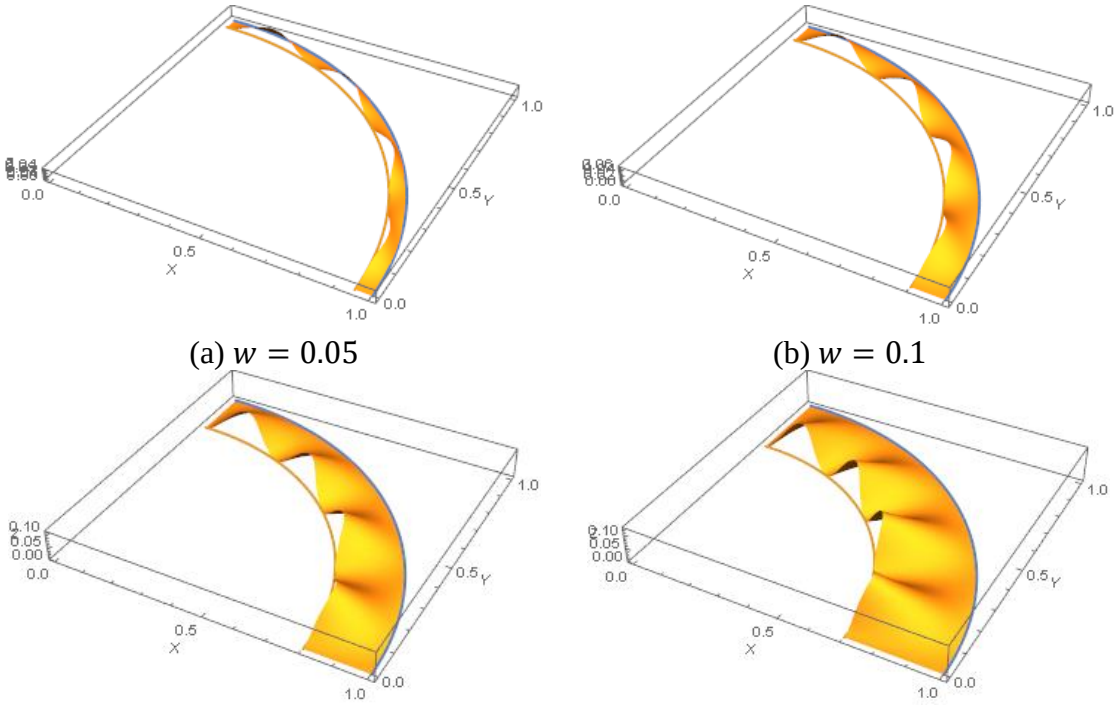

(a) $w = 0.05$ (b) $w = 0.1$

(c) $w = 0.2$ (d) $w = 0.3$

Figure 3.6. Effect of tow width on the wrinkles' amplitude

3.2.2 Examples for Paths on a General surface

The first step in the analysis of a 3D towpath is to specify the surface on which the tow is laid down. To do so, the NURBS form of a surface is used since it is compatible with and implemented in most CAD software packages and offers a wide flexibility for the user. A NURBS surface is given by:

$$\boldsymbol{S}(u,v) = \frac{\sum_{i=0}^{n}\sum_{j=0}^{m} N_{i,p}(u)\, N_{j,q}(v) w_{i,j} P_{i,j}}{\sum_{i=0}^{n}\sum_{j=0}^{m} N_{i,p}(u)\, N_{j,q}(v) w_{i,j}}. \tag{3.48}$$

The $P_{i,j}$ are the control points (control net), $w_{i,j}$ are the corresponding weights, $N_{i,p}(u)$ and $N_{j,q}(v)$ are the non-uniform rational B-Splines basis functions of degree p and q, respectively, which are defined over the knot vectors $\boldsymbol{U}$ and $\boldsymbol{V}$ (see [60] for details on NURBS surface parameterization).

To illustrate the calculation presented previously for a general surface, a quasi-random NURBS surface (Figure 3.7) is considered with the following parameters:

$$P_{i,j} = \begin{Bmatrix} \{\{1,1,-0.643\},\{1,2,-0.404\},\{1,3,-0.795\},\{1,4,-0.513\}\}, \\ \{\{2,1,0.692\},\{2,2,0.281\},\{2,3,-0.458\},\{2,4,-0.14\}\}, \\ \{\{3,1,0.085\},\{3,2,0.986\},\{3,3,-0.693\},\{3,4,0.678\}\}, \\ \{\{4,1,0.502\},\{4,2,-0.999\},\{4,3,0.804\},\{4,4,0.475\}\} \end{Bmatrix} \quad (3.49)$$

$$w_{ij} = \{\{1\,,1\,,1\,,1\}\,,\{1\,,1\,,1\,,1\}\,,\{1\,,1\,,1\,,1\}\,,\{1\,,1\,,1\,,1\}\} \quad (3.50)$$

$$\boldsymbol{U} = \boldsymbol{V} = \{0\,,0\,,0\,,0\,,1\,,1,1\,,1\} \quad (3.51)$$

$$p = q = 3 \quad (3.52)$$

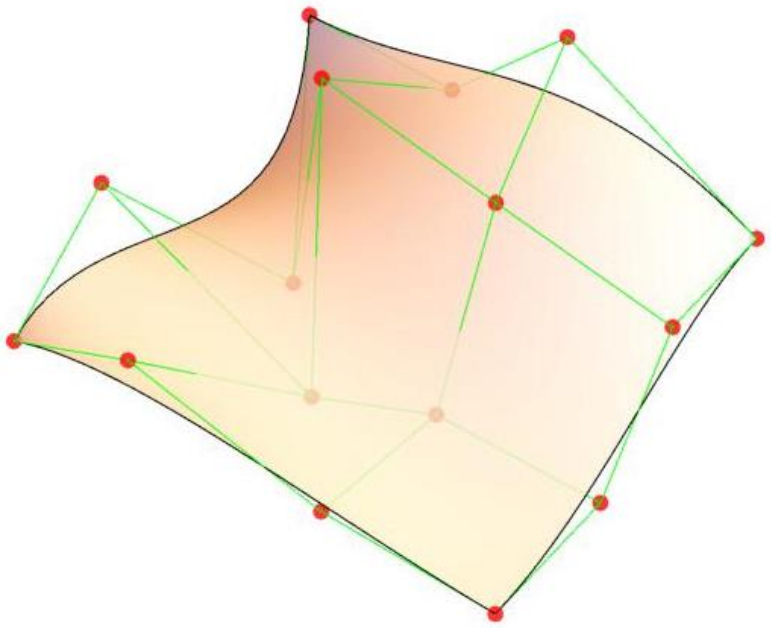

Figure 3.7 Example NURBS surface

The *Z*-coordinate of the control points is a randomly generated real number, whereas the *X* and *Y* coordinates are equally spaced to form a square mesh between 1 and 4 (units). The knot vectors are uniform, and the weights are equal to 1. In this case, the NURBS surface is a special case of a B-Spline surface. This case is used for demonstration purpose and is displayed in Figure 3.7.

For demonstration purposes, the path to be analyzed is chosen to have the following functional form parameters:

$$u_c(t) = \sin\left(\frac{\pi}{2}t\right), v_c(t) = t\,. \tag{3.53}$$

Therefore, the reference path $\boldsymbol{C}(t)$ has the following equation:

$$\boldsymbol{C}(t) = \boldsymbol{S}\big(u_c(t), v_c(t)\big) = \boldsymbol{S}\left(\sin\frac{\pi}{2}t\,, t\right), \qquad 0 \le t \le 1. \tag{3.54}$$

Calculation of the geodesic curvature using equation (3.25) along the length of this curve on the NURBS surface is shown in Figure 3.8.

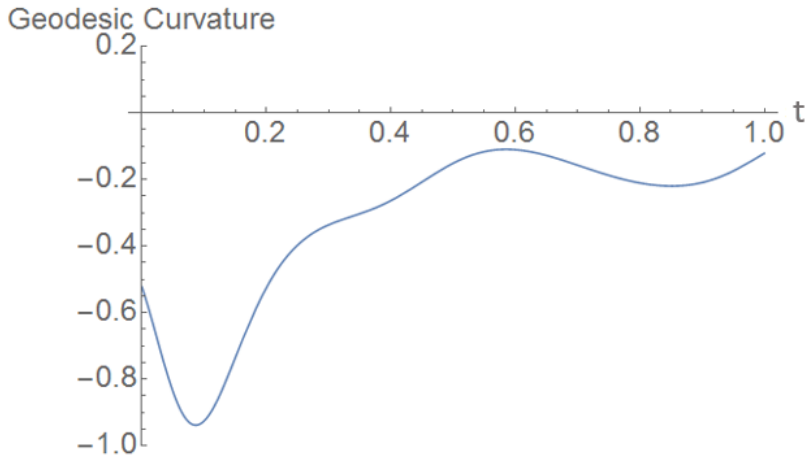

Figure 3.8 Geodesic curvature of the reference path on the NURBS surface

Inspection of the geodesic curvature indicates that the amplitude of the wrinkles will be higher in the first section of the path and lower in the later section. The first four mode shapes generated by implementing the wrinkled shape of the tow from equation (3.29) are shown in Figure 3.9 which agrees with the prediction that the wrinkles are proportional to the geodesic curvature.

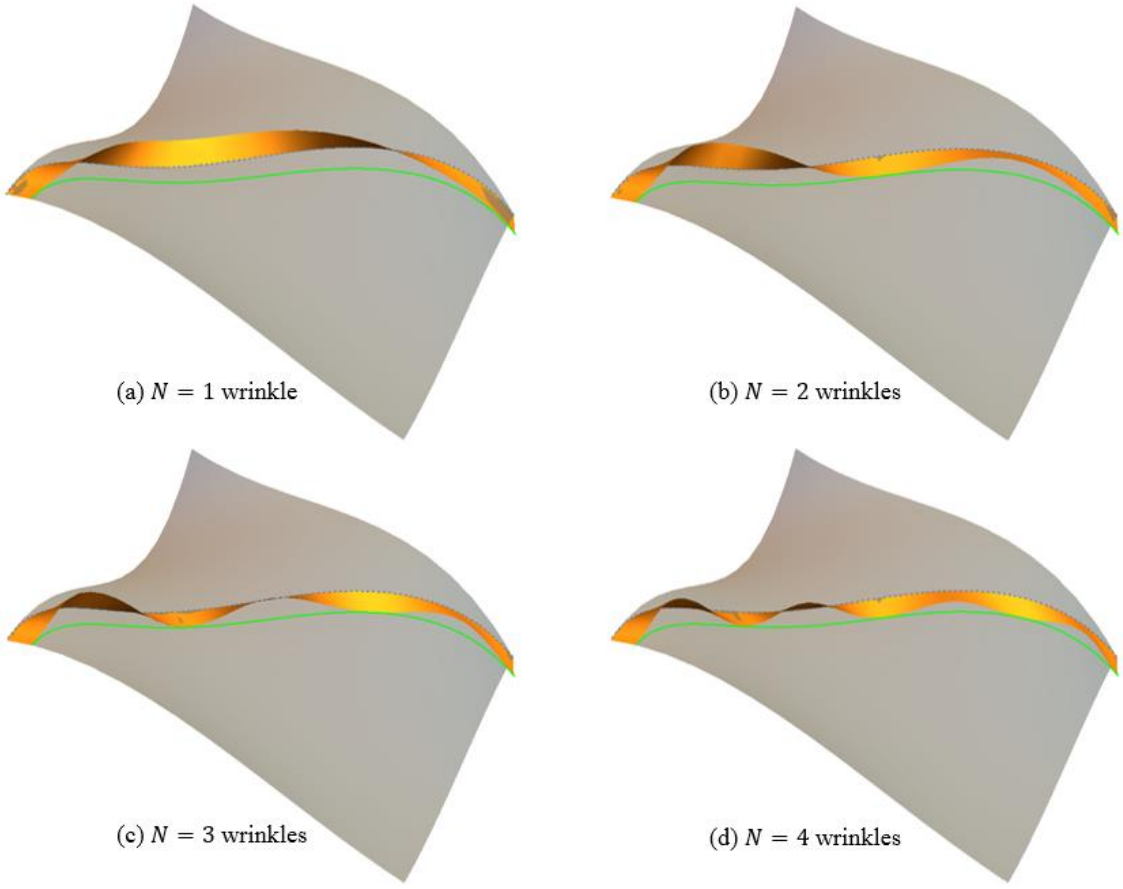

Figure 3.9 First 4 mode shapes of a tow placed on a NURBS surface

Another feature that this method can offer is a general color map of the tows indicating the locations where wrinkles might appear and their severity, as demonstrated in Figure 3.11. Four different constant angle layups on the general surface are shown in Figure 3.11. Based on the differential length between the two sides of the tow (directly related to the geodesic curvature), the calculations can be used to detect the possible location of the wrinkle. A positive differential length (colored in blue) indicates that wrinkles might appear on the dashed blue side of the represented tow, whereas a negative differential length (colored in yellow red) indicates that the wrinkles might appear on the solid orange side of the tow. The green region is the best from manufacturing perspective since it is the least portion where wrinkling defect might appear. In addition, the wrinkling

equations are applied to the layup at a 45° angle, where the wavelength of the wrinkles are assumed to be equal over the entire layup. The results are shown in Figure 3.10. For visualization purposes, the wrinkled tows are colored with their amplitude normalized with the tow width. A comparison between the geodesic curvature map of this layup (Figure 3.11) and the wrinkling map (Figure 3.10) shows a good agreement between the two on the location of the critical wrinkles and their direction.

Comparing the different angled layup, it can be clearly noticed that the critical regions of the wrinkles do not depend only on the surface geometry, but also on the chosen paths. For instance, the bottom left corner of the 0° layup is relatively wrinkle free, whereas this area is the most critical for the 45° layup. This implies that a wrinkling analysis is necessary for each layup prior to manufacturing since each layup will behave differently as shown in Figure 3.11.

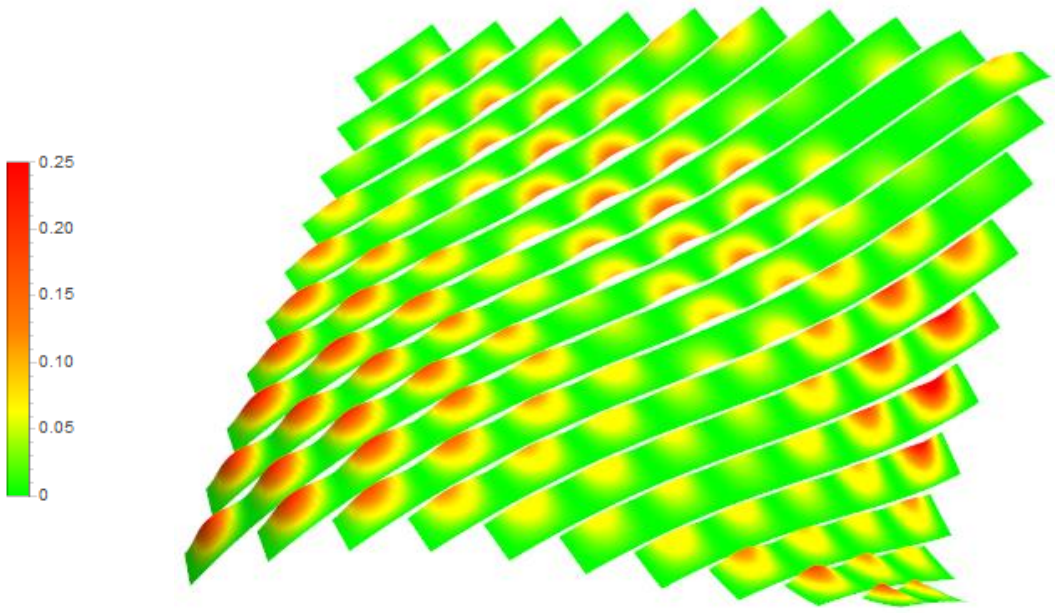

Figure 3.10 Wrinkling map for the 45° layup on the NURBS surface

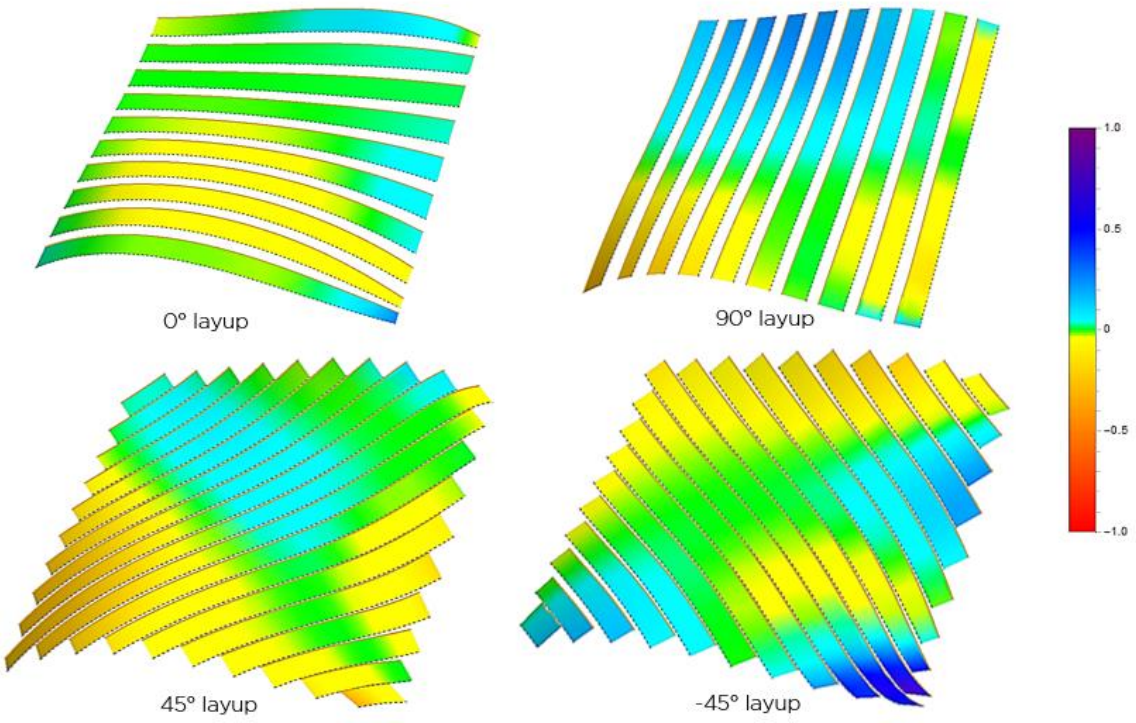

Figure 3.11 Geodesic curvature color map for different layup on the NURBS surface

3.3 MODEL IMPROVEMENTS AND APPLICATION TO THERMOSET MATERIALS

This section describes the improvement to the existing geometrical model by including information from the experimental measurements and other physics-based models from the literature. The reason behind these additions is that geometrical model lacks necessary information regarding the material used during the AFP process. In the geometrical model presented earlier, multiple wrinkles patterns can be generated for a given layup representing a worst-case scenario which may not be realistic due to other deformation mechanisms within the tow. In addition, one of the generated patterns may be true for a given material system, however, does not apply for other material systems. Hence, a better approximation is needed and will be described below.

The first improvement is based on mechanics models from existing literature [17,23,24]. In these models, tow wrinkling is modeled as a buckling problem of an orthotropic plate resting on an elastic foundation. Assuming an adequate shape function, and using the Raleigh-Ritz method to minimize the total energy of the system, closed form solutions for the critical steering radius and the buckle wavelength can be obtained [24]. Using the same approach described in [24], an improved two-parameters Pasternak elastic foundation is used in [17] to obtain the closed form solutions which will be used later in this section. For a steering radius above the critical radius, no wrinkles occur, and all the differential length is absorbed through compressive/tensile strains. When steering below the critical radius, wrinkles will occur with a prescribed wavelength obtained from these models which depends on the material used and the steering radius. The amplitude of the wrinkles can therefore be obtained from the length calculations presented earlier in the geometrical model.

In addition, experimental measurements for the wrinkle wavelength, width, and amplitude for several steering radii is accomplished and detailed in [59] and later on in Chapter 5. In a similar way, a critical steering radius can be determined above which no wrinkles will occur. Below that radius, a wrinkle wavelength and width are used to generate the wrinkles, and the amplitudes are calculated using the geometrical model. Lastly, multiple steering examples are used to validate the presented improvements.

3.3.1 Wrinkle wavelength from mechanics models

For the improved geometrical model based on mechanics information, the wrinkle wavelength for a given radius of curvature and material properties can be obtained from closed form solutions available in the literature [17,23,24]. The deformed shape of the tow

can therefore be generated for the given wavelength using a cosine function consistent with the assumed shape function in the Raleigh-Ritz method used to find the closed form solution. As a result, the wrinkle wavelength can be obtained by solving the following biquadratic equation [17]:

$$\mathcal{A}\, L^4 + \mathcal{B}\, L^2 + \mathcal{C} = 0\,, \tag{3.55}$$

with:

$$\mathcal{A} = 90D_{22}\left(\frac{1}{\pi m b^2}\right)^2 + \frac{9}{2}k\left(\frac{1}{\pi m}\right)^2 + 30G\left(\frac{1}{\pi m b}\right)^2, \tag{3.56}$$

$$\mathcal{B} = 160\, D_{66}\left(\frac{1}{b}\right)^2 - 40D_{12}\left(\frac{1}{b}\right)^2 - (6-\alpha)\left(\frac{E_1 hb}{\alpha R}\right) + 6G\,, \tag{3.57}$$

$$\mathcal{C} = 24D_{11}(\pi m)^2\,. \tag{3.58}$$

The D_{ij} terms in equations (3.56) - (3.58) are the components of the bending stiffness matrix of a composite plate, which for a single layer, can be expressed as:

$$D_{11} = \frac{E_1 h^3}{12(1-\nu_{12}\nu_{21})}\,, \qquad D_{12} = \nu_{21}D_{11}, \qquad D_{22} = \frac{E_2}{E_1}D_{11}, \qquad D_{66} = \frac{G_{12}h^3}{12}. \tag{3.59}$$

The remaining parameters required to solve (3.55) are defined as follows: k and G are the normal and shear stiffnesses of the elastic foundation, b and h are the tow width and thickness respectively, m is the number of wrinkle wavelength (m is taken to be equal to 1 for an isolated wrinkle in these models), α is the load non-uniformity coefficient ($\alpha = 0$ corresponds to uniform compression, $\alpha = 1$ corresponds to a load decaying from the inner tow edge to the outer one, and $\alpha = 2$ corresponds to pure bending). Note that equation (3.55) admits a real solution only when $\mathcal{B}^2 \geq 4\mathcal{A}\mathcal{C}$.

Assuming that the material properties of the tow and substrate can be obtained through accurate experimental measurements, and these properties are consistent along the length of the tow-path (which might not be totally true if the substrate has defects or the layup temperature is variable thus changing the material properties locally), the only

remaining variable affecting the wavelength of the wrinkles would be the radius of curvature of the path R. For the material properties of an uncured tow obtained from the literature [17,23,27] and presented in Table 3.1, the relationship between the wavelength and the steering radius is plotted based on the solution of equation (3.55) and shown in Figure 3.12. Note that only the positive increasing root is chosen from the solution of (3.55) and shown in Figure 3.12. It can be observed that the relationship between the wavelength and the steering radius is linear for a significant range of the steering radius. In addition, the closed form solution for the critical steering radius provided in [17] results in $R_{critical} = 1303\ mm$ for the provided parameters in Table 3.1. For a steering radius above this value, the roots for (3.55) becomes complex numbers, and wrinkles do not occur along the path.

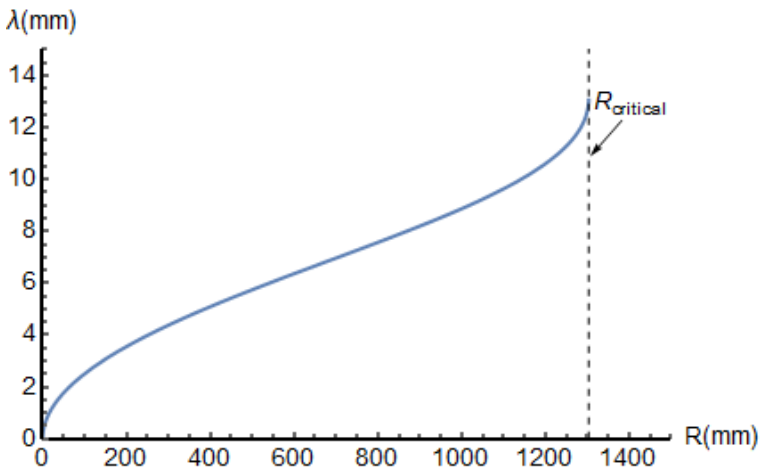

Figure 3.12 Wrinkle wavelength as a function of steering radius based on mechanics model (3.55)

Table 3.1 Material properties and geometry of uncured tow obtained from [17,23,27]

E1 (GPa)	**E2 (MPa)**	**G12 (MPa)**	$\boldsymbol{\nu_{12}}$	$\boldsymbol{\nu_{21}}$	**h (mm)**	**b (mm)**	$\boldsymbol{\alpha}$	**G (N/m)**	**k (N/m3)**
31	0.046	3.025	0.2	0.02	0.2	6.35	2	605	2.65×10^{8}

The algorithm for the improved geometrical model based on mechanics information is described as follows. For a given path, the steering radius (inverse of curvature (3.42))

should be captured first. For the regions where the steering radius is above the critical steering radius, no wrinkles occur, and the wrinkled tow surface remains the same as the original tow surface which can be accomplished by setting k, the amplitude of the rotation angle in (3.31) to zero. For the areas where the radius of curvature is below the critical one, the corresponding boundaries of the wrinkles can be obtained successively by relating the radius to the wavelength obtained from the mechanics model. Once these boundaries are determined, the wrinkled surface of the tow can be obtained by carrying the length calculations as described earlier in the geometrical model. Therefore, as the analysis progresses along the length of the path, local wrinkles can be generated with different sizes depending on the path curvature and having the other material properties fixed.

This approach can be generalized and applied for curves on general surfaces by taking the geodesic curvature of the path (3.25) to be the relevant parameter for the wrinkle formation since it is responsible for the tow bending in a plane tangent to the surface at the given location. The geodesic curvature is then compared to the critical curvature from the mechanics model and the algorithm proceeds similarly to the flat case. However, by doing so, the effect of the normal curvature of the path is not be taken into consideration. This can be justified since the normal curvature for paths placed on realistic large aerospace structures is usually negligible compared to the geodesic curvature.

For the case where this model is to be used for highly curved surfaces and for large tow/tape width, the geodesic curvature of the original path cannot be used as a measure for wrinkling since the parallel edges of the tow/tape have significantly different geodesic curvatures. Instead, the strain along the parallel edges should be computed using (3.26) and

compared to the critical strain at which wrinkling occurs. The critical strain can be related to the critical steering radius, tow width, and the load non-uniformity coefficient α by [24]:

$$\varepsilon_{critical} = \frac{b}{\alpha\, R_{critical}}. \tag{3.60}$$

For the case where the strain is below the critical one, no wrinkles occur, otherwise, the algorithm proceeds to generate the wrinkles boundaries and the deformed tow surface.

3.3.2 Wrinkle wavelength and width from experimental results

Another approach to improve the geometrical model is to include information from steering experiments. The key difference between the pure geometrical model, its improvement based on mechanics model and the presented model in this section is that the wrinkle is characterized not only by its wavelength, but also by its width. The wrinkle wavelength λ_w is defined as the distance between two adjacent peaks along a path, and the wrinkle width l_w as the total length the tow is separated from the substrate. In general, the wrinkle width is smaller than the wavelength. By identifying these two key parameters, a more accurate representation of the wrinkles can be achieved especially for thermoset materials where significant areas of the tow remain adhered to the substrate. The representations for the shape of the wrinkles including these parameters as well as the original assumption are shown below in Figure 3.13 and Figure 3.14.

Several experimental trials are accomplished, and measurements of wrinkles' wavelengths, amplitudes, and widths are accomplished using stereo DIC for different radii of curvature. The detailed methodology and results are shown later in Chapter 5. For the purpose of this section, these quantities are plotted against the steering radius and shown in Figure 3.15, Figure 3.16, and Figure 3.17. Linear interpolation functions are used to fit the experimental data points. These functions are extrapolated to intersect with radius axes

for the amplitude and width hence resulting in a critical steering radius. The obtained critical radii are 1410 mm and 1482 mm for the amplitude and width respectively. Hence an average of 1446 mm is used as a critical radius for wrinkles to occur for the thermoset material and the set of process parameters used in [59].

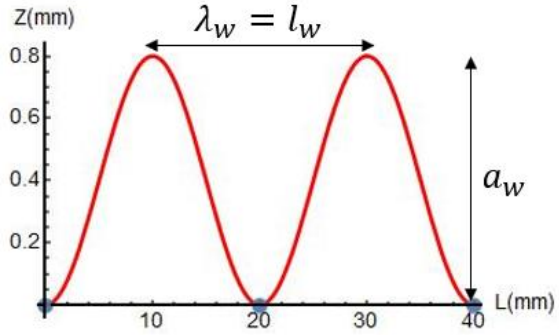

Figure 3.13 Shape of the wrinkle used in geometrical model and the improved model based on mechanics

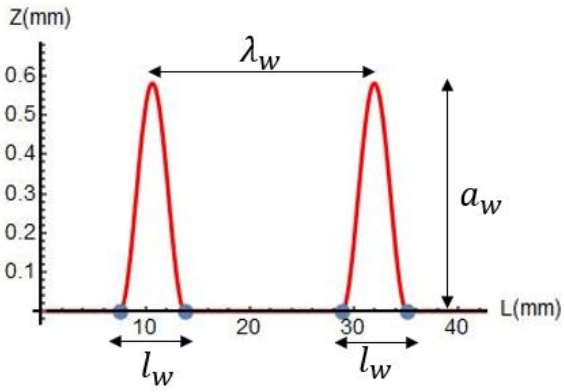

Figure 3.14 Shape of the wrinkle used in the improved model based on experimental data

Based on the critical steering radius, the geometrical model identifies the critical areas where the curvature is exceeded and generates wrinkles. The shape of the wrinkle however is different for this case: for a given wavelength, some areas along the length remain bonded to the substrate due to other deformation mechanisms that occur, and a cosine function is only applied to the width of the wrinkle as shown in Figure 3.14. It is assumed that the wrinkle width is centered along the wavelength, and two equal regions of bonded material is assumed from each side. Based on these assumptions, the boundaries where the wrinkle separates from the substrate can be determined, and the length calculation can be carried to determine the final shape and amplitude of the wrinkle. As the analysis progresses along the length of the tow-path, different wrinkles wavelength, width and amplitudes are generated based on the curvature. This approach creates a more realistic

case where out-of-plane wrinkles are not the only deformation mechanisms that occur. This approach can also be extrapolated to curves on general surfaces by taking the geodesic curvature as the key parameter for wrinkle formation as described in the previous section.

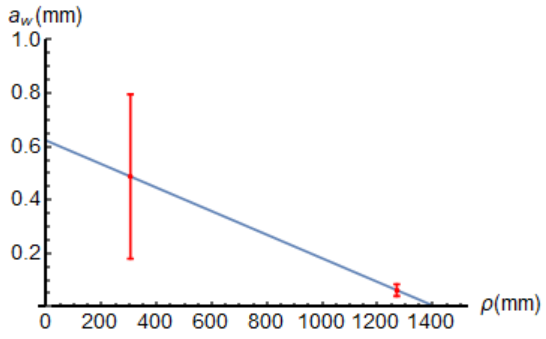

Figure 3.15 Measured wrinkle amplitude as a function of steering radius

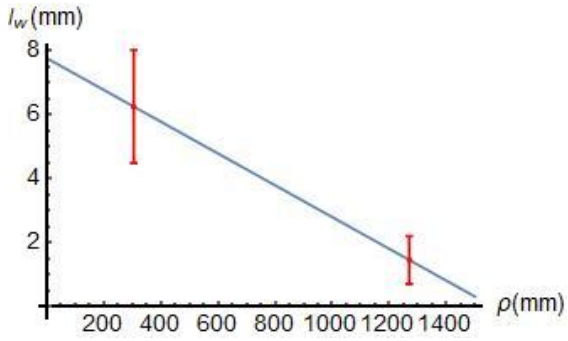

Figure 3.16 Measured wrinkle width as a function of steering radius

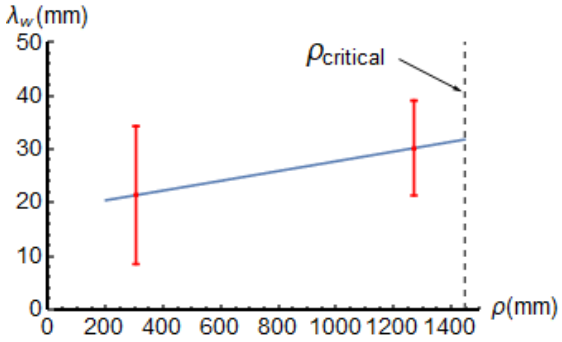

Figure 3.17 Measured wrinkle wavelength as a function of steering radius

Another improvement can be made for this model by including additional statistical information from the measured data such as the standard deviation. From experimental measurements, and even for a constant radius of curvature, wrinkles appear with different sizes, hence taking the average of the measured quantities is an approximation. A probabilistic model can therefore be implemented by assuming a normal distribution (or other valid distribution) for the wrinkle's wavelength, width, and/or amplitude, thus generating different wrinkles even for the same steering radius.

3.3.3 Application to thermoset materials

In this section, the improved model based on experimental results from thermoset material is applied for several examples. In a first step, the calculations of the wrinkle shape and amplitude from the geometrical model is compared to the original geometrical model and to the actual shape measurement obtained from DIC. To do so, a 6.35 mm wide tow is place on a constant curvature path steered at 305 mm radius is considered for analysis. For a constant curvature path, the wrinkle's wavelength and width are constant along the path and are equal to 21.43 mm and 8.03 mm respectively [59]. A comparison between the prediction of the original geometrical model and the improved one for the same wavelength is shown in Figure 3.18. It can be observed that the improved model gives a better approximation of tow wrinkling for thermoset materials by considering additional bonded areas to the substrate.

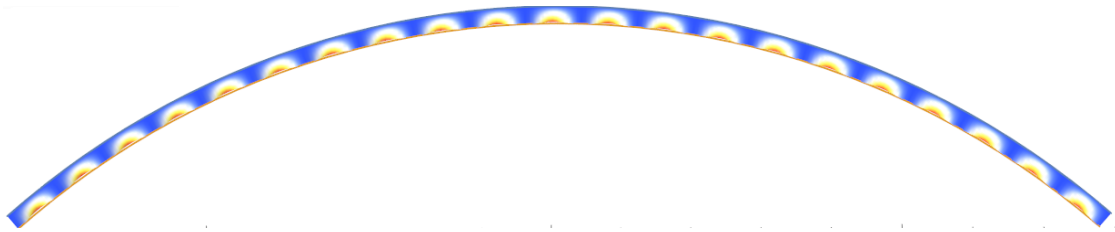

(a) Geometrical model with 21.43 mm wavelength

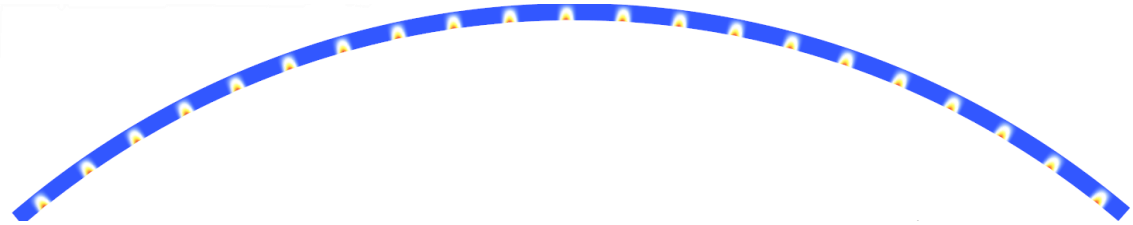

(b) Improved model from experiment

Figure 3.18 Comparison between the geometrical model and the improved model from experimental data for a steering radius of 305 mm

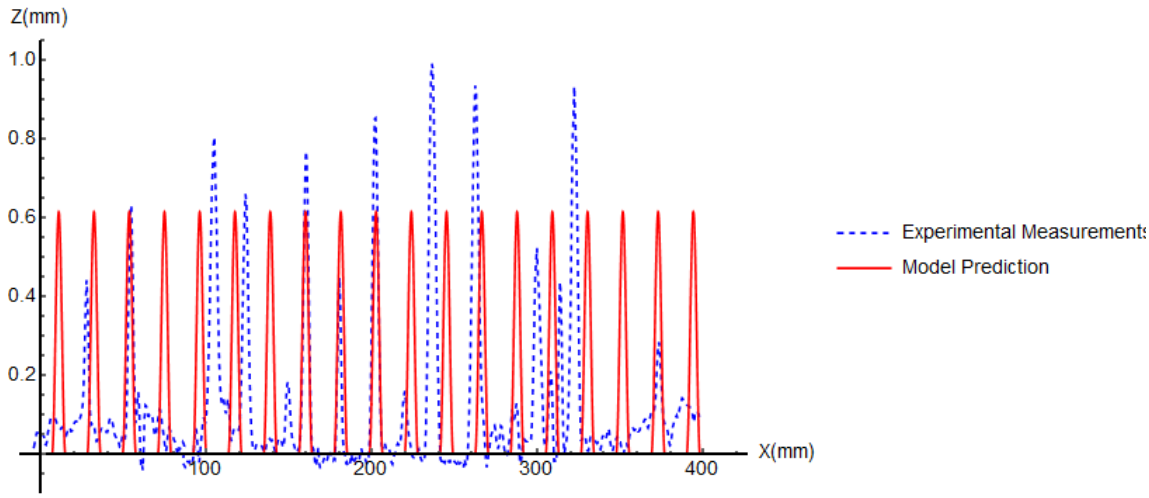

Figure 3.19 Model prediction vs experimental measurements of the out-of-plane displacements for a path steered at 305 mm radius at a line 1 mm above the bottom edge

Another example containing variable curvature paths is considered for analysis. It consists of multiple sinusoidal path with varying amplitudes. This family of curves is defined by:

$$\boldsymbol{C}(t) = \{300\pi t, a_m \sin(2\pi t) + c, 0\}, \quad 0 \leq t \leq 1\,, \tag{3.61}$$

where a_m is the amplitude of the sine waves ranging from 10 mm to 80 mm with an increment of 10 mm, and c is a constant for translation along the y-axis to avoid overlapping paths. The tow width is taken at 6.35 mm consistently with the experimental results. The wrinkles patterns for these paths obtained from the improved model based on the experimental data are shown in Figure 3.20. It can be observed that for the path with $\alpha = 10\,mm$ no wrinkles appear along the path. A further examination of the curvature reveals that the minimum steering radius for this path is 2250 mm which is above the critical radius obtained from the experiments. As the amplitude of the sine waves increases, the curvature of the paths increases as well, and wrinkles start to appear along the tow. In addition, with higher curvature, the wrinkles become wider, larger, and closer to each other consistent with the trends observed in the experiments.

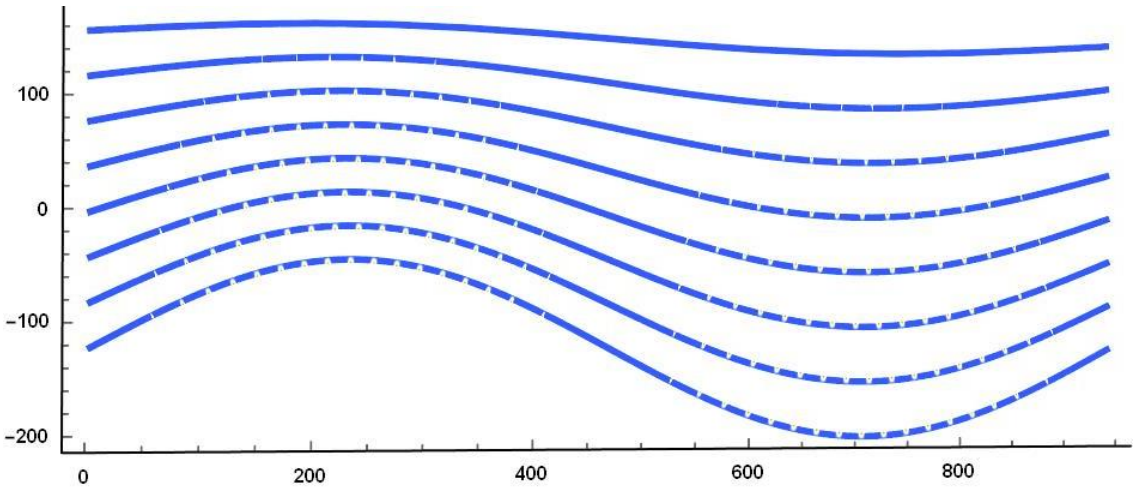

Figure 3.20 Wrinkle prediction for a layup sinusoidal paths with variable amplitudes (units in mm)

3.4 CONCLUSIONS

Several defects might arise during manufacturing of fiber reinforced composite structures using the Automated Fiber Placement process, one of them is tow wrinkling. The main reason behind the occurrence of tow wrinkling is the mismatch in length between the tow-path on the placement surface and the actual length of the tow delivered from the machine head. Modeling tow wrinkling is a complex task that involves process parameters, material properties and geometry. In the presented chapter, geometrical parameters affecting tow wrinkling are only investigated, neglecting the elastic properties, tackiness of the tow and other process parameters. A worst-case scenario is assumed where all the differential length is absorbed by wrinkles formation in the out-of-plane direction when steered or placed on a general curved surface.

Based on these assumptions, governing equations for tow wrinkling along an arbitrary path on a general surface are derived. The tow is assumed to wrinkle on its compressive edge where the length of the tow-path is smaller than the length of the actual tow leading the outer edge to lift totally from the surface to form a wrinkle. The shape of

the wrinkle is assumed to be a cosine function similar to the buckling of a beam with clamped-ends conditions. Further simplifications of the relevant equations are also presented to account for the special case of curved paths placed on a flat surface.

The implementation of the wrinkling governing equations to several examples is also presented. The case of a constant curvature circular path placed on a flat surface is first considered where the effect of the tow width and wrinkle numbers is studied. Results show that increasing the tow width will lead to higher amplitude of wrinkles. However, increasing the number of wrinkles within a prescribed path results in a lower wrinkling amplitude. Higher number of wrinkles can be achieved in the presence of good adhesion between the tow and the underlying surface.

For the case of paths on a general surface, an arbitrary path on a quasi-random NURBS surface is analyzed. The results show that the wrinkles amplitude is proportional to the geodesic curvature of the path. In addition, four different constant angle layups ($\pm 45°, 0°$, and $90°$) on the same NURBS surface are analyzed and results are shown in colored maps indicating possible regions of wrinkling. It is concluded that for the same placement surface, different angled layups have different critical regions for wrinkling.

Improvements to the geometrical model are presented for two cases: (1) based on mechanics models from the literature, and (2) based on data from experimental measurements. For the first case, a closed form solution for the critical steering radius and the wrinkle wavelength can be obtained as a function of the tow material properties and geometry. The wrinkle wavelength can be used to calculate the amplitude of the wrinkles from the geometrical model when the steering radius drops below the critical value. For the second case, relationship between the wrinkle wavelength, width and steering radius

are derived from experimental data. In a similar way, the amplitude of the wrinkles can be found geometrically based on the steering radius, wrinkle wavelength and width.

CHAPTER 4

PHYSICS-BASED MODEL OF TOW DEFORMATIONS IN AFP

This chapter investigates several aspects of tow deformations when placed on steered path using AFP process. The interest is to find the deformed shape of the tow when placed on a curved path based on the tow and path geometry and based on a set of material properties for the tow and substrate. In order to capture the exact tow deformations, there are no predefined deformation functions assumed in this chapter (such as the deformation assumed in the literature for plate buckling [23],[24]), rather a numerical solution is implemented to determine the shape of the deformed tow based on equilibrium equations. The tow is modeled as multiple fiber bundles laying on a stiff foundation. Since the tow in its uncured state is highly anisotropic (the fiber direction is orders of magnitude stiffer than the transverse direction), the interaction of multiple fiber bundles in the transverse direction may be negligible, hence it is first ignored in Sections 4.1 and 4.2 but later investigated in Section 4.3. In addition, only in-plane deformations are investigated in the first section where tensile/compressive strains, fiber waviness and fiber bunching are the main deformation mechanisms. In Section 4.2, out-of-plane deformation for a single fiber bundle are included, thus allowing all deformations to occur. Lastly, the interaction of the fiber bundles through transverse and shear strains is investigated in Section 4.3.

4.1 IN-PLANE DEFORMATIONS FOR A SINGLE FIBER BUNDLE

In this section, the carbon fiber tow is modeled as multiple fiber bundles which do not interact with each other due to the weak properties in the transverse directions. Only in-plane deformations are allowed for a single fiber bundle. The governing equations are derived for the case of small strains but large rotations. A novel numerical solution is implemented to solve the governing equations and determine the final shape of the deformed tow. The details of this section are published in reference [61].

4.1.1 Governing Equations

During the AFP process, the roller forces the tow to adhere to a substrate following a prescribed path. Hence, the problem here is formulated in a way that the boundary of the tow satisfies a specific displacement field imposed by the roller due to steering. The thin tow is considered as several fiber bundles laying on a stiff foundation. A single bundle is shown in Figure 4.1.

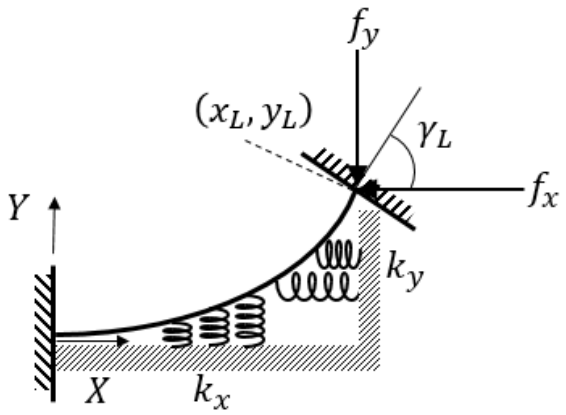

Figure 4.1: Schematic of a tow during AFP

The total energy Π of the system shown in Figure 4.1 can be expressed as:

$$\Pi = U - W + K\,, \tag{4.1}$$

where U is the elastic strain energy, K is the energy stored in the elastic foundation, and W is the work generated by the applied forces necessary to satisfy the boundary conditions. The strain energy U of a thin composite laminate structure can be expressed as:

$$U = \frac{1}{2}\iint \left[A_{11}{\epsilon_s^o}^2 + 2A_{12}\epsilon_s^o\epsilon_r^o + A_{22}{\epsilon_r^o}^2 + A_{66}{\gamma_{sr}^o}^2 + D_{11}{\kappa_s^o}^2 + 2D_{12}\kappa_s^o\kappa_r^o + D_{22}{\kappa_r^o}^2 + D_{66}{\kappa_{sr}^o}^2\right] ds dr, \tag{4.2}$$

where s and r represent the directions along and perpendicular to the path, respectively, ϵ^o and κ^o are the mid-plane strains and curvatures, and A_{ij} and D_{ij} are components of the extensional and bending stiffness matrices. In the first step of the in-plane tow deformations modeling the tow is restricted to deform in-plane only, hence out-of-plane terms in the elastic strain energy equation are dropped. In addition, the fiber bundle is assumed to be very stiff in the longitudinal direction, whereas the stiffness in the transverse and shear directions are mainly governed by the uncured resin. In a way, the tow is highly anisotropic, and the A_{12}, A_{22}, and A_{66} terms are orders of magnitude smaller in comparison to A_{11}. Therefore, ϵ_s^o will be the first term investigated for the case where the strains are small, but large rotations are applied. Hence, ϵ_s^o has the form of:

$$\epsilon_s^o = l^{'}(s) - r\,\kappa_r^o(s)\,, \tag{4.3}$$

where $l^{'}(s)$ is the change in length along the fiber direction, and $\kappa_r^o(s) = \gamma^{'}(s)$ is the in-plane curvature due to the fiber's rotation. From classical lamination theory, and using Kirchhoff-Love assumptions, the components of the stiffness matrix A_{ij} are obtained from:

$$A_{ij} = \sum_{k=1}^{n} \left\{Q_{ij}\right\}_n (z_k - z_{k-1}). \tag{4.4}$$

For the case of a single layer tow $n = 1, z_0 = -H/2$ and $z_1 = H/2$ with H being the thickness of the tow, the A_{11} term becomes:

$$A_{11} = Q_{11} H, \tag{4.5}$$

with:

$$Q_{11} = \frac{E_1^2}{E_1 - \nu_{12}^2 E_2} \cong E_1, \tag{4.6}$$

since the modulus in the transverse direction E_2 is order of magnitudes smaller than the modulus in the longitudinal direction E_1 for an uncured thermoset prepreg tow. Therefore, the strain energy can be expressed as:

$$U = \frac{1}{2}\int_0^L \int_{-\frac{w_b}{2}}^{\frac{w_b}{2}} A_{11}\, \epsilon_s^{o\,2}\, dr\, ds = \frac{1}{2}\int_0^L E_1 \left(A\, l'^2(s) + I_\gamma\, \gamma'^2(s) \right) ds\,, \tag{4.7}$$

with $A = H\, w_b$ being the cross-sectional area of the tow bundle, $I_\gamma = (H\, w_b^3)/12$ its moment of inertia, and $\kappa_r^o(s) = d\gamma/ds = \gamma'$.

The total work W generated by the applied forces $\boldsymbol{F} = \{f_x, f_y\}$ can be expressed as:

$$W = \boldsymbol{F} \cdot \boldsymbol{\Delta}\,, \tag{4.8}$$

with $\boldsymbol{\Delta} = \{(x_L - x_0) - L, (y_L - y_0) - 0\}$ being the total displacement vector. The relationship between differential lines in the x and y-directions (dx and dy), strain, arc-length, and rotation is shown in Figure 4.2, and can be expressed as:

$$dx = (ds + dl)\cos\gamma = \left(1 + \frac{dl}{ds}\right)\cos\gamma\ ds\,, \tag{4.9}$$

$$dy = (ds + dl)\sin\gamma = \left(1 + \frac{dl}{ds}\right)\sin\gamma\, ds\,. \tag{4.10}$$

Integrating both sides of equations (4.9) and (4.10) between 0 and a total length L, it can be shown that:

$$x_L - x_0 = \int_0^L \left(1 + l'\right)\cos\gamma\ ds\,, \tag{4.11}$$

$$y_L - y_0 = \int_0^L \left(1 + l'\right)\sin\gamma\ ds\,. \tag{4.12}$$

Replacing equations (4.11) and (4.12) into equation (4.8), the total amount of work required at equilibrium can be obtained as follows:

$$W = f_x \left[\int_0^L (1 + l') \cos\gamma \; ds - L \right] + f_y \int_0^L (1 + l') \sin\gamma \; ds \, . \tag{4.13}$$

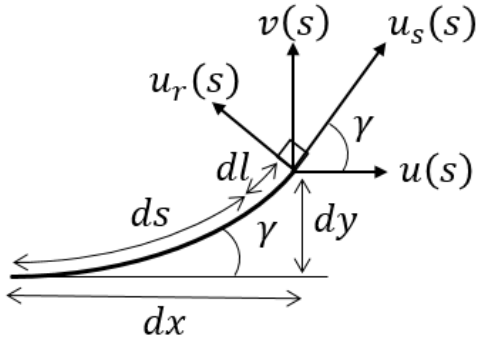

Figure 4.2 Strain-rotation relationship
and displacement components

Lastly, the energy term resulting from the elastic foundation can be expressed as:

$$K = \frac{1}{2} \int_0^L k_x \, u^2(s) \, ds + \frac{1}{2} \int_0^L k_y \, v^2(s) \, ds \, , \tag{4.14}$$

where, k_x and k_y are the modulus of the foundation in the x and y direction respectively and having the dimension of a force divided by the square of a length. Here, $u(s)$ and $v(s)$ refer to the displacement in the x and y directions respectively, and are expressed as:

$$u(s) = x(s) - x_{ref}(s), \tag{4.15}$$

$$v(s) = y(s) - y_{ref}(s), \tag{4.16}$$

$x_{ref}(s)$ and $y_{ref}(s)$ are the reference coordinates of the initial undeformed tow. Hence the total potential energy of the deformed tow is expressed as:

$$\Pi = \frac{1}{2}\int_0^L (E_1 A l'^2 + E_{11} I \gamma'^2)\, ds - f_x \left[\int_0^L (1 + l')\cos\gamma \; ds - L\right] - f_y \int_0^L (1 + l')\sin\gamma \; ds + \frac{k_x}{2}\int_0^L u^2(s)\, ds + \frac{k_y}{2}\int_0^L v^2(s)\, ds\,. \tag{4.17}$$

The total energy represented by equations (4.17) contains 4 unknown functions $\gamma(s),\ l(s),\ x(s)$, and $y(s)$, and 2 unknown constants f_x and f_y. Note that $x(s)$ and $y(s)$ can be expressed in terms of $\gamma(s)$ and $l(s)$ by integrating equations (4.9) and (4.10), hence, the functional Π can be expressed in terms of the first two functions only as:

$$\Pi\big(\gamma(s), l(s)\big) = \int_0^L \mathcal{F}\big(s, \gamma(s), \gamma'(s), l'(s)\big)\, ds \tag{4.18}$$

Using Euler-Lagrange principle to minimize the total energy Π, the following set of partial differential equations has to be satisfied:

$$\begin{cases} \dfrac{d}{ds}\left(\dfrac{\partial \mathcal{F}}{\partial \gamma'}\right) - \dfrac{\partial \mathcal{F}}{\partial \gamma} = 0 \\ \dfrac{d}{ds}\left(\dfrac{\partial \mathcal{F}}{\partial l'}\right) - \dfrac{\partial \mathcal{F}}{\partial l} = 0\,. \end{cases} \tag{4.19}$$

By evaluating the partial derivatives in equation (4.19), and including the two additional equations relating $x(s)$ and $y(s)$ to $\gamma(s)$ and $l(s)$, the following system of differential equations can be obtained:

$$\boldsymbol{System}\big(f_x, f_y, s\big) = \begin{cases} E_1 I\, \gamma'' - f_x\left(1 + l'\right)\sin\gamma + f_y\left(1 + l'\right)\cos\gamma + k_x u\, y - k_y v\, x = 0 \\ E_1 A\, l' = F + f_x \cos\gamma + f_y \sin\gamma - k_x u\, x - k_y v\, y \\ x' = \left(1 + l'\right)\cos\gamma \\ y' = \left(1 + l'\right)\sin\gamma \end{cases} . \tag{4.20}$$

4.1.2 Numerical Solution Approach

Equation (4.20) contains a 2nd order derivative of γ and 1st order derivatives for $l, x,$ and y in addition to the unknown forces f_x and f_y. Hence, seven boundary conditions are needed. The starting point of the path can provide four of them:

$$\text{At s} = 0\text{: } \gamma(0) = l(0) = x(0) = y(0) = 0\,, \tag{4.21}$$

and the remaining boundary conditions are obtained at the endpoint:

$$\text{At s} = \text{L: } x(L) = x_L, \qquad y(L) = y_L, \qquad \gamma(L) = \gamma_L. \tag{4.22}$$

Let us consider the unknown forces f_x and f_y. These forces are employed to satisfy the two boundary conditions x_L and y_L; the coordinates of the endpoint of the fiber bundle enforced by the roller at $\text{s} = \text{L}$. To accomplish that, an iterative approach is implemented as shown in Figure 4.3. First, initial values for the forces are assumed. A good starting point can be assumed as $f_{x_o} = f_{y_0} = 0$. Then, the system in (4.20) can be solved for these assumed values, and the functions $x(s)$ and $y(s)$ can be obtained. To ensure the boundary conditions are fulfilled, the following vector function providing two additional equations must be satisfied:

$$\boldsymbol{G}(f_x, f_y) = \begin{Bmatrix} x^*(f_x, f_y) - x_L \\ y^*(f_x, f_y) - y_L \end{Bmatrix} = \mathbf{0}\,, \tag{4.23}$$

where x^* and y^* are the values of $x(s)$ and $y(s)$ evaluated at $\text{s} = \text{L}$. Newton-Raphson method is applied to the system of equations in (4.23) iteratively to determine the forces f_x and f_y such that:

$$\begin{Bmatrix} f_{x_{n+1}} \\ f_{y_{n+1}} \end{Bmatrix} = \begin{Bmatrix} f_{x_n} \\ f_{y_n} \end{Bmatrix} - c\,J^{-1}\left(f_{x_n}, f_{y_n}\right)\,\boldsymbol{G}\left(f_{x_n}, f_{y_n}\right), \tag{4.24}$$

where $J\left(f_{x_n}, f_{y_n}\right)$ is the Jacobian matrix for the vector function $\boldsymbol{G}\left(f_{x_n}, f_{y_n}\right)$:

$$J = \left[\frac{\partial \boldsymbol{G}\left(f_{x_n}, f_{y_n}\right)}{\partial f_x} \quad \frac{\partial \boldsymbol{G}\left(f_{x_n}, f_{y_n}\right)}{\partial f_y}\right]. \tag{4.25}$$

Note that the vector function $\boldsymbol{G}(f_x, f_y)$ requires solving the system in (4.20) numerically then evaluating the numerical values of x^* and y^* at $s = L$. Therefore, the partial derivatives in the Jacobian matrix (4.25) cannot be evaluated analytically and a numerical method must be used. Here, a finite difference technique such as the central difference is used to approximate the numerical value of the Jacobian matrix:

$$J \cong \left[\frac{\boldsymbol{G}\left(f_{x_n} + \delta, f_{y_n}\right) - \boldsymbol{G}\left(f_{x_n} - \Delta, f_{y_n}\right)}{2\Delta} \quad \frac{\boldsymbol{G}\left(f_{x_n}, f_{y_n} + \Delta\right) - \boldsymbol{G}\left(f_{x_n}, f_{y_n} - \Delta\right)}{2\Delta}\right]. \tag{4.26}$$

Note that $x^*\left(f_x + \Delta, f_y\right)$ and $y^*\left(f_x + \Delta, f_y\right)$ require solving $\boldsymbol{System}(f_x + \Delta, f_y, s)$.

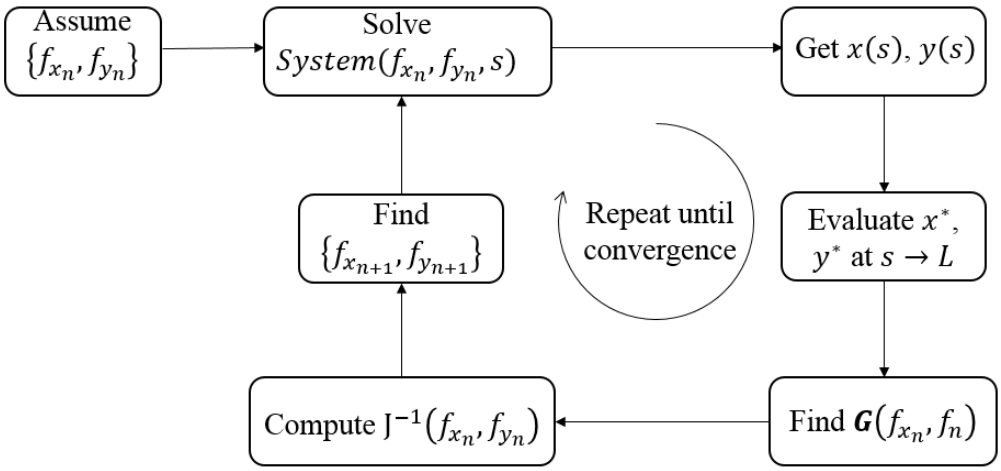

Figure 4.3 Iterative approach to obtain the unknown forces f_x and f_y

4.1.3 Results and Discussions for a Constant Curvature Path

In this section, the developed governing equations and numerical solution approach are implemented for the specific case of a tow placed on a flat surface and following a constant curvature path. The corresponding end-point boundary conditions are first

presented. Then, the results are shown for compressive and tensile regions within the tow and at different tow lengths. The effects of the foundation stiffness as well as the steering radius are also investigated.

4.1.3.1 Path Definition and Boundary Conditions

A steered tow-path at a constant curvature is considered for investigation. A possible arc-length parametrization for a constant curvature path (circular arc) is:

$$\boldsymbol{C}(s) = \{x(s), y(s)\} = \begin{cases} \rho \ \sin\dfrac{s}{\rho} \\ \rho\left(1 - \ \cos\dfrac{s}{\rho}\right) \end{cases}, \quad 0 \le s \le L, \tag{4.27}$$

where ρ is the constant radius of curvature. If we consider that $\boldsymbol{C}(s)$ is the centerline of the tow-path, then the parallel edges of the tow-path can be found by taking the parallel curves to $\boldsymbol{C}(s)$ which can be expressed as follows:

$$\boldsymbol{C_p}(s) = \left\{x_p(s), y_p(s)\right\} = \begin{cases} (d+\rho)\sin\dfrac{s}{\rho} \\ \rho - (d+\rho)\cos\dfrac{s}{\rho} \end{cases}, \tag{4.28}$$

where d can be either a positive or a negative distance. For the case where d is positive, the parallel edge obtained by equation (4.28) corresponds to a path $\boldsymbol{C_p}(s)$ longer than the reference path $\boldsymbol{C}(s)$, or in other words, the tensile side of the tow. Whereas a negative value of d corresponds to the compressive edge of the tow. The enforced boundary condition at the endpoint can be obtained using the following:

$$\begin{cases} x_L = x_p(L) \\ y_L = y_p(L) + d \\ \tan\gamma_L = \dfrac{y_p^{'}(L)}{x_p^{'}(L)} \end{cases}. \tag{4.29}$$

Note that for numerical convenience, the parallel paths are shifted along the y-axis by a distance d, so that the y-coordinate of the start point corresponds to zero.

4.1.3.2 Results for a compressive region

In a first step to analyze the problem in hand, a worst-case scenario is considered where there is no adhesion ($k_x = k_y = 0$). Other relevant parameters such as radius of curvature, tow thickness, width and modulus for an uncured thermoset pre-impregnated tow are shown in Table 4.1. The shape of the deformed fibers in the compressive side of the tow are shown in Figure 4.4 for different tow length ranging from 5 mm to 40 mm. For this case, half the tow width is assumed under compression, and four equal separate regions within the compressive side are analyzed. The deformed curve representing the centroid of each fiber bundle is shown in Figure 4.4 using a solid line, whereas the neutral axis and the compressive edge are shown using dashed lines. The first bundle is chosen to be the closest to the neutral axis, and the remaining bundles are aligned within a distance d corresponding to 1/8th of the tow width.

Table 4.1 Material property and geometry of the tow

$\boldsymbol{E_1}$[23]	$\boldsymbol{H}$ [16]	$\boldsymbol{w_t}$	$\boldsymbol{\rho}$	$\boldsymbol{k_x = k_y}$
130 GPa	0.184 mm	6.35 mm	0.4 m	0

At a small length, the fibers on the compressive side can absorb the differential length by the mean of compressive strains (Figure 4.4, (a) and (b)), hence the fibers remain parallel to the neutral axis as intended in the design. However, at a larger length, and in the absence of adhesion, the fibers tend to deform towards the neutral axis in the form of fiber waviness (Figure 4.4, (c) and (d)). This form of deformation results in fiber angle deviation

from the designed angles which can be quantified directly from the solution of the tangent angle γ obtained by solving the system of equations in (4.20).

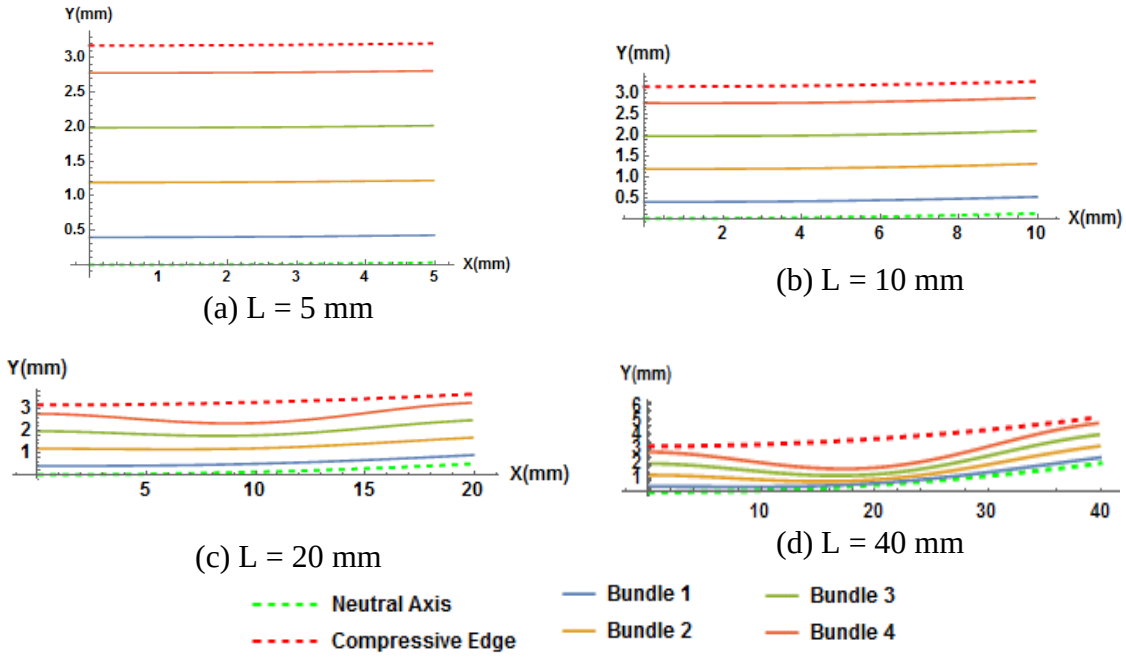

Figure 4.4. Deformed fiber bundles under compression at different tow length

The solution of the four unknown functions γ, $l', x,$ and y from that system are shown in Figure 4.5 for a tow length L = 20 mm. It can be noticed from Figure 4.4 (c) that the fiber bundle closest to the neutral axis remains parallel to the path. This is also reflected in the solution of the in-plane rotation γ in Figure 4.5 (a): the blue line corresponding to the first bundle's tangent angle is linear (since the path has a constant curvature, the tangent angle γ is a linear function of the arc-length *s*). The remaining fiber angles deviate from the original design by ±4° (deviation from the linear increase in the angle represented by the blue line in Figure 4.5 (a)). As for the strain along the length l' shown in Figure 4.5 (b), all four bundles experience compressive strains, where the bundle closest to the compressive edge experiences the most compressive strains. As for the x-coordinate shown in Figure 4.5 (c), it can be noticed that *x* is a linear function of *s*, and the difference between

the bundles across the tow width is negligible: this is due to the fact that the compressive strains and the rotation angle are relatively small ($1 + l' \cong 1$ and $\cos\gamma \cong 1$ thus from equation (4.20), $x' \cong 1$ hence $x(s) \cong s$). Lastly, the y-coordinate shown in Figure 4.5 (d) indicates that the fiber bundle closest to the compressive edge undergoes the most deformation in that direction.

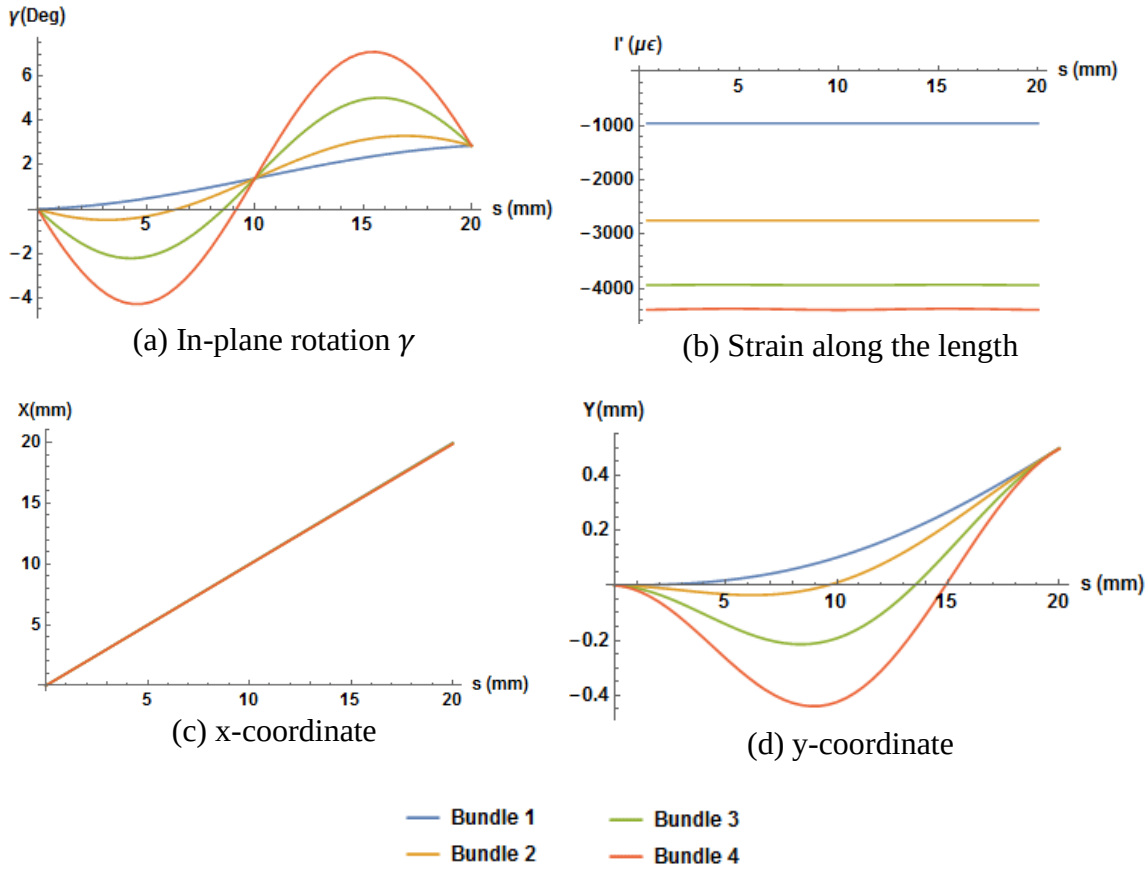

Figure 4.5. Solution of equation (4.20) for 4 bundles under compression at L = 20 mm

4.1.3.3 Results for a tensile region

In this section, the analysis of fiber bundles undergoing tension within the tow is shown. Similar to the previous section, a worst-case scenario is considered when there is no adhesion between the fiber bundles and the substrate. The same material properties and tow geometry are used which can be found in Table 4.1. Half of the tow width is assumed

to be under tension, and it is divided into four separate regions for analysis. The boundary conditions corresponding to the tensile case can be obtained from equations (4.28) and (4.29) using a positive distance d. The results corresponding to the deformed shape of the fiber bundles at four different tow-lengths (L = 10 mm, 20 mm, 40 mm, and 100 mm) are shown in Figure 4.6.

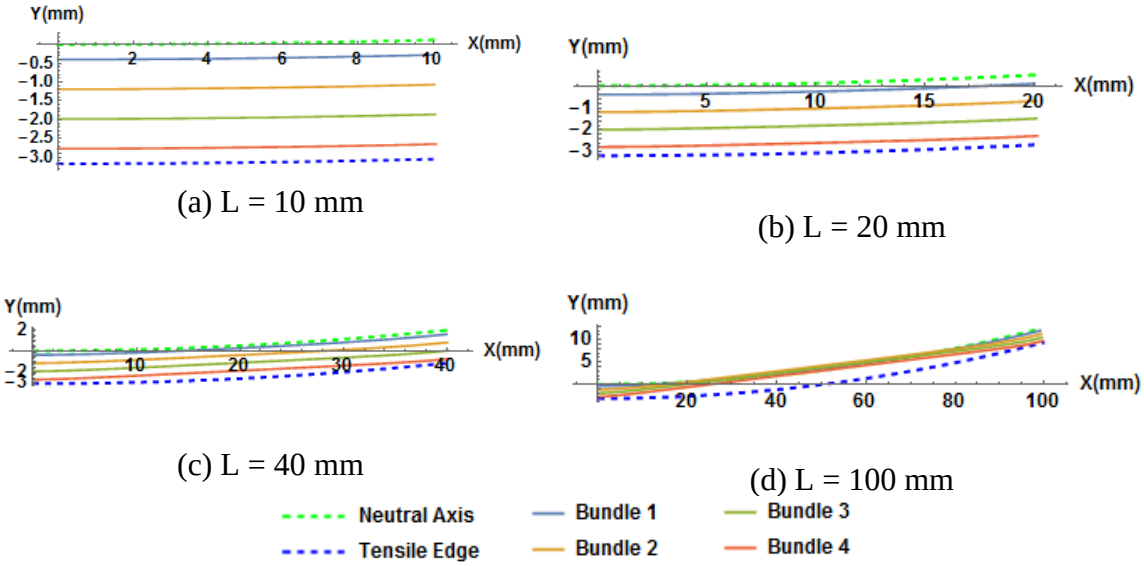

Figure 4.6. Deformed fiber bundles under tension at different tow length

Similar to the compressive case, at small length, tensile strains absorb the difference in length between the path and the fiber bundles (Figure 4.6 (a) and (b)). However, at a larger length, the fiber bundles tend to straighten or bunch towards the centerline as shown in Figure 4.6 (c) and (d). In order to observe the bunching phenomenon, a larger tow length is needed in the analysis compared to the ones considered in the compression section. This is needed since the bunching phenomenon occurs at a larger scale compared to the in-plane waviness. The solutions for the unknown functions of equation (4.20) are shown in Figure 4.7 for four bundles at L = 40 mm. The fiber straightening phenomenon can be interpreted from the solution of the tangent angle γ shown in Figure 4.7 (a): the fiber angle tends to be

constant (≅ 3°) at the mid-length of the tow. This behavior is more visible for the fiber bundle closest to the tensile edge. In addition to the fiber bunching, tensile strains are still a significant mode of deformation as shown in Figure 4.7 (b) where the fiber bundle closest to the tensile edge experiences the most strain. Similar to the previous section, the results for the x-coordinates show a linear relationship between the x-coordinate and the arc-length. Finally, the results for the y-coordinate in Figure 4.7 (d) show the bunching/ straightening deformation mode of the fiber bundles.

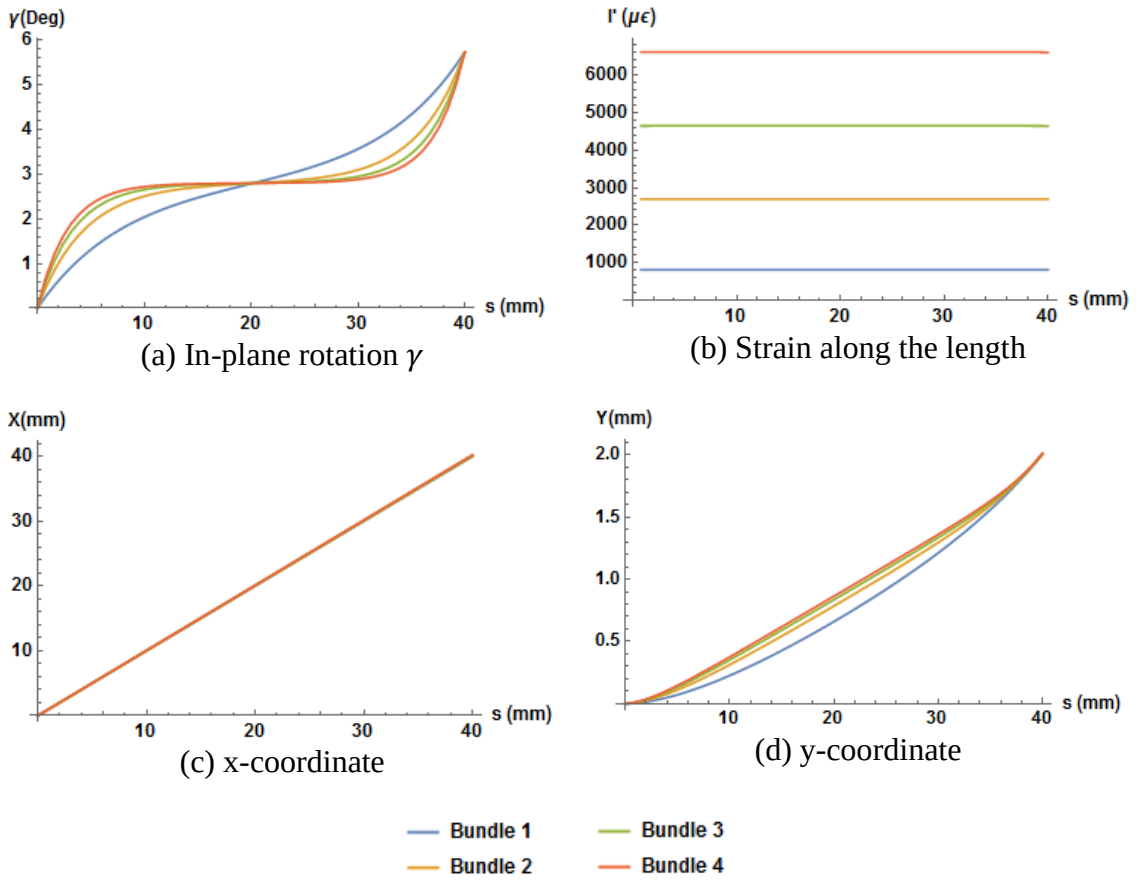

Figure 4.7. Solution of equation (4.20) for 4 bundles under tension at L = 40 mm

4.1.3.4 Effect of the foundation's stiffness

In this set of results the effect of the stiffness foundation on the deformed shape of the fibers is investigated. A reasonable assumption can be made where the foundation is

isotropic having similar values in the x and y-directions. Other material properties and tow geometry are shown in Table 4.2. In this case, the length of the tow section, as well as the steering radius are kept constant, whereas the value of the foundation stiffness is varied between 0 and 10^{10} N/m^2. The tow is assumed to be under pure bending: half of the tow is under tension and the other half is under compression. Five equal separate regions are considered for the analysis, where two of them represent the fiber bundles under tension, two for the compression, and one coincides with the neutral axis. An example of the deformed fiber bundles with $k = 10^6\ N/m^2$ is shown in Figure 4.8: bundle 1 and 2 are under tension, bundle 3 coincides with the neutral axis, and bundles 4 and 5 are under compression and undergo some fiber waviness.

Table 4.2 Material property and geometry of the tow

$\boldsymbol{E_1}$ [23]	$\boldsymbol{H}$ [16]	$\boldsymbol{w_t}$	$\boldsymbol{L}$	$\boldsymbol{\rho}$
130 GPa	0.184 mm	6.35 mm	30 mm	0.4 m

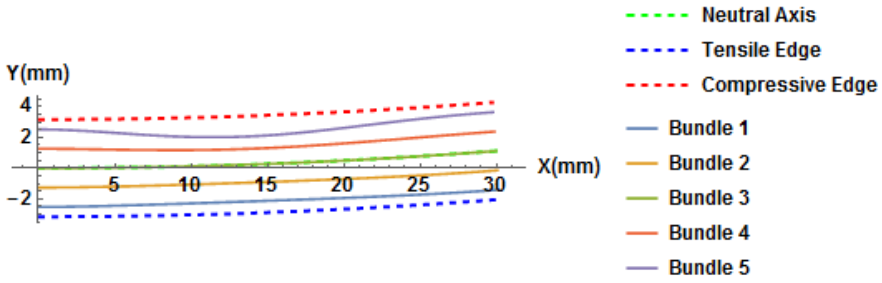

Figure 4.8: Deformed fiber bundles for $k = 10^6\ N/m^2$

To quantify the effect of the foundation's stiffness on the deformation of the fiber bundles, the displacement in the transverse direction to the fibers $u_r(s)$ is considered. $u_r(s)$ (Figure 4.2) can be computed from the displacements in the x- and y-directions $u(s)$ and $v(s)$ using:

$$u_r(s) = v(s)\cos\gamma(s) - u(s)\sin\gamma(s)\,. \tag{4.30}$$

A zero value for u_r means that the fiber bundle remains in the same location as placed by the AFP machine head. The maximum value of the u_r (in absolute value) for the five different fiber bundles is shown in Figure 4.9 for different values of the foundation's stiffness (logarithmic scale). Large values of k ($k > 10^7\ N/m^2$) result in almost zero displacement in the transverse direction: this means that the foundation is stiff enough to hold the fibers in their intended location. For small values of k ($k < 10^6\ N/m^2$), the displacement in the transverse direction is constant and does not change from the value of $k = 0$. This indicates that the foundation is very weak and unable to resist other deformation modes. Finally, there is an intermediate phase where k is between $10^6\ N/m^2$ and $10^7\ N/m^2$ during which the fiber bundles experience a slight increase in the displacement and then a sudden drop. In this phase, all energy terms are equally important in the governing equations resulting in a highly nonlinear system. The slight increase in the displacement is due to the fact that the waviness and bunching are not evenly distributed throughout the whole length anymore, but they are localized in one section of the tow. It is also worth to mention that fiber straightening on the tensile side of the tow is not as severe as the fiber waviness on the compressive side: the maximum displacement for bundles 1 and 2 is much smaller than the one for bundles 4 and 5. Note that the fiber bundle coinciding with the neutral axis does not experience any displacement in the transverse direction and remains in its intended location.

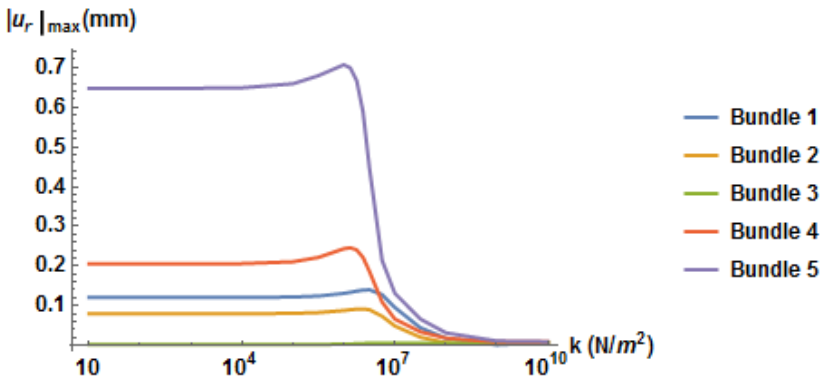

Figure 4.9: Effect of the foundation stiffness on the displacement in the transverse direction

4.1.3.5 Effect of the steering radius

In this section the effect of the steering radius is investigated. The same tow properties provided in **Error! Reference source not found.** are considered in this section w hile varying the steering radius. The tow is assumed to be under pure bending, and it is divided into five sections: two under tension (bundle 1 and 2), two under compression (bundle 4 and 5), and one coinciding with the neutral axis (bundle 3). Similar to the previous section, the maximum (absolute value) of the displacement in the transverse direction is monitored as a function of the steering radius for two values of the foundation's stiffness: $k = 0$ and $10^7\ N/m^2$. The results are shown in Figure 4.10 and Figure 4.11 respectively. It can be observed that increasing the steering radius decreases the displacement of the fiber bundles in the transverse. This is predictable since a smaller steering radius of curvature means a larger difference in length between the fiber and the path. For the first case (worst case scenario) where the stiffness of the foundation is zero, a minimum steering radius of 1.5 m is required for a significantly small u_r. However, for the case where $k = 10^7\ N/m^2$, only small radii of curvature $\rho < 0.5$ m lead to a significant displacement of the fiber bundles in the transverse direction.

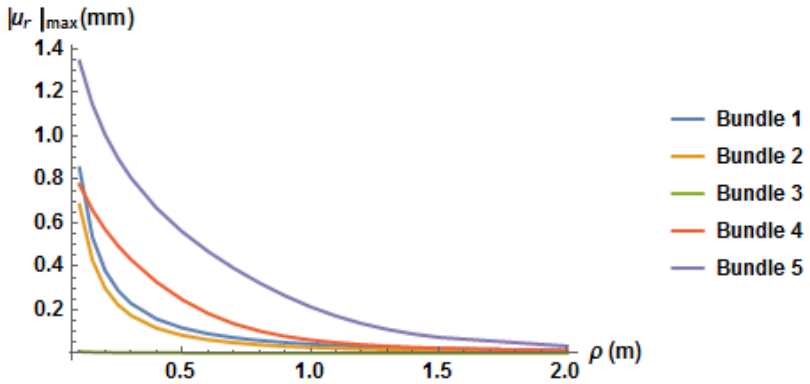

Figure 4.10: Effect of the steering radius on the displacement in the transverse direction for $k = 0$

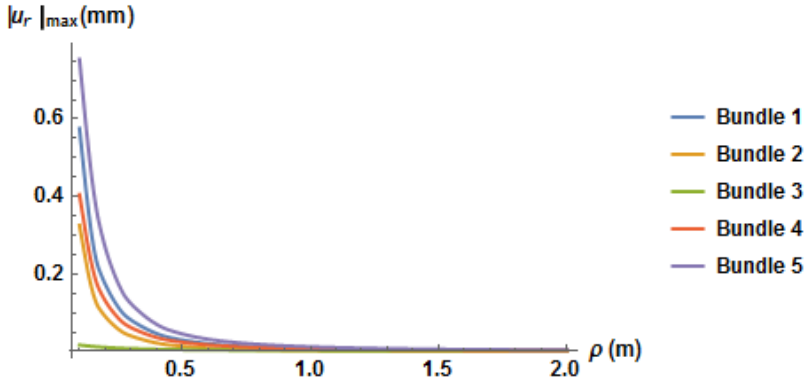

Figure 4.11: Effect of the steering radius on the displacement in the transverse direction for $k = 10^7\ N/m^2$

4.2 OUT-OF-PLANE DEFORMATIONS FOR A SINGLE FIBER BUNDLE

This section investigates the out-of-plane deformation mechanisms for a single bundle laying on a stiff foundation.

4.2.1 Governing equations

Since the previous derivations restrict the fiber to a planar deformation behavior, this section elaborates on including an out-of-plane term to allow the fiber to deform in space if a solution can exist at lower energy in the 3rd dimension. The relationship between the out-of-plane rotation angle β, the in-plane rotation γ and the corresponding arc-length and strain is visualized in Figure 4.12. For this case, the required amount of work at equilibrium is:

$$dW = f_x dx + f_y dy + f_z dz, \tag{4.31}$$

or, in terms of the strains and rotations:

$$\begin{aligned} dW = f_x \left(1 + \frac{dl}{ds}\right) \cos\gamma \cos\beta \, ds + f_y \left(1 + \frac{dl}{ds}\right) \sin\gamma \cos\beta \, ds \\ + f_z \left(1 + \frac{dl}{ds}\right) \sin\beta \, ds \, . \end{aligned} \tag{4.32}$$

Hence, the total work is obtained by integrating over the length:

$$\begin{aligned} W = f_x \int_0^L (1 + l') \cos\gamma \cos\beta \; ds + f_y \int_0^L (1 + l') \sin\gamma \cos\beta \; ds \\ + f_z \int_0^L (1 + l') \sin\beta \, ds \, . \end{aligned} \tag{4.33}$$

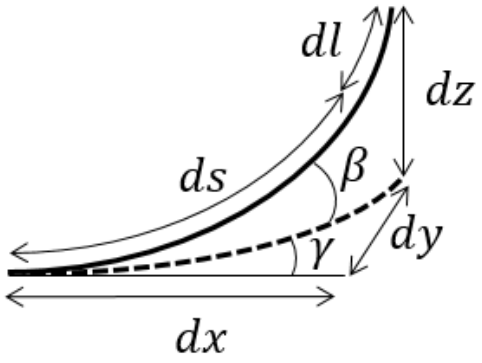

Figure 4.12: Strain-rotation relationship in 3D

The strain energy equation including the out-of-plane rotation can be expressed by:

$$U = \frac{1}{2} \int_0^L \int_{-\frac{w_b}{2}}^{\frac{w_b}{2}} \left[A_{11} \left(l'(s) - r \, \kappa_r^o(s) \right)^2 + D_{11} {\kappa_s^o}^2(s) \right] dr \, ds \tag{4.34}$$

Here, $\kappa_r^o(s) = d\gamma/ds = \gamma'$ and $\kappa_s^o(s) = d\beta/ds = \beta'$ correspond to the in-plane and out-of-plane curvatures respectively, and the D_{11} can be obtained from the classical laminate theory:

$$D_{ij} = \frac{1}{3} \sum_{k=0}^{n} \left\{ Q_{ij} \right\}_k \left(z_k^3 - z_{k-1}^3 \right) \tag{4.35}$$

For a single layer tow $n = 1$, $z_0 = -H/2$ and $z_1 = H/2$, and neglecting the transverse stiffness, the D_{11} term becomes:

$$D_{11} = \frac{1}{12} E_1 H^3. \tag{4.36}$$

After integration over the transverse direction r, the expression of the strain energy becomes:

$$U = \frac{1}{2} \int_0^L E_1 \left(w_b \, H \, l' + I_\gamma \gamma'^2 + I_\beta \, \beta'^2 \right) ds \tag{4.37}$$

Let's denote by I_γ and I_β the moments of inertia corresponding to the in-plane bending and out-of-plane bending respectively. For the case of a rectangular cross section tow and assuming that its shape does not change along the length, I_γ and I_β can be expressed as:

$$I_\gamma = \frac{1}{12} H \, w_b^3, \qquad I_\beta = \frac{1}{12} w_b \, H^3 \tag{4.38}$$

Lastly, the energy term resulting from the elastic foundation can be expressed as:

$$K = \frac{1}{2} \int_0^L k_x \, u^2(s) \, ds + \frac{1}{2} \int_0^L k_y \, v^2(s) \, ds \; + \frac{1}{2} \int_0^L k_z \, w^2(s) \, ds \, , \tag{4.39}$$

where, k_z is the stiffness of the foundation in the z-direction, and $w(s)$ is the displacement in that direction expressed as:

$$w(s) = z(s) - z_{ref}(s) = \int_0^s \left(1 + l'(s^*) \right) \sin \beta(s^*) \, ds^* - z_{ref}(s) \, . \tag{4.40}$$

The Euler-Lagrange system that satisfies the minimum of the functional $\Pi(\gamma, \beta, l) = \int_0^L \mathcal{F}(s, \gamma, \gamma', \beta, \beta', l') \, ds$ is:

$$\begin{cases} \dfrac{d}{ds}\left(\dfrac{\partial \mathcal{F}}{\partial \gamma'}\right) - \dfrac{\partial \mathcal{F}}{\partial \gamma} = 0 \\ \dfrac{d}{ds}\left(\dfrac{\partial \mathcal{F}}{\partial \beta'}\right) - \dfrac{\partial \mathcal{F}}{\partial \beta} = 0 \\ \dfrac{d}{ds}\left(\dfrac{\partial \mathcal{F}}{\partial l'}\right) - \dfrac{\partial \mathcal{F}}{\partial l} = 0 \end{cases} \tag{4.41}$$

The necessary partial derivatives of the displacement terms with respect to $\gamma(s), \beta(s)$ and $l'(s)$ are as follows:

$$\frac{\partial u}{\partial \gamma} = -\int_0^s \left(1 + l'(s^*)\right) \sin\gamma(s^*) \cos\beta(s^*)\, ds^* = -y(s) \tag{4.42}$$

$$\frac{\partial v}{\partial \gamma} = \int_0^s \left(1 + l'(s^*)\right) \cos\gamma(s^*) \cos\beta(s^*)\, ds^* = x(s) \tag{4.43}$$

$$\frac{\partial w}{\partial \gamma} = 0 \tag{4.44}$$

$$\frac{\partial u}{\partial \beta} = -\int_0^s \left(1 + l'(s^*)\right) \cos\gamma(s^*) \sin\beta(s^*)\, ds^* = -\xi(s) \tag{4.45}$$

$$\frac{\partial v}{\partial \beta} = -\int_0^s \left(1 + l'(s^*)\right) \sin\gamma(s^*) \sin\beta(s^*)\, ds^* = -\psi(s) \tag{4.46}$$

$$\frac{\partial w}{\partial \beta} = \int_0^s \left(1 + l'(s^*)\right) \cos\beta(s^*)\, ds^* = \zeta(s) \tag{4.47}$$

$$\frac{\partial u}{\partial l'} = \int_0^s \cos\gamma(s^*) \cos\beta(s^*)\, ds^* \cong x(s) \tag{4.48}$$

$$\frac{\partial v}{\partial l'} = \int_0^s \sin\gamma(s^*) \cos\beta(s^*)\, ds^* \cong y(s) \tag{4.49}$$

$$\frac{\partial w}{\partial l'} = \int_0^s \sin\beta(s^*)\, ds^* \cong z(s) \tag{4.50}$$

Using the results of equations (4.28)-(4.40), (4.42)-(4.50) and inserting them into (4.41), the new system to be solved is as follows:

$$
\begin{gathered}
E_1 I_\gamma \, \gamma'' - f_x \sin\gamma \cos\beta + f_y \cos\gamma \cos\beta + k_x u y - k_y v x = 0 \\
E_1 I_\beta \beta'' - f_x \cos\gamma \sin\beta - f_y \sin\gamma \sin\beta + f_z \cos\beta + k_x u \xi + k_y v \psi - k_z w \zeta = 0 \\
l' = \frac{1}{E_1 A}\left(F + f_x \cos\gamma \cos\beta + f_y \sin\gamma \cos\beta + f_z \sin\beta - k_x u x - k_y v y - k_z w z\right) \\
x' = (1 + l')\cos\gamma \cos\beta \\
y' = (1 + l')\sin\gamma \cos\beta \\
z' = (1 + l')\sin\beta \\
\xi' = (1 + l')\cos\gamma \sin\beta \\
\psi' = (1 + l')\sin\gamma \sin\beta \\
\zeta' = (1 + l')\cos\beta
\end{gathered}
\tag{4.51}
$$

Note that it is necessary to introduce the intermediate equations in terms of ξ', ψ', and ζ' to avoid having their integral form (equations (4.47),(4.48),(4.49)) in the second equation of (4.51) in term of β.The numerical solution approach used to solve the above system is similar to the one presented previously in section 4.1.2 with the addition of the variables in the 3rd dimension. For completeness, the numerical solution approach for the out-of-place case is presented below.

4.2.2 Numerical Solution Approach

The system of equations shown in (4.51) is a system of nonlinear differential equations, containing 2nd order derivatives for γ and β, and 1st order derivatives for $l, x, y, z, \xi, \psi,$ and ζ. Hence, eleven boundary conditions are needed for these functions. The starting point of the path can provide nine of them:

$$
\begin{gathered}
\text{At s} = 0\text{: } \gamma(0) = \gamma_0, \beta(0) = 0, l(0) = l_0, x(0) = x_0, y(0) = y_0, z(0) = 0\,, \\
\xi(0) = \psi(0) = \zeta(0) = 0.
\end{gathered}
\tag{4.52}
$$

Note that the intermediate variables are chosen to be zero at the start point for numerical convenience. The remaining two boundary conditions are obtained at the endpoint:

$$\text{At s} = \text{L: } \gamma(L) = \gamma_L, \beta(L) = 0. \tag{4.53}$$

In addition to the unknown functions, the system of equations shown in (4.51) contains three unknown forces f_x, f_y and f_z. These forces have to satisfy three remaining boundary conditions x_L, y_L and z_L; the coordinates of the endpoint of the fiber bundle enforced by the roller at $\text{s} = \text{L}$. To accomplish that, an iterative approach is implemented as shown in Figure 4.13. Here, $System(f_x, f_y, f_z, s)$ refer to the system of equations (4.51) where the forces are unknown. First, an initial value for the forces is assumed. A good starting point can be assumed as $f_{x_0} = f_{y_0} = f_{z_0} = 0$. Then, the system in (4.51) can be solved for these assumed values, and the functions $x(s), y(s)$ and $z(s)$ can be obtained. To ensure the boundary conditions are fulfilled, the following vector function providing three additional equations must be satisfied

$$\boldsymbol{G}(f_x, f_y, f_z) = \begin{Bmatrix} x^*(f_x, f_y, f_z) - x_L \\ y^*(f_x, f_y, f_z) - y_L \\ z^*(f_x, f_y, f_z) - z_L \end{Bmatrix} = \mathbf{0}\,, \tag{4.54}$$

where $x^*, y*$ and z^* are the values of $x(s), y(s)$ and $z(s)$ evaluated at $\text{s} = \text{L}$. The Newton-Raphson method is applied to the system of equations in (4.58) iteratively to determine the forces f_x, f_y and f_z such that:

$$\begin{Bmatrix} f_{x_{n+1}} \\ f_{y_{n+1}} \\ f_{z_{n+1}} \end{Bmatrix} = \begin{Bmatrix} f_{x_n} \\ f_{y_n} \\ f_{z_n} \end{Bmatrix} - c\, J^{-1}\left(f_{x_n}, f_{y_n}, f_{z_n}\right)\, \boldsymbol{G}\left(f_{x_n}, f_{y_n}, f_{z_n}\right), \tag{4.55}$$

where $J\left(f_{x_n}, f_{y_n}, f_{z_n}\right)$ is the Jacobian matrix for the vector function $\boldsymbol{G}\left(f_{x_n}, f_{y_n}, f_{z_n}\right)$:

$$J = \left[\frac{\partial \boldsymbol{G}\left(f_{x_n}, f_{y_n}, f_{z_n}\right)}{\partial f_x} \quad \frac{\partial \boldsymbol{G}\left(f_{x_n}, f_{y_n}, f_{z_n}\right)}{\partial f_y} \quad \frac{\partial \boldsymbol{G}\left(f_{x_n}, f_{y_n}, f_{z_n}\right)}{\partial f_y} \right]. \tag{4.56}$$

Note that the vector function $\boldsymbol{G}(f_x, f_y, f_z)$ requires solving the system in (4.51) numerically then evaluating the numerical values of x^*, y^* and z^* at $s = L$. Therefore, the partial derivatives in the Jacobian matrix in (4.56) cannot be evaluated analytically and a numerical method must be used, such as a finite difference technique.

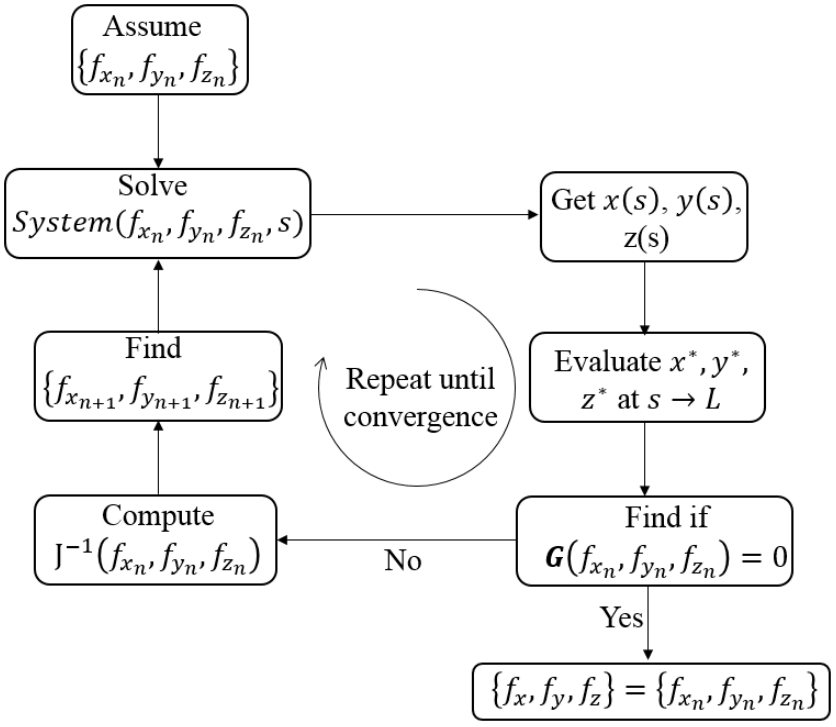

Figure 4.13 Iterative approach to obtain the unknown forces

4.2.3 Results and Discussions

The following sections describe several solutions from the above system and investigate several aspects of the assumed solution parameters. In particular, the results are investigated for a combined tensile/compressive region with no adhesion, the effect of tow length and the foundation stiffness are also presented.

4.2.3.1 Results for a combined tensile/compressive region

In a first step to analyze the out-of-plane, a worst-case scenario is considered where there is no adhesion ($k_x = k_y = k_z = 0$). Other relevant parameters such as radius of curvature, tow thickness, width and modulus for an uncured thermoset pre-impregnated tow are shown in Table 4.3. The shape of the deformed fibers in the compressive side of the tow as well as the tensile side are shown in Figure 4.14 for a length of 4 cm. For this case, half the tow width is assumed under compression, and the other half under tension. Five bundles are chosen here for analysis where two of them are laying in the region under compression, two in the region under tension, and one coinciding with the neutral axis. The deformed curve representing the centroid of each fiber bundle is shown in Figure 4.14 using a dotted line, whereas the tensile and compressive edges are shown using solid lines.

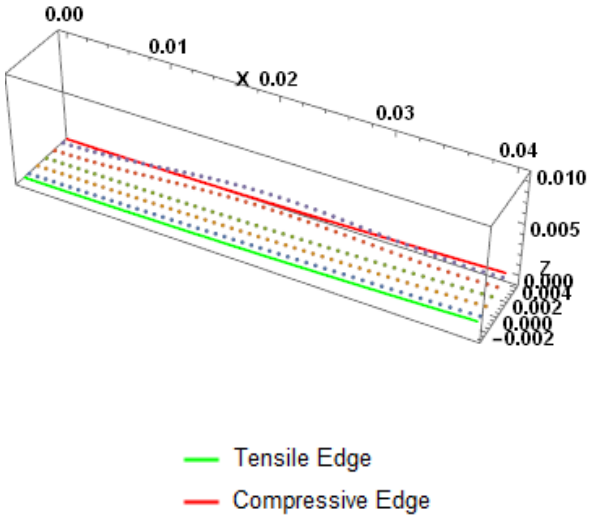

Figure 4.14: Deformed fiber bundles in 3D under combined loading

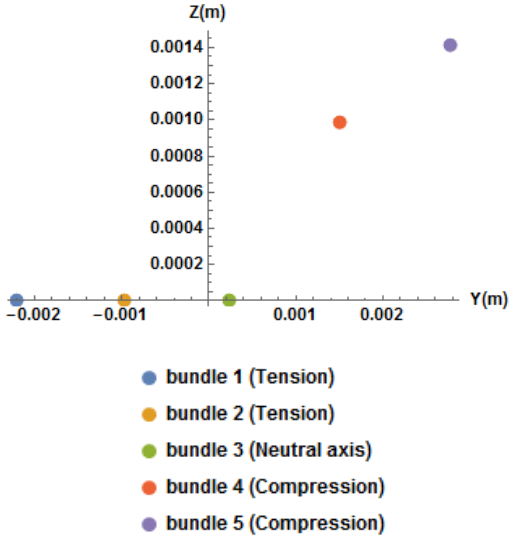

Figure 4.15: Maximum z-displacement of the fiber bundles at L/2

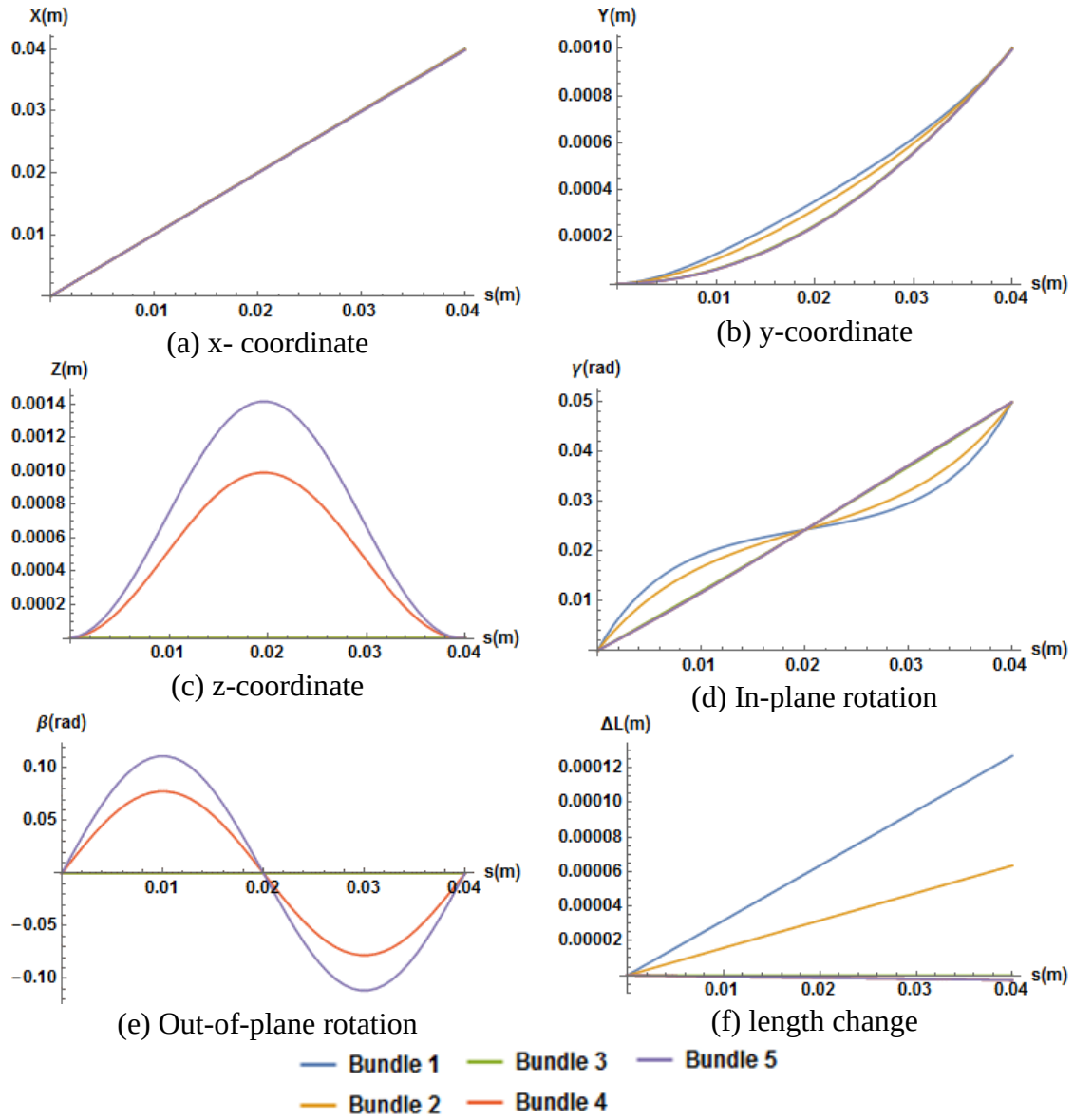

(a) x- coordinate

(b) y-coordinate

(c) z-coordinate

(d) In-plane rotation

(e) Out-of-plane rotation

(f) length change

Figure 4.16: Solution of equation (4.51) for 5 bundles under combined loading

Table 4.3 Material property and geometry of the tow deforming out-of-plane

E_1 [23]	H [16]	w_t	ρ	$k_x = k_y = k_z$	L
130 GPa	0.184 mm	6.35 mm	0.8 m	0	40 mm

A first look at the deformed shape of the tow in Figure 4.14 shows that the fiber bundles on the compressive edge of the tow have deformed in the out-pf-plane direction to form a wrinkle. The remaining fiber bundles laying on the neutral axis and in the tensile

region have deformed in-plane. A detailed view of tow cross-section taken at half-length showing the maximum displacement in the z-direction is shown in Figure 4.15. This confirms that only the bundles under compression are deforming in the out-of-plane direction. Details of the results of the governing equation (4.51) for the five bundles are shown in Figure 4.16. Bundles 4 and 5 in the compressive region deform out-of-plane as shown in the z-coordinate plot and the out-of-plane rotation angle β. Bundle 3 coinciding with the neutral axis remains in-plane and parallel to the path, whereas the bundles under tension deformed in-plane in the fiber bunching/straightening mode. This is reflected in the plot of the y-coordinate as well as in the in-plane rotation angle γ. Lastly, the axial strain represented in the length change plot shows that the fiber bundles on the tensile side have extended significantly to absorb the length difference, however, the axial strain for the bundles under compression is significantly smaller, indicating that most of the length difference is compensated for by the out-of-plane deformation.

4.2.3.2 Effect of the length

In this section, the effect of the length of the fiber bundles is investigated for five bundles placed under compression. The material properties and tow geometry are the same as the one used in the above section (see Table 4.3). Three different bundle lengths (1, 2, and 4 cm) are investigated, and the results showing the deformed shape of the tow bundles are presented in Figure 4.17. At a small length of 1 cm, the fiber bundles remain in-plane, and the differential length is absorbed by means of compressive strains. However, as the length increases, the fiber bundles closest to the compressive edge starts to deform in the z-direction as shown for the case of L = 2 cm, except the fiber bundle closest to the neutral axis which remains in-plane. This is due to the fact that the differential length close to the

neutral is small and increases as the fiber are placed further away from the neutral axis. At a significantly larger length, all fiber bundles under compression buckle in the out-of-plane direction to form a wrinkle.

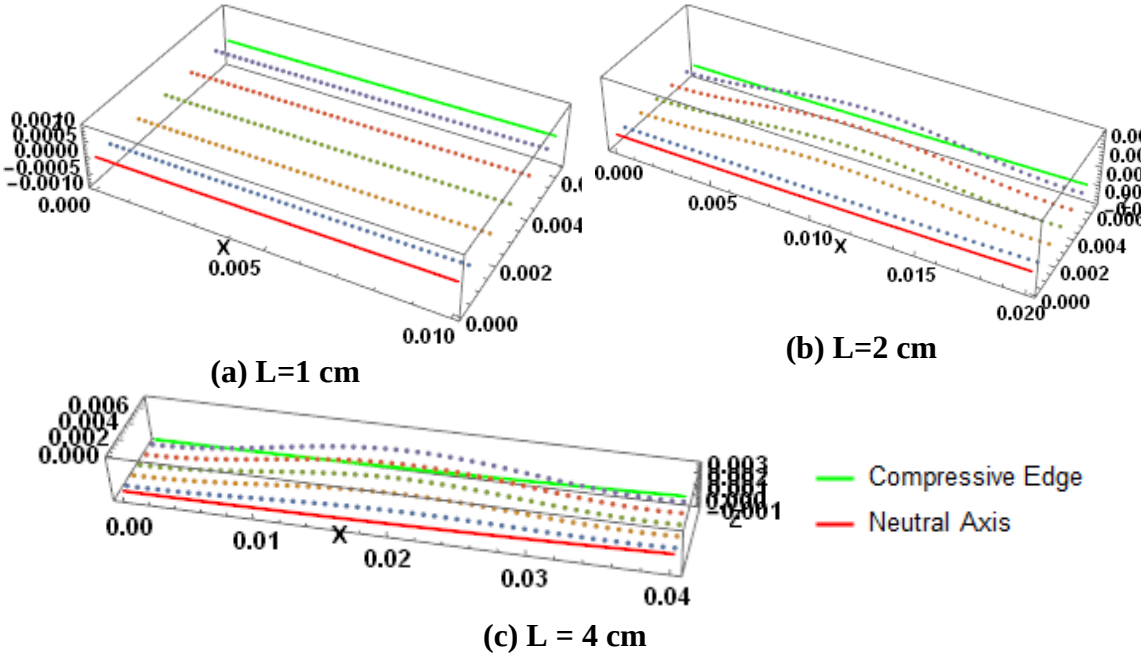

Figure 4.17: Effect of the length on the out-of-plane deformation of bundles under compression

4.2.3.3 Effect of the foundation's stiffness

In this set of results the effect of the stiffness foundation on the deformed shape of the fiber bundles is investigated. A reasonable assumption can be made where the foundation is isotropic having similar values in the x , y and z-directions. Other material properties and tow geometry are shown in Table 4.4. In this case, the length of the tow section, as well as the steering radius are kept constant, whereas the value of the foundation stiffness is varied between 0 and 10^8 N/m^2. The tow is assumed to be under compression, where five equal separate regions are considered for the analysis.

To quantify the effect of the foundation's stiffness on the deformation of the fiber bundles, we focus on the displacement in the z- direction. This corresponds to the z-

coordinate, since it is assumed that the fiber bundles are placed on a flat surface. The results for the five fiber bundles are shown in Figure 4.18 for different values of the foundation's stiffness (logarithmic scale). Large values of k ($k > 10^6\ N/m^2$) result in zero displacement in the z- direction: this means that the foundation is stiff enough to hold the fibers in their intended location, and the layup is wrinkle free. For small values of k ($k < 10^5\ N/m^2$), the displacement in the z- direction is constant and does not change from the value of $k = 0$. This indicates that the foundation is very weak and unable to resist the out-of-plane deformation.

Table 4.4 Material property and geometry of the tow

E_{11} [23]	H [16]	w_t	L	ρ
130 GPa	0.184 mm	6.35 mm	2 cm	0.8 m

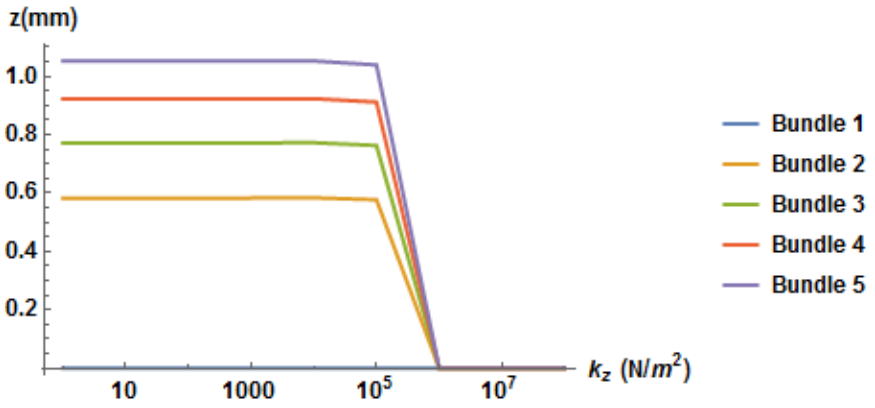

Figure 4.18: Effect of the foundation stiffness in the z-direction on the wrinkle formation

4.3 INTERACTION OF FIBER BUNDLES IN THE TRANSVERSE DIRECTION

4.3.1 Governing Equations for the in-plane case

The previous derivations showed the physics of a single fiber bundle within a tow laying on a stiff foundation. In this section, the interaction of several adjacent bundles is

investigated by considering the strain energies in the transverse direction and shear as shown in Figure 4.19 and Figure 4.20. This behavior is dominated by the properties of the matrix system used during fiber placement. In essence, the displacements of the adjacent bundles in the longitudinal and transverse directions are restricted due to shear and transverse stiffnesses between the adjacent bundles. Here, we define the transverse strain as the difference between the transverse displacements of the bundles divided by the original distance (which is the bundle width). We similarly define the shear strain as the difference between the rotations of the cross sections of the fiber bundles. In a perfect case where all fiber bundles bend in-plane and the strains are absorbed through the fiber bundles extension, the transverse and shear strains between the bundles are negligible. However, for the case where large in-plane deformations start to occur such as waviness and bunching, transverse and shear strains at the interface between the bundles will resist these deformations as shown in the figures below.

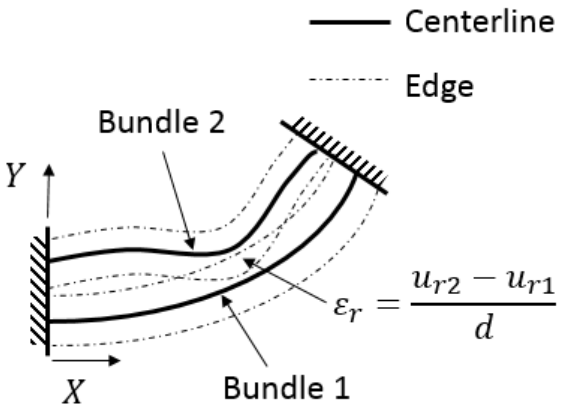

Figure 4.19. Transverse strain between neighboring fiber bundles

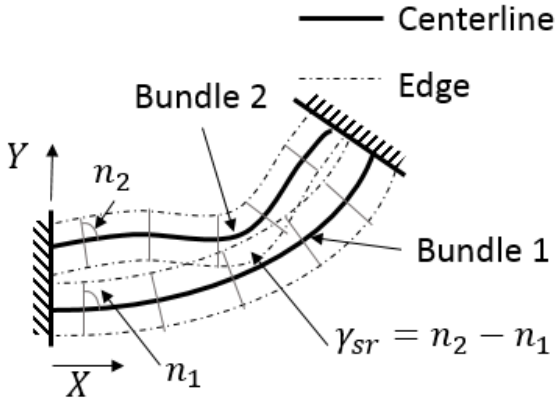

Figure 4.20 Shear strain between neighboring fiber bundles

For the case of two fiber bundles, the additional strain energy terms due to the interaction of the fibers in the transverse direction and shear can be expressed as:

$$U_r = \frac{1}{2}\int_0^L \int_{-w_b/2}^{w_b/2} A_{22}\, \varepsilon_r^2\, dr\, ds\,, \tag{4.57}$$

$$U_s = \frac{1}{2}\int_0^L \int_{-w_b/2}^{w_b/2} A_{66}\, \gamma_{sr}^2\, dr\, ds, \tag{4.58}$$

with:

$$\varepsilon_r = \frac{u_{r_2} - u_{r_1}}{d}\,, \tag{4.59}$$

$$\gamma_{sr} = n_2 - n_1 = \gamma_2 + \frac{\pi}{2} - \left(\gamma_1 + \frac{\pi}{2}\right) = \gamma_2 - \gamma_1. \tag{4.60}$$

Here, u_r corresponds to the displacement of the fiber bundle in the transverse direction, and it can be expressed in terms of the displacements in the x- and y-directions as:

$$u_r(s) = v(s)\cos\gamma(s) - u(s)\sin\gamma(s)\,, \tag{4.61}$$

From classical laminate theory, the A_{22} and A_{66}terms for a single layer can obtained using equation (4.4) such that:

$$A_{22} = Q_{22}H = \frac{E_1\, E_2}{E_1 - \nu_{12}^2\, E_2}\, H \cong E_2 H, \tag{4.62}$$

$$A_{66} = Q_{66}H = G_{12}H \tag{4.63}$$

The total energy of the combined system Π_t can be obtained by adding the terms of the transverse and shear strain energy to the total energy of each fiber bundle:

$$\Pi_t = \Pi_1 + \Pi_2 + U_r + U_s. \tag{4.64}$$

Generalizing the above equations for n fiber bundles, the total energy can be expressed as:

$$\begin{aligned}\Pi_t = \sum_{i=1}^{n} \Pi_i + \frac{1}{2}E_{22}Hw_b \sum_{i=1}^{n-1}\int_0^L \left(\frac{u_{r_{i+1}} - u_{r_i}}{d_i}\right)^2 ds \\ + \frac{1}{2}G_{12}Hw_b \sum_{i=1}^{n-1}\int_0^L (\gamma_{i+1} - \gamma_i)^2 ds.\end{aligned} \tag{4.65}$$

The total energy is therefore a function of single independent variable s, and other functions $\gamma_i, \gamma_i^{'}$ and $l_i^{'}$:

$$\Pi_t = \int_0^L \mathcal{F}\left(s, \gamma_1, \gamma_2, \dots, \gamma_n, \gamma_1', \gamma_2', \dots, \gamma_n', l_1', l_2', \dots, l_n'\right) ds. \tag{4.66}$$

Therefore, the corresponding Euler-Lagrange equations that minimize the total energy are:

$$\begin{cases} \dfrac{d}{ds}\left(\dfrac{\partial \mathcal{F}}{\partial \gamma_i'}\right) - \dfrac{\partial \mathcal{F}}{\partial \gamma_i} = 0 \\ \dfrac{d}{ds}\left(\dfrac{\partial \mathcal{F}}{\partial l_i'}\right) - \dfrac{\partial \mathcal{F}}{\partial l_i} = 0 \end{cases}. \tag{4.67}$$

Expanding the above equation for n fiber bundles and assuming that the distance d_i is the same between the fiber bundles and equal to the width of an individual bundle w_i, the following set of $2n$ equations has to be satisfied to minimize the total energy:

$$\begin{aligned}
&E_1 I_\gamma \gamma_1'' - \frac{\partial \Pi_1}{\partial \gamma_1} + \frac{E_2 H}{w_{b1}} \frac{\partial u_{r_1}}{\partial \gamma_1}\left(u_{r_2} - u_{r_1}\right) + G_{12} A\left(\gamma_2 - \gamma_1\right) = 0 \\
&E_1 A\, l_1' - F_1 + \frac{\partial \Pi_1}{\partial l_1'} - \frac{E_2 H}{w_{b1}} \frac{\partial u_{r_1}}{\partial l_1'}\left(u_{r_2} - u_{r_1}\right) - G_{12} A\left(\gamma_2 - \gamma_1\right) = 0 \\
&\qquad\qquad \vdots \\
&\qquad\qquad \vdots \\
&E_1 I_\gamma \gamma_i'' - \frac{\partial \Pi_i}{\partial \gamma_i} + \frac{E_2 H}{w_{bi}} \frac{\partial u_{r_i}}{\partial \gamma_i}\left(u_{r_{i-1}} - 2u_{r_i} + u_{r_{i+1}}\right) + G_{12} A\left(\gamma_{i-1} - 2\gamma_i + \gamma_{i+1}\right) = 0 \\
&E_1 A\, l_i' - F_i + \frac{\partial \Pi_i}{\partial l_i'} - \frac{E_2 H}{w_{bi}} \frac{\partial u_{r_i}}{\partial l_i'}\left(u_{r_{i-1}} - 2u_{r_i} + u_{r_{i+1}}\right) - G_{12} A\left(\gamma_{i-1} - 2\gamma_i + \gamma_{i+1}\right) = 0 \\
&\qquad\qquad \vdots \\
&\qquad\qquad \vdots \\
&E_1 I_\gamma \gamma_n'' - \frac{\partial \Pi_n}{\partial \gamma_n} + \frac{E_2 H}{w_{bn}} \frac{\partial u_{r_n}}{\partial \gamma_n}\left(u_{r_{n-1}} - u_{r_n}\right) + G_{12} A\left(\gamma_{n-1} - \gamma_n\right) = 0 \\
&E_1 A\, l_n' - F_n + \frac{\partial \Pi_n}{\partial l_n'} - \frac{E_2 H}{w_{bn}} \frac{\partial u_{r_n}}{\partial l_n'}\left(u_{r_{n-1}} - u_{r_n}\right) - G_{12} A\left(\gamma_{n-1} - \gamma_n\right) = 0
\end{aligned} \tag{4.68}$$

In addition to the equilibrium equations presented above, $2n$ equations relating $x_i(s)$ and $y_i(s)$ to $\gamma_i(s)$ and $l_i(s)$ have to be provided similar to the ones presented in equation (4.20). Thus, a system of $4n$ nonlinear 1st and 2nd order differential equations with constants unknowns $\left\{f_{x_i}, f_{y_i}\right\}$ have to be solved with their corresponding boundary conditions. A rapid and efficient numerical solution is developed to solve the system by using a combination of Newton's method (to linearize the system) and the finite difference

technique (to transform the linearized differential equation into a set of algebraic equations). The details of the numerical solution is presented in Appendix A Numerical Solution.

4.3.2 Results and Discussions for the in-plane case

This section includes results and discussions regarding the effect of the transverse stiffness and shear on the in-plane fiber bundles response. These results heavily depend on the magnitude of the transverse modulus of E_2 and the shear modulus of G_{12}.These moduli will be changed from a value of zero to $10\ GPa$. By doing so, several material systems can be covered throughout the analysis: a very small value of these stiffnesses correspond to dry fiber tows, values in the MPa range correspond to soft matrix systems (such as uncured thermoset resins), and high values in the GPa range correspond to cured matrix systems such as thermoplastic tows.

4.3.2.1 Pure Compression with no adhesion

To investigate the effect of the transverse stiffness and shear on the deformation mechanisms, a pure compression case is examined first where the foundation has a zero stiffness. In addition, the first set of results will investigate the effect of E_2 only while neglecting the effect of shear and taking $G_{12} = 0$. In, the second set of results, the effect of G_{12} will be investigated while taking $E_2 = 0$.

4.3.2.1.1 Effect of transverse stiffness

Four bundles placed in a compressive region are considered in this analysis and having properties as shown in Table 4.5. For these given conditions, the shape of the deformed tows is shown in Figure 4.21 for two significantly different values of E_2: for a very soft matrix with $E_2 = 10^4\ Pa$ and for a matrix with intermediate stiffness of $E_2 =$

$10^8\ Pa$. It can be observed that for a soft matrix, the interaction between the deformed bundles is negligible, and the obtained shape is the same as the case where no interaction is assumed ($E_2 = 0$, see Figure 4.5). However, if the matrix is somehow stiff ($E_2 = 0.1\ GPa$) the distance between the fiber bundles remains the same to minimize the transverse strain energy, and therefore the bundles are parallel. However, at a significant length as shown in Figure 4.21 (b), the fiber bundles cannot absorb additional length in the axial direction, and all fibers deform in the transverse direction while remaining parallel. This means that the transverse displacement is the same for all bundles, even for the bundle closest to the neutral axis which did not experience this amount of displacement at smaller values of E_2.

To further examine the effect of the transverse stiffness on the defomration of the fiber bundles in the transverse direction, a logarithmic plot showing the maximum transverse displacement as a function of E_2 is shown in Figure 4.22. At small values of E_2 ($E_2 < 10^{5.5} Pa$), the fiber bundles behave independantly, and the interaction between them is very minimal. For intermediate values of the stiffness ($10^{5.5} < E_2 < 10^{7.5} Pa$), the interaction between the fiber bundles is somehow significant, and the transverse displacement between the bundles starts to decrease. For a somehow strong matrix ($E_2 > 10^{7.5} Pa$), the transverse displacements of the four bundles under compression converge to an intermediate value where all bundles are deforming with the same magnitude while remaining parallel and forming in-plane waves.

Table 4.5 Material property and geometry of the tow deforming out-of-plane

$\boldsymbol{E_1}$ [23]	$\boldsymbol{H}$ [16]	$\boldsymbol{w_t}$	$\boldsymbol{\rho}$	$\boldsymbol{k_x = k_y}$	$\boldsymbol{L}$
130 GPa	0.184 mm	6.35 mm	0.8 m	0	40 mm

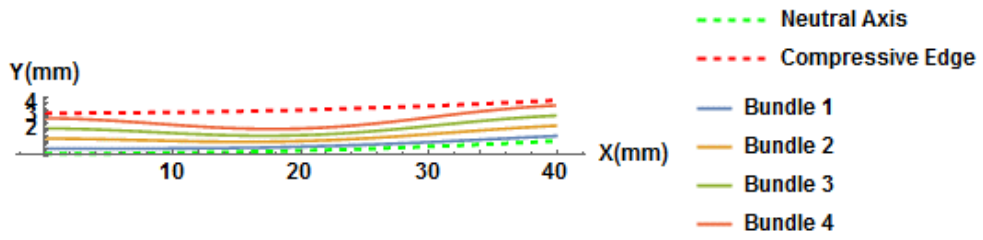

(a) $E_2 = 10^4\ Pa$

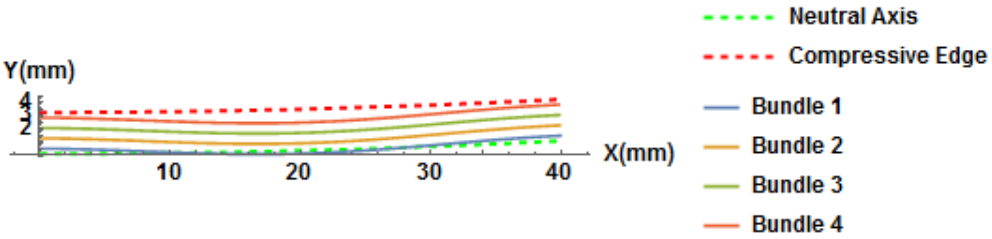

(b) $E_2 = 10^8\ Pa$

Figure 4.21: Deformed fiber bundles under compression with variable E2

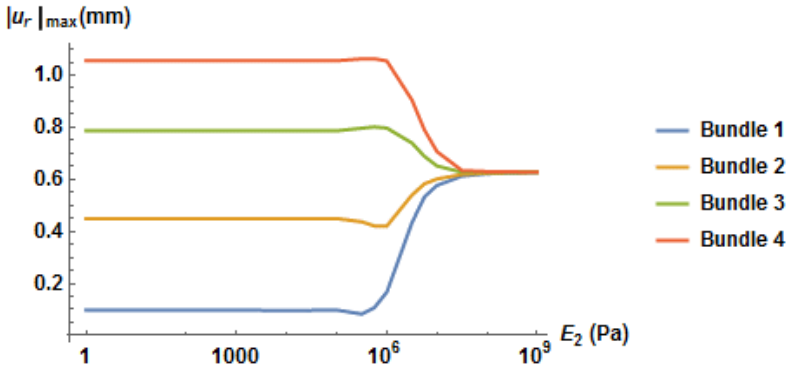

Figure 4.22: Effect of E2 on the maximum transverse displacement for fibers under compression

4.3.2.1.2 Effect of shear stiffness

Similarly to the above section, 4 fiber bundles are considered in the analysis, and placed in a compressive region within the towpath. The material properties and geometry used for the analysis are shown in Table 4.5. For a very soft matrix where the shear modulus is $G_{12} = 10^4\ Pa$, the same results as are obtained as above, where most of the additional length is absorbed through waviness, while the fibers close to the neutral axis do not experience significant large deformations. For the case of a stiffer matrix, all fiber bundles

remain parallel to minimize the shear betwee them, while sliding in-plane to absorb the additional leght by means of waviness. These results can be observed below in Figure 4.23.

To further examine the effect of the shear stiffness on the defomration of the fiber, a logarithmic plot showing the maximum transverse displacement as a function of G_{12} is shown in Figure 4.24. At small values of G_{12} ($G_{12} < 10^7 Pa$), the fiber bundles behave independantly, and the interaction between them is very minimal. For intermediate values of the stiffness ($10^7 < G_{12} < 10^9 Pa$), the interaction between the fiber bundles is somehow significant, and the transverse displacement between the bundles starts to decrease. For a somehow strong matrix wher the shear modulus $G_{12} > 10^9 Pa$, the transverse displacements of the four bundles under compression converge to an intermediate value where all bundles are deforming with the same magnitude while remaining parallel and forming in-plane waves.

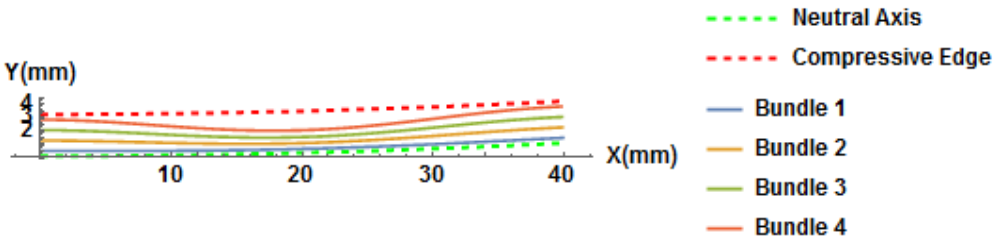

(a) $G_{12} = 10^4\ Pa$

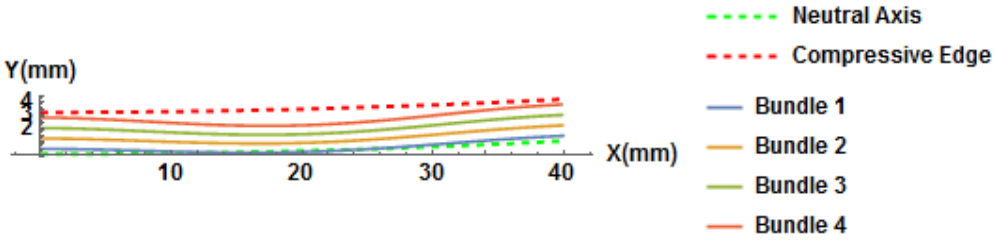

(a) $G_{12} = 10^9\ Pa$

Figure 4.23: Deformed fiber bundles under compression with variable G_{12}

Comparing the two cases where the transverse stiffness E_2 and the shear stiffness G_{12} are isolated and their effect is studied seperatly, it can be concluded that larger values for the shear stiffness are required to obtain significant interaction between the bundles ($G_{12} > 10^9 Pa$). However, similar behavior can be obtained when $E_2 > 10^{7.5} Pa$. Hence, the interaction between the fiber bundles is more sensitive to the transverse modulus E_2 than the shear modulus G_{12}. Based on that, the remaining section will only examine the effect of the transverse stiffness while neglecting the shear.

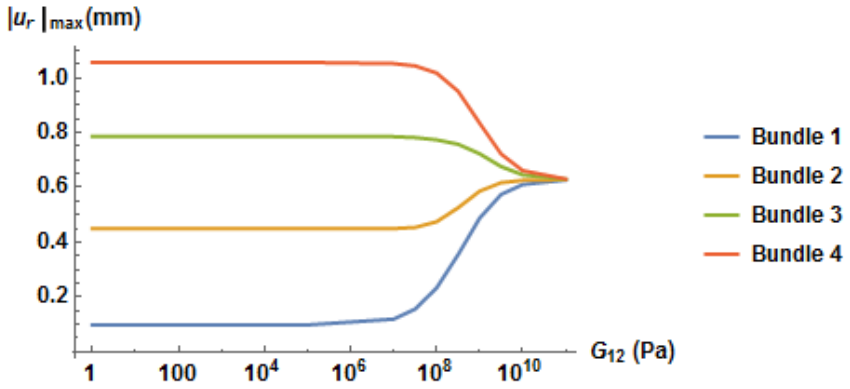

Figure 4.24: Effect of G12 on the maximum transverse displacement for fibers under compression

4.3.2.2 Combined loading conditions

In this section, the interaction between the fiber bundles is examined along the effect of the foundation's stiffness for bundles placed in tensile and compressive regions. For this case, the applied conditions are the same as the ones used in the "Effect of the foundation's stiffness" section of Part I. The properties and results for $E_2 = 0$ are found in **Error! Reference source not found.** and Figure 4.9. In essence, bundles 1 and 2 are placed i n a tensile region, bundles 4 and 5 in a compressive region, and bundle 3 coincides with the neutral axis. The logarithmic plots showing the effect of the stiffness k on the maximum transverse displacement $|u_r|_{max}$ for three values of E_2 ($E_2 = 10^6, 10^7$ and $10^9 Pa$) are

shown in Figure 4.25 . For a small valued of E_2 ($E_2 = 10^6 Pa$), the behavior of the fiber bundles is the same as the ones obtained when there is no interaction (compare Figure 4.9 and Figure 4.25 (a)). In this case, the fiber bundles under tension (bundles 1 and 2) experience smaller transverse displacement than the ones under compression (bundles 4 and 5), while bundle 3 remains in its intended location for small values of k, whereas for large values of k, all fiber bundles remain in their locations. For the case where $E_2 = 10^7 Pa$ (Figure 4.25 (b)), it can be noticed that bundle 3 is deformed even with small values of k due to some small but significant bundle interactions. However, the response is similar to the case of $E_2 = 10^6$. However, for the case where $E_2 = 10^8\ Pa$, the bundles' deformations are much different: at first with the absence of adhesion, the transverse displacement for bundle 5 is around 50% smaller than the previous cases. In addition, the displacement of the fiber bundles does not converge to the same value similar to the pure compression case. Instead, the fibers bunch together towards the neutral axis/centerline while the compressive bundles still have the larger displacement. However, for all cases when $k > 10^7 N/m^2$ the bundles displacement drops significantly to below $0.1\ mm$.

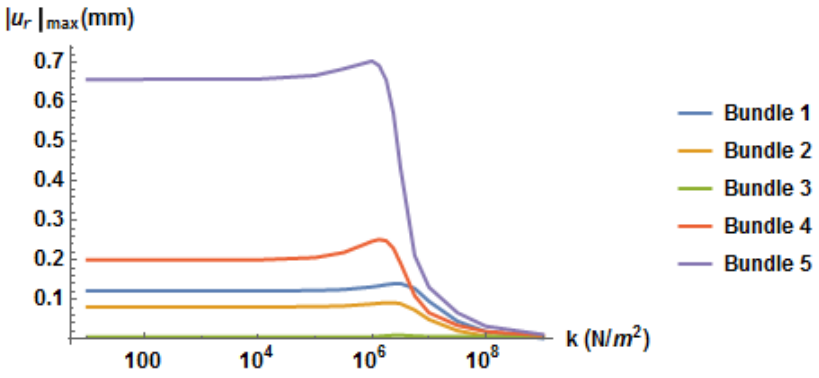

(a) $E_2 = 10^6$

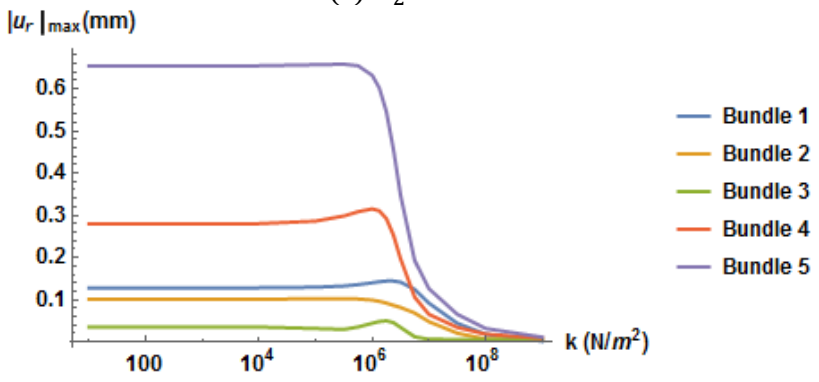

(b) $E_2 = 10^7$

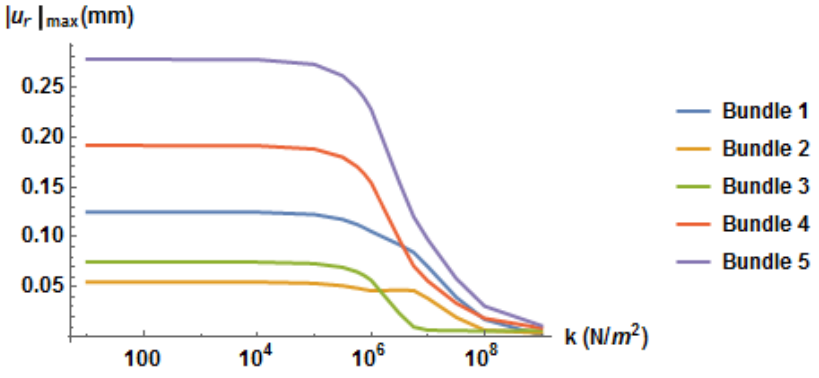

(c) $E_2 = 10^8$

Figure 4.25: Effect of E_2 and k on the maximum transverse displacement for fibers under combined loading

4.3.3 Governing equations for the out-of-plane case

The total energy for n fiber bundles deforming in the out-of-plane direction including the transverse effects of E_2 but ignoring shear can be expressed as:

$$\Pi_t = \sum_{i=1}^{n} \Pi_i + \frac{1}{2} E_2 H w_b \sum_{i=1}^{n-1} \int_0^L \left(\frac{u_{r_{i+1}} - u_{r_i}}{d_i} \right)^2 ds. \tag{4.69}$$

where the Π_i terms correspond to the contribution of individual fiber bundles including the out-of-plane terms. The expression of $u_r(s)$ for the in-plane case can be found from (4.61), however, for the out-of-plane case, the expression of $u_r(s)$ has to include the out-of-plane rotation angle β such as:

$$u_r(s) = v(s)\cos\gamma(s)\cos\beta(s) - u(s)\sin\gamma(s)\cos\beta(s) + w(s)\sin\beta(s). \tag{4.70}$$

The corresponding derivatives of $u_r(s)$ with respect to the variables $\gamma(s), \beta(s)$ and $l'(s)$ are needed in the derivation of the governing equations. These derivatives are expressed as:

$$\frac{\partial u_r}{\partial \gamma} = \left(x_{ref}(s)\cos\gamma(s) + y_{ref}(s)\sin\gamma(s) \right)\cos\beta(s) \tag{4.71}$$

$$\begin{aligned} \frac{\partial u_r}{\partial \beta} = &\left(\xi(s)\sin\gamma(s) - \psi(s)\cos\gamma(s) + w(s) \right)\cos\beta(s) \\ &+ \left(\zeta(s) - v(s)\cos\gamma(s) + u(s)\sin\gamma(s) \right)\sin\beta(s) \end{aligned} \tag{4.72}$$

$$\frac{\partial u_r}{\partial l'} = -x(s)\sin\gamma(s)\cos\beta(s) + y(s)\cos\gamma(s)\cos\beta(s) + z(s)\sin\beta(s) \tag{4.73}$$

The total energy of the system is expressed as:

$$\Pi_t = \int_0^L \mathcal{F}(s, \gamma_1, \gamma_2, \dots, \gamma_n, \gamma_1', \gamma_2', \dots, \gamma_n', \beta_1, \beta_2, \dots, \beta_n, \beta_1', \beta_2', \dots, \beta_n', l_1', l_2', \dots, l_n') ds \tag{4.74}$$

To minimize the total energy, the following set of Euler-Lagrange equations have to be satisfied:

$$\begin{cases} \dfrac{d}{ds}\left(\dfrac{\partial \mathcal{F}}{\partial \gamma_i'} \right) - \dfrac{\partial \mathcal{F}}{\partial \gamma_i} = 0 \\ \dfrac{d}{ds}\left(\dfrac{\partial \mathcal{F}}{\partial \beta_i'} \right) - \dfrac{\partial \mathcal{F}}{\partial \beta_i} = 0 \\ \dfrac{d}{ds}\left(\dfrac{\partial \mathcal{F}}{\partial l_i'} \right) - \dfrac{\partial \mathcal{F}}{\partial l_i} = 0 \end{cases} \tag{4.75}$$

This will result in the following set of equations:

$$\begin{cases} E_1 I_\gamma \gamma_1'' - \dfrac{\partial \Pi_1}{\partial \gamma_1} + \dfrac{E_2 H}{w_{b1}} \dfrac{\partial u_{r_1}}{\partial \gamma_1}\left(u_{r_2} - u_{r_1}\right) = 0 \\ E_1 I_\beta \beta_1'' - \dfrac{\partial \Pi_1}{\partial \beta_1} + \dfrac{E_2 H}{w_{b1}} \dfrac{\partial u_{r_1}}{\partial \beta_1}\left(u_{r_2} - u_{r_1}\right) = 0 \\ E_1 A\, l_1' - F_1 + \dfrac{\partial \Pi_1}{\partial l_1'} - \dfrac{E_2 H}{w_{b1}} \dfrac{\partial u_{r_1}}{\partial l_1'}\left(u_{r_2} - u_{r_1}\right) = 0 \\ \vdots \\ \vdots \\ \vdots \\ E_1 I_\gamma \gamma_i'' - \dfrac{\partial \Pi_i}{\partial \gamma_i} + \dfrac{E_2 H}{w_{bi}} \dfrac{\partial u_{r_i}}{\partial \gamma_i}\left(u_{r_{i-1}} - 2u_{r_i} + u_{r_{i+1}}\right) = 0 \\ E_1 I_\beta \beta_i'' - \dfrac{\partial \Pi_i}{\partial \beta_i} + \dfrac{E_2 H}{w_{bi}} \dfrac{\partial u_{r_i}}{\partial \beta_i}\left(u_{r_{i-1}} - 2u_{r_i} + u_{r_{i+1}}\right) = 0 \\ E_1 A\, l_i' - F_i + \dfrac{\partial \Pi_i}{\partial l_i'} - \dfrac{E_2 H}{w_{bi}} \dfrac{\partial u_{r_i}}{\partial l_i'}\left(u_{r_{i-1}} - 2u_{r_i} + u_{r_{i+1}}\right) = 0 \\ \vdots \\ \vdots \\ \vdots \\ E_1 I_\gamma \gamma_n'' - \dfrac{\partial \Pi_n}{\partial \gamma_n} + \dfrac{E_2 H}{w_{bn}} \dfrac{\partial u_{r_n}}{\partial \gamma_n}\left(u_{r_{n-1}} - u_{r_n}\right) = 0 \\ E_1 I_\beta \beta_n'' - \dfrac{\partial \Pi_n}{\partial \beta_n} + \dfrac{E_2 H}{w_{bn}} \dfrac{\partial u_{r_n}}{\partial \beta_n}\left(u_{r_{n-1}} - u_{r_n}\right) = 0 \\ E_1 A\, l_n' - F_n + \dfrac{\partial \Pi_n}{\partial l_n'} - \dfrac{E_2 H}{w_{bn}} \dfrac{\partial u_{r_n}}{\partial l_n'}\left(u_{r_{n-1}} - u_{r_n}\right) = 0 \end{cases} \tag{4.76}$$

4.3.4 Results and Discussions for the out-of-plane case

In this section, the effect of the transverse stiffness on the out-of-plane displacement is investigated. To do so, the material properties and geometry shown in Table 4.6 are considered. Five bundles are placed in a compressive region, and the deformed shape of the bundle is similar to the case presented earlier in Figure 4.17 (b) for small values of E_2. For this case, 4 out of five bundles deform in the out-of-plane direction, whereas the bundle closest to the neutral axis remains in-plane. This behavior can also be depicted in Figure 4.26, where the maximum displacement in the z-direction is plotted as a function of the transverse stiffness. As shown in Figure 4.26, for small values of E_2 ($E_2 < 10^7 Pa$) the

behavior of the bundles does not change from the case where the interaction between the bundles is neglected. However, for the case where E_2 is significantly large ($E_2 = 10^8 Pa$), the bundle closest to the neutral axis also deforms in the out-of-plane direction. This is due to the fact that the interaction of the fibers in the transverse direction is significantly large so that the bundles in the compressive areas can pull the bundle closest to the neutral axis to deform in the out-of-plane direction by the mean of the high transverse stiffness. Note that for this case, the out-of-plane displacement for the five bundles is still different, indicating a rotation of the overall tow cross-section.

Table 4.6 Material property and geometry of the tow deforming out-of-plane

E_1 [23]	H [16]	w_t	ρ	$k_x = k_y = k_z$	L
130 GPa	0.184 mm	6.35 mm	0.8 m	0	20 mm

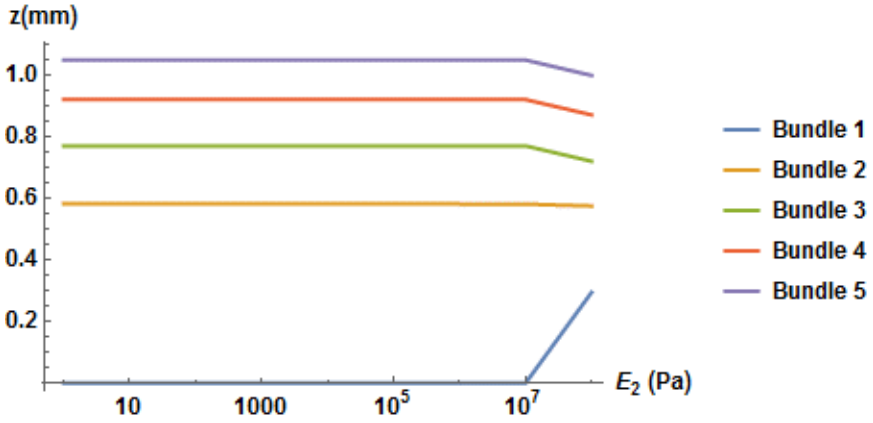

Figure 4.26: Effect of E2 on the out-of-plane displacement of the fiber bundles

CHAPTER 5

EXPERIMENTAL INVESTIGATIONS OF AFP STEERED TOWS

Several experimental trials are carried and presented in this chapter concerning steered tows on flat and curved surfaces. The first section highlights the main points of the published article "Experimental investigation of prepreg slit tape wrinkling during automated fiber placement process using StereoDIC" [59]. In this work, several tow deformations are captured using stereo DIC. In the second section, the effect of the process parameters on tow deformations is investigated. A benchmark curved path on a flat surface is proposed to reduce experimental trials and to easily determine a critical steering radius as a function of the process parameters. Lastly, steering on an industrial scale cylindrical mandrel is performed using the same proposed curves while monitoring the process parameters, highlighting manufacturing challenges, and proposing a new quality assessment technique based on image processing of profilometry scanned layups.

5.1 EXPERIMENTAL INVESTIGATION OF PREPREG TOW WRINKLING USING STEREO DIC

The main findings in this section are summarized based on the co-authored work published in reference [59]. For further details, readers can refer to the published full text of reference [59]. Additional experimental trials using the DIC technique are also discussed in the last subsection (5.1.4) but not published in [59]. These experiments include some

adjustments in the designed curves, substrate quality, and the number of speckled tows within the course.

5.1.1 Experimental Setup

The stereo DIC setup used in the image acquisition process consists of: (1) a stereo camera pair, (2) mounting frame for the stereo cameras, (3) tripod to mount the cameras and frame, (4) a calibration grid for the cameras, (5) a computer with digital image correlation software installed (VIC-3D) [ref] and (6) a suitable high contrast speckle pattern on the surface of the tow. The details regarding the cameras, lens, and stereo DIC parameters are shown in Table 5.1 and Table 5.2. Linear polarizing filters are used for both the LED light source and the camera lenses to remove reflections from the tow surface, since additional paint coating may alter the mechanical response. The speckle pattern is applied and evaluated using two different techniques: (1) a fine spray of high temperature (stable up to 700°C) white flat paint, and (2) white airbrush paint. The black carbon fiber tow background gave good contrast for the speckled surface. Both techniques are found to be suitable for the application and can withstand abrasion due to the AFP process.

Table 5.1 Camera and lens parameters for stereovision system [59]

	Camera and lens parameters
Camera	5 MP CMOS PointGrey camera, 2448 × 2048 pixels^2 array 3.45 μm pixel size
Calibration	12 × 9 dot grid, 1.5 mm dot size, 5 mm dot spacing More than 120 stereo image pairs
Lens	Nikon Micro-Nikkor 25 mm focal length
Lens Filter	Linear polarizer
Light Source	LED with linear polarizing film
Lens Distortion	3rd Order Radial Distortion Correction

Table 5.2 Stereo DIC parameters [59]

	StereoDIC parameters
Subset size	25 × 25 pixels^2
Step size	7 pixels
Filter type	Center-weighted Gaussian filter
Strain Filter size	5 × 5 data points (area of 35 × 35 pixels^2)
Strain measure	Lagrangian large strain tensor definition for all strain components
Field of view	114 mm × 95 mm
Magnification	0.045 mm/pixel
Average speckle size	0.15 mm

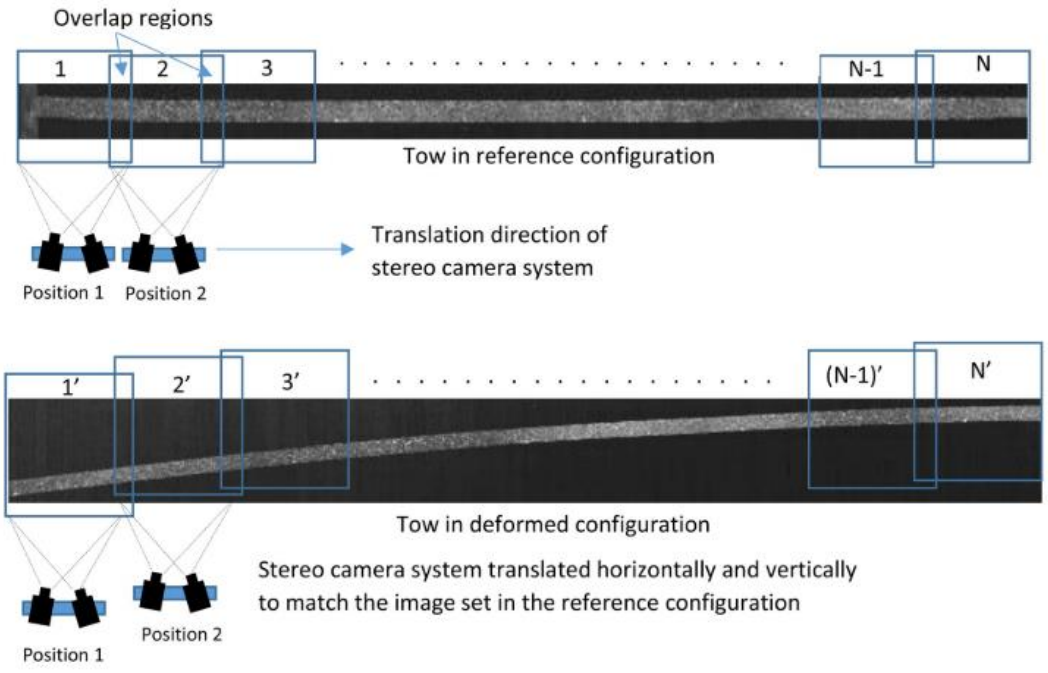

Figure 5.1 Image acquisition process [59]

Since the aspect ratio of the tow is relatively high (the tow length used is around 610 mm per path compared to 6.35 mm tow width), obtaining a single high magnification image able to characterize deformations across the width with the available digital cameras (field of view 114 mm x 95 mm) is not possible. To obtain the required spatial resolution a single stereo camera system is used to capture multiple images by rigidly translating and

rotating the system to acquire images spanning the entire tow length. The neighboring images are configured to have an overlap of ~15–20% of the field of view to enable image stitching and reconstructing the whole tow in a later step within the VIC 3D software. A schematic of the image acquisition process is shown in Figure 5.1.

To obtain accurate measurement using this technique two conditions should be met: (1) the relative position of the two cameras in the stereo vision system should be fixed and the internal parameters in both cameras (e.g., focal lengths, distortion correction parameters) should remain the same, and (2) the tow must be stationary during the image acquisition process in both the reference and deformed configurations. To ensure condition (1), the cameras are mounted on a rigid platform and calibrated first to the required magnification/field of view, then the rigid platform is translated and/or rotated to acquire the images. To ensure condition (2), the tow is unspooled from the AFP machine head, laid flat on the tool surface with slight tension, speckled, and then reference images are taken. The tow is respooled into the machine, placed on the required path, then the images of the deformed tow are taken.

The material used during the AFP process is 6.35 mm wide thermoset prepreg tows (Hexcel IM7/8552-1). The AFP machine in the McNair center at the University of South Carolina is used (Horizontal Lynx® AFP from Ingersoll Machine Tools). The design consists of 4 different paths: a straight path, and 3 constant curvature arcs with the following turning radii 2540 mm (100 in), 1270 mm (50 in), and 305 mm (12.5 in) (refer to Figure 5.2 for the stitched images of the deformed tows). The steered paths are placed on a substrate with the same material having the following stacking sequence [90/0/90].

All process variables including lay-up speed (2438 mm/min), temperature (40 °C) and compaction force (200 N) are maintained throughout the layup process.

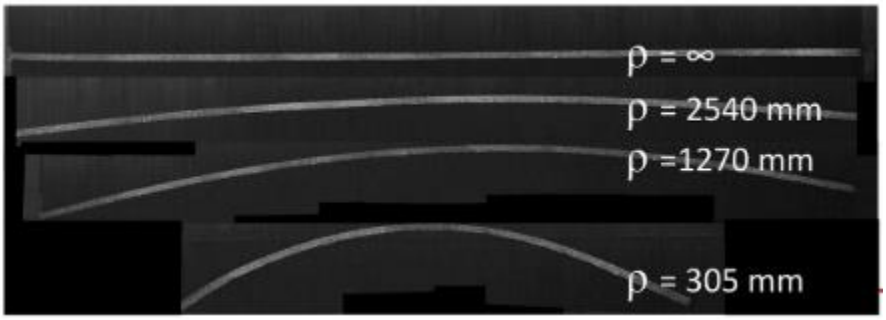

Figure 5.2 Speckled and stitched images of the 4 different paths [59]

To apply the speckle pattern and capture reference speckle images the procedure described earlier is followed: tows are manually drawn from the AFP machine head, placed flat with slight tension on the tool surface, the speckle pattern is applied, then reference images are obtained by overlapping neighboring images. A photograph of this process is shown in Figure 5.3. Once the entire length is speckled, the tow is respooled into the machine (which is done automatically by turning on the tow tensioner) and then placed on the designed paths. Lastly, to investigate the influence of time and the effect of heating during the placement of adjacent tows, the process is repeated to capture additional set of images (a) one hour after placement and (b) reheating of the as-placed tow by exposing the specimen to the same levels of heating as employed during the initial lay-up without mechanical loading. Heating is performed using the IR heating element of the AFP system, which is brought very close to the steered tow (within 38 mm) as it is traversed along the length of the tow at 2438 mm/min. For all experimental results reported in the following sections, analysis of the speckle images is performed using commercial DIC software, VIC-3D, with the Stereo DIC parameters shown in Table 5.2.

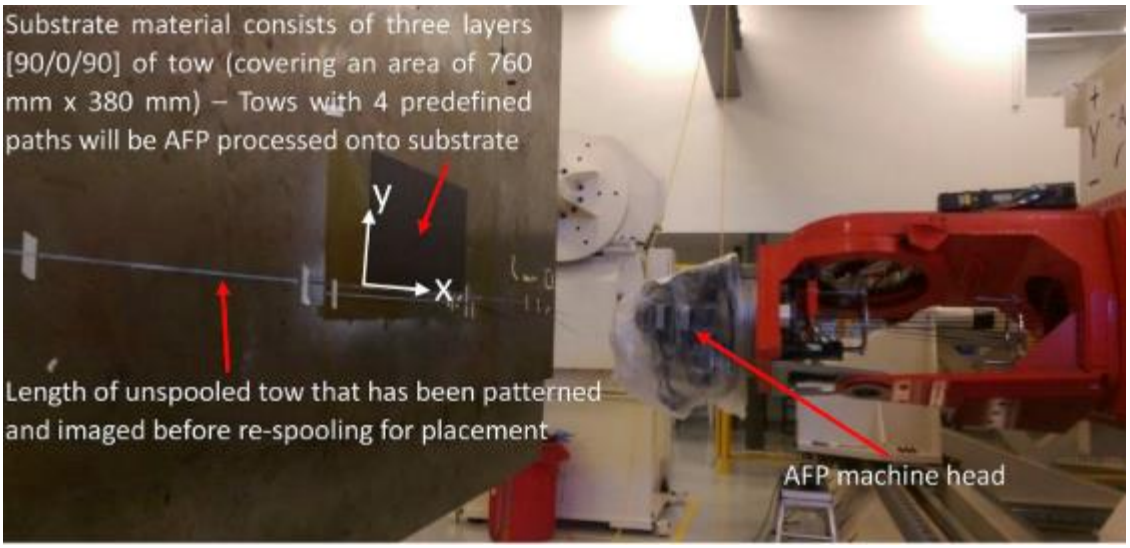

Figure 5.3 Photograph of the tool, initial layers of the substrate, AFP head and initial length of patterned, unspooled tow that is imaged before re-spooling [59]

5.1.2 Experimental Results

To investigate the validity of the applied method, the straight path is first considered for investigations. The profile of the out-of-plane displacement extracted for a line along the length of the straight tow is shown in Figure 5.4. It can be observed that there is a regular, repeating pattern of out-of-plane waviness located approximately every 100mm along the length. Further investigation of this surface profile confirms that these local variations in the shape of the straight tow are due to the presence of tow overlaps in the as-manufactured laminate substrate. Tow overlaps occurred every 16 tows (101.6 mm) in the manufactured substrate which is equivalent to the width of a single course (also equal to the roller width).

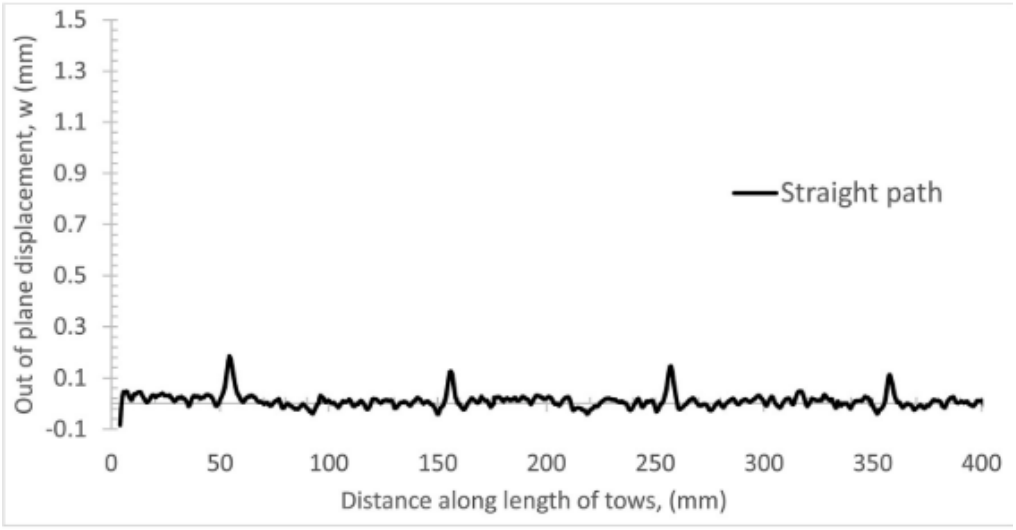

Figure 5.4 Out-of-plane displacement for the straight path showing the locations and magnitudes of the overlaps in the substrate [59]

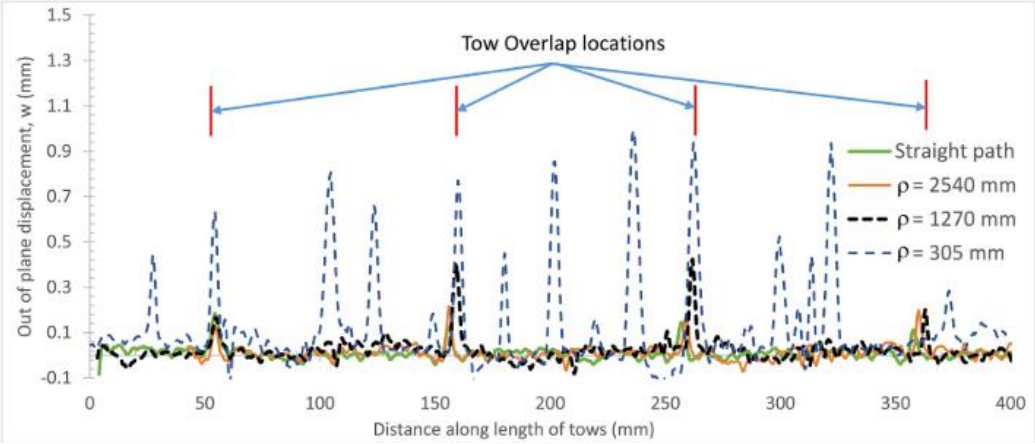

Figure 5.5 Out-of-plane displacement for the 4 different path at a line 1 mm above the bottom edge of the tow in the reference configuration [59]

The out-of-plane displacements for the remaining steered tows taken at a line along the tow length and located at 1 mm from the bottom edge of the tow in the reference configuration are shown in Figure 5.5. For the tow steered at 2540 mm radius, there are no out-of-plane displacement except for the locations where overlaps in the substrate occurred. For all other steered paths, larger wrinkles developed at the overlap locations; thus, leading to the conclusion that substrate imperfections such as overlaps serve as

nucleation sites for wrinkle formation in steered paths. A magnified image of this effect for the smallest radius of curvature is shown in Figure 5.6. For the path steered at 1270 mm radius, additional small amplitude wrinkles appear along the length of the tow. For the smallest radius of curvature of 305 mm, there is a remarkable difference in the wrinkle amplitude and frequency. The number and amplitude of new local wrinkles that are not due to substrate defects have increased significantly.

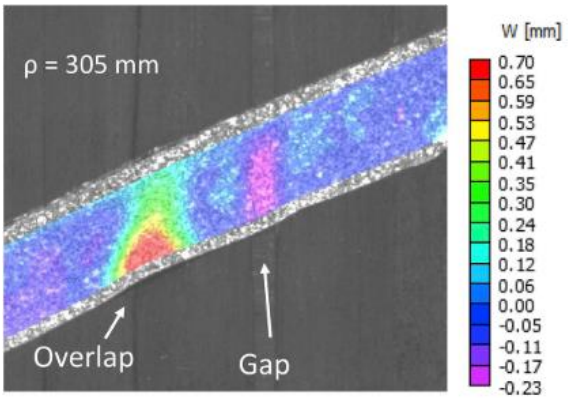

Figure 5.6 Effect of substrate gap and overlap on the out-of-plane displacement for the 305 mm radius path [59]

Defining the measured distance between the peaks of adjacent wrinkles as the wavelength λ, the width of the wrinkle l_w to be the distance along the length where the tow is separated from the surface, and the amplitude as the maximum height of the wrinkles in the out-of-plane direction, the average and standard deviation of these measure quantities are reported in Table 5.3. The following points can be deduced from the measurements reported in Table 5.3: (1) steering at a smaller radius of curvature will increase the number of wrinkles within the paths, (2) wrinkles at smaller radius are larger in both width and amplitude directions, and (3) at smaller radius, the wrinkles are more irregular with larger standard deviation for both wavelength and wrinkle width.

Table 5.3 Summary of the wavelength, width, and amplitude measurements of the wrinkles [59]

ρ (mm)	Number of wrinkles for length of 400 mm	Wavelength λ (mm)	Width l_w (mm)	Amplitude (mm)
∞	4	100.10 ± 0.63	6.62 ± 0.97	0.136 ± 0.033
2540	4	101.14 ± 0.66	6.02 ± 1.61	0.172 ± 0.045
1270	12	102.09 ± 0.61	7.80 ± 1.45	0.296 ± 0.145
		30.25 ± 8.89[c]	1.45 ± 0.75[a]	0.062 ± 0.022[a]
305	18	106.57 ± 1.36	9.04 ± 2.87	0.644 ± 0.242
305	22[b]	21.30 ± 12.93[c]	8.03 ± 1.77[a]	0.488 ± 0.308[a]
		15.55 ± 7.14[b]	7.26 ± 2.32[b]	0.504 ± 0.324[b]

In order to investigate viscoelastic effects of the tow, a separate experiment is carried out for a tow that is placed at the smallest radius of 305 mm. The substrate imperfections due to overlap and gaps are minimized in this lay-up process by improving the substrate quality. Measurements are taken at 3 different steps: (1) immediately after layup, (2) an hour after placement, and (3) after applying heat to the tow simulating the layup of a neighboring course. The results for the out-of-plane displacements along the same line located at 1 mm from the bottom edge of the tow in the reference configuration for the 3 measurements are shown in Figure 5.7. It can be observed that the amplitude of the wrinkles slightly increases over time. However, the most significant change occurs after applying heat, where a larger increase in the wrinkles' amplitudes and width can be observed. In addition, neighboring small wrinkles have merged to form one larger wrinkle. These observations indicate that the process is time and temperature dependent, and viscoelastic effects should be taken into considerations.

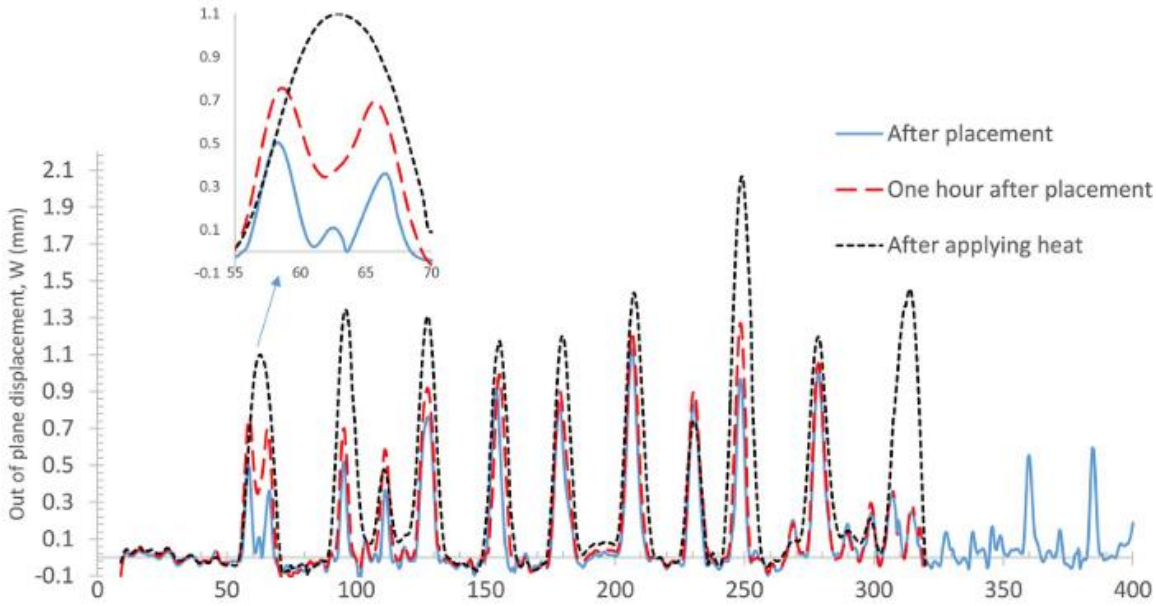

Figure 5.7 Out-of-plane displacement for a line at 1 mm above the bottom edge of the reference configuration for the path steered at 305 mm [59]

5.1.3 Further Observations

In addition to the measurements of out-of-plane wrinkles that occur on the compressive edge of the tow, investigations regarding tow deformations on the tensile edge are presented. For the tow steered at 305 mm radius, the Lagrangian transverse strain map is shown in Figure 5.8. It can be observed that large compressive transverse strains occur at the tensile edge of the tow with an order of $-0.1\ \varepsilon$ especially across the locations where an out-of-plane wrinkle is developed on the compressive edge. The occurrence of such transverse strains validates the assumed bunching mechanisms where the fibers on the tensile side, in presence of high adhesion, slide transversely towards a neutral surface to minimize the axial tensile strains.

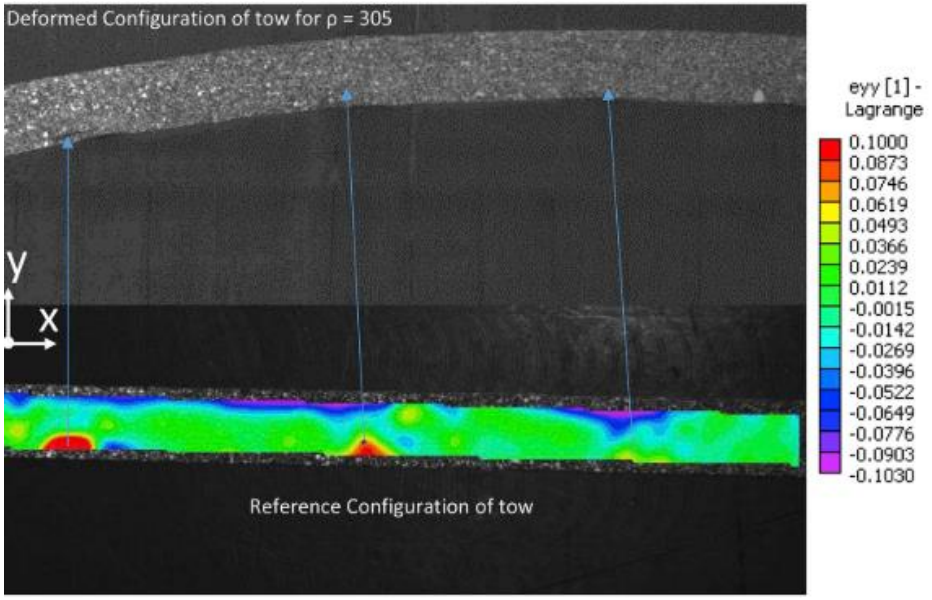

Figure 5.8 Transverse strain map for the tow steered at 305 mm radius [59]

Additional commonly observed defects during tow placement are shown in Figure 5.9, and includes: (a) folding over of tows during placement and (b) crack formation/matrix failure, and (c) bunching of fibers combined with matrix cracking. Tow folding is observed on the tensile edge of the tow especially when there is lack of adhesion to keep the fibers in-plane or to bunch towards a neutral surface. Matrix cracking is observed in relatively weak matrix especially on the compressive edge of the tow where large transverse tensile strains lead to matrix failure.

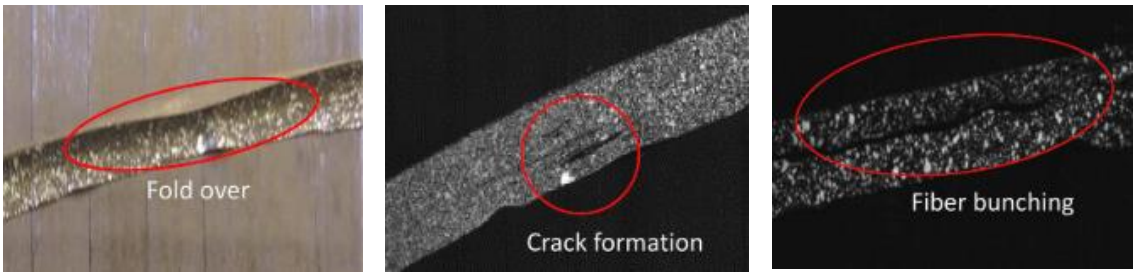

(a) Folding (b) Matrix cracking (c) Fiber bunching

Figure 5.9 Observed defects other than wrinkling during steering [59]

5.1.4 Additional Steering Experiments on Flat Surface using Stereo DIC

In addition to the work presented in the previous section, other steering experiments are accomplished and detailed in this section. Measurements using the same DIC setup described earlier are carried to further investigate the effect of the substrate, as well as the deformations of neighboring tows within a course when steered along constant curvature paths.

5.1.4.1 Second Steering Design

In addition to the first set of experiments, further investigations of tow deformations are performed to highlight other aspects of steered tows. A second layup is designed including the following changes. First, the straight path and the path steered at 2540 mm (100 in) radius are discarded since no large deformations were observed in previous experiments. An additional path steered at 635mm (25 in) radius is included to have a better understanding of tow deformations at this intermediate curvature. The second design includes a total of 6 courses and investigating 3 different radii of curvature: 1270, 635, and 318 mm (50, 25, and 12.5 in) respectively. Each radius of curvature is repeated twice for consistency. The length of the path is made shorter (~ 370 mm) to reduce the time to acquire the necessary images for DIC. Each course has 8 tows speckled and activated to study the different deformations of neighboring tows across the roller. The substrate stacking sequence is [90/0/90/S], where "S" stands for the special layer with steered paths.

The second design shown in Figure 5.10 and Figure 5.11 is repeated twice. In the first trial, the manufactured substrate had severe gaps and overlaps that occurred every 8 tows (equivalent to a single course). These substrate defects lead to the occurrence of aligned tow wrinkles across all 8 tows within the steered courses. Additional defects such

as folded, loose, and split tows for the 635 mm (25 in) radius of curvature are shown in Figure 5.12. The same design is repeated with an improved substrate to alleviate some of the bias in the obtained wrinkles at the overlap locations. A photograph of the partially completed layup while it is being manufactured is shown in Figure 5.11. In addition to improving the substrate quality, the layup speed for the steered paths is decreased and the temperature is increased during the second trial to improve the adhesion between the tows and the substrate. This improvement led to a decrease in the loose and folded tows especially on the tensile side of the roller. Another photograph of the second trial is shown in Figure 5.13. This photograph is taken after completing the layup and showing additional wrinkles that developed over the time especially for the 1270 mm (50 in) radius where no wrinkles were observed during manufacturing.

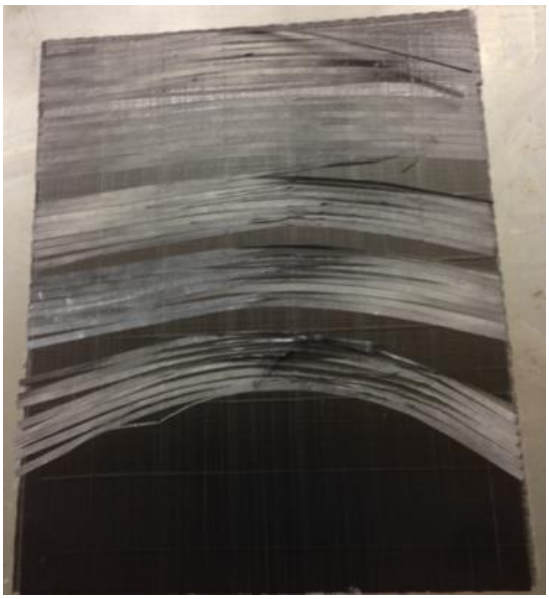

Figure 5.10 Second steering design during the first manufacturing trial

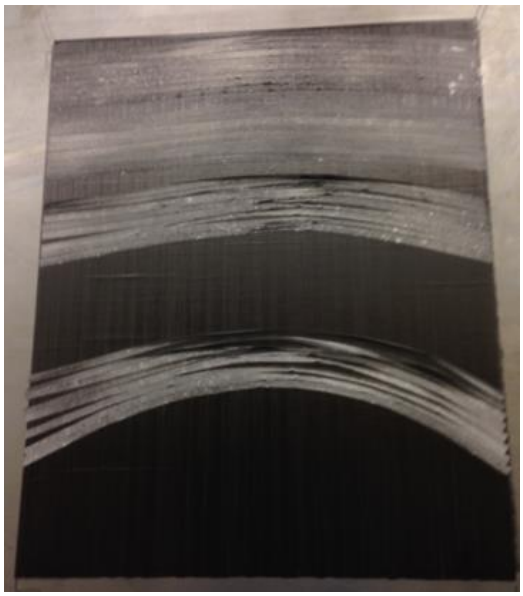

Figure 5.11 Second steering design during the second manufacturing trial

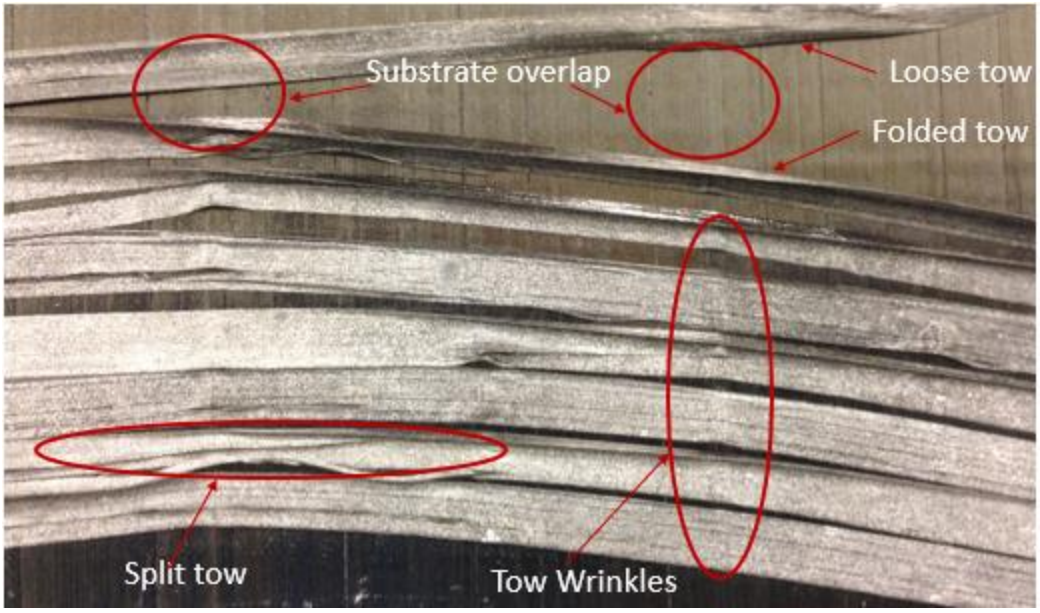

Figure 5.12 Obtained defects in the second design during the first trial for 635 mm radius

Figure 5.13 Completed second design (photograph taken after completing the experiment)

The major findings during the manufacturing of the second design are summarized below. The last 101 mm (4 inches) for each course located at the left side of the panels did

not show any major deformation due to steering (the machine motion is set to start from right to left during manufacturing). This is because the cutting length of the AFP machine is 101.8 mm, hence at the end of each course when the tows are cut, there is no tension to guide the tows to follow the required path. Hence, the tows become loose and follow a stress-free path which is a straight line. This tow misalignment can be especially observed in the tightest radius of curvature of 318 mm, where the deviation from the path is the most significant for the last 101.8 mm. A second observation is that there are no major tow deformations at the start of the course at the right side of the panel. This can be caused by the additional temperature and compaction pressure that the machine head provides at the beginning of the course to ensure a good adhesion and to avoid tows debonding and falling of the tool surface. Another observation regarding neighboring tows within a course is the difference in the deformation mechanisms even for the same process parameters and very similar steering radius. Note that the designed steering radius is set to the centerline of the course, hence each tow above or below the course centerline has a slightly different radius of curvature (designed radius ± 25.4 mm). It is observed that the tow placed on the smallest radius within a course (bottom tow within the course) undergoes the most compression, whereas the tow placed at the largest radius (top tow within the course) undergoes the most tension. This can be due to one or more of the following reasons: (1) due to machine kinematics, the top tows are placed at a faster speed compared to the bottom ones, (2) the feed rate for the parallel tows is not individually controlled and all the tows within the course have the same federate, (3) the feed rate may be individually controlled however it is not well calibrated to compensate for the steering. The top 2 – 3 tows within the course have severe folding due to the high tension. This led to obscuring the DIC pattern and no

data were collected for the folded tow. In addition to folding, tow splitting (cracks developing along the fiber direction) under compression is also an issue that hinders the correlation between the reference image and the split tows. Concerning wrinkling, small wrinkles occurred on the compressive edge of the tows. In some cases, both wrinkles and folds occurred for the same tow (see the third tow from the top in Figure 5.12). Even with an improved substrate, small gaps (~ 0.5 mm) that occur between adjacent tows will lead to a wrinkle in the successive steered layer.

The stereo DIC technique is used to measure the shape of the deformed tows, and the out-of-plane displacement is extracted following a line along the length of the bottom edge of the tows, thus capturing the height of the wrinkles. Further calculations are carried to extract the wrinkles amplitude, width, and wavelength. The average and standard deviations of these quantities are plotted as function of the steering radius and are shown in Figure 5.14, Figure 5.15, and Figure 5.16. Previous trends regarding the amplitude of the wrinkles as function of the steering radius is observed, where at lower radius larger wrinkles (higher amplitudes) occur. The time and temperature dependency of the wrinkles amplitude and width is also captured; this can be depicted by comparing the top course to the bottom one. Since the top course is placed earlier than the bottom one and sustained an adjacent heat source during the placement of the second course, the measured wrinkles amplitude and width are larger than the bottom course. Lastly, the trends for the wrinkle's wavelength as function of the steering radius is not depicted in this experiment. The reduced quality of the substrate that includes gaps and overlaps lead to some bias in the results.

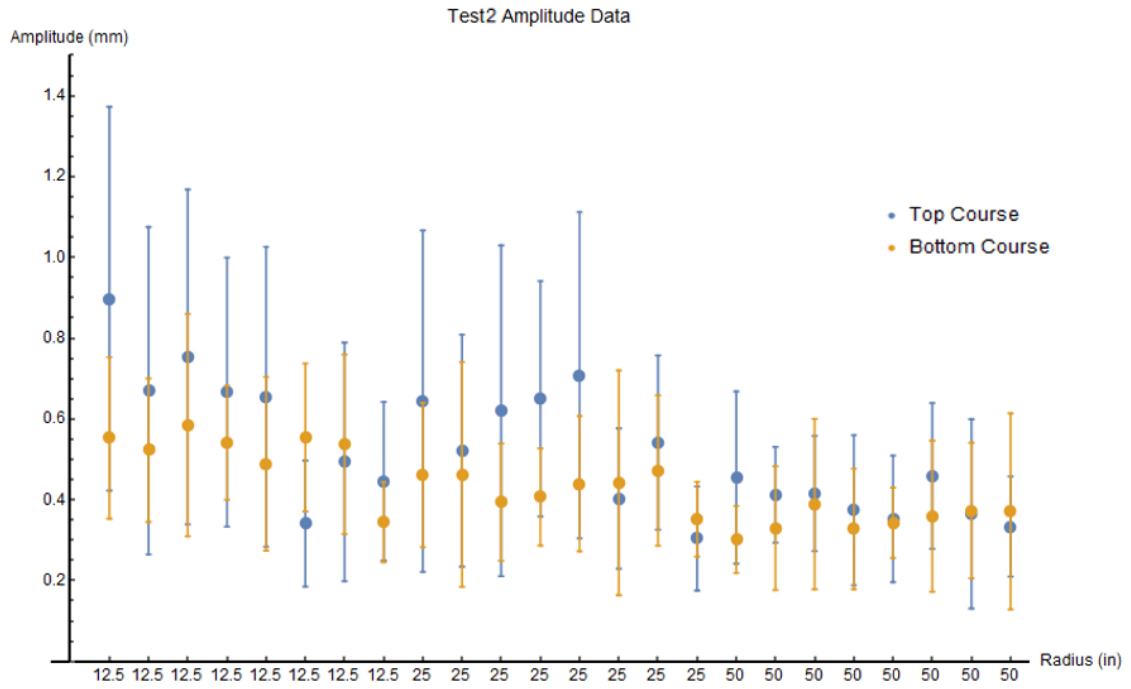

Figure 5.14 Average of the measured wrinkles amplitude for the placed tows during test2

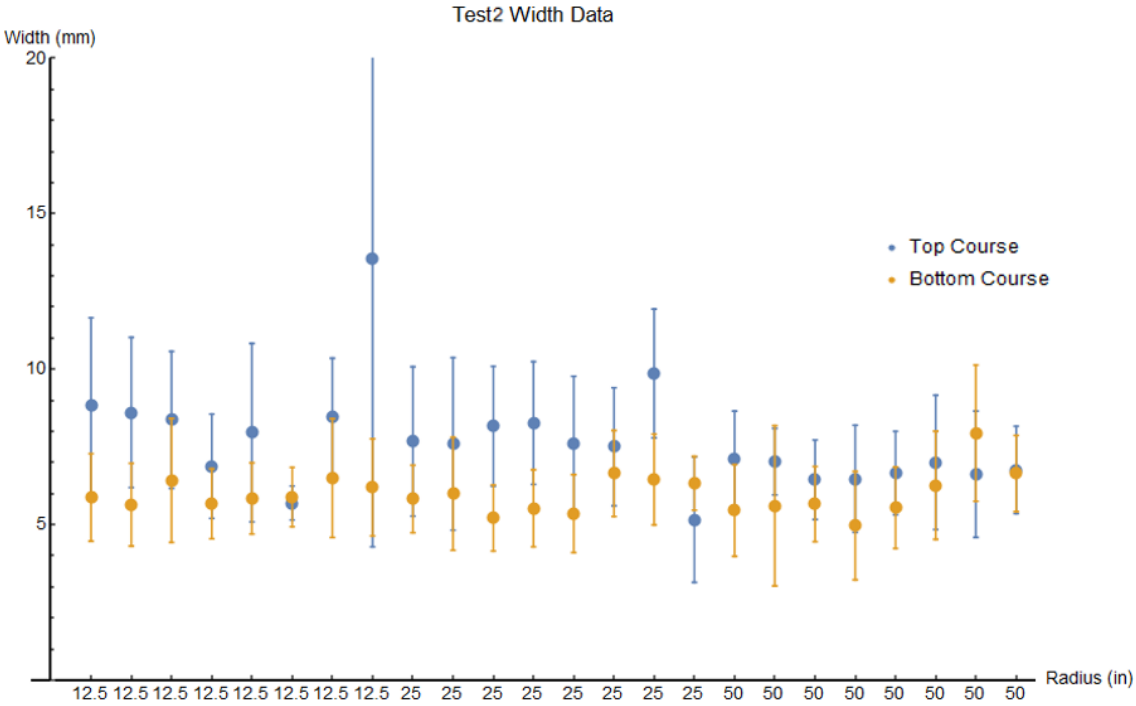

Figure 5.15 Average of the measured wrinkles width for the placed tows during test2

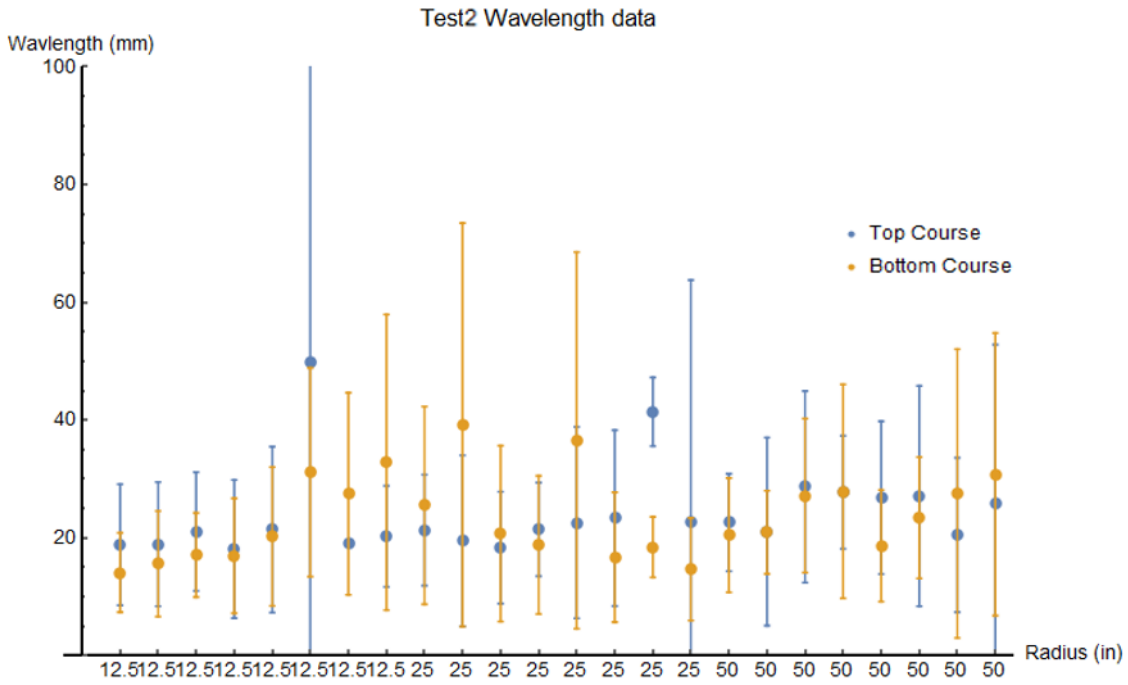

Figure 5.16 Average of the measured wrinkles wavelength for the placed tows during test 2

5.1.4.2 Third Steering Design

To solve some of the issues presented during the manufacturing of the second design, a third design is proposed with the following changes. First, a straight 4-inch-long segment is added to the start and end of each course. The straight lines are tangent to the path to avoid abrupt change in the path continuity (the path is $C^{(1)}$ continuous: smooth change in the tangent angle but not in the curvature). As a result, the length of the path is increased to be close to the original design to have a significant length for DIC investigation. A straight path is added back at the top of the panel to obtain a reference profile for the placed substrate and to investigate if gaps and/or overlaps exist. Three paths with different radii of curvature are used: 1270, 635, and 318 mm (50, 25, and 12.5 inches). Nine tows are activated within a course where only 3 tows are speckled within the course: the top, middle, and bottom tow (5 out of 9 of the tows are below the centerline of the

course with the designed curvature). A prepreg unidirectional sheet is used as a substrate to completely remove gaps and overlaps between tows manufactured by the AFP machine. The third design is shown blow in Figure 5.17 just after completion of the manufacturing process using the similar process parameters as used in earlier experiments.

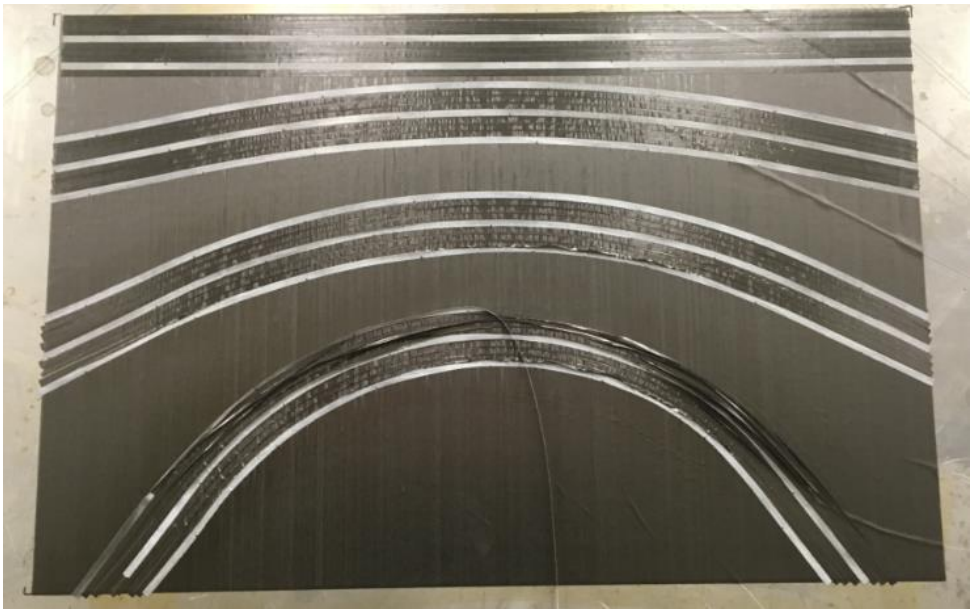

Figure 5.17 Third steering design

The paths steered at 1270 and 635 mm do not show any severe large-scale deformations. Small sized out-of-plane wrinkles appear for the steered section for all paths. For the smallest radius of curvature, tow pull up, folding, and debonding is a major defect observed mostly for the tows in the top half of the course where tension is more significant. A close-up image showing tow deformations for the course steered at 318 mm is shown in Figure 5.18. The upper-most speckled tow suffered debonding halfway through the placement process. Tow folding on the tensile edge of the tows is observed in almost all tows in the upper half of the course, whereas fiber bunching (in-plane) is observed to occur on the tensile edge of the 5 tows at the bottom half of the course. Small wrinkles are observed in almost every tow. Multiple large wrinkles waves are observed on the second

tow from the bottom: a reasonable explanation for this observation is that the second tow from the bottom wandered from its intended location to partially overlap the bottom speckled tow. The presence of the speckled pattern on the bottom tow reduced the adhesion of the top surface which lead to the creation of the large wrinkle patterns.

Figure 5.18 Steering defects during the 3rd design for 318 mm radius of curvature

Similarly, the out-of-plane displacement for the speckled tows is extracted along a line near the bottom edge. The amplitude, width, and wavelength of the wrinkles are extracted and shown in Figure 5.19, Figure 5.20, and Figure 5.21 respectively. The improved quality of the substrate shows better trends for the measured quantities as function of the steering radius. In addition, comparing the amplitude of the wrinkles for neighboring tows within a course, it can be concluded that tows undergoing more compression (bottom tows) have wrinkles with larger amplitudes than the tows on the tensile side of the course. Similar conclusion can be drawn regarding the wrinkle's width as function of the steering radius (Figure 5.20), where wider wrinkles occur at smaller

steering radii. Similarly, fewer wrinkles (larger wavelength) occur at higher steering radii (Figure 5.21).

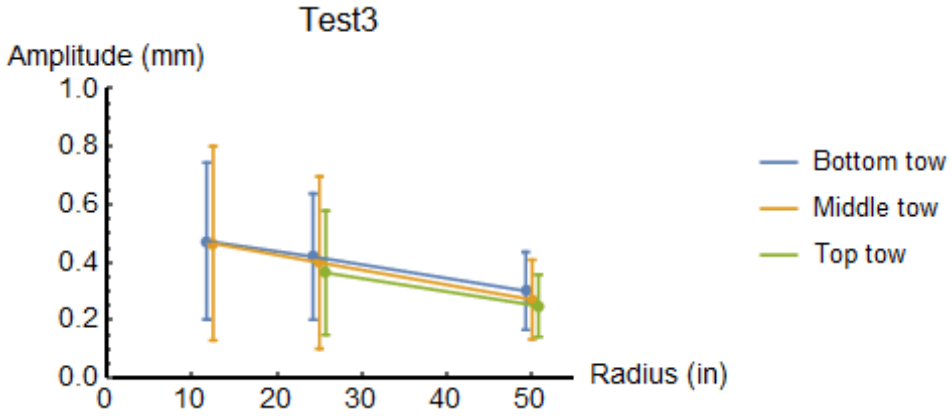

Figure 5.19 Average of the measured wrinkles amplitude for the placed tows during test 3

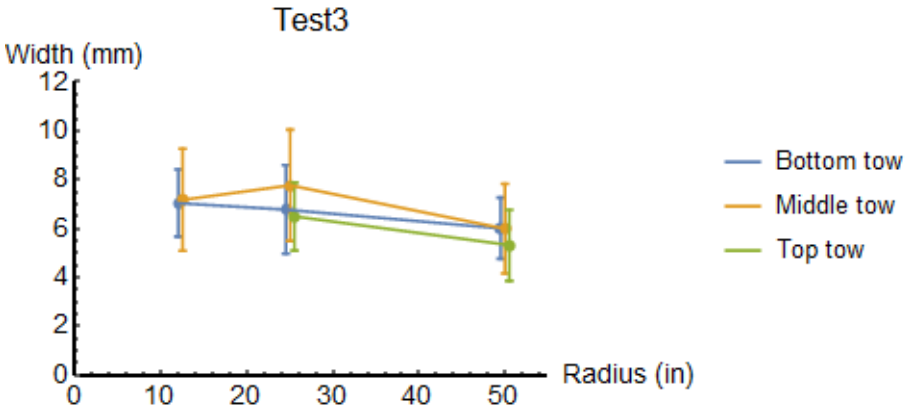

Figure 5.20 Average of the measured wrinkles width for the placed tows during test 3

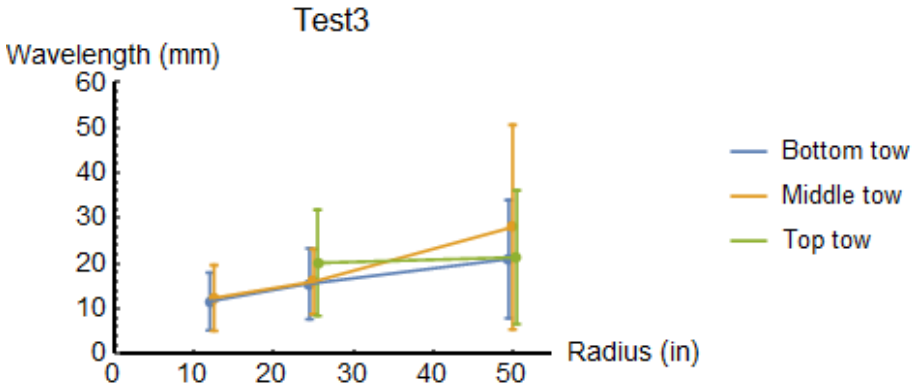

Figure 5.21 Average of the measured wrinkles wavelength for the placed tows during test 3

5.2 EFFECT OF PROCESSING PARAMETERS ON TOW DEFORMATIONS

In this section, the effect of the process parameters on the tow deformations is investigated for a steered path on a flat surface. A benchmark path is defined whit a linear variation in the curvature, thus minimizing the number of experimental trials if constant curvature arcs where to be used. The main investigated AFP process parameters are the layup speed, temperature, compaction, and tow tension. Measurements for the substrate temperature and roller compaction are acquired using thermocouples and pressure sensors placed along the length of the curved path. The quality of the layup is assessed by visual inspection of the courses placed on a substrate layer, and by determining the location (and therefore the corresponding critical curvature) of the first visible defect along the length of the steered courses. The interaction of the process parameters on the defect formation is also discussed.

5.2.1 Background

It has been shown in the literature [17–20] and in the previous work shown in the above sections that the deformability of the tow material and its ability to adhere properly to a substrate is not only dependent on the geometry of the path, but also on the AFP processing parameters, such as the deposition speed, the surface temperature, the roller pressure and others. Changing the processing parameters, especially the temperature, can alter the material properties of the tow locally thus potentially alleviating the formation of large-scale defects such as wrinkling during the layup of curvilinear paths. In order to understand the effect of the process parameters on the defect generation, experimental investigation of a predefined set of process parameter is needed along with a benchmark path. Constant curvature paths (circular arcs) are the main shapes investigated in the

literature (Figure 5.22 and Figure 5.23) to determine a critical radius of curvature below which defects start to appear along the path. Multiple curves with different constant radii of curvature are usually tested while also varying the process parameters (temperature, speed, pressure, etc.) within a predefined range. This usually results in a very large set of trials to run using the AFP machine, especially if each radius of curvature is tested alone using all combinations of the process parameters. In addition, the discrete jump in curvature between the tested curves makes it difficult to determine the exact critical radius of curvature for a given set of parameters; it would rather give an approximate bound for the steering radius within which defect may start to appear.

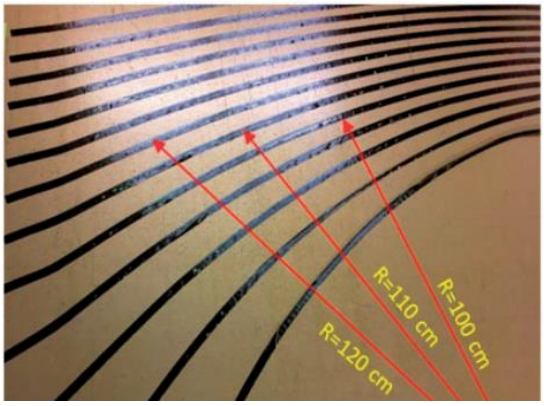

Figure 5.22 Single tow steered at different radii of curvature [17]

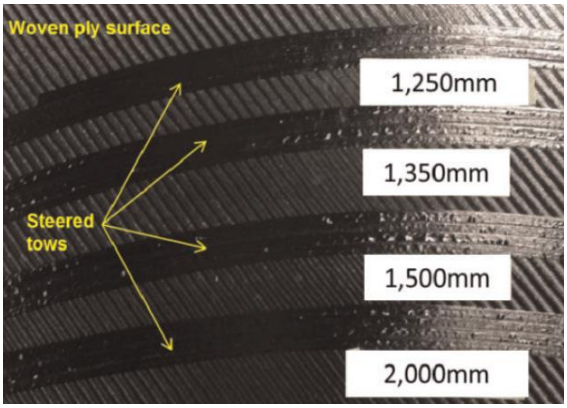

Figure 5.23 Eight tows course steered at different radii of curvature [19]

In order to better approximate the critical steering radius and to reduce the number of experimental trials, a different type of curve is proposed in this section. This path does not have a constant curvature but rather has a smooth transition for the curvature starting from zero (equivalent to a straight line) and gradually increasing to a maximum specified value. By doing so, as the AFP lays the tows along this path, a good layup quality should be obtained at the beginning where the path is mostly straight or slightly curved. As the machine head progresses along the path, the curvature increases gradually to a critical value

at which a first defect will appear. Based on the location of the first significant defect that appears along the path, the critical curvature (or steering radius) can be determined for the used set of process parameters.

5.2.2 Benchmark Path Definition

Instead of using constant curvature paths (i.e. circular arcs) for experimental testing of the AFP process parameters, a simple linear variation of the curvature κ as a function of the arc-length s is chosen for the benchmark path. Therefore, the curvature of the path can be expressed as:

$$\kappa(s) = a\, s\,, \tag{5.1}$$

where a is a constant (rate of change of curvature) to be specified. From differential geometry [53], the in-plane tangent angle to the path γ and the coordinates x and y can be related using:

$$\gamma'(s) = \kappa(s)\,, \tag{5.2}$$

$$x'(s) = \cos\gamma(s)\,, \tag{5.3}$$

$$y'(s) = \sin\gamma(s)\,, \tag{5.4}$$

where the prime sign represents the differentiation with respect to the arc-length s.

By plugging (5.1) into (5.2), integrating with respect to s, then replacing the value into (5.3) and (5.4), the coordinates can be expressed in integral form:

$$x(s) = \int_0^s \cos\left(a\frac{s^{*2}}{2}\right) ds^*\,, \tag{5.5}$$

$$y(s) = \int_0^s \sin\left(a\frac{s^{*2}}{2}\right) ds^*\,. \tag{5.6}$$

The integrals in (5.5) and (5.6) are known as the Fresnel's Integrals [53], and can be solved numerically depending on the specified value of a. The shape obtained by

plotting the solution of (5.5) and (5.6) is called a clothoid, Euler spiral, or Cornu spiral. An example of the solution for a $= 0.5$ and a $= 1$ ($0 < s < 4$) is shown in Figure 5.24.

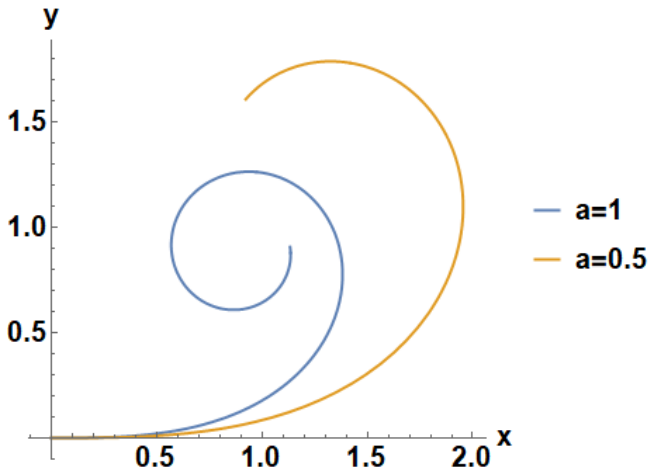

Figure 5.24 Example of a clothoid with different values of a and $0 < s < 4$

In the context of creating a benchmark path for testing steering in AFP, additional boundary conditions must be supplied to obtain a unique shape for the proposed spiral. Mainly, a value for the rate of change of curvature is needed along with a value for the maximum length to be placed. To determine a value for a with a physical significance to the AFP process, enforcing a curvature, tangent angle, x or y coordinate at a given point can be used. Here, the value of a is computed by setting a maximum curvature κ_{max} (or a minimum steering radius R_{min}) at a given arc-length of the curve L_{max} which corresponds to the endpoint. In other words, by setting the total length of the path and a maximum curvature beyond which there is no interest in steering, a unique shape of the spiral can be obtained. Using equation (5.1), the rate of change of the curvature a can be related to those parameters by:

$$a = \frac{\kappa_{max}}{L_{max}} = \frac{1}{R_{min}\ L_{max}}. \tag{5.7}$$

Based on the results reported by the authors in [59], a steering radius of 305 mm exhibited significant wrinkles along the length of the path for tapes that are quarter inch wide. Therefore, a minimum steering radius of $R_{min} = 300\,mm$ is chosen for the benchmark path with a convenient maximum length of $L_{max} = 750\,mm$. For wider tapes, a different value may be used. Solving equations (5.5) and (5.6) numerically with the corresponding value of $a = 4.44 * 10^{-6}\,mm^{-2}$, the shape of the benchmark path is visualized in Figure 5.25.

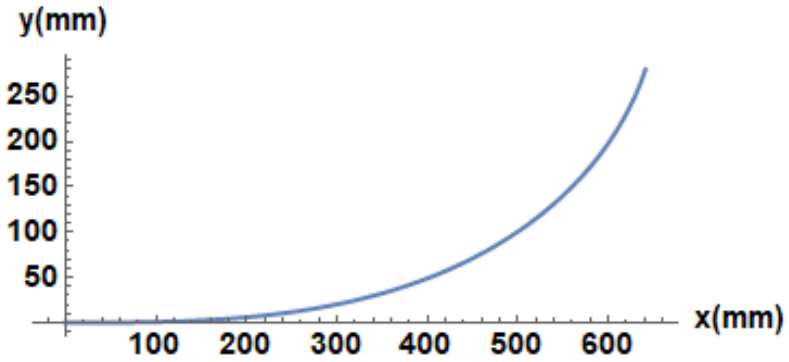

Figure 5.25 Benchmark path with $R_{min} = 300\,mm$ and $L_{max} = 750\,mm$

Usually of-the-shelf CAD software do not have the capabilities to solve equations (5.5) and (5.6) numerically. Therefore, in order to facilitate transferring the data to an AFP machine, the coordinates of the benchmark path along with the corresponding tangent angle are sampled at $3\,mm$ spacing along the length s. The obtained points are then imported into CATIA and four paths are programmed within a $1000 \times 600\,mm$ rectangular boundary (see Figure 5.26). Linear translation operations are applied to shift the paths within the boundary to avoid interference and overlapping between the adjacent courses. In addition to the curved portion of the path, two $101.6\,mm$ ($4\,in$) long tangential straight lines are added at the start and end of each path. The length of these lines is equal to the

minimum cut length of the AFP machine, thus ensuring accurate deposition of the tows on the curved path especially for the last portion.

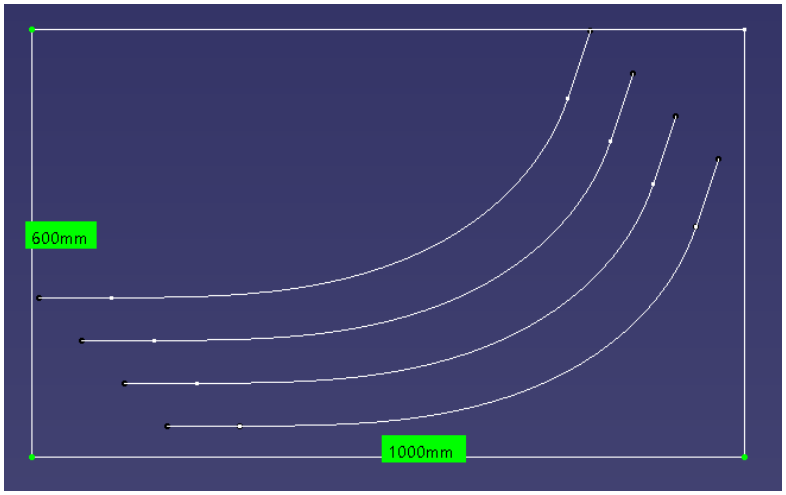

Figure 5.26 Programmed curved paths in CATIA

5.2.3 Process Parameters

Regarding the AFP process parameters, the main ones investigated in this section are the layup speed (or also referred to as feed rate), temperature, compaction, and tow tension. A design of experiment is followed where each of these parameters is varied within a specified range and the effect of their interaction is observed on the layup quality. Concerning the layup temperature, a 6 kW HUMM3 light source heater is attached to the AFP head and used to vary the surface temperature. For such type of heaters, the temperature is proportional to the power output. Three different parameters can be changed to control the power of the heater: the voltage, the pulse duration, and the frequency of the light source. For a constant frequency of 60 Hz, the power output is recorded by the manufacturer for different voltages and pulse durations and provided in Figure 5.27. For a given pulse width, the curve leading to the highest power output is chosen from Figure 5.27 which corresponds to 2 ms. Hence, by only varying the voltage of the heater and keeping

the pulse and frequency constants, the temperature varies proportionally to the 2 ms pulse curve in Figure 5.27. For the purpose of this experiment, the voltage is changed at the following levels: 100, 125, 150, 175, and 200 Volts (V).

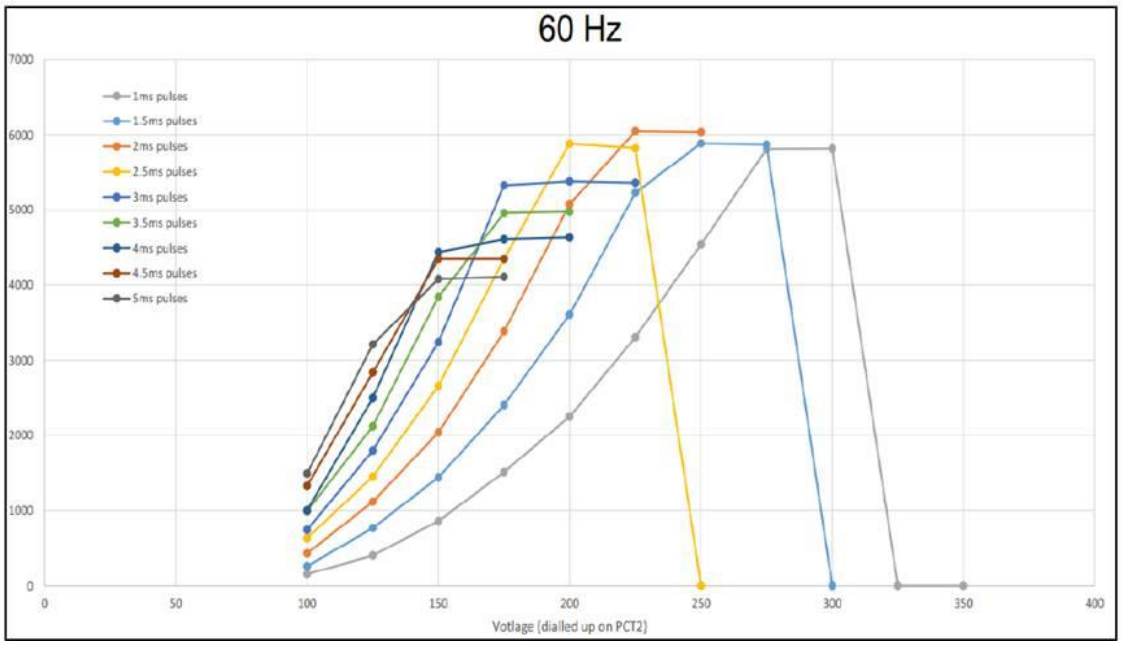

Figure 5.27 Power of Humm3 (Watts) as function of voltage and pulse duration for 60 Hz frequency

For the layup speed, four different levels are investigated: 20, 40, 60, and 100% of the programmed speed of 20,000 mm/min. The compaction force of the roller is also varied at the following levels: 178, 300, 445, 600, and 750 N, where 178 N corresponds to the lower bound of the machine capability, and 445 N (100 lbs) is the standard recommended compaction. Lastly, the tow tension is changed using the following values: 0, 1.5, 3, 5, and 10 N. From previous experiments [22], higher tow tension restricted the tows from being fed through the AFP machine head. The baseline values of the process parameters to be improved are chosen at 40% speed, 150 V for the heater, 445 N compaction, and 3 N tow tension. The summary of the used process parameters and their corresponding levels is shown in Table 5.4 with the baseline values highlighted in bold.

Table 5.4 Process parameters and their corresponding levels for the steering tests

Test	Course	S (%)	P(N)	T(V)	t (N)
Speed	101	20	445	150	3
	102	40	445	150	3
	103	60	445	150	3
	104	100	445	150	3
Temperature	101	40	445	100	3
	102	40	445	125	3
	103	40	445	175	3
	104	40	445	200	3
Compaction	101	40	178	150	3
	102	40	300	150	3
	103	40	600	150	3
	104	40	750	150	3
Tension	101	40	445	150	0
	102	40	445	150	1.5
	103	40	445	150	5
	104	40	445	150	10
High STP	101	60	600	175	3
	102	60	600	200	3
	103	60	750	175	3
	104	60	750	200	3

5.2.4 Data Acquisition

A live recording of the machine monitor during the layup of each course is saved to ensure that the actual speed of the layup coincides with the programmed/set ones as shown Figure 5.28. A speed profile as a function of time is extracted from the live recording to monitor any unexpected changes in the actual layup speed. As for the temperature, six thermocouples are placed along the length of the path to record the change in temperature over time as shown in Figure 5.29. In addition, two pressure sensors are placed at the same location of the first two thermocouples across the width of the course. No instrumentation was used to record the tow tension, it was solely set in the machine parameters.

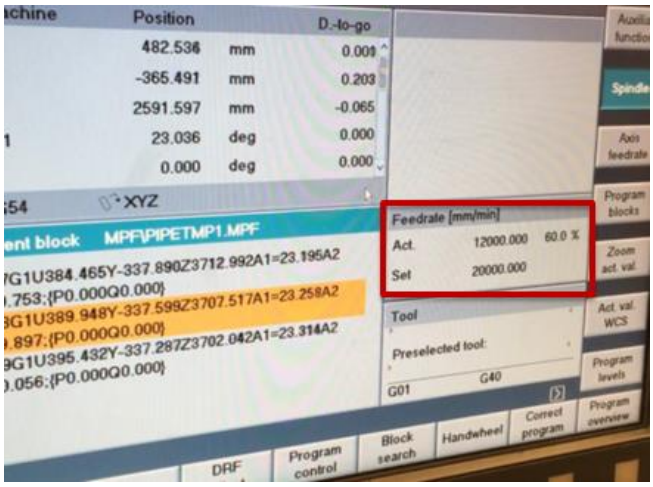

Figure 5.28 AFP monitor displaying the actual feed rate during manufacturing

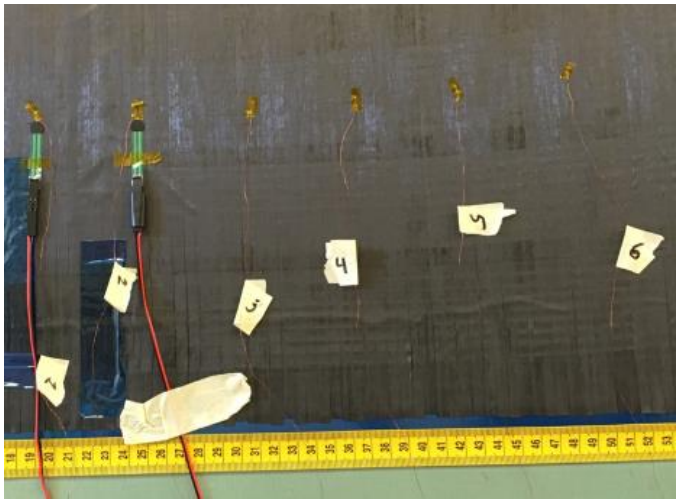

Figure 5.29 Pressure sensors and thermocouples placed along the curved path

5.2.5 Recommended Parameters

The following guidelines are provided by the material supplier for the operation of the AFP machine (Table 5.5). The process parameters are varied according to the levels provided in the earlier section while recording the actual output of temperature, speed, and compaction. For all manufacturing operations, the room temperature and relative humidity

did not exceed the provided limits. Regarding the measured temperature at the nip point, the cases where the recommended value is exceeded are noted.

Table 5.5 Recommended process parameters

Head pressure	90 lbs. < P < 100 lbs. (400N < P < 445N)
Nip point temperature	TNP < 200°F (TNP < 93.3°C)
Room temperature	60°F < TR < 80°F (15.6°C < TR < 26.7°C)
Relative humidity	RH < 65%

5.2.6 Quality Assessment

The effect of the process parameters on the quality of the laid courses is determined visually by inspecting the courses and recording the location and type of the first visible defect along the course. Based on the x-coordinate of the defect, the corresponding arc length at which it occurred can be determined (by solving the inverse of equation (5.5)) and therefore the critical curvature can be deduced using equation (5.1). The location of the first visible defect is determined for each of the eight tows within the course since the type as well as the location may be different for the tows across the course. The details regarding the obtained critical radius of curvature as function of the process parameters and for all placed tows are reported in Appendix B. Concerning the type of defects detected during the steering experiments, 4 major types are used to classify them and visualized in Figure 5.30 through Figure 5.33. Tow wrinkling and in-plane waviness occur on the inner (compression) edge of the tow, whereas tow folding occurs on the outer (tensile) edge of the tow. It was difficult to visually distinguish between fiber bunching and small folds on the tensile side during these experiments. This is due to the fact that during steering at a continuously increasing curvature, fiber bunching is usually followed by folding, and it is easier to visually detect the fold and mark it as a first visible defect compared to fiber bunching. Hence, in the following section, fiber bunching is not considered as a visible

defect, but rather the folding that occurs just after it. In addition to the deformation mechanisms described above and throughout this document, a new deformation mechanism is observed during these experiments: through-thickness tow splitting (see Figure 5.33). During this deformation mechanism, the bottom surface of the tow on the tension side remains adherent to the substrate whereas the fibers on the top surface bunch towards the center revealing fibers through the thickness of the tow. The revealed fibers can be easily observed due to their darker shade (possibly due the lower resin content within the tow compared to the top surface).

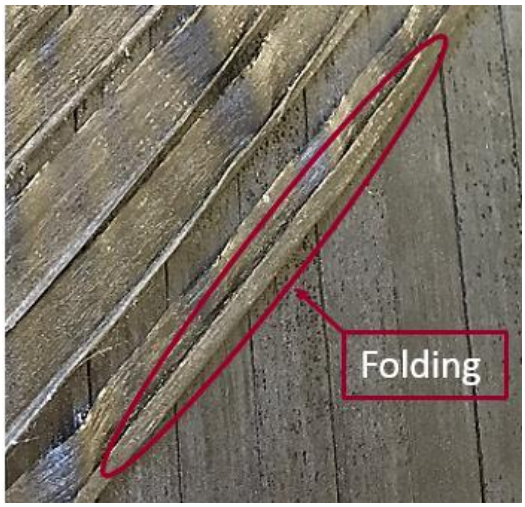

Figure 5.30 Tow folding

Figure 5.31 Tow wrinkling

Figure 5.32 In-plane fiber waviness

Figure 5.33 Through thickness tow splitting

5.2.7 Speed Test

The purpose of this set of experiment is to evaluate the effect of the layup speed on the quality of the layup at the baseline values of the process parameters. The percentage of the programmed speed (20,000 mm/min) of the four courses is varied from 20, 40, 60 to 100% while keeping the compaction force and the heater voltage settings at 445 N and 150 V respectively. The process parameters for this test are summarized in Table 5.4 and the obtained courses are shown in Figure 5.34. By visual inspection, the courses placed at lower speed have a better quality with less observed defects along the length of the path. As the layup speed increases, additional defects can be observed especially folding on the tensile edges of the tow which can be clearly observed for the course 103 placed at 60% of the programmed layup speed. The worst case was for course 104 placed at 100% speed where some tows did not adhere to the tool surface due to lack of adhesion.

Figure 5.34 Obtained layup for the speed test

To ensure that the actual speed of the machine head is following the prescribed percentage, the speed profile for each course is extracted from the live recording of the

AFP console and shown in Figure 5.35. For course 101 placed at 20% of the programmed speed, it is observed that the feed rate is constant at 4,000 mm/min all the way through the placement of the course until the last second where a small decrease in the feed rate occurs. This decrease in the layup speed can be related to the cut speed of the tows; the machine slows down when firing the blade cutters at the end of the course. This decrease in the feed rate is consistently observed in all courses. For courses 102 and 103, and additional decrease in the federate occurs along the path which occurs at the last portion of the curved path where the curvature is relatively high; however, for the most portion of the path, the feed rate remains constant. Lastly, for course 104 placed at 100% of the programmed speed, the machine could not maintain a constant speed along the course and the feed rate decreased significantly and sporadically from the set value. A possible reason for this behavior is the limitation the machine has on the rotational axes which cannot perform the required rotation to place the tows on the tightly curved path at the prescribed speed. To fully understand the effect of the layup speed on the other process parameters and the layup quality, it is preferred to maintain a constant speed along the path to acquire consistent temperature and pressure data. Therefore, laying courses beyond 60% of the programmed speed is not performed in further experimental trials. In addition, it was determined that the location where the decrease in speed occurs for the courses placed at 40% and 60% is well beyond the locations where the sensors are placed as well as the location where the first visible defects occur. Therefore, the decrease in the layup speed at the end of these courses is neglected since it does not affect the data acquired during the experiment.

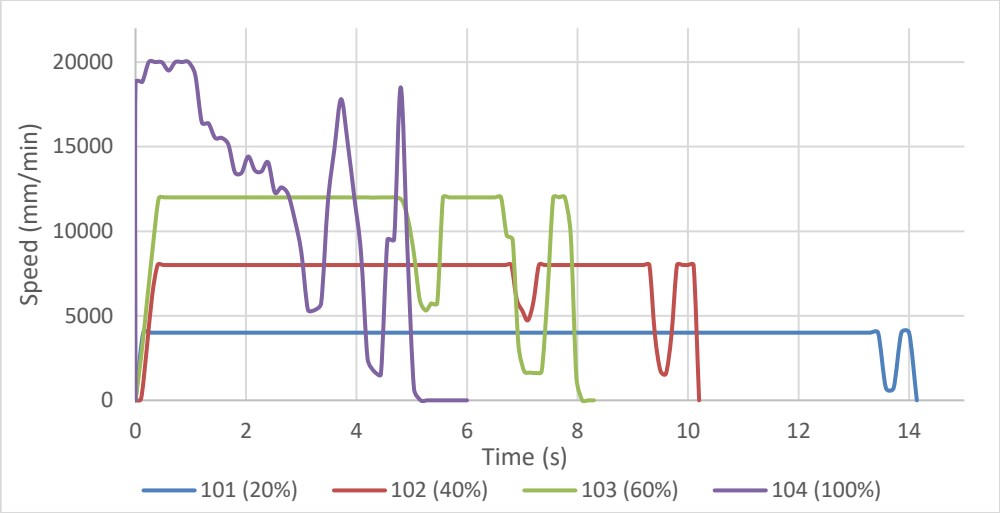

Figure 5.35 Speed profiles for the placed courses

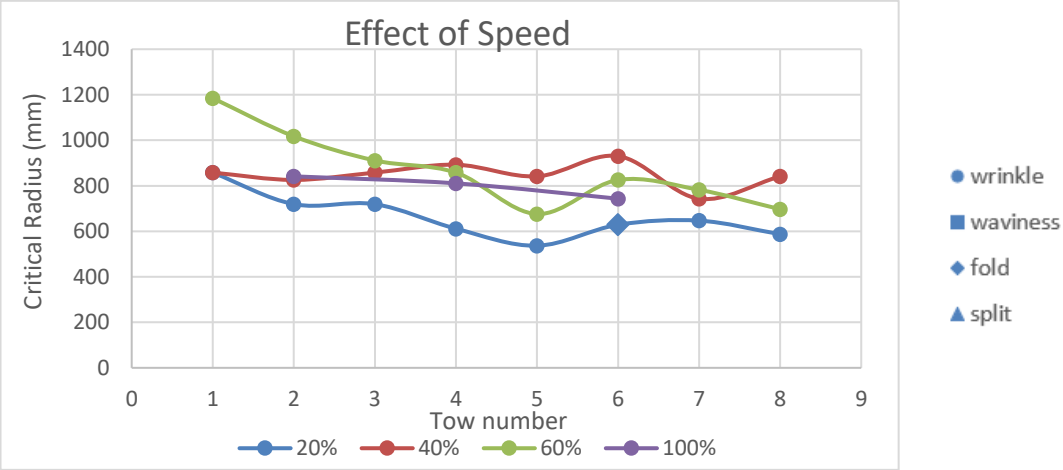

Figure 5.36 Critical radius of curvature for the laid tows during the speed test

After laying the courses, the location and type of the first visible defect along the length of each tow is recorded, and the corresponding critical curvature is determined. The results for the critical radius of curvature for the speed test are shown in Figure 5.36. It can be clearly observed that the course placed at the lowest speed of 20% (equivalent to 4,000 mm/min) has the lowest critical radius, or in other words, this course has achieved more steering without defects compared to the other laid courses. For the course laid at 100%

speed, several data points are missing due the fact that not all the tows are laid properly and some of them did not adhere to the surface.

5.2.8 Temperature Test

The purpose of this set of experiment is to evaluate the effect of the temperature on the quality of the layup. To do so, the compaction force and the layup speed are kept at their baseline values of 445N and 40% while changing the voltage of the heater to 100, 125, 175, and 200V. The process parameters for this test are summarized in Table 5.4 and the placed courses are shown in Figure 5.37. At the lowest heater voltage (100 V), the level of adhesion is not enough to hold the tows in place, and all eight tows within the course detach from the substrate. Using a 125V as heater setting result in a slight improvement in adhesion where the tows stick to the substrate, however, due to steering, it is observed that large scale deformations are prominent, thus resulting in a poor quality (see course 102 Figure 5.37). At voltage settings higher than the baseline value, the quality for courses 103 and 104 is significantly improved compared to the other courses, and no significant folding is observed along the course.

For each of the placed courses, temperature measurements are taken along the length of the path using six thermocouples. In addition, the two pressure sensors are placed at the same location of the first two thermocouples. A typical measurement of the temperature and pressure as function of time for course 103 is shown in Figure 5.38. The thermocouples are connected to channels 1 through 6 reading instantaneous temperature of the substrate in °C, whereas the pressure sensors are connected to channels 7 and 8 reading the compaction in volts which is later converted to kPa through appropriate calibration. During the layup, the temperature of the substrate experiences a sudden increase just before

the tow is fed and compacted on the substrate. When the tow becomes to contact with the substrate, the temperature drops significantly since the incoming tow from the creel is at a lower temperature than the heated substrate. Then the temperature decays slowly to reach back the room temperature once the heat is dissipated through the part and the tool. This behavior is observed in all the measurements acquired by the thermocouples.

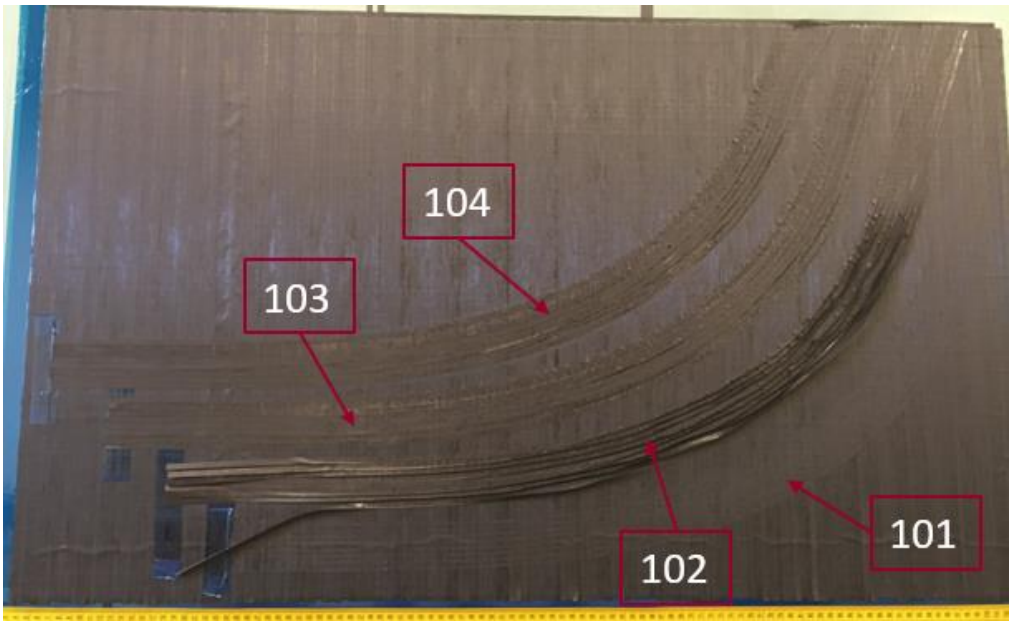

Figure 5.37 Obtained layup for the temperature test

The average of the peak temperatures captured by the thermocouples for each of the laid courses during this experiment are summarized and shown in Figure 5.39 as function of the heater voltage. It can be clearly observed that increasing the heater voltage increases the peak temperature during the layup. At the lowest voltage settings (100 V), it can be observed that the temperature of the substrate is only few degrees above the room temperature which is not enough to achieve a good adhesion for the tows. At 200 V and 40% of the programmed speed (equivalent to 8,000mm/min), the peak temperature reaches on average 96.1°C. It should be noted that this temperature exceeds the recommended limit of the maximum nip point temperature (Table 5.5). Also, at higher temperatures, the

variability in the measured temperature is higher; a higher standard deviation between the thermocouples is obtained for the measured peak temperatures. As shown in Figure 5.40, increasing the temperature of the layup beyond the recommended value only achieved better steering for three out of the eight placed tows compared to the course laid at 175 V. In addition, the type of first visible at lower temperature (125 V) is not only wrinkle, but also fold (tow 4) and missing tow (tows 7 and 8), as well as the obtained critical radius is larger, indicating a lower quality for the layup at lower temperature.

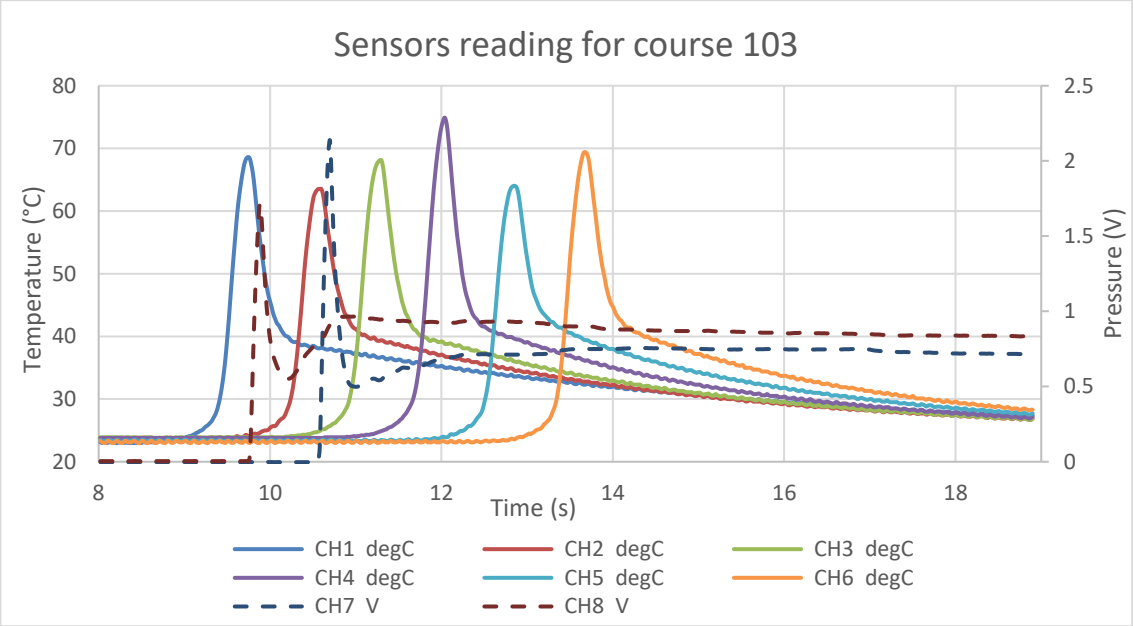

Figure 5.38 Temperature and pressure measurements for course 103 during the temperature test

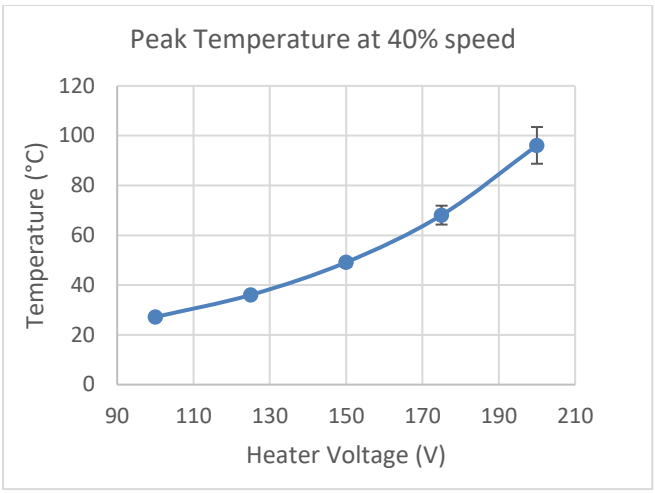

Figure 5.39 Measured peak temperature as function of heater voltage

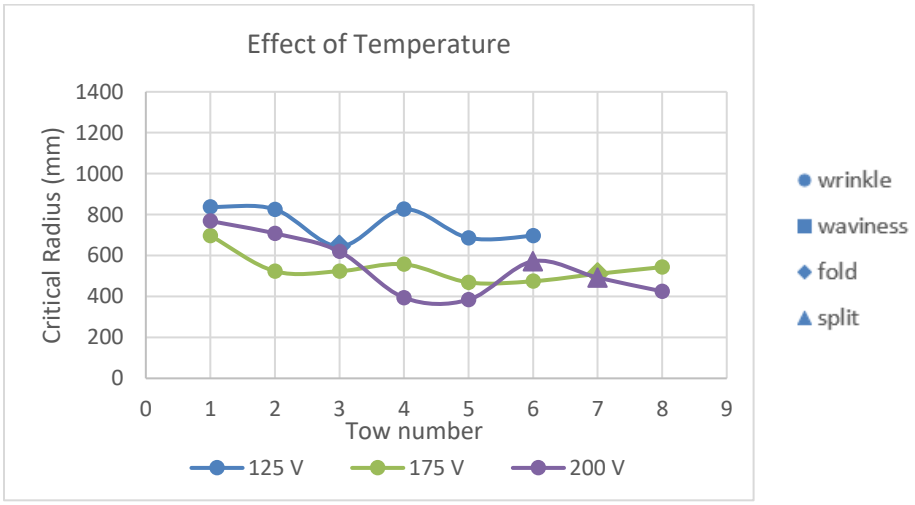

Figure 5.40 Critical radius of curvature for the laid tows during the temperature test

5.2.9 Compaction Test

The purpose of this set of experiment is to evaluate the effect of the compaction on the quality of the layup. To do so, the heater voltage and the layup speed are kept at their baseline values of 150 V and 40% while changing the compaction force to 178, 300, 600, and 750 N. The process parameters for this test are summarized in Table 5.4 and the placed courses are shown in Figure 5.41. By inspecting the quality of the layup, it is observed that

the occurrence of tow folding is delayed by increasing the compaction force. Course 101 with the lowest compaction force observed the most tow folds (Figure 5.42). In addition, more out-of-plane defects such as wrinkles are observed at the lower compaction settings, whereas in-plane waviness is more observed at higher compaction force instead of out-of-plane wrinkles (Figure 5.43) indicating a change in the deformation mechanisms at higher compaction.

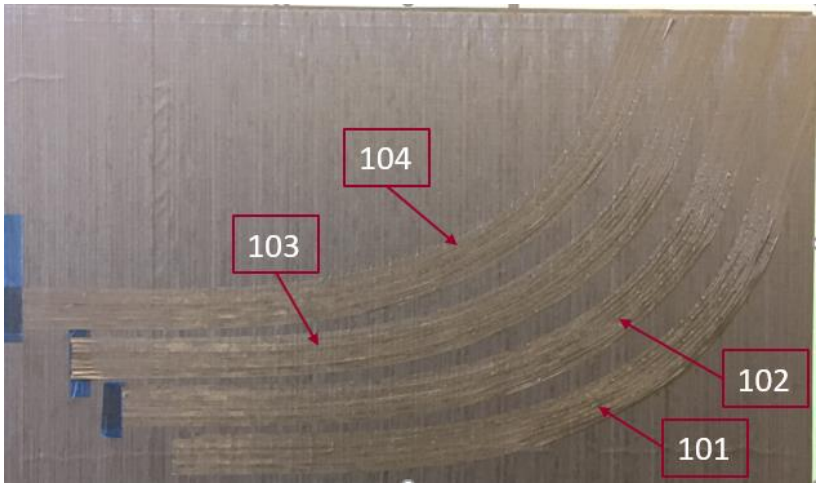

Figure 5.41 Obtained layup for the compaction test

By visually inspecting the first defect along the path, and deducing the corresponding critical radius of curvature, the results for the four courses are shown in Figure 5.44. It can be easily concluded that at higher compaction values, more steering is achieved for all tows for the case of 750 N compaction. It should be noted that the type of the first visible defect changes at higher compaction values from wrinkle to in-plane waviness for the middle tows (4 & 5), and tow splitting rather than folding for the outer tow (tow number 8).

Figure 5.42 Tow folding at low compaction force (course 101, 178 N compaction)

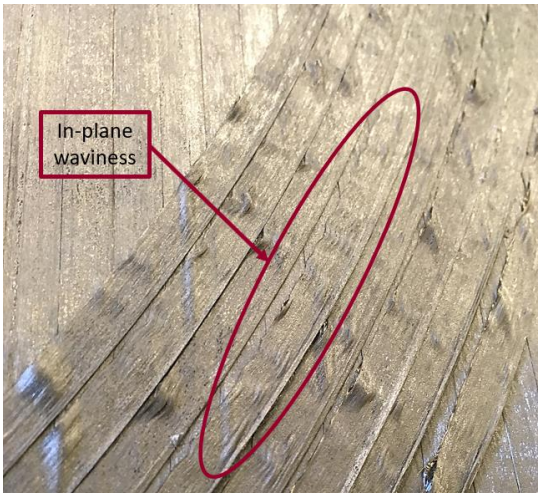

Figure 5.43 In-plane waviness at high compaction force (course 104, 750 N compaction)

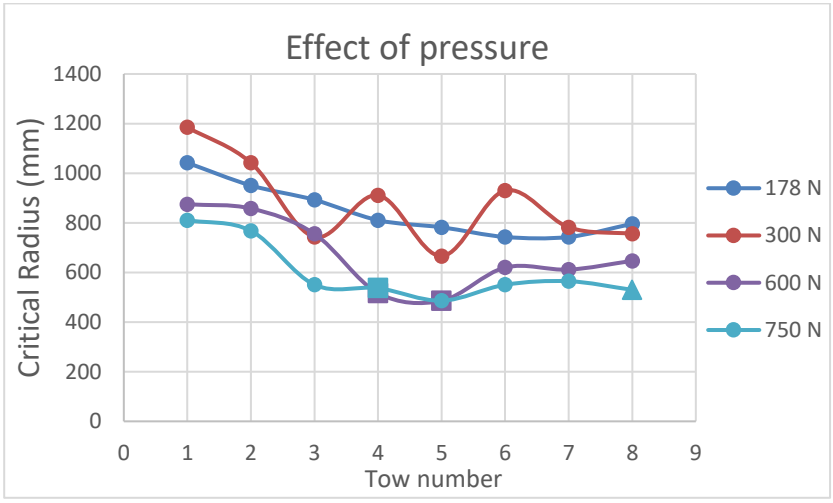

Figure 5.44 Critical radius of curvature for the laid tows during the compaction test

5.2.10 Tow Tension Test

During this test, the effect of the tow tension on the layup quality is evaluated. All other process parameters are kept at their nominal values, whereas the tow tension is changed from 0, 1.5, 5, and 10N. The process parameters and the obtained layup are shown in Table 5.4 and Figure 5.45 respectively. It can be observed that at higher tension the tows experience additional folding compared to lower tow tension setting. No additional

observations are made regarding the influence of the tow tension on the wrinkling occurrence by simply observing the overall layup quality.

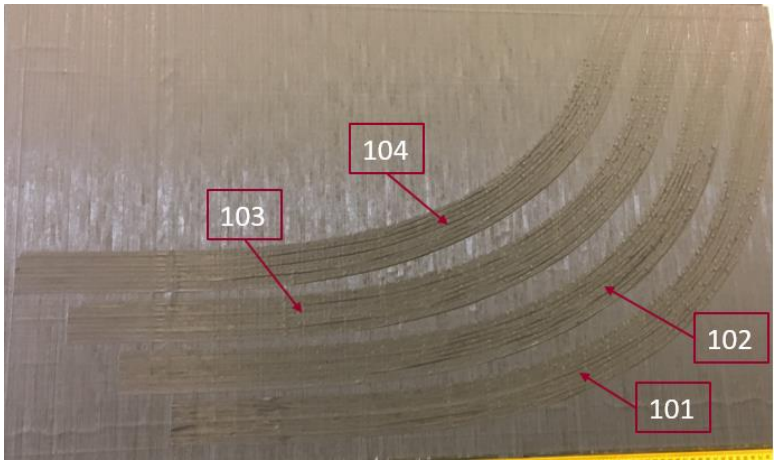

Figure 5.45 Obtained layup for the tow tension test

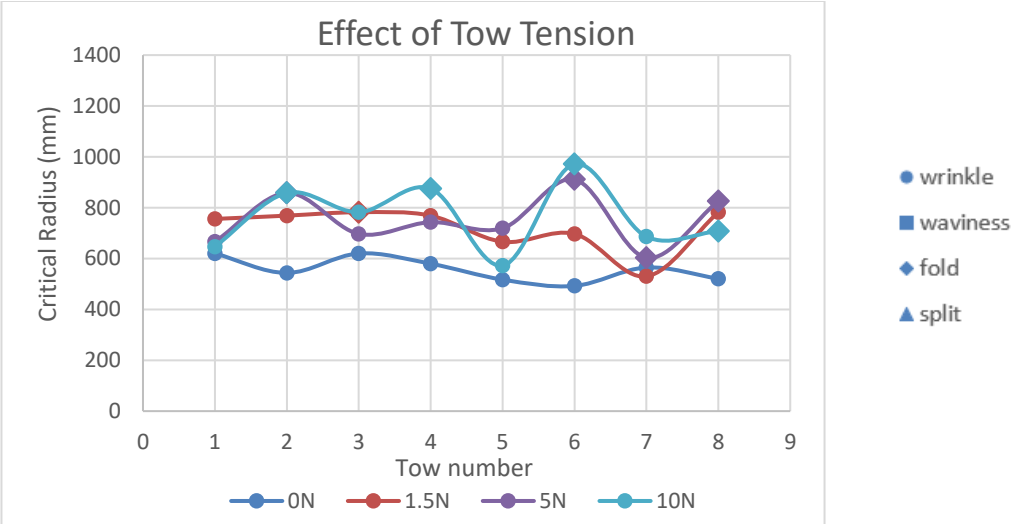

Figure 5.46 Critical radius of curvature for the laid tows during the tow tension test

To get a better understanding of the effect of tow tension on defects occurrence and tow deformations, the first visible defect for each tow within the laid courses are noted, and their corresponding critical radius of curvature is shown in Figure 5.46. It can be observed that the course laid at 0 tension achieved the best steering compared to other courses. Increasing the tow tension did not necessarily improve steering since at higher

tension tow folds starts to occur at earlier locations than wrinkles compared to lower tow tension values.

5.2.11 High Speed, Pressure, and Temperature Test

The purpose of this test is to increase the productivity of the layup by increasing the layup speed while maintaining an acceptable quality. To accomplish that, the compaction force and the heater voltage are also increased from their baseline values. The process parameters used in this experiment are shown in Table 5.4 and the obtained layup is shown in Figure 5.47. By increasing the compaction force and the layup temperature simultaneously, a better layup quality is obtained with fewer out-of-plane defects (wrinkles and folds). The level of adhesion achieved at higher temperature and pressure is significantly improved resulting in an increase in the occurrence of the newly described tow deformation mechanism: through-thickness fiber splitting (Figure 5.33).

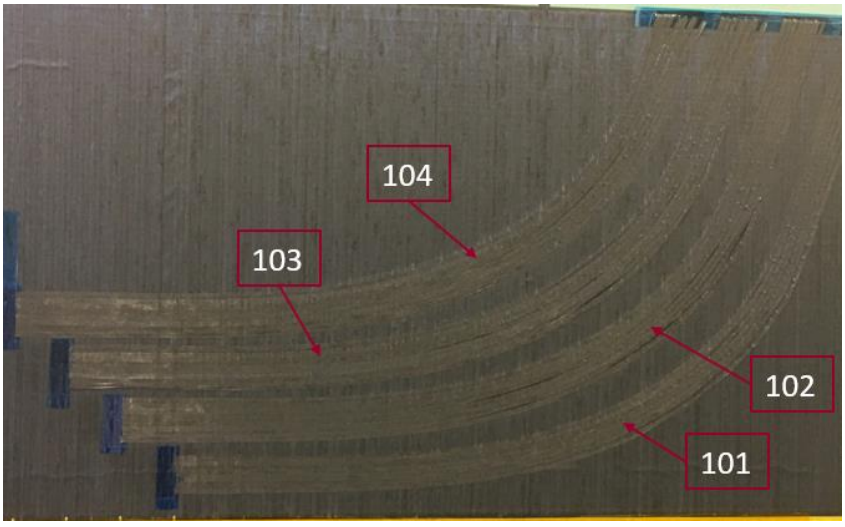

Figure 5.47 Obtained layup for the high speed, pressure, and temperature test

The critical radii of curvature corresponding the first visible defect for the laid courses during this experiment are shown in Figure 5.46. It can be observed that the laid courses have on average very similar values for the critical steering radius. It should also

be noted that during this test a critical radius of 318 mm is achieved for tow number 5 for course 102 which is the lowest achieved steering radius for all performed experiments within this section.

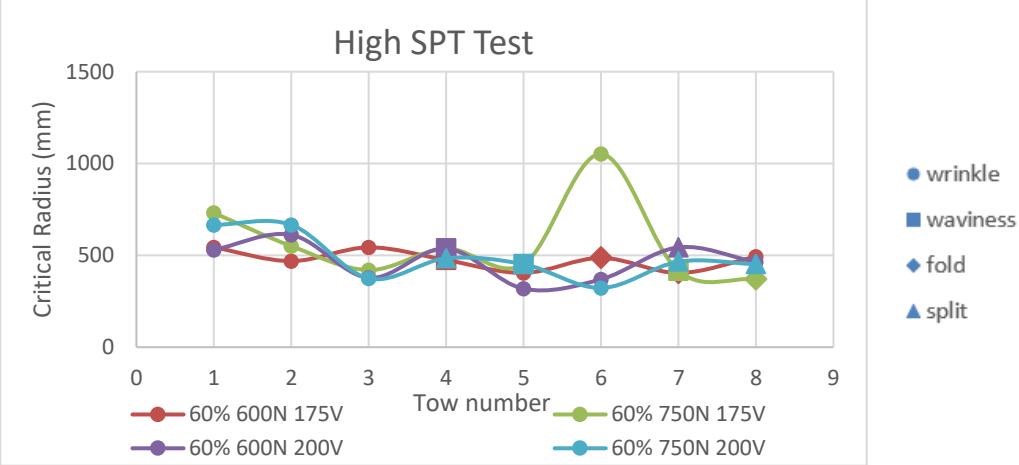

Figure 5.48 Critical radius of curvature for the laid tows during the tow tension test

5.2.12 Linear Tests

In order to gather additional data regarding speed, temperature, and compaction, further linear AFP layups are performed, mainly to validate the repeatability of the measured data during the steering experiments, and to check for any discrepancies if any exist between steering and linear tests. In a similar data acquisition process, two pressure sensors are placed at the same location with other two thermocouples along the length of the path. Additional four thermocouples are placed along the path to capture more temperature data. The setup for the data acquisition for the linear tests is shown in Figure 5.49. A total of 19 trials is performed with different process parameters combinations as summarized in Table 5.6. Regarding the layup speed, it is observed that the actual layup speed is the same as the set one even for the 100% full speed (20,000 mm/min), and hence no additional measurements are taken. This is due to the fact that linear paths are easier to

manufacture from a kinematics standpoint since they require fewer machine axes interaction. The collected data from these tests are summarized and presented in the next section along with the data collected during the steering tests.

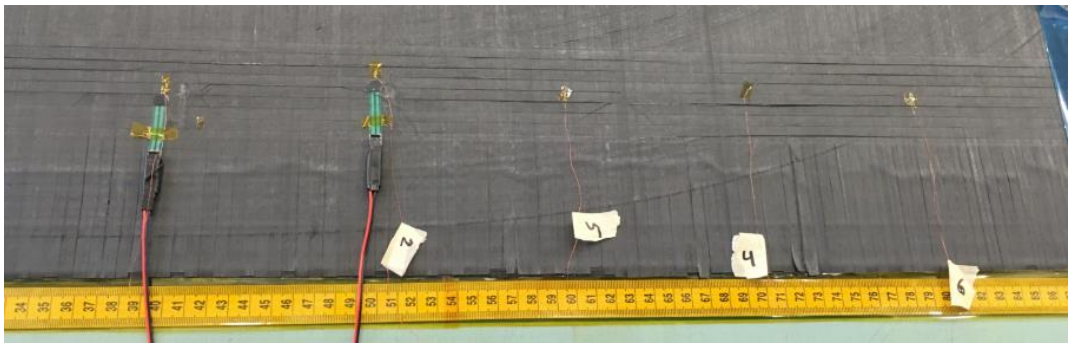

Figure 5.49 Sensors placed along the length of a course oriented at 0°

Table 5.6 Process parameters used in the linear tests

Test #	**S (%)**	**P (N)**	**T (V)**	**t (N)**
1	20	445	150	3
2	40	445	150	3
3	60	445	150	3
4	100	445	150	3
5	20	445	175	3
6	40	445	175	3
7	60	445	175	3
8	100	445	175	3
9	40	445	200	3
10	60	445	200	3
11	100	445	200	3
12	40	178	150	3
13	40	300	150	3
14	40	600	150	3
15	40	750	150	3
16	60	178	150	3
17	60	300	150	3
18	60	600	150	3
19	60	750	150	3

5.2.13 Interaction of Process Parameters

The interaction of the main process parameters affecting the measured temperature of the layup and the measured pressure between the tow and the substrate are investigated in this section. The data collected throughout the steering and linear tests are summarized and presented here. Starting with the temperature, the average of the peak temperature measured by the six thermocouples during each test is calculated along with the corresponding standard deviation (presented in error bars format). The results for the temperature as function of the layup speed and heater voltage are show in Figure 5.50 for both linear (L) and steered (S) tests. Comparing the results between the linear and steered tests, and by taking into consideration the sensitivity of the measuring system (± 5℃), it can be concluded that the heating is consistent for both cases showing similar trends as function of speed and heater voltage. In addition, it can be observed that higher heater voltage and lower layup speed result in higher substrate temperature. At lower speeds and high voltage (20% 175V and 40% 200V), the measured temperature exceeds the maximum recommended temperature by the material supplier (93.3°C see Table 5.5), and hence these combinations of process parameters should be avoided in future manufacturing activities even though the obtained quality for these layup is acceptable. In addition, at higher voltage options and lower layup speed, the variation in the measured temperature is larger. This can be related to thermocouples used during the experiment which may have a lower accuracy at higher layup temperatures.

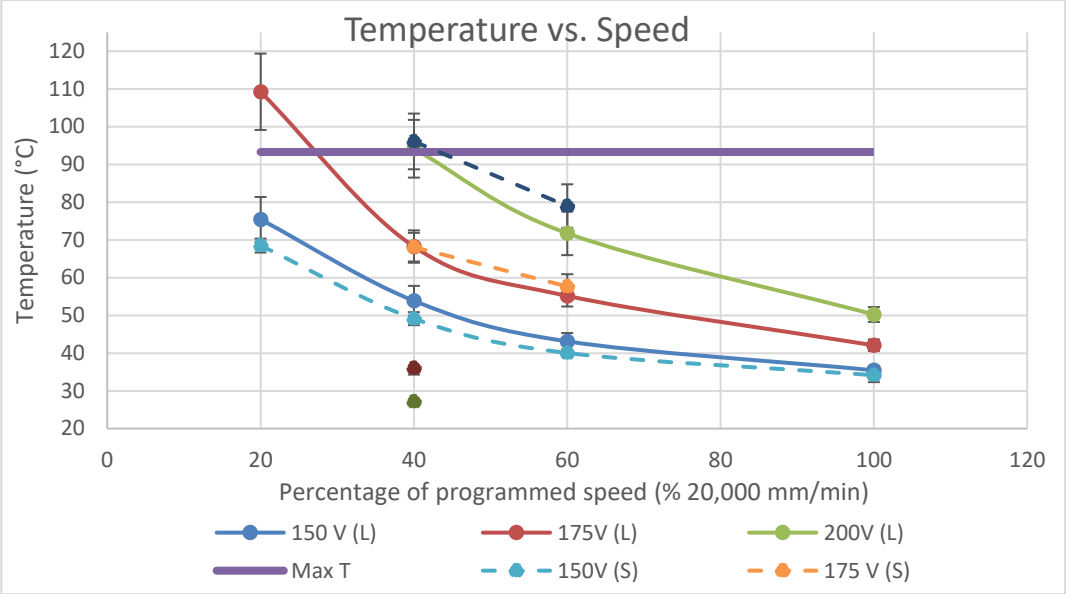

Figure 5.50 Average of measured peak temperatures as function of layup speed and heater voltage for both linear and steered tests

Regarding the interaction of pressure with the other process parameters, the measured voltage from each sensor is converted to the corresponding kPa value through appropriate calibration. In a similar way, the average of the peaks captured by the 2 sensors and the corresponding standard deviation are calculated and presented in the following Figure 5.51 and Figure 5.52. Starting with the results presented in Figure 5.51, the average of the measured pressure is shown as function of the roller compaction and the layup speed for both linear and steered tests. In general, increasing the compaction force increases the measure pressure between the laid tow and substrate. In addition, increasing the layup speed decreases the pressure for the same compaction settings. This may be due to the dynamic effect during the layup. Finally, a slight increase in the measured pressure is observed for all trials at the nominal compaction settings of 445N that does not fit the trend between pressure and compaction. A reasonable explanation for this phenomenon is yet to be determined.

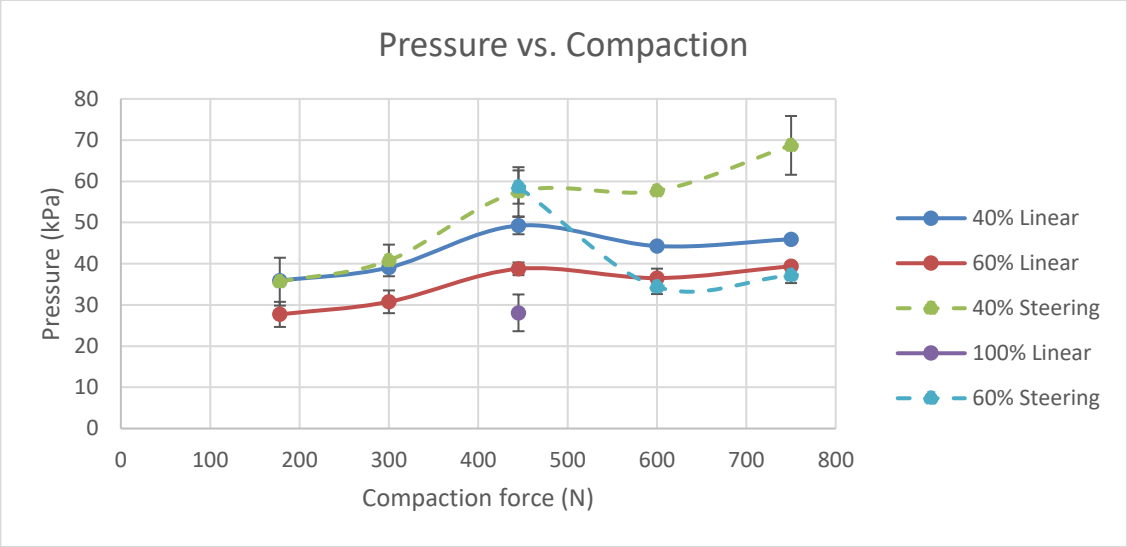

Figure 5.51 Average of measured pressure as function of roller compaction and layup speed for both linear and steered tests

Lastly, the effect of the heater voltage and layup speed on the measured pressure at a constant compaction force of 445 N is shown in Figure 5.52 for the linear tests. Similar to the previous conclusion, it is clearly observed that increasing the layup speed will results in a reduction in the measured pressure by the sensors even for the same compaction settings. In addition, it can be determined that the heater voltage (or the temperature of the substrate) does not affect the pressure readings; for the same layup speed and compaction force, the measured pressure for the three different heater voltage are very close and fall within the range of the standard deviation.

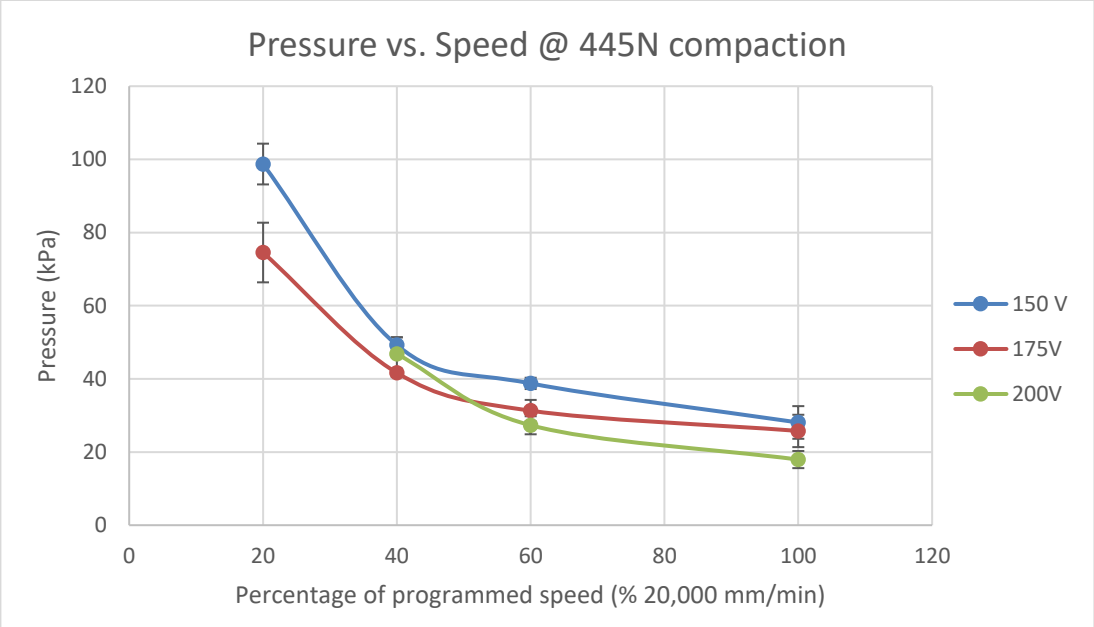

Figure 5.52 Average of measured pressure as function of speed and heater voltage for the linear tests at constant compaction force of 445N

5.3 STEERING EXPERIMENTS ON CYLINDRICAL SHELL

In this section, steering tests are carried over a 1220 mm (48 inches) diameter cylindrical mandrel. Multiple constant curvature arcs and spiral curves are placed over the cylindrical tool while varying the process parameters. The layup speed and temperature are captured during the layup. A profilometry scan of the placed courses is acquired after the layup. The obtained black and white images are used to assess the quality of the placed courses by applying image processing techniques detecting in-plane and out-of-plane tow deformations. Based on the quantity of detected defects within the course, recommendation regarding a set of process parameters is provided.

5.3.1 Experimental Design

The approach adopted for this experimental investigation is to utilize the previously manufactured curved paths on the flat surface and to replicate them on a cylindrical surface.

These paths consist of two types of curves: constant curvature arcs (at 1270, 635, and 318 mm) and linearly increasing curvature spiral curves (the same benchmark path described in 5.2.2). In order to design these paths on the cylindrical surface, the differential geometry steps described earlier in Chapter 3 are followed. First, an arc-length parametric definition of the cylinder's surface is determined as function of the circumference c, the cylinder's length z, and the radius r ($r = 609.6\ mm$):

$$cylinder(c,z) = \left\{r\ \cos\frac{c}{r}, r\ \sin\frac{c}{r}, z\right\},$$
$$0 \le c \le 2\pi r, \tag{5.8}$$
$$z_{min} \le z \le z_{max}$$

To obtain the spiral curve on the cylinder's surface, the 2D parametrization $\{x(s), y(s)\}$ of the curved path (equations (5.5) and (5.6)) is used with proper translation $\{t_1, t_2\}$ so that $\{x(s) + t_1, y(s) + t_2\} \in \Omega$ the rectangular domain of definition of the flattened cylinder bounded by the minimum and maximum of the circumference c and the cylinder's length z (see Figure 5.53). Then, the spiral path on the cylinder's surface can be obtained using:

$$Spiral3D(s) = cylinder(x(s) + t_1, y(s) + t_2)\,. \tag{5.9}$$

A similar approach is used for the constant curvature arcs with their corresponding 2D parametrization and translations respectively. The translated paths bounded by the domain of definition of the flattened cylinder and their corresponding transformed 3D paths on the cylinder's surface are visualized in Figure 5.53 and Figure 5.54 respectively.

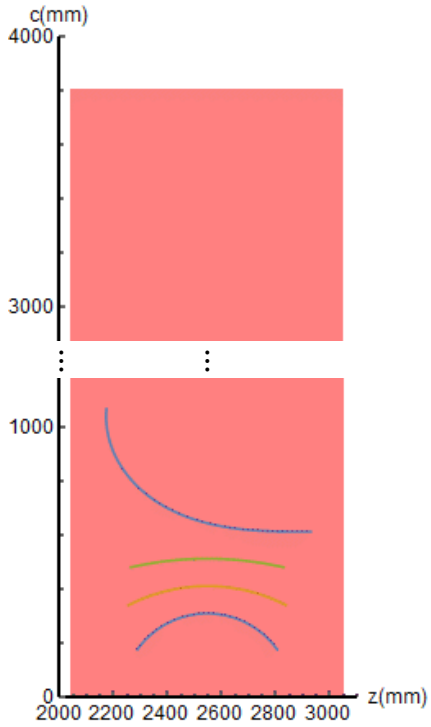

Figure 5.53 Steered paths on flattened cylinder

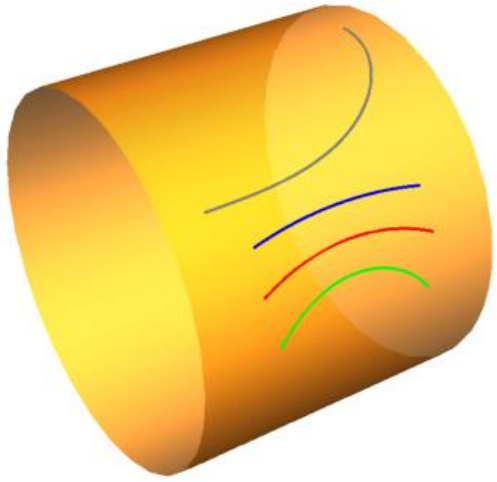

Figure 5.54 Steered paths on cylinder

Using the above transformation from the 2D domain to the 3D cylinder's surface, the geodesic curvature of the paths on the cylinder coincides with the 2D curvature of the paths. However, the total curvature of the paths is different due to the contribution of the normal curvature of the cylinder.

5.3.2 Programming and Manufacturing

The generated 3D curved paths in the design section are sampled at 3 mm spacing along the length s and exported to CATIA as a cloud of points. The curves are then reconstructed and projected on the tool surface (even though the sampled points coincide on the surface, the reconstructed 3D curve may not). A total of 9 courses are programmed for each type of curve. The courses are spaced by applying rotations and mirroring options in the CAD software so that the cylinder's surface is fully covered without overlapping between the courses. The designed courses are visualized in Figure 5.55 and Figure 5.56.

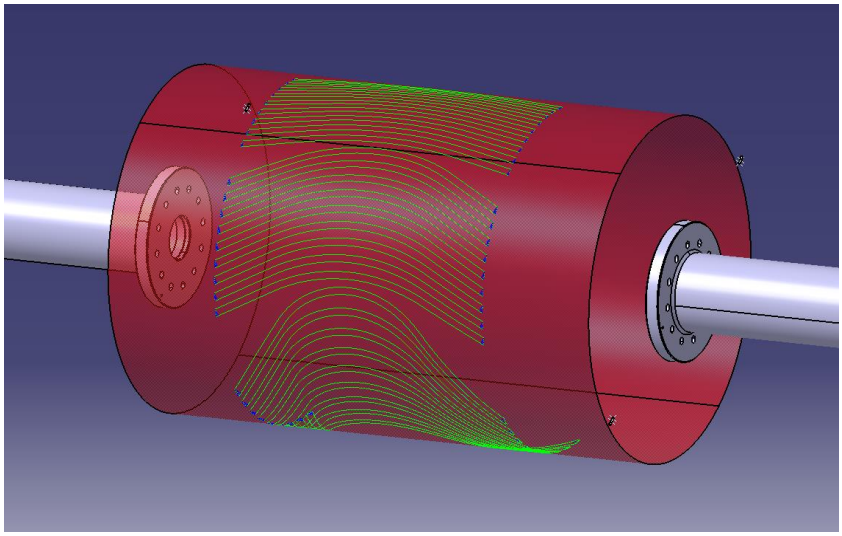

Figure 5.55 Programmed constant curvature arcs on cylindrical mandrel

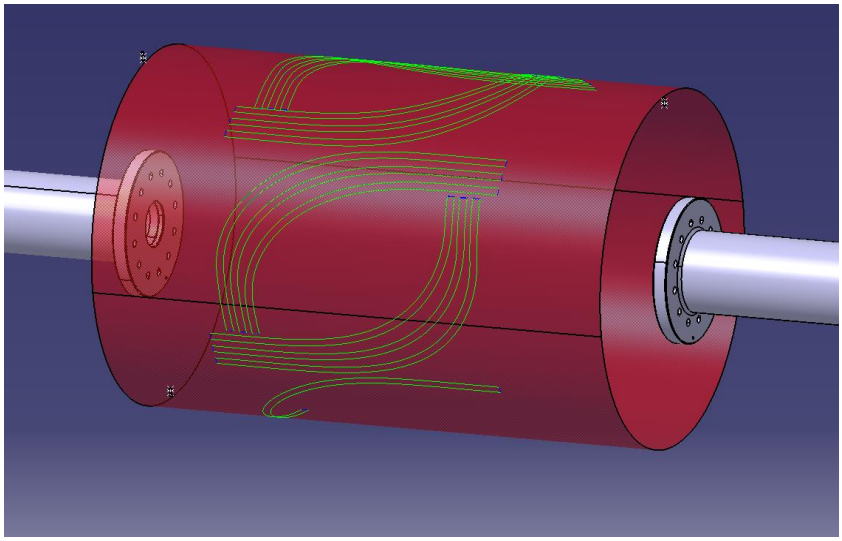

Figure 5.56 Programmed spiral curves on cylindrical mandrel

Instead of laying the steered paths directly on the cylinder's metallic surface, two 90° hoop plies are laid first as a substrate. If these plies were to be placed at exactly 90°, the courses have to be cut along a certain line along the cylinder's length. Instead, a small angle deviation is allowed so that a single course can wrap the entire cylinder's surface. Using geometrical relationships, the deviated angle is found to be function of the course

width, the interband offset (offset distance between adjacent courses) and the mandrel's circumference:

$$\alpha = tan^{-1}\left(\frac{course\ width + interband\ offset}{mandrel\ circumferance}\right). \quad (5.10)$$

Using the above relationship and the AFP setting, the calculated substrate direction is found to be ±89.224°. The two substrate plies are added in opposite directions with an adequate stagger shift to remove any gaps that might occur. The steering experiments are performed as a third ply.

5.3.3 Investigated Process Parameters

The main process parameters investigated in this experiment are the layup speed, the compaction pressure, and the layup temperature. Each of these parameters is varied within a specified range and the effect of their interaction is observed on the layup quality. For the layup speed, five different levels are investigated:10, 20, 40, 60, and 100 % of the programmed speed of 25,000 mm/min. Concerning the layup temperature, a 6 kW xenon light heater HUMM3 heater attached to the AFP head is used where voltage, frequency and pulse duration of the light source can be changed to control the layup temperature. For the purpose of this experiment, the frequency and pulse duration are kept constant at 60 Hz and 2000 μs respectively, and only the voltage is changed at the following levels: 150, 170, 180, and 190 Volts (V). The corresponding power of the heater using these settings can be extracted from Figure 5.27. The compaction force of the roller is also varied at the following levels: 300, 445, 600, and 750 N. These parameters are summarized in Table 5.8. The steering experiments are carried individually for each course and having different combination of parameters. The course number, its description, and the process parameter

combination (% of speed, compaction force, heater voltage) used to manufacture are summarized in Table 5.7.

Table 5.7 Course description and corresponding process parameters

Course#	Radius (mm)	S (%)	P(N)	T(V)
130	1270	30	600	150
131	1270	50	445	170
132	1270	100	445	150
133	1270	50	445	170
134	1270	100	300	170
135	1270	100	600	170
136	1270	20	600	170
137	1270	20	750	170
138	1270	20	445	170
139	635	30	600	170
140	635	20	600	170
141	635	10	600	170
142	635	10	600	150
143	635	10	750	170
144	635	20	750	170
145	635	50	750	190
146	635	30	750	180
147	635	100	750	190
148	318	10	600	170
149	318	10	445	170
150	318	10	300	170
151	318	10	177.9	170
152	318	50	445	180
153	318	50	445	150
154	318	100	445	180
155	318	6	445	150
117	$1/(a\ s)$	10	445	170
118	$1/(a\ s)$	100	445	170
119	$1/(a\ s)$	100	445	150
120	$1/(a\ s)$	100	300	170
121	$1/(a\ s)$	100	300	170
122	$1/(a\ s)$	100	177.9	170
124	$1/(a\ s)$	100	177.9	150
125	$1/(a\ s)$	100	177.9	190

For process monitoring during the layup, a recording of the layup speed for each course is captured to note any discrepancy between the actual speed of the layup and the

programmed/set one. As for the temperature, four thermocouples are placed along the length of the paths to record the change in temperature over time. No instrumentation is used to monitor the roller compaction, it was solely set in the machine parameters.

Table 5.8 The parameters and levels considered in the steering experiments on the cylinder

Parameters	**Levels**				
Compaction force (N)	178	300	445	600	750
Heater voltage (V)	150	170	180	190	
Feed rate (%)	10	20	30	50	100

5.3.4 Feedrate Monitoring Results

Usually during AFP experimentation, it is desired to have constant feedrate at the programmed level throughout the deposition of the course. However, in the case of steering (on flat or cylindrical mandrel) it gets increasingly difficult to maintain a constant feedrate especially at the high-speed settings. This occurs due to the increased complexity in the motion of the AFP head, where more axes are needed to achieve the required paths, which means the motion is less constrained and hence, the feedrate is bound by the speed and acceleration thresholds of the slowest axis (i.e. the axis having the smallest motor). In the case of 0° motion, only the X-axis is involved and therefore the feedrate can comfortably reach up to 25000 mm/min. In the case of steering on the cylindrical mandrel, almost all the axes are involved in the motion. Consequently, during these experiments, the feedrate is not at a constant level, and a continuous monitoring is required. The actual feedrate from the AFP console is recorded, and data points are extracted at 0.1 s resolution. The results are then plotted with respect to arc-length rather than time. An example of the recorded feedrate for three different configurations of the 1270 mm radius courses (at 100%, 50%,

and 20%) is shown in Figure 5.57. It can be observed that the target/programmed feedrate is not achieved at any location within the course due to kinematics restrictions. Instead, significant fluctuations in the feedrate are observed at higher percentage of the programmed speed, which would hence cause fluctuations in the nip point temperature. At low percentage of the programmed speed, the speed profile of the layup is nearly constant resulting in more consistent layup temperature.

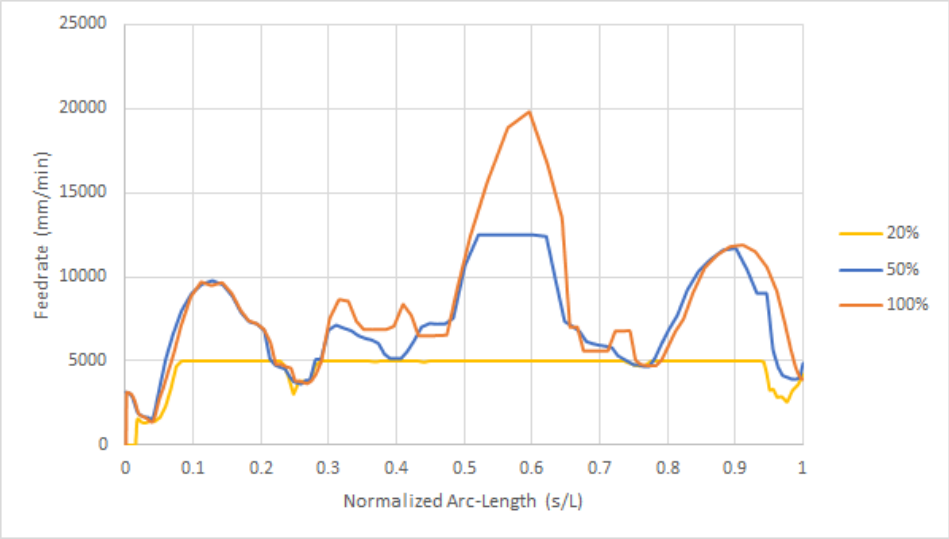

Figure 5.57 Recorded feedrate at 10% and 100% for courses 150 and 154 respectively

5.3.5 Temperature Monitoring Results

For each of the placed courses, temperature measurements are taken along the length of the path using four thermocouples. A typical measurement of the temperature as function of time is shown in Figure 5.58 for course 137 (20% speed, 750 N compaction, 170V heater voltage). During the layup, the temperature of the substrate experiences a sudden increase just before the tow is fed and compacted on the substrate. When the tow contacts the substrate, the temperature drops significantly since the incoming tow from the creel is at a lower temperature than the heated substrate. Then the temperature decays

slowly to reach back the room temperature once the heat is dissipated through the part and the tool. This behavior is observed in all the measurements acquired by the thermocouples.

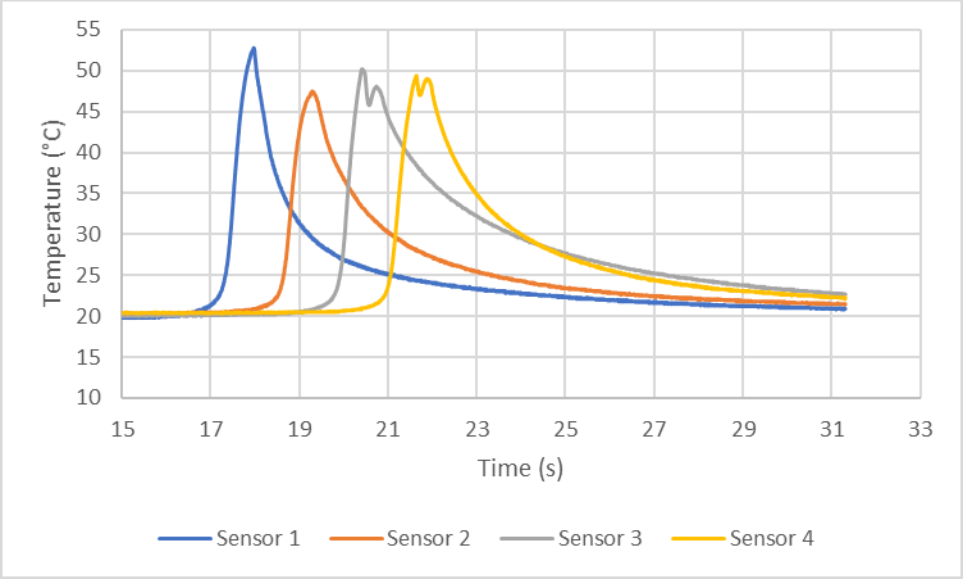

Figure 5.58 Temperature readings from the thermocouples for course 137

Naturally, there exists a strong dependency between temperature and feed-rate, where at the same power settings the temperature can vary greatly depending on the feedrate used. To obtain consistent results along the placed courses, it is desirable to have a constant feedrate and therefore a constant nip point temperature. For the results shown in Figure 5.58 where course 137 is laid at low speed settings (20 % speed), the peak temperatures captured by the thermocouples fall within the same range. Usually, this is not the case where the layup speed fluctuates. Hence, capturing the temperature at only four locations along the length of the path is not enough. Instead, these measurements are used as an indicator of the average temperature.

To solve this problem, a series of measurements are performed on courses along the 0° direction, where the speed is varied between 1500 mm/min and 25000 mm/min, at three power levels and three compaction levels. This results in a series of temperature

readings from which a relationship between the heater voltage, layup speed, and temperature can be extracted. This relationship can then be used to predict the nip point temperature for variable courses with variable feedrate. In addition, it is observed that different levels of compaction have a minimal effect on the variation in the measured temperature (2-3 ℃) hence the average of the three measurements is taken. The results for the average measured temperature as function of the layup speed and heater voltage is shown in Figure 5.59. It can be clearly observed that the relationship between temperature and feedrate is nonlinear and there is a drastic decrease in the substrate temperature as the layup speed is increased.

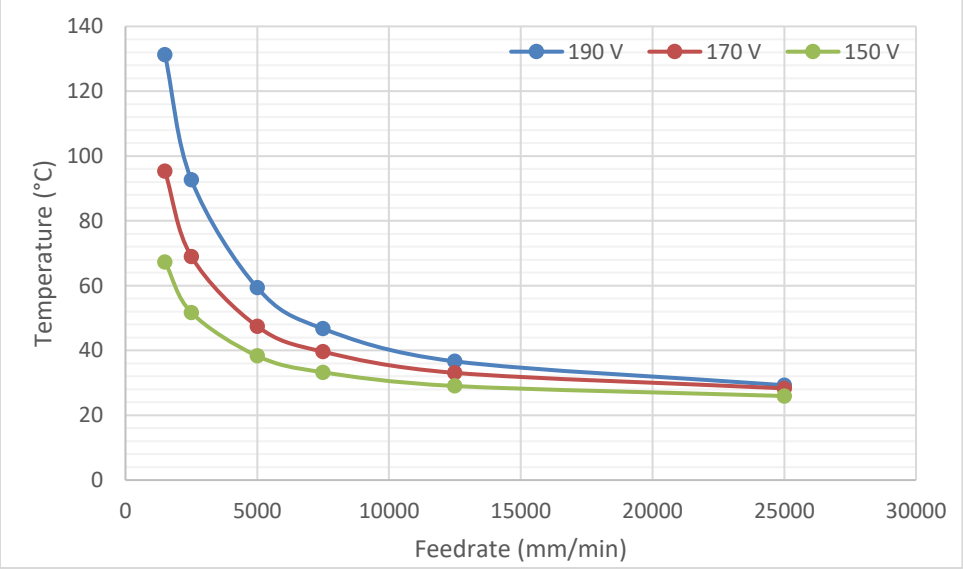

Figure 5.59 Measured temperature as function of the feedrate

5.3.6 Quality Assessment

To assess the effects of the parameters and the quality of the process profilometry scans of the layup are captured using the ACSIS system developed by IMT (Figure 5.60). Several of the previous work done at the McNair center have dealt with inspection using the ACSIS system and the identification of novel ways to extract size and shape

characteristics from AFP defect scans, reader can refer to the following references [62–64] In addition, regular photographs of defects as well as photographs through magnifying glass are also captured. An example of these defects is shown in Figure 5.61 and Figure 5.62.

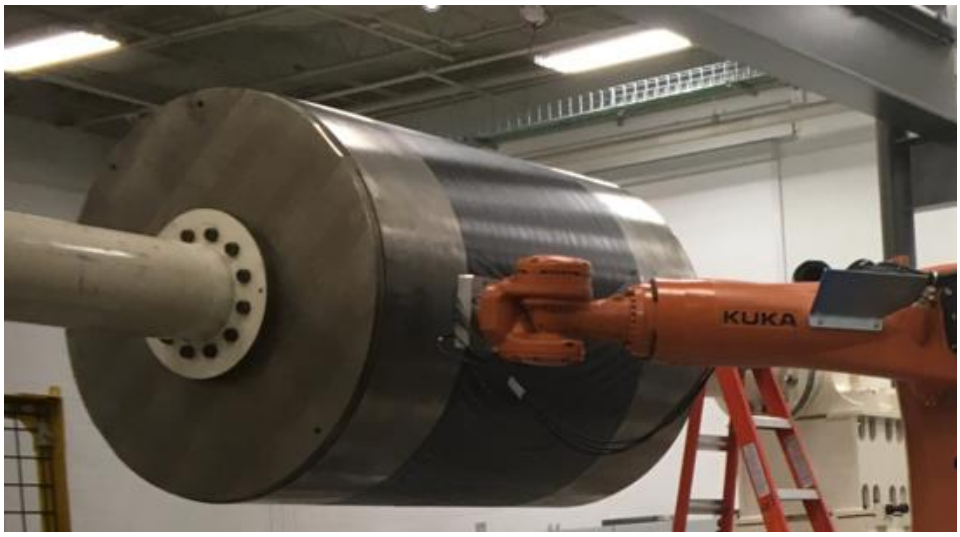

Figure 5.60 Profilometry scanning of steered layup using ACSIS system

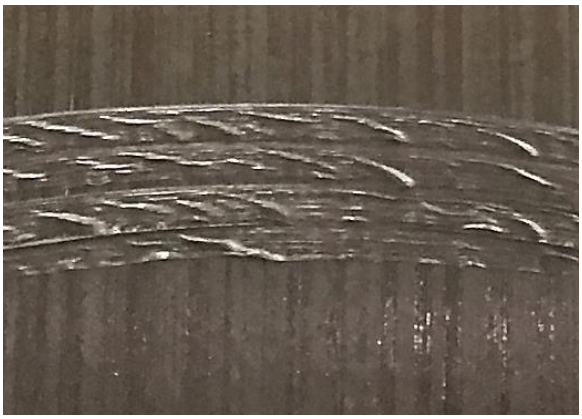

Figure 5.61 Sheared tows

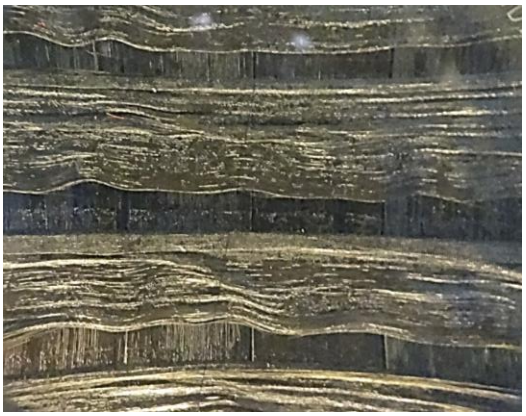

Figure 5.62 Fiber waviness

The linear profilometry scans are visualized in black and white images. An image is generated for each of the 4 profilometers mounted on the robotic arms. These images are later stitched together to reconstruct the surface of the layup. The stitched scans for the placed courses are shown in Figure 5.63 through Figure 5.65 and Figure 5.68. It should be

noted that the linear scans compress the images in length direction by a factor of 3.5. This explains why the linear section of the courses steered at higher curvature are seen with much smaller width compared to the center portion of the course.

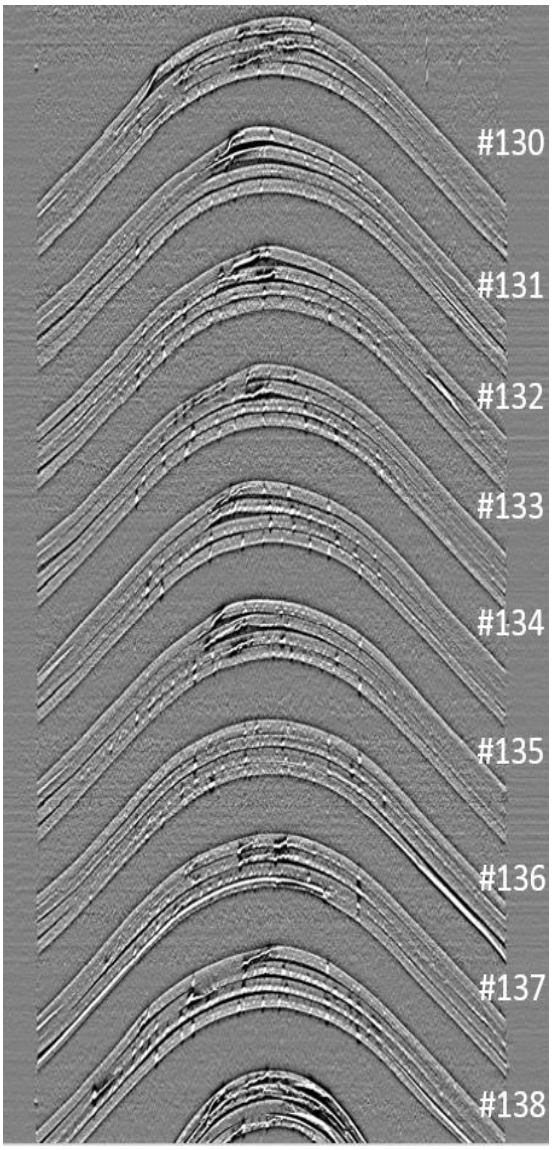

Figure 5.63 Stitched scans for R50

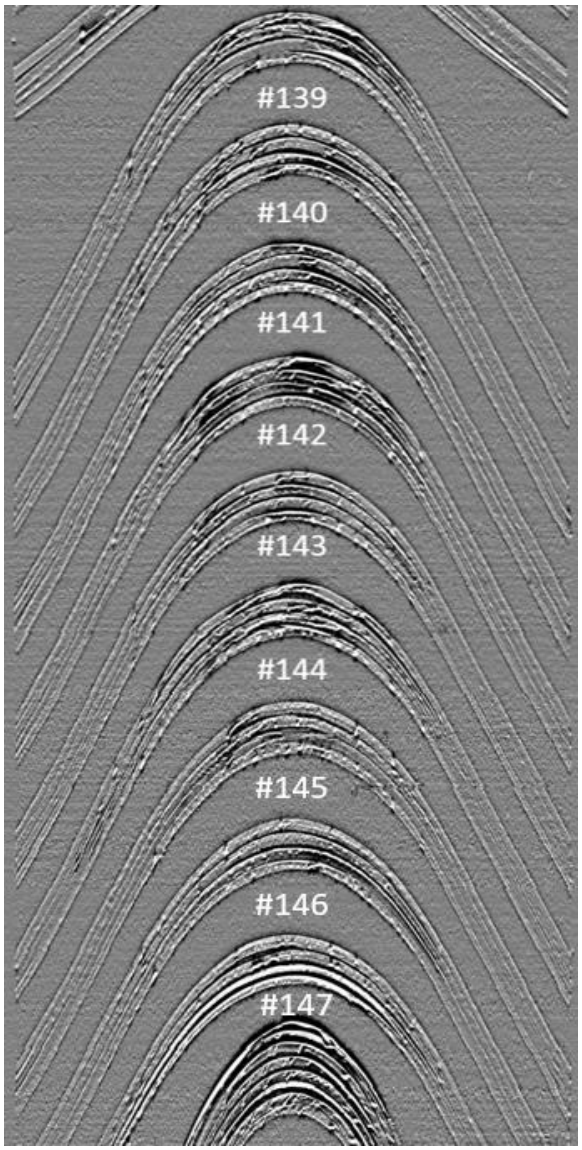

Figure 5.64 Stitched scans for R25

By observing the scanned images of the layup, it can be concluded that the courses steered at 1270 mm radius have the smallest quantity of defects, whereas courses steered at higher curvature experienced severe defects. The type of defects observed during this

experiment ranges from in-plane waviness, bunching, and gaps between tows, to out-of-plane deformations such as wrinkles, folds and sheared tows.

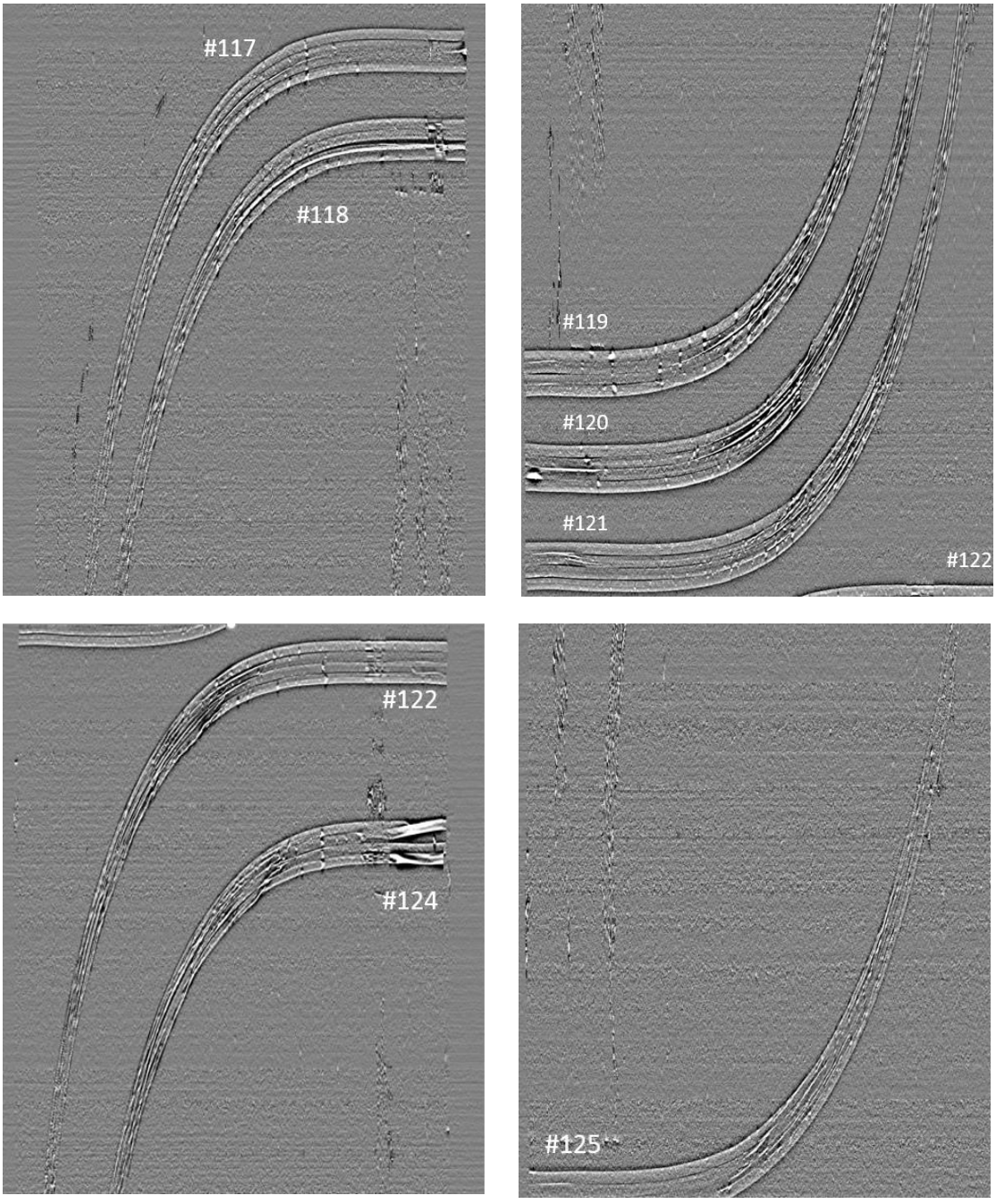

Figure 5.65 Stitched scans for the spiral courses

5.3.7 Image Processing and Defect Detection

In order to quantify the defects obtained during the layup and to assess the influence of the process parameters, the stitched black and white images of the layup are analyzed. A simple high-low filter is used to capture the in-plane and the out-of-plane deformations. Out-of-plane deformation usually colored in white shades in the scanned images are detected and highlighted in orange, whereas the in-plane deformations are usually colored in darker shades and highlighted in green. The processed image for the placed courses are shown in Figure 5.66, Figure 5.67, Figure 5.69 and Figure 5.70. It can be observed that not only defects due to steering are captured, but also gaps, overlaps, folds, and twists in the linear portions of the courses are depicted as well.

In order to extract the defects along the length of the placed courses, several segments perpendicular to the centerline of each course are taken along the length, and their intersection with in-plane (tow displacement) and out-of-plane defects is calculated as a fraction of the course width. To assess the influence of the process parameters on the steering induced defects, only the curved portions of the steered paths are considered for analysis. By summing the defects fraction over the curved portion of the path, a fraction of total area where defects occurred can be calculated. A summary of the obtained results for the percentage of defect within the steered portion of the courses is shown in Table 5.9.

It can be observed that courses 136, 145, 155 and 125 have the lowest percent of total defects for the 1270 mm, 635 mm, 318mm, and spiral courses. Relating the quality to the process parameters, it can be determined that low speed, intermediate/high compaction, and high voltage resulted in the best layup quality for the steered paths. Future work in this regard should focus on the correlation between the instantaneous measure of defects and

the speed, temperature, compaction, and curvature. By doing so, a better ranking of the process parameters can be obtained.

Table 5.9 Areal percentage of defects for the steered portion of the constant curvature arcs and the spiral curves

Course	Radius (mm)	Out-of-plane (%)	In-plane (%)	Total (%)
130	1270	6.4503	7.512726	13.96303
131	1270	3.693975	12.67345	16.36742
132	1270	5.950793	10.79281	16.74361
133	1270	5.258487	6.133148	11.39163
134	1270	4.993494	11.16412	16.15761
135	1270	5.189613	10.11839	15.30801
136	1270	5.365953	4.593783	9.959736
137	1270	10.10426	8.577742	18.68201
138	1270	7.449821	10.23219	17.68201
139	635	9.855483	14.33028	24.18576
140	635	10.35913	12.34439	22.70353
141	635	10.56208	11.28042	21.8425
142	635	8.716623	18.73904	27.45567
143	635	10.41867	9.731803	20.15047
144	635	12.1896	16.3805	28.5701
145	635	8.740874	7.27481	16.01568
146	635	8.202171	9.490939	17.69311
147	635	12.94638	20.80297	33.82284
148	318	10.20567	12.55277	22.75844
149	318	10.55127	13.02424	23.57552
150	318	12.67843	11.56185	24.24028
151	318	10.35486	8.111133	18.46599
152	318	13.47447	7.601208	21.07568
153	318	14.76475	11.78584	26.55059
154	318	8.85086	10.2141	19.06496
155	318	6.4503	7.512726	13.96303
117	$1/(a\ s)$	5.090405	3.116463	8.315881
118	$1/(a\ s)$	8.23804	8.322541	16.56058
119	$1/(a\ s)$	8.530569	4.622007	13.28132
120	$1/(a\ s)$	9.548965	6.425223	15.98114
121	$1/(a\ s)$	6.389142	4.804556	11.1937
122	$1/(a\ s)$	7.633073	5.563172	13.27807
124	$1/(a\ s)$	9.666125	7.172288	16.84165
125	$1/(a\ s)$	4.015428	1.399382	5.41481

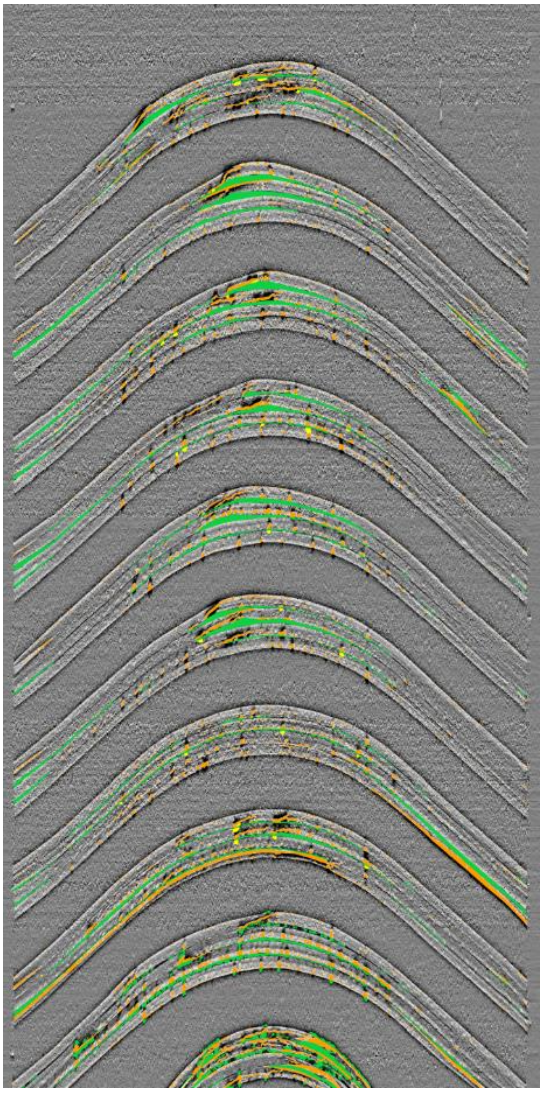

Figure 5.66 Defect detection for the processed scan of the R50 courses

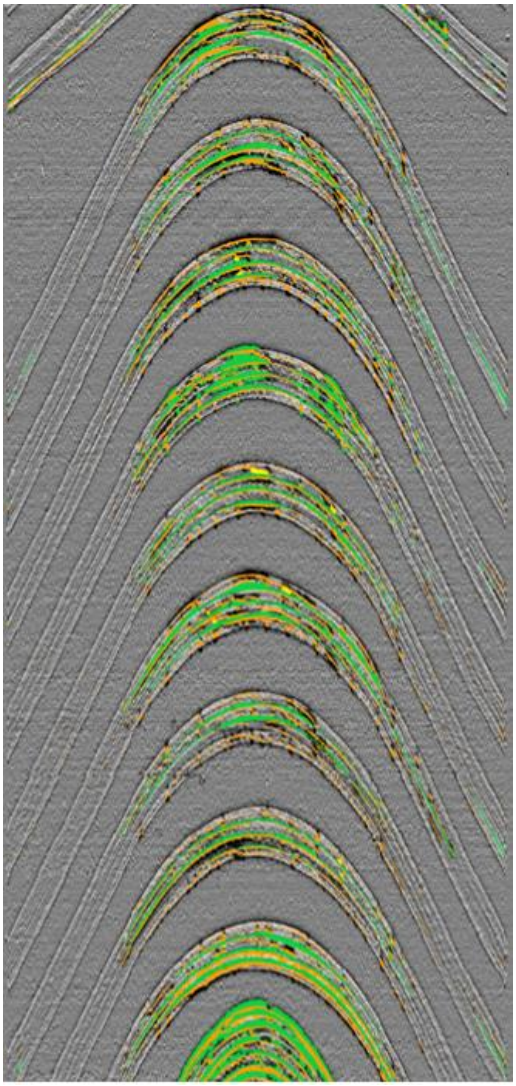

Figure 5.67 Defect detection for the processed scan of the R25 courses

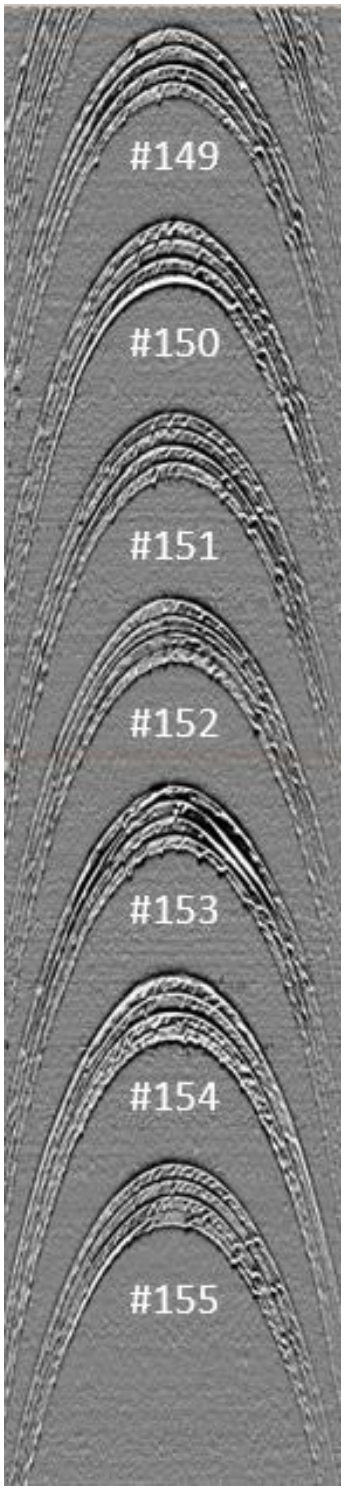

Figure 5.68 Stitched scans for R25

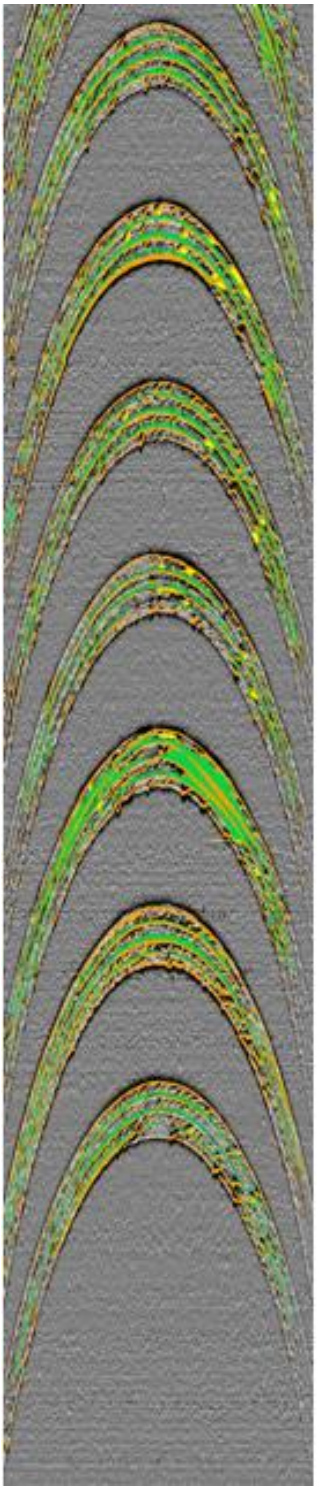

Figure 5.69 Defect detection for the processed scan of the R12.5 courses

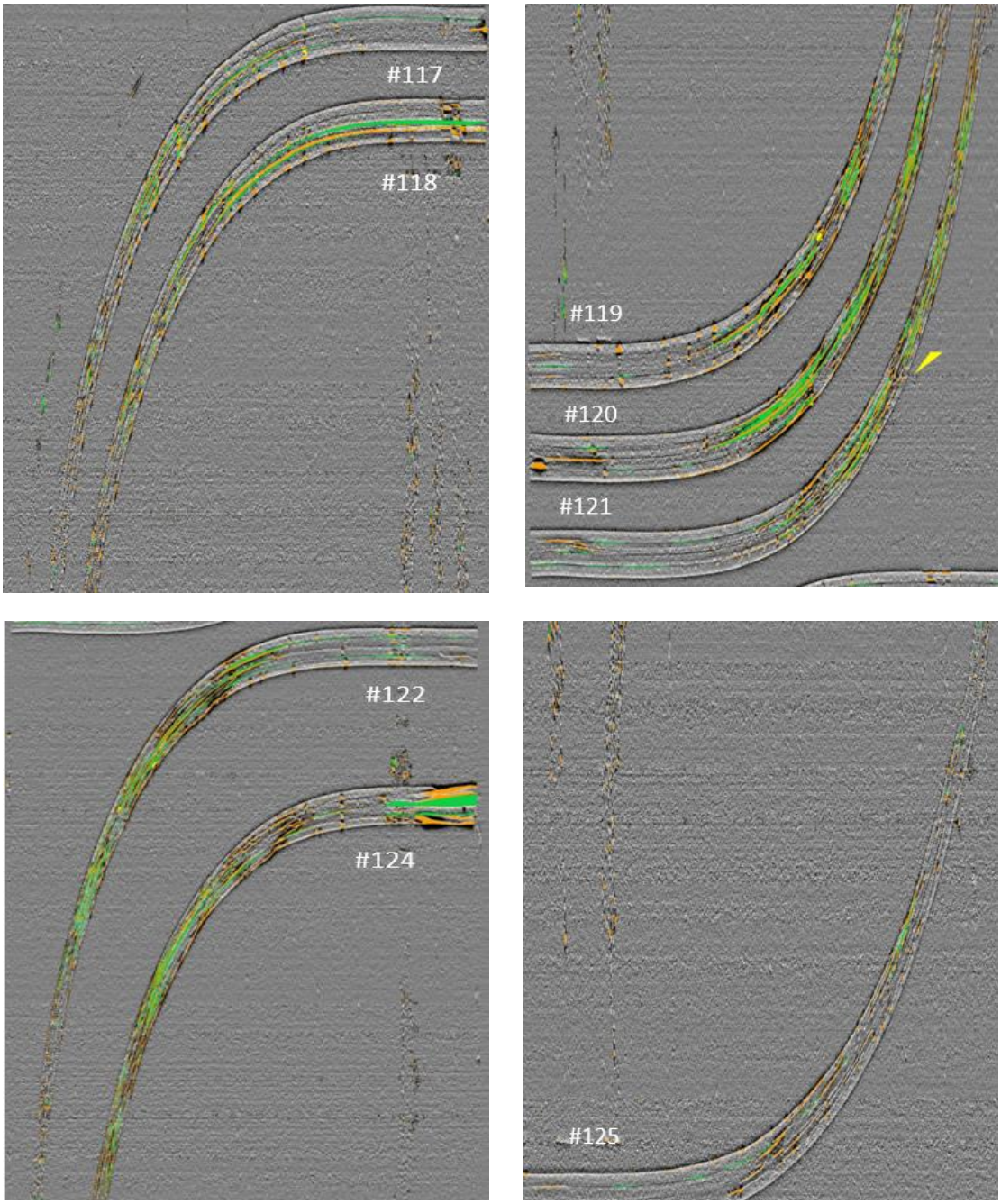

Figure 5.70 Defect detection for the spiral courses

CHAPTER 6

CONLUSIONS AND FUTURE WORK

In order to manufacture complex aerospace structures using the AFP process, the machine head has to follow intricate curved paths while depositing finite-width strips of carbon tows. Due the curved geometry of the tow-path, a length mismatch occurs between the parallel edges of the path, hence the originally straight tow has to somehow deform to adhere to the curved path. The focus of this work is to understand possible mechanisms for tow deformation during the AFP process.

Due to the high anisotropy and inhomogeneity of the uncured thermoset carbon fiber tows used during the AFP process, several deformation mechanisms can occur to absorb the differential length between the parallel edges of the path. These mechanisms are classified into three categories: (1) strain deformations (tensile, compressive and shear), (2) large in-plane deformations (fiber waviness and bunching), and (3) large out-of-plane deformations (tow wrinkling and folding). Usually, large scale deformations are undesirable and are considered as defects. The occurrence of all these deformation mechanisms is investigated from three perspectives: geometrical modeling, physics-based modeling, and experimental investigations.

From a geometrical standpoint, understanding the nature of the curved path is necessary to determine critical locations for defect occurrence. A worst-case scenario is considered where all other deformation mechanisms are suppressed in favor of out-of-plane wrinkling. Governing equations for a tow placed on a general surface are derived, and a

simple deformation function is applied to the shorter edge of tow showing different wrinkle patterns along the length. A simplified form of the governing equations is provided for the special case of tows steered on a flat surface. Using these assumptions, geometrical features such as tow width, path curvature, and number of wrinkles are investigated. Modeling results show that increasing the tow width or the path curvature results in larger wrinkles, whereas increasing the number of wrinkles within the path results in smaller wrinkles. In addition, the geometrical analysis is carried for different angled layups and it is concluded that for the same tool surface, different angled layups have different critical regions for wrinkling. The geometrical model is applied for thermoset materials where information regarding the wrinkles wavelength and width is obtained form available mechanics models in the literature or from experimental measurements. More realistic wrinkles patterns are therefore generated for thermoset layups, where the calculated wrinkles amplitude geometrically falls within the range of the experimentally measured ones.

In the physics-based model, the influence of the relevant material properties and tow geometry on the deformations is studied. A novel modeling approach is presented to capture the different tow deformations mechanisms. Due to high anisotropy of the uncured thermoset tow, the transverse and shear stiffnesses are first neglected, and the tow is modeled as multiple independent fiber bundles laying on a stiff foundation. In a first step, only in-plane deformations are allowed, thus capturing the elastic deformation mode (tensile/compressive strains) and the large in-plane deformations (fiber waviness and bunching). The effect of the foundation stiffness and the steering radius are also studied. In a second step, out-of-plane deformations are allowed, enabling the modeling of additional tow deformations mentioned earlier such as tow wrinkling. Finally, the

interaction between the neighboring fiber bundles is investigated by considering the transverse and shear stiffness properties of the uncured tow. Parametric studies are performed regarding the effect of the uncured transverse and shear stiffness on tow deformations. Results show that at low stiffness values, the fiber bundles behave independently from each other's. However, at larger stiffness values, the fiber bundles have a rigid plate-like behavior.

On the experimental side, and for the first time, measurements of tow deformations for steered path are acquired during manufacturing using stereo DIC. It is concluded that steering at a smaller radius of curvature will increase the amplitude, width and number of wrinkles within a path. In addition, it is determined that imperfections in the substrate act as nucleation sites for wrinkles in steered paths. The time and temperature effects are captured by measuring the amplitude of the wrinkles immediately after placement, an hour after placement, and after applying heat from a neighboring source. It is found that the amplitude of the wrinkles slightly increases after one hour, however, a significant increase in the amplitude is measured after applying heat. Regarding the tensile edge of the tow, large compressive transverse strains are measured (up to $-0.1\,\epsilon$) thus confirming the occurrence of the fiber bunching mechanism.

The effect of the process parameters on tow deformations is investigated experimentally. A path with a linear variation in the curvature is proposed for this study. The path starts with a zero curvature up to a maximum limit beyond which there is no interest in steering. Different combinations of process parameters are used to place tows along the proposed course. The process parameters are assessed based on the location of the first visible defect that occurs along the path which can be related to a critical steering

radius. Better layup quality is obtained at higher nip point temperature, higher compaction pressure, and lower layup speeds. At these conditions, large in-plane deformations (waviness and bunching) are more favorable to occur compared to the large out-of-plane deformations (wrinkling and folding) due to a better adhesion between the tow and the substrate. Finally, steering experiments are performed on a 48” diameter cylindrical mandrel. Controlling the process parameters such as the layup speed and therefore the nip point temperature is more challenging especially when engaging all seven axes of the AFP machine which is necessary to perform the complex steered paths on the cylinder. Several steered paths are placed with different process parameters combinations. Profilometry scanning of the manufactured layups is acquired after fiber placement, and a novel image processing technique is proposed to quantify in-plane and out-of-plane tow deformations. Based on the analyzed scans of the steered paths, recommendations regarding an optimal set of process parameter is provided for future manufacturing activities using similar material.

As this work comes to an end, one can always ask the questions: what is the next step? What can be added to improve and build on what is accomplished? To answer these questions, possible future work is discussed for the three aspects of this work: geometrical modeling, physics based modeling, and experimental investigations.

For the geometrical modeling aspect, including information from mechanics models and experimental measurements is accomplished in this work resulting in a more accurate modeling of wrinkles’ size and occurrence. Including the effect of the process parameters can be a useful addition to this model. From the experimental investigations of the process parameters, relationships between temperature, compaction, layup speed, and

critical radius of curvature can be determined. These relationships can be included in the geometrical model; therefore, the wrinkles wavelength, width, and amplitude do not only depend on the steering radius, but also on the chosen set of process parameters. This can lead to a useful offline AFP programming tool, where for a given layup geometry, tow material, and AFP process parameters, critical locations of defects with approximate sizes and dimensions can be predicted. In addition, once these relationships are established, an optimization for the AFP manufacturing time can be performed by taking into consideration the layup quality or the size of produced defects. A simple prediction of the results of such optimization could be increasing the layup speed in linear regions to reduce manufacturing time, whereas increasing the nip point temperature, increasing compaction pressure, and reducing layup speed at higher curvature locations to reduce defects size.

Regarding the physics-based modeling, to have a more accurate depiction of several tow defamations, an accurate measurement of the uncured material properties of the tow is necessary. This includes, but not limited to, longitudinal, shear, and transverse stiffness, the stiffness of the foundation in the x, y and z-directions. A reasonable reformulation of the stiffness of the foundation can be accomplished in term of the arc-length, radial, and z-directions (s, r, z-coordinates). This can lead to more relatable values from the experimental measurements, especially when considering the effect of the substrate direction when measuring adhesion (or foundation stiffness). In addition, these uncured properties have to be related to the process parameters especially temperature and compaction. Thus, measurements of the uncured material properties of the tow as function of temperature are necessary for better tow deformations modeling. On the other hand, since temperature and compaction may be variable along the tow-path, an expression of

the material properties as function of the arc-length for a given path and set of process parameters may also be necessary. In addition, the time dependency of tow deformations should be addressed: for a given location along the length of path, a temperature and pressure gradient occur during manufacturing. These gradients are captured using thermocouples and pressure sensors in the experimental work presented earlier. Therefore, solving the deformation problem over time with the corresponding measured material properties of the uncured tow can possibly address the time dependency problem of tow deformations. Another improvement to the model is to address the additive nature of the AFP process. The deformation problem has to be solved over different length steps and by taking into considerations the deformed path as an initial solution for the newly added portion of the length. Lastly, two more tow deformation mechanisms are not captured in the bundles concept: tow folding (Figure 5.30) and through thickness tow splitting (Figure 5.33). To capture tow folding, it may be necessary to include the mid-plane twist curvature κ_{xy} and the corresponding measurement of the torsional rigidity of the uncured tow. However, it would be more difficult to capture the through thickness tow splitting in the presented model since a 3D stress gradient is driving this deformation mechanism. Finally, a comparison between the proposed fast solution and other available commercial solvers is necessary to validate the results and to note the improvements in computational time.

From the experimental side, steering on flat and single curvature convex surface (outer surface of the cylinder) is accomplished. In general, aerospace structures can have more complex surfaces, with a possibility of having concave and doubly curved surfaces. Therefore, investigations of tow deformations over such surfaces is necessary for future work where other deformations may be observed such as tow bridging for concave

surfaces. In addition to smooth surfaces, other realistic features in composite structures can be present during AFP such as variable thickness layups with tow drops, pad up regions, gaps, and overlaps. Laying tows on top of such features should be investigated with the possible tow deformations that can occur. Moving from the tool geometry to the process parameters, a full understanding of the roller compaction is needed, especially the dynamic effect of the compaction pressure as function of the layup speed, roller geometry and stiffness. In addition, an accurate measurement of the uncured material properties of the tows should be captured as function of the process parameters. One important property to highlight is tack, and the influence of temperature, compaction, contact time, fiber orientation on its significance should be investigated properly. It has to be noted that keeping a track of the environmental conditions such as room temperature and relative humidity, as well as the out time of uncured material is necessary to obtain accurate measurements of the uncured properties especially tackiness. On the other hand, and from a layup quality assessment point of view, a novel image processing technique is proposed in this work to capture the in-plane and out-of-plane tow deformations. Advanced data analytics techniques can be applied to get better correlations and further understanding of the effect of process parameters especially when having a variable layup speed. Additional image acquisition from experimental trials with variable process parameters and path curvature can pave the way to a data driven predictive model for tow deformations. Such model could also include images/data from a previously laid substrate with existing features or defects, and possibly predict the tow deformations based on these existing features.

Finally, it should be noted that the work presented here focuses on understanding and predicting serval tow deformations for a given layup. However, the persistence of these deformations in successive layers during the additive process is still yet to be researched. For instance, the interaction of the roller with an existing wrinkle or fold in the substrate while laying another course on top of it has not been investigated. For instance, a fold can be flattened down after passing the roller on top of it, or it could transform to a partial overlap over the bottom side of the tow. Similarly, a wrinkle may be suppressed to some form of in-plane waviness. In addition, the persistence of these defects during an autoclave cycle and the final shape of the cured defect within the laminate is still unknown. Proper characterization techniques of the final cured shape of the deformed tow is required. CT scanning, volumetric DIC, or acoustic scanning may be possibly employed for such characterization. Based on the final cured shape of the deformed tow within the laminate, a knock-down factor on the stiffness or strength of the composite laminate can be applied with proper computational work to back it up. Based on the significance of the degradation in the material property of the cured part due to the presence of such tow deformation, it can be determined whether or not the size of a wrinkle or fold during manufacturing is significant, and if necessary, repairs are required.

REFERENCES

[1] Lukaszewicz DHJA, Ward C, Potter KD. The engineering aspects of automated prepreg layup: History, present and future. Compos Part B Eng 2012;43:997–1009. https://doi.org/10.1016/j.compositesb.2011.12.003.

[2] Croft K, Lessard L, Pasini D, Hojjati M, Chen J, Yousefpour A. Experimental study of the effect of automated fiber placement induced defects on performance of composite laminates. Compos Part A Appl Sci Manuf 2011;42:484–91. https://doi.org/10.1016/j.compositesa.2011.01.007.

[3] Eran S, Marder M, Swinney HL. Leaves, Flowers and Garbage Bags: Making Waves. Am Sci 2004;92:254–61. https://doi.org/10.1511/2004.47.932.

[4] Genzer J, Groenewold J. Soft matter with hard skin: From skin wrinkles to templating and material characterization. Soft Matter 2006;2:310. https://doi.org/10.1039/b516741h.

[5] Cerda E, Mahadevan L. Geometry and Physics of Wrinkling. Phys Rev Lett 2003;90:074302. https://doi.org/10.1103/PhysRevLett.90.074302.

[6] Friedl N, Rammerstorfer FG, Fischer FD. Buckling of stretched strips. Comput Struct 2000;78:185–90. https://doi.org/10.1016/S0045-7949(00)00072-9.

[7] Silvestre N. Wrinkling of stretched thin sheets: Is restrained Poisson's effect the sole cause? Eng Struct 2016;106:195–208. https://doi.org/10.1016/j.engstruct.2015.09.035.

[8] Huang ZY, Hong W, Suo Z. Nonlinear analyses of wrinkles in a film bonded to a compliant substrate. J Mech Phys Solids 2005;53:2101–18. https://doi.org/10.1016/j.jmps.2005.03.007.

[9] Gutowski TG, Dillon G, Chey S, Li H. Laminate wrinkling composites scaling laws for ideal. Compos Manuf 1995;6:123–34.

[10] Dodwell TJ, Butler R, Hunt GW. Out-of-plane ply wrinkling defects during consolidation over an external radius. Compos Sci Technol 2014;105:151–9. https://doi.org/10.1016/j.compscitech.2014.10.007.

[11] Çinar K, Ersoy N. Effect of fibre wrinkling to the spring-in behaviour of L-shaped composite materials. Compos Part A Appl Sci Manuf 2015;69:105–14. https://doi.org/10.1016/j.compositesa.2014.10.025.

[12] Dodwell TJ. Internal buckling instabilities in layered media. Philos Mag 2015;6435:1–19. https://doi.org/10.1080/14786435.2015.1034221.

[13] Lightfoot JS, Wisnom MR, Potter K. A new mechanism for the formation of ply wrinkles due to shear between plies. Compos Part A Appl Sci Manuf 2013;49:139–47. https://doi.org/10.1016/j.compositesa.2013.03.002.

[14] Potter KD. Understanding the origins of defects and variability in composites manufacture. 17 Th Int Conf Compos Mater 2009:27–31. https://doi.org/10.1016/j.compositesa.2015.07.008.

[15] Potter K, Khan B, Wisnom M, Bell T, Stevens J. Variability, fibre waviness and misalignment in the determination of the properties of composite materials and structures. Compos Part A Appl Sci Manuf 2008;39:1343–54. https://doi.org/10.1016/j.compositesa.2008.04.016.

[16] Hormann PM. Thermoset automated fibre placement - on steering effects and their prediction. Verlag Dr. Hut, 2016; n.d.

[17] Belhaj M, Hojjati M. Wrinkle formation during steering in automated fiber placement: Modeling and experimental verification. J Reinf Plast Compos 2018;37:396–409. https://doi.org/10.1177/0731684417752872.

[18] Bakhshi N, Hojjati M. An experimental and simulative study on the defects appeared during tow steering in automated fiber placement. Compos Part A Appl Sci Manuf 2018;113:122–31. https://doi.org/10.1016/j.compositesa.2018.07.031.

[19] Smith R, Qureshi Z, Scaife R, El-Dessouky H. Limitations of processing carbon fibre reinforced plastic/polymer material using automated fibre placement technology. J Reinf Plast Compos 2016;35:1527–42. https://doi.org/10.1177/0731684416659544.

[20] Zhao C, Xiao J, Huang W, Huang X, Gu S. Layup quality evaluation of fiber trajectory based on prepreg tow deformability for automated fiber placement. J Reinf Plast Compos 2016;35:1576–85. https://doi.org/10.1177/0731684416659933.

[21] Bakhshi N, Hojjati M. Effect of compaction roller on layup quality and defects formation in automated fiber placement. J Reinf Plast Compos 2019:073168441986884. https://doi.org/10.1177/0731684419868845.

[22] Radwan AB. Experimental Analysis of the Automated Fiber Placement Manufacturing Parameters for High and Low Tack Prepreg Material. University of South Carolina, 2019.

[23] Beakou A, Cano M, Le Cam JB, Verney V. Modelling slit tape buckling during automated prepreg manufacturing: A local approach. Compos Struct 2011;93:2628–35. https://doi.org/10.1016/j.compstruct.2011.04.030.

[24] Matveev MY, Schubel PJ, Long AC, Jones IA. Understanding the buckling behaviour of steered tows in Automated Dry Fibre Placement (ADFP). Compos Part A Appl Sci Manuf 2016;90:451–6. https://doi.org/10.1016/j.compositesa.2016.08.014.

[25] Potter K. Bias extension measurements on cross-plied unidirectional prepreg. Compos - Part A Appl Sci Manuf 2002. https://doi.org/10.1016/S1359-835X(01)00057-4.

[26] Alshahrani H, Mohan R, Hojjati M. Experimental Investigation of In-Plane Shear Deformation of Out-of-Autoclave Prepreg 2015;5:81–7. https://doi.org/10.5923/j.cmaterials.20150504.03.

[27] Bakhshi N, Hojjati M. Time-dependent wrinkle formation during tow steering in automated fiber placement. Compos Part B Eng 2019;165:586–93. https://doi.org/10.1016/j.compositesb.2019.02.034.

[28] López Jiménez F, Pellegrino S. Folding of fiber composites with a hyperelastic matrix. Int J Solids Struct 2012;49:395–407. https://doi.org/10.1016/j.ijsolstr.2011.09.010.

[29] Forghani A. A Physics-Based Modelling Framework for Simulation of Prepreg Tack in AFP Process. SAMPE 2017 Conf. Proceeding, 2017.

[30] Hutten V, Forghani A, Silva P, Hickmott C, Sreekantamurthy T, Wohl C, et al. A Validation Study of a Physics-Based Tack Model for an Automated Fiber Placement Process Simulation. SAMPE Conf. Proc., 2019.

[31] Dubois O, Le Cam JB, Béakou A. Experimental analysis of prepreg tack. Exp Mech 2010;50:599–606. https://doi.org/10.1007/s11340-009-9236-7.

[32] Endruweit A, Choong GYH, Ghose S, Johnson BA, Younkin DR, Warrior NA, et al. Characterisation of tack for uni-directional prepreg tape employing a continuous application-and-peel test method. Compos Part A Appl Sci Manuf 2018. https://doi.org/10.1016/j.compositesa.2018.08.027.

[33] Endruweit A, De Focatiis DSA, Ghose S, Johnson BA, Younkin DR, Warrior NA. Characterization Of Prepreg Tack To Aid Automated Material Placement. SAMPE Conf Proc 2016.

[34] Crossley RJ, Schubel PJ, Warrior NA. Composites : Part A The experimental determination of prepreg tack and dynamic stiffness. Compos Part A 2012;43:423–34. https://doi.org/10.1016/j.compositesa.2011.10.014.

[35] Crossley RJ, Schubel PJ, Focatiis DSA De. Composites : Part A Time – temperature equivalence in the tack and dynamic stiffness of polymer prepreg and its application to automated composites manufacturing. Compos Part A 2013;52:126–33. https://doi.org/10.1016/j.compositesa.2013.05.002.

[36] Wohl C, Palmieri FL, Forghani A, Hickmott C, Bedayat H, Coxon B, et al. Tack measurements of prepreg tape at variable temperature and humidity. CAMX 2017 - Compos Adv Mater Expo 2017;2017-Decem.

[37] Rajan S, Sutton MA, McMakin W, Compton E, Kidane A, Gurdal Z, et al. Characterization of Mode I and Mode II traction–separation laws for cohesive separation of uncured thermoset tows. Int J Fract 2019. https://doi.org/10.1007/s10704-019-00399-1.

[38] Rousseau G, Wehbe R, Halbritter J, Harik R. Automated Fiber Placement Path Planning: A state-of-the-art review. Comput Aided Des Appl 2018;16:172–203. https://doi.org/10.14733/cadaps.2019.172-203.

[39] Chen H, Fuhlbrigge T, Li X. A review of CAD-based robot path planning for spray painting. Ind Robot An Int J 2009;36:45–50. https://doi.org/10.1108/01439910910924666.

[40] Li L, Wang X, Xu D, Tan M. A Placement Path Planning Algorithm Based on Meshed Triangles for Carbon Fiber Reinforce Composite Component with Revolved Shape 2014;1:23–32.

[41] Schueler K, Miller J, Hale R. Approximate Geometric Methods in Application to the Modeling of Fiber Placed Composite Structures. J Comput Inf Sci Eng 2004;4:251. https://doi.org/10.1115/1.1736685.

[42] Shirinzadeh B, Cassidy G, Oetomo D, Alici G, Ang MH. Trajectory generation for open-contoured structures in robotic fibre placement. Robot Comput Integr Manuf 2007;23:380–94. https://doi.org/10.1016/j.rcim.2006.04.006.

[43] Yan L, Chen ZC, Shi Y, Mo R. An accurate approach to roller path generation for robotic fibre placement of free-form surface composites. Robot Comput Integr Manuf 2014;30:277–86. https://doi.org/10.1016/j.rcim.2013.10.007.

[44] Limaiem A, Trochu F. Geometric algorithms for the intersection of curves and surfaces. Comput Graph 1995;19:391–403. https://doi.org/10.1016/0097-8493(95)00009-2.

[45] Blom AW, Tatting BF, Hol JMAM, Gürdal Z. Fiber path definitions for elastically tailored conical shells. Compos Part B Eng 2009;40:77–84. https://doi.org/10.1016/j.compositesb.2008.03.011.

[46] Han Z, Qiangqiang F, Fan Y, Yunzhong F, Hongya F. A Path Planning Algorithm of Closed Surface for Fiber Placement. Proc 1st Int Conf Mech Eng Mater Sci 2012:509–12. https://doi.org/10.2991/mems.2012.100.

[47] Hély C, Birglen L, Xie WF. Feasibility study of robotic fibre placement on intersecting multi-axial revolution surfaces. Robot Comput Integr Manuf 2017;48:73–9. https://doi.org/10.1016/j.rcim.2017.02.005.

[48] Lopes CS, Gürdal Z, Camanho PP. Variable-stiffness composite panels: Buckling and first-ply failure improvements over straight-fibre laminates. Comput Struct 2008;86:897–907. https://doi.org/10.1016/j.compstruc.2007.04.016.

[49] Blom AW, Abdalla MM, Gürdal Z. Optimization of course locations in fiber-placed panels for general fiber angle distributions. Compos Sci Technol 2010;70:564–70. https://doi.org/10.1016/j.compscitech.2009.12.003.

[50] Kim BC, Potter K, Weaver PM. Continuous tow shearing for manufacturing variable angle tow composites. Compos Part A Appl Sci Manuf 2012;43:1347–56. https://doi.org/10.1016/j.compositesa.2012.02.024.

[51] HONDA S, NARITA Y, SASAKI K. Maximizing the Fundamental Frequency of Laminated Composite Plates with Optimally Shaped Curvilinear Fibers. J Syst Des Dyn 2009;3:867–76. https://doi.org/10.1299/jsdd.3.867.

[52] Waldhart C. Analysis of Tow-Placed , Variable-Stiffness Laminates. Virginia Polytechnic Institute and State University, 1996.

[53] Gray A. Modern differential Geometry of Curves and Surfaces with Mathematica. Second Edi. CRC Press LLC; 1998.

[54] Gálvez A, Iglesias A, Puig-Pey J. Computing parallel curves on parametric surfaces. Appl Math Model 2014;38:2398–413. https://doi.org/10.1016/j.apm.2013.10.042.

[55] Bruyneel M, Zein S. A modified Fast Marching Method for defining fiber placement trajectories over meshes. Comput Struct 2013;125:45–52. https://doi.org/10.1016/j.compstruc.2013.04.015.

[56] Wehbe R, Tatting BF, Harik R, Gürdal Z, Halbritter A, Wanthal S. Tow-path based modeling of wrinkling during the automated fiber placement process. CAMX 2017 - Compos. Adv. Mater. Expo, 2017.

[57] Wehbe R. Modeling Of Tow Wrinkling In Automated Fiber Placement Based On Geometrical Considerations. University of South Carolina, 2017.

[58] Blom AW, Setoodeh S, Hol JMAM, Gürdal Z. Design of variable-stiffness conical shells for maximum fundamental eigenfrequency. Comput Struct 2008;86:870–8. https://doi.org/10.1016/j.compstruc.2007.04.020.

[59] Rajan S, Sutton MA, Wehbe R, Tatting B, Gürdal Z, Kidane A, et al. Experimental investigation of prepreg slit tape wrinkling during automated fiber placement process using StereoDIC. Compos Part B Eng 2019;160:546–57. https://doi.org/10.1016/j.compositesb.2018.12.017.

[60] Piegl L, Tiller W. The NURBS book. Second Edi. Springer; 1997.

[61] Wehbe RY, Harik R, Gurdal Z. In-plane tow deformations due to steering in automated fiber placement. AIAA Scitech 2019 Forum, Reston, Virginia: American Institute of Aeronautics and Astronautics; 2019. https://doi.org/10.2514/6.2019-1271.

[62] Sacco C, Radwan AB, Harik R, Tooren M Van. Automated Fiber Placement Defects: Automated Inspection and Characterization. SAMPE 2018 Conf. Proceeding, Long Beach, California: 2018.

[63] Sacco C, Baz Radwan A, Beatty T, Harik R. Machine learning based AFP inspection: A tool for characterization and integration. Int. SAMPE Tech. Conf., 2019. https://doi.org/10.33599/nasampe/s.19.1594.

[64] Sacco C. Machine Learning Methods for Rapid Inspection of Automated Fiber Placement Manufactured Composite Structures. University of South Carolina, 2019.

APPENDIX A

NUMERICAL SOLUTION FOR NONLINEAR SYSTEMS OF DIFFERENTIAL EQUATIONS

The derived governing equations for the tow deformations in Chapter 4 are presented in the form of a system of first and second order nonlinear differential equations. The boundary conditions for the governing equations can be specified at each end of the tow. Problem of this type are termed Boundary Value Problems (BVP), as opposed to Initial Value Problems (IVP) where the conditions are specified at one point of the domain. An efficient method to solve linear ordinary differential equations (ODEs) with BVP type is the finite difference technique. However, a linearization of the system of equations is required first. Therefore, Newton's method is used to linearize the equations, and then the finite difference technique is used to transform the linearized system of ODEs into a system of algebraic equations. Then the boundary conditions are applied accordingly, and the

A.1 NEWTON'S METHOD FOR NONLINEAR PROBLEMS

The governing equations describing the tow deformations for the in-plane case (4.68) and the out-of-plane case (4.76) can be rearranged along with the geometrical relations between the x, y, z-coordinates and the strain-rotations into the form of:

$$\mathbf{f}(s, \boldsymbol{F}, \boldsymbol{X}, \boldsymbol{X}', \boldsymbol{X}'') = 0 \tag{A.1}$$

where $\mathbf{f}$ is a system of nonlinear equations, s is the variable along the length, $\boldsymbol{F} = \left\{f_{x_i}, f_{y_i}, f_{z_i}\right\}$ is the force vector containing the unknown constant forces at the endpoint (do

not depend on the arclength), and $\boldsymbol{X} = \{\gamma_i, \beta_i, l_i, x_i, y_i, z_i, \xi_i, \psi_i, \zeta_i\}$ is a vector containing the unknown functions. $\boldsymbol{X}'$ and $\boldsymbol{X}''$ are the derivative of $\boldsymbol{X}$ with respect to s, and $i = 1, \dots, n$, n being the number of considered bundles within the tow. The idea is to assume initial solutions $\boldsymbol{X_0}(s)$ and $\boldsymbol{F_0}$ satisfying the boundary conditions, and to find a solution that satisfies the nonlinear system $\mathfrak{f}$ in the neighborhood of $\boldsymbol{X_0}(s)$ and $\boldsymbol{F_0}$. In essence, a perturbation is applied to the independent variable s and the unknowns $\boldsymbol{F}$ such that:

$$\boldsymbol{X}(s) = \boldsymbol{X_0}(s) + \delta\boldsymbol{X}(s) \text{ and } \boldsymbol{F} = \boldsymbol{F_0} + \delta\boldsymbol{F}. \tag{A.2}$$

Substituting (A.2) into (A.1) and performing a Taylor series expansion at $\boldsymbol{X_0}(s)$ and $\boldsymbol{F_0}$ results in the following:

$$\begin{aligned} &\frac{\partial \mathfrak{f}}{\partial \boldsymbol{X}}\Big|_{\boldsymbol{X_0},\boldsymbol{F_0}} \cdot \delta\boldsymbol{X} + \frac{\partial \mathfrak{f}}{\partial \boldsymbol{X}'}\Big|_{\boldsymbol{X_0},\boldsymbol{F_0}} \cdot \delta\boldsymbol{X}' + \frac{\partial \mathfrak{f}}{\partial \boldsymbol{X}''}\Big|_{\boldsymbol{X_0},\boldsymbol{F_0}} \cdot \delta\boldsymbol{X}'' + \frac{\partial \mathfrak{f}}{\partial \boldsymbol{F}}\Big|_{\boldsymbol{X_0},\boldsymbol{F_0}} \cdot \delta\boldsymbol{F} + \boldsymbol{\mathcal{O}}(\delta^2) \\ &\qquad = -\mathfrak{f}(s, \boldsymbol{F_0}, \boldsymbol{X_0}, \boldsymbol{X_0'}, \boldsymbol{X_0''}) \,. \end{aligned} \tag{A.3}$$

If the initial solutions $\boldsymbol{X_0}(s)$ and $\boldsymbol{F_0}$ are close to the correct one, the term on the right-hand side will be close to zero as well as $\delta\boldsymbol{X}$ and $\delta\boldsymbol{F}$. Hence, the error term $\boldsymbol{\mathcal{O}}(\delta^2)$ can be neglected, and equation (A.3) is a linear system of ODE in $\delta\boldsymbol{X}$ and containing unknown constants $\delta\boldsymbol{F}$. The final solution is obtained by solving for $\delta\boldsymbol{X}$ and $\delta\boldsymbol{F}$ in (A.3) and updating the corresponding values of $\boldsymbol{X}(s)$ and $\boldsymbol{F}$ in (A.2) over several iteration until convergence is achieved. Convergence can be set such that the magnitude of the right-hand side is technically zero, or the increments $\delta\boldsymbol{X}$ and $\delta\boldsymbol{F}$ are negligible.

A.2 FINITE DIFFERENCE TECHNIQUE FOR LINEAR ODE

The finite difference technique used to solve the system of linear ODEs (A.3) consists of discretizing the domain of interest $0 \leq s \leq L$ into several intervals separated by a finite distance Δ (Figure A.1). Then, the unknown functions and their derivatives are

approximated by their values at the discretized points within the domain. The derivatives are approximated based on their definition through the theory of limits by replacing the parameters h with the finite step Δ:

$$\delta \boldsymbol{X}'(s) = \lim_{h \to 0} \frac{\delta \boldsymbol{X}(s+h) - \delta \boldsymbol{X}(s)}{h} \approx \frac{\delta \boldsymbol{X}(s+\Delta) - \delta \boldsymbol{X}(s)}{\Delta}. \tag{A.4}$$

Hence, at each point termed with the superscript j, where $j = 0, \dots, N$, the first derivatives can be expressed as:

$$\delta \boldsymbol{X}'^{(j)} \approx \frac{\delta \boldsymbol{X}^{(j+1)} - \delta \boldsymbol{X}^{(j)}}{\Delta}. \tag{A.5}$$

This approximation is termed "forward difference", and it will be used to approximate the first order derivatives. For the second order derivatives, a "central difference" technique is used such as:

$$\delta \boldsymbol{X}''^{(j)} \approx \frac{\delta \boldsymbol{X}^{(j+1)} - 2\delta \boldsymbol{X}^{(j)} + \delta \boldsymbol{X}^{(j-1)}}{\Delta^2}. \tag{A.6}$$

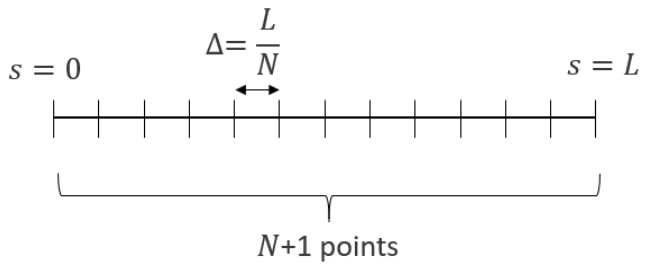

Figure A.1 Finite difference region of interest

Replacing the approximations of the first and second order derivatives (A.5) and (A.6) into the linearized system (A.3) and rearranging:

$$M_1 \cdot \delta \boldsymbol{X}^{(j-1)} + M_2 \cdot \delta \boldsymbol{X}^{(j)} + M_3 \cdot \delta \boldsymbol{X}^{(j+1)} + M_4 \cdot \delta \boldsymbol{F} = -\mathbf{f}_0^{(j)} \tag{A.7}$$

where the matrices M_1 through M_4 are expressed as:

$$M_1 = -\frac{1}{\Delta}\frac{\partial \tilde{\mathbf{f}}}{\partial \boldsymbol{X}'}\Big|_{\boldsymbol{X_0},\boldsymbol{F_0}} + \frac{1}{\Delta^2}\frac{\partial \tilde{\mathbf{f}}}{\partial \boldsymbol{X}''}\Big|_{\boldsymbol{X_0},\boldsymbol{F_0}}, \tag{A.8}$$

$$M_2 = \frac{\partial \tilde{\mathbf{f}}}{\partial \boldsymbol{X}}\Big|_{\boldsymbol{X_0},\boldsymbol{F_0}} + \frac{1}{\Delta}\frac{\partial \tilde{\mathbf{f}}}{\partial \boldsymbol{X}'}\Big|_{\boldsymbol{X_0},\boldsymbol{F_0}} - \frac{2}{\Delta^2}\frac{\partial \tilde{\mathbf{f}}}{\partial \boldsymbol{X}''}\Big|_{\boldsymbol{X_0},\boldsymbol{F_0}}, \tag{A.9}$$

$$M_3 = \frac{1}{\Delta^2}\frac{\partial \tilde{\mathbf{f}}}{\partial \boldsymbol{X}''}\Big|_{\boldsymbol{X_0},\boldsymbol{F_0}}, \tag{A.10}$$

$$M_4 = \frac{\partial \tilde{\mathbf{f}}}{\partial \boldsymbol{F}}\Big|_{\boldsymbol{X_0},\boldsymbol{F_0}}. \tag{A.11}$$

Equation (A.7) represents a set of $(N+1)$ algebraic equations with $\delta\boldsymbol{X}^{(j)}$ being the unknowns. In addition, $3n$ equations must be supplied along with (A.7) in order to solve for the remaining $3n$ unknowns $\delta\boldsymbol{F}$. Those $3n$ equations are based on the additional enforced boundary conditions at the end point and will be discussed in the next section. Hence, (A.7) and the additional $3n$ equations can be arranged in matrix form (Figure A.2):

$$\mathcal{M} \cdot \boldsymbol{\mathcal{X}} = \boldsymbol{\mathcal{B}}, \tag{A.12}$$

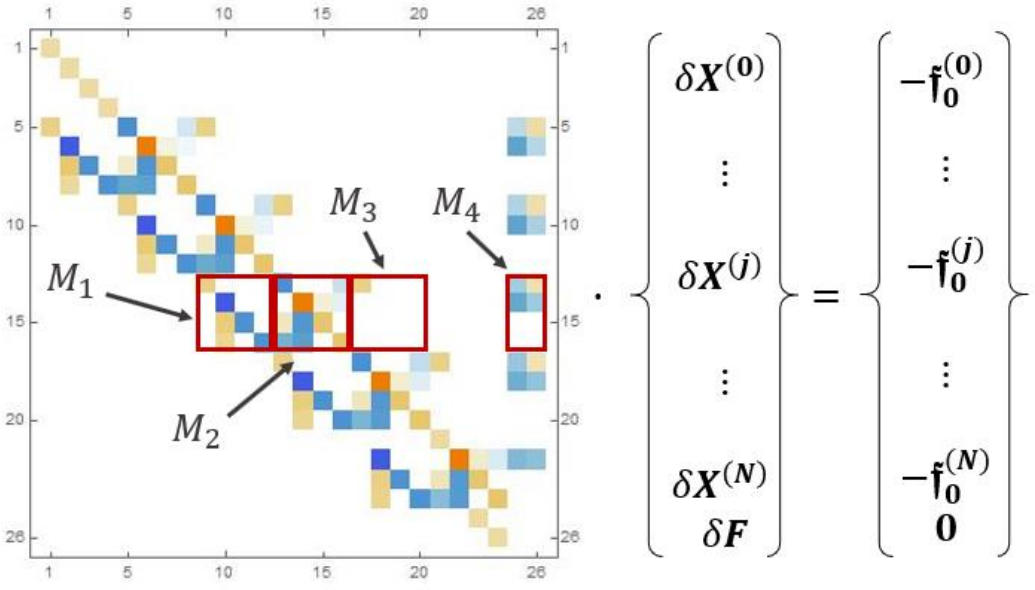

Figure A.2 The governing algebraic equations in matrix form

where the final matrix $\mathcal{M}$ can be assembled from a sparse matrix having the sub-matrices M_1 through M_3 as diagonals, and M_4 as the last column. The matrices M_1 through M_4 are evaluated at each point j. The vector $\boldsymbol{\mathcal{X}}$ contains the unknowns $\delta\boldsymbol{X}^{(j)}$ and $\delta\boldsymbol{F}$. The vector $\boldsymbol{\mathcal{B}}$ includes the original system evaluated at the initial conditions $-\mathbf{f}_{\mathbf{0}}^{(j)}$ and a $3n$ zero vector corresponding to the additional boundary condition equations. The final system is visualized in the form of matrix plot in Figure A.2.

A.3 INITIAL & BOUNDARY CONDITIONS

The governing equations describing the tow deformations for the in-plane case (4.68) and the out-of-plane case (4.76) contain second order differential equations in terms of γ_i and β_i, hence two boundary conditions need to be supplied for each of these variables. These conditions are supplied at the start point : $\gamma_i(0) = 0, \beta_i(0) = 0$,and the end point $\gamma_i(L) = \gamma_{i_L}$, $\beta_i(L) = 0$. For the remaining variables $l_i, x_i, y_i, z_i, \xi_i, \psi_i$ and ζ_i, the governing equations contain only their first derivatives, hence only conditions at the starting point need to be provided. These conditions can be generalized from the conditions of a single bundle deforming in 3D as described in equation (4.52) and applied to a system of n bundles. Lastly, by enforcing the coordinates of the end-point for each bundle, $3n$ equations can be generated and added to (A.7) thus enabling us to solve for the unknowns $\delta\boldsymbol{F}$. These boundary conditions can be expressed in the following form:

$$\{x_i(L), y_i(L), z_i(L)\} = \{x_{i_L}, y_{i_L}, \mathbf{0}\}. \tag{A.13}$$

Regarding the initial conditions, Newton's method for nonlinear system requires an estimation of the initial solutions $\boldsymbol{X_0}(s)$ and $\boldsymbol{F_0}$ satisfying the boundary conditions. These conditions are derived based on the assumption that each placed bundle will remain in its intended location and no other deformation mechanisms will occur except tensile and

compressive strains. Hence, if the steering radius is considered constant, the in-plane rotation angle is a linear function of the arclength satisfying the boundary conditions as follows:

$$\gamma_{i_0}(s) = \frac{\gamma_{i_L}}{L} s \,. \tag{A.14}$$

The above assumption results in the suppression of all out-plane, transverse, and shear deformations. Therefore, the initial conditions for the variables related to the out-of-plane cases are set equal to zero:

$$z_{i_0}(s) = \xi_{i_0}(s) = \psi_{i_0}(s) = \zeta_{i_0}(s) = 0 \,. \tag{A.15}$$

Regarding an initial condition for the coordinates $x_{i_0}(s), y_{i_0}(s)$ and the length $l_{i_0}(s)$, inserting (A.14) into the geometrical relations (4.9) and (4.10), integrating, and applying both boundary conditions at $s = 0$ and $s = L$, the following initial conditions can be obtained:

$$x_{i_0}(s) = \frac{x_{i_L}}{\sin\gamma_{i_L}} \sin\left(\frac{\gamma_{i_L}}{L} s\right), \tag{A.16}$$

$$y_{i_0}(s) = \frac{-y_{i_L}}{1-\cos\gamma_{i_L}} \cos\left(\frac{\gamma_{i_L}}{L} s\right) + \frac{y_{i_L}}{1-\cos\gamma_{i_L}}, \tag{A.17}$$

$$l_{i_0}(s) = \left(\frac{x_{i_L}\gamma_{i_L}}{L\ \sin\gamma_{i_L}} - 1\right) s \,. \tag{A.18}$$

Regarding the initial conditions for the out-of-plane rotation angles $\beta_{i_0}(s)$ it can be shown from the second equation of (4.51) that:

$$\beta_{i_0}(s) = c_1 \sin\left(\frac{m\,\pi}{L} s\right), \quad m = 0,1,2,\ldots \tag{A.19}$$

In order to obtain (A.19), in-plane and out-of-plane rotations are assumed to be small, the effect of the stiffness of the foundation is neglected, and the bundles are considered to

behave independently, thus resulting in a second order ODE in β. In (A.19), m is the mode shape of the deformation and c_1 is a constant usually taken as a very small number (~ 0.001, a small perturbation near 0). For $m = 0$, all out-of-plane deformations are automatically suppressed resulting only in in-plane deformations. For $m = 2$, the solution usually converges to a single out-of-plane wrinkle (under compression). There is no interest in higher even integers mode shapes. For the case where m is an odd integer, the resulting shape is unrealistic since the z-displacement will have to go through the placement surface in the negative z-direction.

Lastly, the initial conditions regarding the forces $\boldsymbol{F_0}$, are taken to be equal to zero:

$$\boldsymbol{F_0} = \mathbf{0} \tag{A.20}$$

Since the assumed initial conditions (A.14) through (A.19) satisfy the boundary conditions, the increments in Newton's method $\delta \boldsymbol{X}$ at the specified start and end points are identically zero thus satisfying (A.2). Therefore, the necessary BCs to be imposed on (A.12) are as follow:

$$\text{at } j = 0,\ \delta \boldsymbol{X}^{(\mathbf{0})} = \mathbf{0}, \tag{A.21}$$

$$\text{at } j = N,\ \delta \gamma_i^{(N)} = \delta \beta_i^{(N)} = 0\,. \tag{A.22}$$

Lastly, using (A.13) and satisfying the increments in Newton's method in (A.2), the additional $3n$ equations to be added to (A.7) are expressed as:

$$\left\{\delta x_i^{(N)}, \delta y_i^{(N)}, \delta z_i^{(N)}\right\} = \{\mathbf{0}, \mathbf{0}, \mathbf{0}\}\,. \tag{A.23}$$

Imposing the boundary conditions (A.21) through (A.23) to the system of equation (A.12) is visualized below in a matrix plot (see Figure A.3). The system (A.12), after adequately applying the boundary conditions, can be solved efficiently using LU

decomposition since the matrix $\mathcal{M}$ is sparse and has the lower triangular part barely populated.

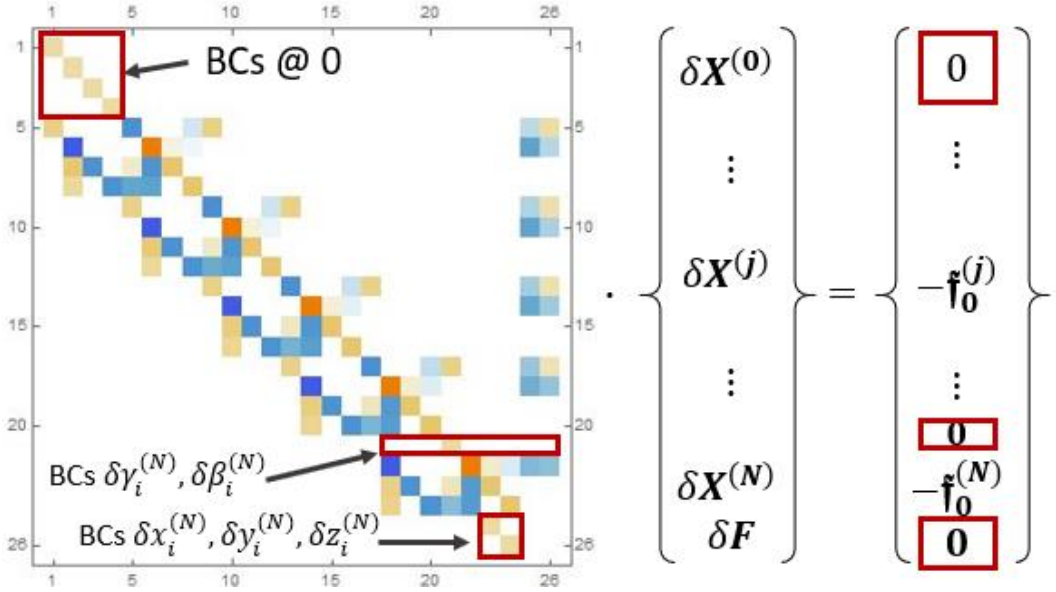

Figure A.3 Boundary conditions applied to the system of algebraic equations

APPENDIX B

CRITICAL RADIUS OF CURVATURE AS FUNCTION OF PROCESS PARAMETERS FOR THE SPIRAL TESTS

The details regarding the critical radius of curvature for the first visible defect during the investigation of the AFP process parameters experiments are reported here. For each course, the AFP settings are reported in the following order: percentage of the programmed speed (%), compaction force (N), heater voltage (V), and tow tension (N). The tows are numbered from 1 to 8, where tow number 1 corresponds to the one in the inner vicinity of the curved path (mostly under compression), and tow number 8 corresponds to the one in the outer vicinity of the curved path (mostly under tension). The type of the first visible defect (wrinkle, fold, waviness, and split) for each tow is noted as well. Cases where tows are not fed from the machine head are noted as missing, other cases where the tow did not adhere to the substrate are noted as having an infinite critical radius with a peel off defect.

Test	**Course#**	**S(%),P(N),T(V),t(N)**	**Tow#**	**R_{crit} (mm)**	**Defect**
Speed	**101**	**(20,445,150,3)**	1	857.8178878	Wrinkle
			2	719.2666085	Wrinkle
			3	719.2666085	Wrinkle
			4	611.5336262	Wrinkle
			5	536.7136565	Wrinkle
			6	628.7127648	Fold
			7	646.8294673	Wrinkle
			8	587.3189429	Wrinkle
Speed	**102**	**(40,445,150,3)**	1	857.8178878	Wrinkle
			2	825.7652013	Wrinkle

			3	857.8178878	Wrinkle
			4	892.6144293	Wrinkle
			5	841.4694581	Wrinkle
			6	930.5235333	Wrinkle
			7	743.112764	Wrinkle
			8	841.4694581	Wrinkle
Speed	**103**	**(60,445,150,3)**	1	1185.010227	Wrinkle
			2	1017.484916	Wrinkle
			3	911.1545442	Wrinkle
			4	857.8178878	Wrinkle
			5	675.9968758	Wrinkle
			6	825.7652013	Wrinkle
			7	782.1503017	Wrinkle
			8	696.9479638	Wrinkle
Speed	**104**	**(100,445,150,3)**	1	Missing	
			2	841.4694581	Wrinkle
			3	Missing	
			4	810.6670819	Wrinkle
			5	Missing	
			6	743.112764	Wrinkle
			7	Missing	
			8	Infinity	Peel off
Temperature	**101**	**(40,445,100,3)**	1	Infinity	Peel off
			2	Infinity	Peel off
			3	Infinity	Peel off
			4	Infinity	Peel off
			5	Infinity	Peel off
			6	Infinity	Peel off
			7	Infinity	Peel off
			8	Infinity	Peel off
Temperature	**102**	**(40,445,125,3)**	1	838.2783307	Wrinkle
			2	825.7652013	Wrinkle
			3	644.9726917	Wrinkle
			4	825.7652013	Fold
			5	686.3107154	Wrinkle
			6	696.9479638	Wrinkle
			7	Infinity	Peel off
			8	Infinity	Peel off
Temperature	**103**	**(40,445,175,3)**	1	696.9479638	Wrinkle
			2	523.4804754	Wrinkle
			3	523.4804754	Wrinkle
			4	557.5112115	Wrinkle

			5	468.837113	Wrinkle
			6	474.5777565	Wrinkle
			7	510.6933751	Fold
			8	543.5130215	Wrinkle
Temperature	**104**	**(40,445,200,3)**	1	768.6680803	Wrinkle
			2	707.9268129	Wrinkle
			3	620.0121467	Wrinkle
			4	394.3334171	Wrinkle
			5	384.3721745	Split
			6	572.0915044	Split
			7	492.2512825	Split
			8	425.1148673	Wrinkle
Compaction	**101**	**(40,178,125,3)**	1	1041.943818	Wrinkle
			2	950.7774597	Wrinkle
			3	892.6144293	Wrinkle
			4	810.6670819	Wrinkle
			5	782.1503017	Wrinkle
			6	743.112764	Wrinkle
			7	743.112764	Wrinkle
			8	796.1397489	Wrinkle
Compaction	**102**	**(40,300,125,3)**	1	1185.010227	Wrinkle
			2	1041.943818	Wrinkle
			3	743.112764	Wrinkle
			4	911.1545442	Wrinkle
			5	665.9893222	Wrinkle
			6	930.5235333	Wrinkle
			7	782.1503017	Wrinkle
			8	755.6644766	Wrinkle
Compaction	**103**	**(40,600,125,3)**	1	874.8514719	Wrinkle
			2	857.8178878	Wrinkle
			3	755.6644766	Wrinkle
			4	517.0341067	Waviness
			5	486.2807376	Waviness
			6	620.0121467	Wrinkle
			7	611.5336262	Wrinkle
			8	646.8294673	Wrinkle
Compaction	**104**	**(40,750,125,3)**	1	810.6670819	Wrinkle
			2	767.8746422	Wrinkle
			3	550.4431608	Wrinkle
			4	536.7136565	Waviness
			5	486.2807376	Wrinkle
			6	550.4431608	Wrinkle

			7	564.7246882	Wrinkle
			8	530.0382872	Split
Tow Tension	**101**	**(40,445,150,0)**	1	620.0121467	Wrinkle
			2	543.5130215	Wrinkle
			3	620.0121467	Wrinkle
			4	579.6199953	Wrinkle
			5	517.0341067	Wrinkle
			6	492.2512825	Wrinkle
			7	564.7246882	Wrinkle
			8	520.8888866	Wrinkle
Tow Tension	**102**	**(40,445,150,1.5)**	1	755.6644766	Wrinkle
			2	768.6680803	Wrinkle
			3	782.1503017	Fold
			4	768.6680803	Wrinkle
			5	665.9893222	Wrinkle
			6	696.9479638	Wrinkle
			7	530.0382872	Wrinkle
			8	782.1503017	Wrinkle
Tow Tension	**103**	**(40,445,150,5)**	1	665.9893222	Wrinkle
			2	857.8178878	Fold
			3	696.9479638	Wrinkle
			4	743.112764	Wrinkle
			5	719.2666085	Wrinkle
			6	911.1545442	Fold
			7	603.2657325	Fold
			8	825.7652013	Fold
Tow Tension	**104**	**(40,445,150,10)**	1	646.8294673	Wrinkle
			2	857.8178878	Fold
			3	782.1503017	Wrinkle
			4	874.8514719	Fold
			5	572.0915044	Wrinkle
			6	971.9771988	Fold
			7	686.3107154	Wrinkle
			8	707.9268129	Fold
High SPT	**101**	**(60,600,175,3)**	1	543.5130215	Wrinkle
			2	468.837113	Wrinkle
			3	543.5130215	Wrinkle
			4	474.5777565	Waviness
			5	404.4362556	Wrinkle
			6	486.2807376	Fold
			7	404.4362556	Fold
			8	492.2512825	Wrinkle

High SPT	**102**	**(60,600,200,3)**	1	530.0382872	Wrinkle
			2	611.5336262	Wrinkle
			3	377.4784678	Wrinkle
			4	536.7136565	Waviness
			5	318.0527212	Waviness
			6	369.6758978	Wrinkle
			7	543.5130215	Split
			8	463.1652684	Wrinkle
High SPT	**103**	**(60,750,175,3)**	1	730.9879441	Wrinkle
			2	550.4431608	Wrinkle
			3	419.8817104	Wrinkle
			4	536.7136565	Split
			5	452.0139526	Wrinkle
			6	1052.072038	Wrinkle
			7	414.6921586	Waviness
			8	369.6758978	Fold
High SPT	**104**	**(60,750,200,3)**	1	665.9893222	Waviness
			2	665.9893222	Wrinkle
			3	374.54318	Wrinkle
			4	483.9153782	Split
			5	452.0139526	Waviness
			6	322.6044965	Wrinkle
			7	465.4259827	Split
			8	452.0139526	Split